JOHANNES GUTENBERG UNIVERSITÄT MAINZ

JG|U

Behavioural and Neuroanatomical Analysis of a Visual Working Memory in *Drosophila melanogaster*

Dissertation

to attain the degree of a

Doctor of Science

from the Department of Biology at Johannes Gutenberg-University Mainz

Anjana Venkataramanan

Born on 16th July, 1992 in Chennai, India

Mainz, April 2020

Date of examination: 4th June, 2020

Table of contents

1. Introduction

1.1 Spatial orientation and memory in insects

"Spatial orientation" is required by almost all species to go about their natural lives. For this purpose, it is important that the organism is aware of its position in space with respect to other objects. In case of humans, this skill, also termed as "spatial navigation", depends on an internal representation that can be seen as a "cognitive map". The cognitive map improves with time as more features and details are added to it every time a person follows the same path, thereby creating a sense of "spatial memory". In case of mammals, this internal map is drawn with the help of the "grid cells" in the meso entorhinal cortex (MEC), and the "place cells" of the hippocampus (Moser et al., 2014). The hexagonal grid cells are activated based on the animal's movement and change in location. Whereas, the place cells, have a strictly site-specific receptive field without any correlation between the firing rate and the change of environment faced by the animal.

Insects on the other hand, rely on their own navigation system which is also based on visually driven spatial memories, known as "path integration" (Collett, 2009; Cruse and Wehner, 2011). This spatial memory has been recorded in insects such as desert ants (*Cataglyphis fortis*), and honeybees (*Apis mellifera*), which always manage to return to the nest after foraging. Path integration also enables the organism to return to a reliable source of food. Navigation using path integration does not require any previous memory of the landscape and is thus extremely useful in novel landscapes (Collett et al., 2013). In case of desert ants in featureless landscapes, this phenomenon relies on the insect's knowledge of its current position, based on summing up its own movements, corrected by receiving directional information from the position of the Sun (Wehner and Muller, 2006). The possibility of ants using a "step integrator system" to calculate the distance travelled, has also been explored (Wittlinger et al., 2006). Honeybees are known to derive additional distance information by monitoring of the optic flow (Srinivasan et al., 1996). One of the key features of path integration which separates it from other types of navigation is that it allows for the organism to redirect its path after a temporary distraction or detour. In 2018, it was reported that the fruit fly, *Drosophila melanogaster* also performs its visual orientation tasks using the Sun as a celestial visual cue to maintain a specific angle towards it, using a special set of neurons called the

"compass neurons" (Giraldo et al., 2018). These neurons, which belong to the central complex of the fly brain, will be addressed in detail in the upcoming chapters of this dissertation. In addition, flies show another independent orientation behaviour called "stripe fixation" (also governed by compass neurons), where tethered flies in a closed loop experiment, orient towards darker regions of a given visual field, if these regions are longer stripes than shorter ones, since the latter are perceived by the flies as spots (Maimon et al., 2008).

In this doctoral dissertation, we primarily focus on the mechanism of a visual working memory using a behavioural apparatus called "the detour paradigm" (Neuser et al., 2008), designed specifically to analyse spatial orientation memory in flies. Over the course of the upcoming chapters, we will focus on the functioning of this spatial orientation memory in *Drosophila*, by means of this behavioural setup, through targeted expression of crucial transgenes and manipulation of neuronal functions in the fly's central brain, with the aid of several neurogenetic tools.

1.2 Introduction to *Drosophila melanogaster*

1.2 (a) Why is *Drosophila* a good model organism to study the neuronal underpinnings of behaviour?

"Cognition and behaviour", has remained as one of the fascinating aspects of neuroscience. Our knowledge regarding the working of the brain, and the neurons which govern specific behaviours and traits, is ever-expanding. When it comes to the world of cognitive neuroscience, primates have contributed to a significant portion for our understanding of the neuronal computations that underlie cognitive decisions through physiological and psychological approaches (Borrell, 2019). However, oweing to their complicated neuroanatomy, there is a dearth of knowledge surrounding the identity, and wiring partners of the recorded neurons. This makes it considerably difficult to identify the neurocircuit that governs a particular behaviour (Kazama, 2015).

The commonly known fruit fly (*Drosophila melanogaster*) serves as a simpler, more ethical alternative animal model, where behaviours can be modulated at the level of genes, cells, and circuits. *Drosophila* has consistently remained as a stable asset in our quest to monitor behaviours which are genetically controlled (Baker et al., 2001), and in our understanding of the neuronal wiring (Otsuna and Ito, 2006; Lin

et al., 2007). Research is constantly carried out to uncover newer aspects of the *Drosophila* neural circuit (Olsen and Wilson, 2008), with the use of ever-advancing neurogenetic tools and techniques (Guo et al., 2019), making the field of behavioural neuroscience in *Drosophila*, that much more exciting and accessible.

In addition, flies also exhibit a rich diversity of complex behaviours, many of which resemble those found in mammals, and are governed by convoluted neural circuits. Oweing to their highly developed sensory system, fruit flies have been used to model a plethora of behaviours such as courtship (Siegel and Hall, 1979), aggression (Chen et al., 2002), and the circadian rhythm (Konopka and Benzer, 1971). Recent studies have even utilized the fruit fly to model a motivation-dependent behaviour and a depression-like state (DLS), which is established after enduring stress (Ries et al., 2017). However, in this doctoral dissertation, we will focus mainly on why *Drosophila melanogaster* is an excellent model organism to study visual working memory.

1.2 (b) The *Drosophila* central complex

The *Drosophila* brain consists of approximately 100 pairs of different neuronal lineages (Lee, 2017), and contains approximately 100,000 neurons (Young and Armstrong, 2010b). Different parts of the *Drosophila* brain arise from discrete lineages, many of which have been identified (Spindler and Hartenstein, 2010; Yang et al., 2013). When it comes to the territory of visual orientation and memory of insects, the central complex (CC), previously known as “central body” (Winer, 1977; Armstrong et al., 1995) is at the epicentre of it all (Weir et al., 2014).

As the name suggests, this complex exists as a distinct neuropile at the centre of the insect brain as a collection of different components. The same applies to *Drosophila*, where the primary components (from posterior to anterior) are, the protocerebral bridge (PB), the fan-shaped body (FB), the ellipsoid body (EB) and the paired noduli (NO) (Young and Armstrong, 2010a). Two other closely associated secondary components are, the ventral bodies (VBO), also known as lateral accessory lobes (LAL), and the lateral triangles (LTR; now known as bulb (BU)) (Hanesch et al., 1989). The CC extends its connections to other regions of the fly brain such as the optic loci and the antennal lobes. The “assymetrical body”, a paired structure located ventral to the FB and adjacent to the NO, has been recently included in this neuropil (Wolff and Rubin, 2018). The development of each of these

components, have been revealed to occur at different stages. The PB and the FB are two of the earliest to be formed in the third instar larva stage, while the NO and the EB follow 12 and 24 hours after the initiation of the pupae formation, respectively. As mentioned earlier, each of these structures arise from a particular lineage that can be distinctively identified (Young and Armstrong, 2010a).

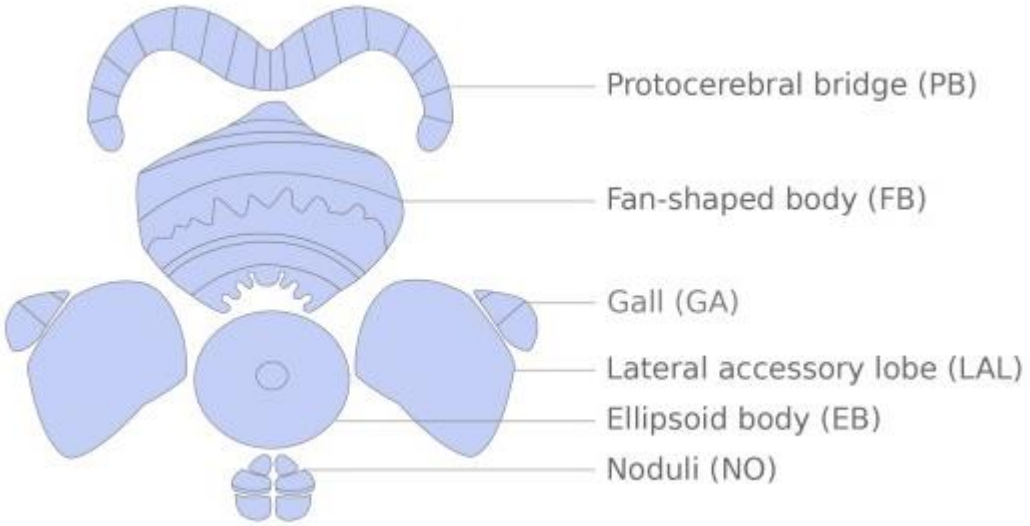

Figure 1: Components of the *Drosophila* central complex

The central complex consists of the handlebar-shaped protocerebral bridge (PB) which consists of 18 glomeruli and is posterior to the multi-layered fan-shaped Body (FB). Anterior to the FB, lies the doughnut-shaped ellipsoid body (EB) consisting of multiple concentric ring neurons. A paired structure called “gall” is on either hemisphere of the EB. Below the EB, lies the paired noduli (NO). Figure adapted from (Franconville et al., 2018).

To distinguish them by appearance, the PB is a curved, rod-shaped structure, located in the dorso-posterior region of the brain, and consists of 18 smaller units called “glomeruli” which are arranged in an array (Wolff et al., 2015). The FB, the largest component of the CC, is a saucer-shaped, three dimensional structure that consists of triangular layers as well as vertical segments. The EB looks like a doughnut with a central canal, which consists of axons, and is composed of concentric zones and radial sectors. Finally, the paired noduli are nearly spherical structures that contain multiple subdomains (Figure 1). In addition, the LAL, the bulb, and the gall are the accessory parts of the CC, and are closely associated with the rest of the structures mentioned above.(Hanesch et al., 1989).

The neurons of the CC can be broadly divided into “small field” and “large field” neurons based on the nature of their innervation pattern. Large field neurons predominantly arborize in one substructure, but have connections in one or two

regions outside of the CC, while still belonging to the central brain. They either extend through the entire neuropil pertaining to one substructure, for example the bridge, or innervate an entire layer of other substructures such as the EB and the FB. Small field neurons, on the other hand, help in connecting a fraction of one substructure to a fraction of another, in an ordered projection pattern.

Additionally, there are some small field neurons called “bridging neurons”, which connect two portions of the same substructure, and are found often in the EB, and FB (Hanesch et al., 1989). The existing knowledge on the assorted requirement of neurotransmitters in the CC is far from complete. However, a study from 2010, aimed to identify the different types of receptors that are distributed in the different substructures of the CC using 6 different metabotropic G protein-coupled receptors (GPCRs). These GPCRs belonged to different neurotransmitters such as Serotonin (5-HT_{1B} and 5-HT_7), Dopamine (DopR), Glutamate ($DmGluR_A$), GABA($GABA_BR$), and neuropeptide F receptor (sNPFR1) (Kahsai et al., 2012).

The study revealed a strong distribution of Serotonin receptors in the anterior as well as posterior regions of the EB without any expression in the FB or the NO and the 5HT7-GAL4 driver was revealed to have expression in approaximately 30 cell bodies in each of the brain hemisphere (Kahsai et al., 2012). Dopamine receptors, on the other hand, were seen to be expressed in multiple substructures, including the EB, FB, and the NO. DopR immunoreactivity was specifically observed in the R3 and R4d (distal) ring neurons of the EB. Immunolabelling of GABAergic neurons with the GAD1 (Glutamate Decarboxylase1) antiserum indicated that it was distributed between the R3 and R4 ring neurons along with the bulb and the PB, with no GAD1 labelling in the NO. Glutamate receptors as well as transporters (vGluT) were also observed in the R3 and R4d ring neurons of the EB along with all three layers of the NO and the protocerebral bridge. Finally, sNPFR1 was present in six different layers of the FB, accompanied by no expression in the EB, PB and the NO.

The ellipsoid body

Anterior to the FB, lies the doughnut-shaped structure termed as the EB. It consists of two major rings, anterior and posterior, and is made of multiple layers/sectors of circular “ring” neurons which are arranged in the form of concentric zones, each demarcating their own sub-family.

There are approximately 176 ring neurons on each hemisphere of the *Drosophila* brain (Omoto et al., 2018). One of the first studies discerning between the different subtypes of ring neurons, identified four different families viz., R1, R2, R3, R4d (distal), and R4m (medial) (Hanesch et al., 1989). The expression patterns of these neurons were later revealed using the GAL4 lines generated by Renn and colleagues (Renn et al., 1999). The R1 and R3 neurons are located in the inner and middle regions of the EB, which arise from the EB canal and project outwardly. The R2 and R4(d&m) neurons have their axons arborizing more towards the outer circumferential rings, and connect to the EB from the periphery. Recently, the EB has been divided into wedges (referred to as “sectors” previously), and tiles. Wedges, represent a triangular sector which has depth to it, and there are 16 wedges dividing the EB structure. Tiles, on the other hand, are 8 in number and are segments as well, but are restricted to the posterior shell of the EB (Wolff et al., 2015).

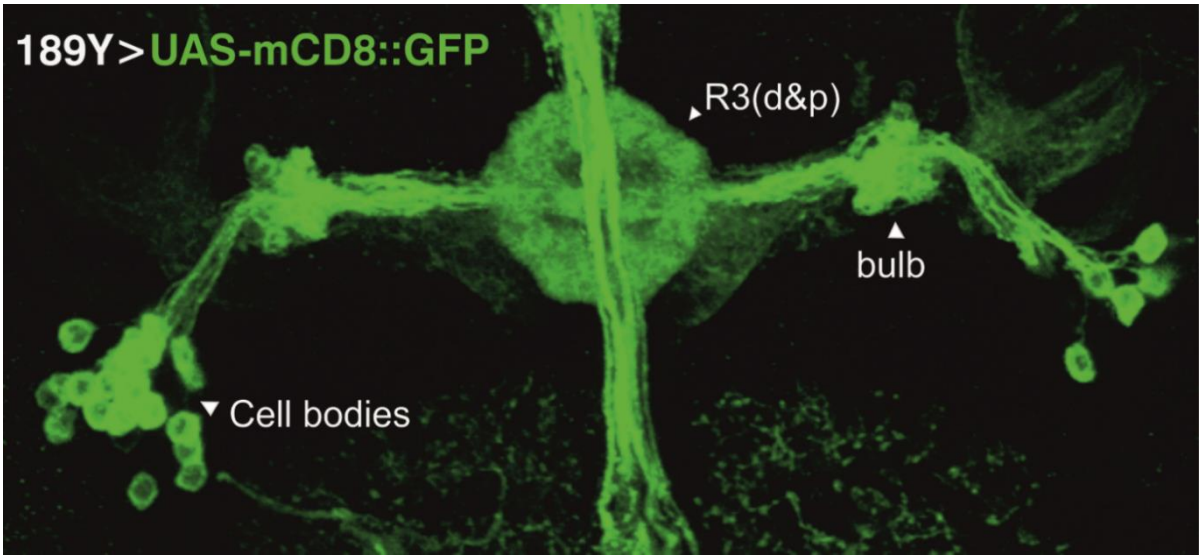

Figure 2: R3 ring neurons of the ellipsoid body

The axonal projections of the R3 (distal and posterior) ring neurons lie in the middle region of the EB while the dendritic projections are extended into the microglomeruli of the inferior bulb (BUi) region. There are approximately 15-20 cell bodies belonging to the R3 (d&p) ring neurons on each hemisphere. Magnification: 63X. Step size: 0.33µm. Stack size: 125 slices.

The ring neurons of the EB neurons arise from a single paired lineage called DALv2/EBa1, and derive their presynaptic input from the descending neurons of the anterior visual pathway (Omoto et al., 2017). The same study (Omoto et al., 2017) also identified a novel R5 ring neuron subclass. Immunohistochemistry studies have revealed that these neurons have their globular dendrites located in the

“microglomeruli” of the bulb, while their axons are present in the circumferential regions of the EB (Figure 2).

Using N-cadherin, which addresses neuropiles, it has been visually shown that the development of different subclasses of ring neurons occurs in a sequential manner, commencing at 16 hours after initation of pupae formation, and continuing to develop well into 48 hours, until all the rings are formed, to complete the structure of the EB (Xie et al., 2017). This study by Xie and colleagues, also included the use of axon-guiding molecules such as Semaphorin1-A (Yu et al., 1998), and plexin-A (Sweeney et al., 2007) to better understand the morphology and lamination of the EB (Xie et al., 2017).

The latest development in the morphological classification of the ring neurons of the EB is that, they are divided into annular domains rather than horizontal slabs (Omoto et al., 2018). This study slices the EB structure into five distinct domains: EB anterior (EBa), EB inner and outer central (EBic and EBoc), EB inner and outer posterior (EBip and EBop). In addition to the EB, the bulb regions adjacent to the EB on both hemispheres, have also been divided into partitions such as: bulb anterior (BUa), bulb superior (BUs), and bulb inferior (BUi), depending on the location, and have connections with different annular zones of the EB (Omoto et al., 2017).

This thorough study (Omoto et al., 2018) achieved the following goals in regards to the classification of the ring neurons: a) it could discern the location of the classical ring neurons (Hanesch et al., 1989) with respect to the updated demarcation of the EB, b) it identified novel and reliable driver lines to address the different ring neurons efficiently, c) it sub-divided the R3 ring neuron subclass into five discrete subtypes depending on their location in the EB as well as the region of their dendritic projections on the bulb, and d) it discovered the presence of a novel R6 ring neuron subclass. Postsynaptic partners of these ring neurons and their subtypes were also identified using the trans-Tango technique (Talay et al., 2017), where, it was shown for the first time that the R2 neurons have R3d (distal) as a postsynaptic partner. The article also sheds light on the different types of extrinsic ring neurons (ExR) (Hanesch et al., 1989), and their innervation patterns within and outside of the EB.

The compass (E-PG) and shift (P-EN) neurons

In the previous section, we discussed the classification of the EB into 16 wedges and 8 tiles (Wolff et al., 2015). The only type of neuron that arborizes in the glomeruli of the bridge and the gall, and has dendritic spines in the wedges of the EB, are the E-PG (Ellipsoid Body- Protocerebral Bridge- Gall; $PB_{G1–8}$.b-EBw.s-D/Vgall.b) neurons (Lin et al., 2013) (Figure 3A). The other type of neuron connecting these two substructures of the CC, are the P-EN (Protocerebral Bridge- Ellipsoid Body- Noduli; $PB_{G2–9}$.s-EBt.b-NO_1.b) neurons, which have their axonal arborizations in the EB while having spiny dendritic projections in the PB and the NO (Figure 3B).

In case of the E-PG neurons, each wedge of the EB is associated with a glomerulus on the PB. The projection from left to right in the EB is oriented from right to left in the glomeruli of the bridge, acting as each other's symmetrical mirror projection. The two halves of the bridge completely enwrap the entire EB, where the left side addresses the clockwise direction, and the right side addresses the counter clockwise direction of the EB (Wolff et al., 2015). Each P-EN neuron on the other hand, potentially has a dendrite in one glomerulus of the PB, which transmits an output to one tile of the EB. This would mean that a single P-EN tile occupies two E-PG wedges in the EB (Wolff et al., 2015).

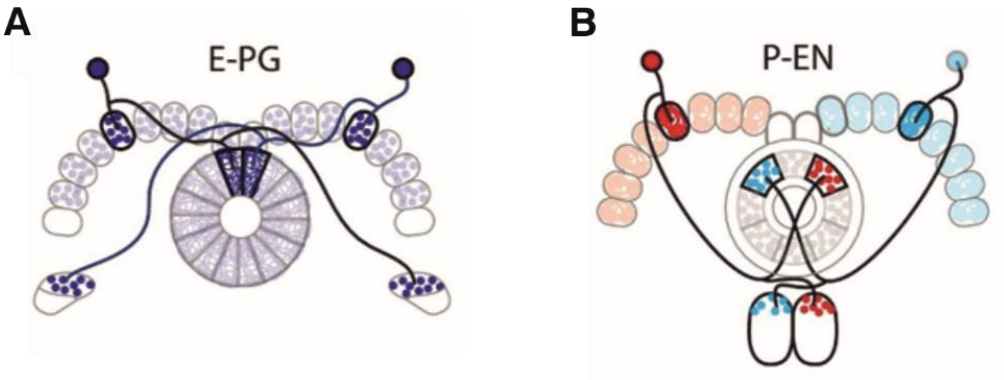

Figure 3: Arborization of the E-PG (compass) and P-EN (shift) neurons

(A) The axons of the E-PG neurons arborize in the PB and the gall with dendritic spines in the wedges of the EB where each wedge in the EB is addressed by a glomerulus on the PB. **(B)** The P-EN neurons have their axons extending into the shells of the EB with dendritic projections in the PB and the NO where each shell on the EB is connected to a glomerulus on the PB. Figure adapted from (Turner-Evans et al., 2017).

A detailed analysis by Turner-Evans and colleagues, focuses on how the compass and shift neurons hold a representation of the heading angle of the fly with respect to a landmark or the Sun. The study made some crucial observations on how

the angular velocity is mirror-symmetrically tuned to the activation of the P-EN neurons, where the neurons innervating the right side of the bridge, preferentially correspond to the clockwise turning direction, and vice versa (Turner-Evans et al., 2017). A reccurent loop between the E-PG and the P-EN neurons was also identified and classified to be both direct and indirect. An overall inhibitory feedback loop that could possibly be recruited by these two neuronal types, was also predicted.

The study also better clarified the sequence and location in which these neurons activate one another by using their relative positions across time, correlated with the rational velocities. This revealed that in case of the glomeruli of the PB, the P-EN activity was lagging behind that of the E-PG neurons. However, a similar measurement in the EB showed that the P-EN activity was leading that of the E-PG neurons, indicating the presence of two types of P-EN neurons. When the P-EN output was silenced by hampering the synaptic transmission of these neurons, the activity of the E-PG neurons was affected, and the activity bumps were significantly weaker (Turner-Evans et al., 2017).

A model representing the possible influence of turning behaviour in *Drosophila* was constructed by the data they had accumulated. One of the key assumptions of this model is that the E-PG and the P-EN neurons are connected. This would lead us to believe that the P-EN neurons are allowed to move the E-PG bump, depending on the direction of turning of the fly, in darkness. The one dendritic bump of the E-PG neuron on the EB, can manifest as two individual bumps in the bridge, where these bumps can be taken up by the P-EN neurons, which have their dendrites on the bridge that can possibly interact with the axons of the E-PG neurons. On the flip side, if the fly turns its head, the P-EN activity on a different side of the bridge will be modulated, depending on the angular velocity input. As a result, the axonal projections on the EB are activated on either side of the existing E-PG bump in the EB. Assuming that the P-EN neurons have excitatory connections with the E-PG neurons (Franconville et al., 2018), this dendritic calcium bump will then be moved along to the corresponding wedge of the EB.

1.3 Types of behaviours observed in *Drosophila melanogaster*

1.3 (a) Locomotion

Now that we are acquainted with the literature available on the structural components of the CC, it is now time to sift through some functional evidence which strongly proves that this complex is highly indispensable for a number of different behavioural phenotypes. Starting with locomotion, 15 structural mutants which were defective for different components of the CC (ex: *central-complex-deranged* (*ccd*), *ellipsoid body open* (*ebo*), *no bridge* (*nob*) and 12 more), were all tested for their walking speed, activity, and leg coordination. All of the 15 mutants appeared to have a decaying walking activity, with majority of them having reduced walking speed as well (Strauss and Heisenberg, 1993). The involvement of the central complex with locomotion has been revisited several times over the years. One study approached this objective through two idependent methods: using mutations that structurally affect the components of the CC, and the other involved silencing of these neurons through tetanus toxin (TNT) expression. Both of these methods yielded similar results in terms of significant reduction in locomotor activity. This study also highlighted the importance of the PB and its connection to the rest of the CC, not for the initiation, but for the maintenance of walking activity (Martin et al., 1999).

Going along these lines, another study approached the subject of locomotion with an aim to discern between walking activity, and rotary stimuli compensation, proposing that they might be controlled by different substructures in the CC. Using the *tay-bridge* structural mutant (tay^{1}), which is known to have deficits in walking behaviour, this study attempted to rescue the defective phenotype in different parts of the fly brain, and was able to zone in on the PB as an important structure that controls walking speed and activity. Optomotor response, on the other hand, seemed to be controlled by a different system (Poeck et al., 2008). In 2010, Kahsai and colleagues investigated the roles of two neuropeptides (*Drosophila* tachykinin (DTK), and short neuropeptide F (sNPF)) with respect to locomotion by knock-down studies, specifically in the CC, and through disruption of synaptic transmission in the CC neurons. This study exposed that these peptides regulate locomotion in a circuit-dependent manner by interacting with specific neuronal substrates belonging to the peptidergic pathways located in the CC (Kahsai et al., 2010).

1.3 (b) Flight behaviour

Flight behaviour and visual control were also tested for three different *ebo* strains by monitoring the optomotor reversal time (ORT) and object fixation (OF) of tethered flies using a flight simulator. Both these factors were defective in the mutant strains in comparison to wild-type flies, indicating a deficit in data integration along the midline of the brain (Ilius et al., 1994).

1.3 (c) Navigation

The navigation in *Drosophila* is carried out by creating a stable internal heading representation. This process is carried out by the shift neurons (P-EN), which carry the angular velocity signals, and the heading cells or compass neurons (E-PG), which are responsible for head-fixed walking behaviour (Kim et al., 2017; Turner-Evans et al., 2017). These two neuronal families, together, help to create a continuous heading representation that goes along with the movement of the fly. The most recent research in this regard, confirmed this hypothesis using a flight simulator experiment showing that flies do orient in a fixed angle towards the Sun or any visual source that is perceived as the Sun, through the regulation of these E-PG neurons (Giraldo et al., 2018). Two very recent papers also discussed the plastic nature of the synaptic interaction between the ring neurons and the E-PG neurons, which was suspected to enable the flexible shift in the inner visual world of the fly during exploration (Fisher et al., 2019) (Kim et al., 2019).

1.4 Learning and memory in *Drosophila melanogaster*

The *Drosophila* brain has been studied with respect to behaviour, and memory, since the late 1900s when Benzer and colleagues first began experiments using mutagenesis to identify novel behavioural mutants (Benzer, 1967; Benzer, 1973). Their study on mutagenesis and mutants revealed for the first time, that behaviour is controlled by specific genes. Learning mutants have been defined as those with observable deficits in acquisition/storage/retrieval of information without having any developmental defects, mainly sensory or motor defects that might potentially contribute to the aberrant behavioural phenotypes (Dudai, 1988). Different types of genetic systems have been put in place to analyse specific learning and memory mechanisms in *Drosophila* (Zars, 2010).

The concept of “learning” has been examined in the *Drosophila* scientific community for over serveral decades. Fruit flies have been shown to learn visual

(Menne and Spatz, 1977), proprioceptive (Booker and Quinn, 1981), and even spatial cues (Wustmann and Heisenberg, 1997). In his review article, Greenspan states that in fly learning, the imposition of order arises from the correspondence between the different memory phases, and the action of particular genes (Greenspan, 1995). Initial learning, is then defined as the extent of conditioning after the training process. In case of classical conditioning experiments, a conditioned response (CR) is elicited when an association is formed between a conditioned stimulus (CS), and the unconditioned stimulus (US), where the CS acts as a predictor for the US.

Memory, on the other hand, can be divided into multiple phases, depending on how long the conditioning is retained by the organism. There are short-term (STM), middle-term (MTM), and long-term memory (LTM) phases that are observed after the learning process (Greenspan, 1995). In addition to these phases, there exists a memory which is associated with courtship (Siegel and Hall, 1979), and an anesthesia-resistant memory (ARM), which persists even after cold-shock treatment. Genes regulating the different memory phases have been studied in detail in *Drosophila*. Very recently, a life-long memory pertaining to the fly's own body-size, has also been established (Krause et al., 2019).

One of the first few studies performed in regards to olfactory learning, revolved around a paradigm designed by Quinn and colleagues (Quinn et al., 1974; Quinn and Dudai, 1976). This paradigm was later improved to fit a Pavlovian model in the context of olfactory associative learning, where the model organism is trained to learn/associate a specific odour either with a reward (appetitive) or an electric shock (aversive), in order to later remember these cues in experiments designed to test for the short/mid/long-term memory of the organism (Tully and Quinn, 1985).

1.4 (a) Olfactory learning and memory

Several learning mutants have been identified in the realm of olfactory learning and memory. The role of cAMP has been implicated to be vital in the process of olfactory learning and memory for nearly four decades now. Two of the first discoveries revealing this, were using the learning mutants for the genes "*dunce*" (mutant: dnc^{1}), and "*rutabaga*" (mutant: rut^{1}) (Tully, 1984; Dudai, 1988), which possess an abnormal regulation of cAMP levels. *rut* has been shown to impact learning by participating in the coincidence detection of the odour paired with electric shock/reward, while spatial regulation is undertaken by *dnc* (Gervasi et al., 2010).

The *dnc* mutants and knock-downs lack the phosphodiesterase-II (PDE-2) enzyme, which hydrolyses cAMP, thereby leading to increased cAMP levels in these learning mutants (Byers et al., 1981). In the year 1984, Friedrich and colleagues conducted a slow-phase decay experiment to compare the rate of cAMP decay between *dunce* mutants and wild-type flies. They inferred that the slow decay in *dunce* mutant flies was due to the protein kinase A (PKA) subunit that was bound to the cAMP (Friedrich et al., 1984).

rutabaga, on the other hand, codes for a subunit of the adenylyl cyclase, which, when mutated, fails to activate cAMP in a Ca^{2+}/Calmodulin-dependent manner, thereby leading to reduced cAMP levels (Livingstone et al., 1984). In order to study the neural synaptic transmission and plasticity in these learning mutants, electrophysiological studies were done to calculate the “excitatory junctional currents” (EJCs) in the larval neuromuscular junctions (NMJs) of these mutants. This study revealed that disrupted cAMP cascade led to a reduced synaptic facilitation and potentiation in these mutants (Zhong and Wu, 1991). Following in this path, research was done in the context of nerve terminal arborization in *dnc* mutants, where the maintenance of cAMP levels was seen to be crucial for the motor axon projections (Zhong et al., 1992).

In the mid 1980’s, it was already proved that the mushroom body (MB) neurons were critical for olfactory learning and memory in *Drosophila* (Heisenberg et al., 1985). In the early 1990’s, it was observed that the *dunce* mRNA, and as a result, cAMP-PDE, were expressed and localised in the MB axons and dendrites, indicating that *dnc* is required in the MB for the formation and functioning of olfactory memory (Nighorn et al., 1991). The very next year, it was shown that *rutabaga* was also expressed in an elevated fashion in the MB neurons, making the MB one of the major learning and memory centres in *Drosophila* (Han et al., 1992). Larval central nervous system (CNS) cultures from these learning mutants, revealed that there were alterations in their growth cones where there was a decrease in the lamellopodial motility (Kim and Wu, 1996). This was inferred to be a reduction in the exploratory and searching behaviour of the growth cones.

Over the years, hundreds of studies have come out exploring the the roles *rut* and *dnc* play in the Kenyon cells of the MB to affect different phases of olfactory memory. The learning centre in the *Drosophila* brain was elucidated to be the MB

neurons for a long time, since morphological defects in the mushroom body led to deficiencies in olfactory associative learning and memory (Heisenberg et al., 1985; Davis, 1993). Chemical ablation of the MB Kenyon cells also led to the destruction of olfactory associative learning (de Belle and Heisenberg, 1994). These findings were later substantiated by a study where the short-term olfactory memory in *rut* mutants was rescued by expressing UAS-*rut* in the MB Kenyon cells (Zars et al., 2000).

Olfactory short-term memory (STM)

When it comes to the functioning of STM, it occurs as a result of rapid alterations in the relevant neurons that ultimatately lead to a changed synaptic efficacy which lasts for about a few minutes to hours. Two of the mutants known to negatively affect olfactory STM, are for the genes *rutabaga* (Livingstone et al., 1984) and *dunce* (Tully and Quinn, 1985), where they show reduced olfactory memory almost immediately after conditioning. The resultant phenotypes of flies mutant for *rut* (rut^1), and *dnc* (dnc^1), are accounted for by the aberrant regulation of cAMP, specifically in the Kenyon cells of the MB (Zars et al., 2000).

In a study, Gervasi and colleagues used AKAR2 (A kinase activity reporter-2), a probe used in FRET (Forster resonance energy transfer) to measure for PKA signalling in living flies. This experiment revealed that the cAMP/PKA activation in the MB axons and dendrites, occurs with differential efficiency during different time courses, and that this activity is modified in the *rut* and *dnc* mutants. This work revealed for the first time that the dopaminergic stimulation, which is triggered by the electric shock during aversive olfactory conditioning, increases the activity of PKA, specifically in the α-lobes of the MB, which is regulated by *dnc*. When these dopamine stimulations are accompanied by increased intracellular Ca^{2+}, a Rut-dependent activation of PKA in the MB neurons is observed, making Rut a coincidence detector (Gervasi et al., 2010).

When it comes to understanding the external factors that control and mediate olfactory STM, “sleep” has remained on the forefront. An interesting study carried out using a sleep deprivation paradigm (slpD), showed that wild-type flies subjected to forced lack of sleep had a significantly worse olfactory STM compared to those that were not (Li et al., 2009). This phenotype could be rescued when the MB α/β neurons were inactivated when the flies were in the slpD paradigm, revealing that these are the neurons which are targeted by the device to impair olfactory STM through sleep

deprivation. In the same year, another study explored the impact of sleep deprivation on STM in flies having a pathology for PD (Parkinson's Disease), by expressing *α-Synuclein* in a pan-neuronal manner. Persisting STM deficits were observed in these flies even 20 days after the initial sleep deprivation of 12 hours. This was ultimately shown to be the result of reduced Dopamine synthesis in the brain (Seugnet et al., 2009a). It is worth mentioning that Dissel and colleagues showed that sleep rescues STM using aversive phototaxic suppression (APS) in *rut* and *dnc* mutants. In the same paper, the authors used courtship conditioning to prove that sleep induction also improved LTM in the very same learning mutants (Dissel et al., 2015).

Studies addressing olfactory STM through manipulations of the circadian rhythm, have also been done to better understand the role of biological clocks in associative STM formation and functioning (Lyons and Roman, 2009). In one of the more recent studies, manipulating of the ORK1 potassium channel led to differential defects in sleep length as well as olfactory STM in flies, depending on whether *ork1* was overexpressed or present in its mutant form (Zhang et al., 2017). In terms of neurotransmitters, Serotonin has been repeatedly reported to be critical for olfactory STM formation (Kandel, 2001; Sitaraman et al., 2012).

Olfactory long-term memory (LTM)

One of the breakthrough research carried out in the field of long-term memory consolidation, was with the expression of a dominant negative form of the transcription factor cAMP responsive element binding protein (*dCREB2-b*), using a heat-shock promoter. Since this inhibitory isoform works by blocking the PKA-responsive transcription activator CREB-2a, it was strongly suggested that the phosphorylation of dCREB by protein kinase A (PKA), is a necessary step for LTM consolidation in *Drosophila*. The phosphorylated form of CREB, can then continue to initiate the transcription of genes that are involved in LTM (Yin et al., 1994). Since then, LTM has been studied using several behaviour paradigms in *Drosophila*, most of them revolving around the requirement of the MB neurons for LTM (McBride et al., 1999; Pascual and Preat, 2001; Heisenberg, 2003). Neuroanatomical studies have shown that LTM is dependent on the synaptic output of the α/ß neurons, but the consolidation part was revealed to rely specifically on the interaction between the MB and the dorsal paired medial neurons (Cervantes-Sandoval et al., 2013; Guven-Ozkan and Davis, 2014).

1.4 (b) Visual learning, memory, and orientation

A part of the *Drosophila* brain that has been dominating the arena of visual learning, memory, and orientation, is the central complex (Bausenwein et al., 1994; Wang et al., 2008b). A multitude of research studies have come out, targeting the learning mutants, and other related genes to study different types of learning, and by virtue of it, memory. The mechanism of visual pattern recognition has been studied extensively in *Drosophila* since the early 1990's (Dill et al., 1993; Dill et al., 1995). But the regions of the CC that are associated with this pattern recognition, orientation, and other behaviours, were not explored until much later. In 2006, a study focussing on the short-term memory for visual pattern recognition, claimed that the FB of the CC is where this type of memory is localised. Neurons belonging to the F5 layer of the FB was shown to be responsible for the memory trace for the pattern parameter "elevation", while those in the F1 layer of the FB, hold the memory trace for "contour orientation" (Liu et al., 2006).

"*foraging*", a gene coding for protein kinase G (PKG), was identified to be essential for visual pattern memory, and was seen to be required specifically in the EB neurons, although the authors debated whether the driver line they used for the rescue experiments might have addressed both EB and FB neurons. They also contemplated whether the memory of the flies may depend on the overall activity of both these neuronal subfamilies. Thus, a rescue of *for* mutant phenotype in the EB might mean that the required combined threshold for both EB and FB might have been achieved with *for* transgene expression in just the EB (Wang et al., 2008b). The following year, another study targeting these two components of the CC, showed that learning mutants of the *rut* gene (rut^{2080}) could be rescued by the targeted expression of the *rut* transgene in the EB or the FB, showing that they are both vital for the process of visual pattern memory. In addition, the study also made an important discovery that the R2 and R4 neurons of the EB are the ones specifically needed for visual pattern memory (Pan et al., 2009).

"Visual place learning", is another concept that has been studied in *Drosophila* through the use of a thermal visual arena, whose floor is made of a uniformly warm suface, with the exception of a single cold-spot, and the cylindrical wall consists of a visual panaroma, where the position of the cool tile with respect to the visual panaroma remains constant. The fly is expected to remember the cold-spot with

respect to the visual stimulus. This study revealed that the R1 neurons (now classified to be R3m neurons), are the ones necessary for this particular type of place learning (Ofstad et al., 2011).

A mechanism that has been applied to study “conditioned visual orientation” in *Drosophila*, is the flight simulator (Xi et al., 2008), which analyses visual orientation in flies whose bodies are tethered i.e., they remain stationary while exposed to two vertical bars facing each other. The original paper concerns flies with mutations in the MB. Using this flight simulator apparatus, a screening of ring neuronal subtypes using *kir2.1* expression was done by Guo and colleagues, which revealed that the R3/R4d neurons were necessary for visual orientation conditioning. In addition, this study identified that *scb*, a gene that codes for integrin, is also required specifically in the R3/R4d ring neurons of the EB for the functioning of visual orientation conditioning (Guo et al., 2014). The EB ring neurons have also been implicated to participate in visual motor learning. This article revealed that the output of R2/R4d neurons within the EB is more reliant on motor actions rather than motor coordination, albeit these neurons being visually responsive (Seelig and Jayaraman, 2013). Thus, the authors deduced that the R2/R4d neurons potentially provide behaviourally relevant visual feature sets to the CC circuits located downstream, based on which, motor decisions are made.

When it comes to other neurons of the CC that aid in visual orientation, Seelig and Jayaraman also explored the role of the E-PG (previously EB.ws) neurons, using closed-loop experiments (Seelig and Jayaraman, 2015). These studies indicated that the E-PG neurons can be considered as an internal compass in the fly brain, which represents the fly’s orientation that is guided by visual landmarks. In addition to visual cues, the study showed that these neurons are also influenced by the angular movements of the animal. The flies were shown to rely on self-motion to facilitate orientation without any visual cues, which is a form of angular path integration (Green et al., 2017). However, this representation of the fly’s orientation remained stable, and was maintained by the E-PG neurons for approximately more than 30 seconds, even when their calcium activity was measured in the dark (no visual cues), or when the flies were stationary (no self-motion cues) (Seelig and Jayaraman, 2015).

A very recent study which utilized the phenomena of Sun menotaxis, and stripe fixation, showed that the activity in the E-PG neurons, is critical for flies to

maintain the Sun in the arbitrary non-frontal positions (Giraldo et al., 2018). Another new study discusses how the E-PG neurons can stably represent heading even in complex, and changing visual environments (Kim et al., 2019). The article delves into the concept of Hebbian plasticity, which is based on synaptic weights. This principle, combined with the ring attractor dynamics, enables the fly to create a complete heading representation from the limited visual information gathered from a novel scene. On the same lines, Fisher and colleagues produced some supporting data with respect to the doubled pattern of “synaptic weights” between the ring neurons and the E-PG neurons, which facilitates a more flexible behaviour from the fly in a naturalistic virtual world, with ever-changing visual inputs (Fisher et al., 2019).

The most recent study pertaining to the processing of visual information in *Drosophila* showed that the CC receives visual input from the optic lobes through the anterior optic tubercle (AOTU) via the bulb regions. Depending on the position of the input in the visual field, it is received by different regions of the bulb, which communicates it to the EB ring neurons particularly addressed by the bulb regions, in a map-like fashion. While the R2/R4 ring neurons are downstream to the superior bulb (BUs) regions, the R3 neurons have their dendrites innervating the inferior subregions of the bulb (BUi). In terms of visual input, both BUi and BUs have been shown to be responsive to bright objects on a dark background (ON signal). However, the R2/R4 neurons receive visual input from the ipsilaterally located neurons, whereas the R3 neurons receive input from the contralaterally located ones. This study confirmed the notion that a number of different behaviours that are dependent on visual stumuli, are processed differently in the CC (Lovick et al., 2017; Omoto et al., 2017).

“Light”, is an external factor that was applied to understand its effect on STM using an aversive phototaxic stimulus (APS), where the fly is expected to avoid light that is paired with an aversive stimulus. This type of associative memory was reduced in flies modelling for neurodegenerative diseases such as Alzheimer’s disease (AD), Parkinson’s disease (PD), and Huntington’s disease (HD). It was also observed in learning mutants (defective for *rut* and *dnc* gene expression), which are known to have impaired cognitive functions, making APS a reliable assay to analyse visual STM in flies (Seugnet et al., 2009b). Throughout history, several types of *Drosophila* STM have been explored using varied behavioural paradigms. One of

them was using a novel visual paradigm (Wolf and Heisenberg, 1991), to test for operant visual orientation behaviour in flies using specifically shaped patterns as visual landmarks with heat as the “punishment”. In this study, flies fed with depolarizing drugs such as KCl (potassium chloride), seemed to lose their visual STM, 1-2 minutes after training, indicating a severe deficit in STM. The authors in this case, inferred that this could be an effect of the accumulation of Ca^{2+} in neurons, which in turn leads to the exit of transmitters (Xia et al., 1997a).

Functioning of a short-term visual orientation memory in *Drosophila*

The working memory (Postle, 2006) for short-term visual orientation, also known as “detour memory”, was first described in the year 2008 by Neuser and colleagues (Neuser et al., 2008). This working memory, involving the behaviour of a fly in a cylindrical arena, depended on the fly’s ability to fixate on directions and visual targets even after their disappearance (Strauss and Pichler, 1998). To investigate spatial/visual orientation memory, a type of working memory in *Drosophila*, a specialized paradigm called the “detour paradigm” was designed by Neuser and colleagues (explained in detail in section 2.3.1). Although this setup is based on the previously established Buridan’s paradigm, which also includes a cylindrical arena with two vertical dark stripes for visual landmarks, the detour paradigm has a critical distinction in terms of what was termed as the “distractor bar” which appears after the original landmarks disappear. This distractor (effectively another dark stripe) appears at right angles to the former landmarks, thereby deviating the fly from its original walking direction, and disappears one second after the fly turns towards it (Neuser et al., 2008). For this exact reason, this arena is highly effective in testing the working memory of flies, because, it depends on instantaneous memory rather than long-term consolidated memory. Since it also does not involve any cues to prompt the fly to remember (as in the case of olfactory memory), this type of memory can be viewed as an “idiothetic” memory. The ability of the fly to now remember the original direction of the landmark it was walking towards, encompasses the principle behind detour memory.

The critical takeaway of this mechanism is that the flies are expected to have a continuously exisiting working memory at any given point in time, making it a type of idiothetic memory that is self-generated from the motion/turns the fly makes, in order to build the memory. The original work proved that wild-type CS flies could

perform this with 80% positive choices, while learning mutants perfomed with contrasting outcomes. While *dnc*^{1} had no defective detour memory, *rut*^{1} flies could not even be tested in the detour paradigm because they did not patrol back and forth towards the vertical stripes within the arena (Neuser et al., 2008). Based on this mechanism, a slew of papers have been published over the years, analysing the nuances of visual working memory by the manipulation of different transgenes (Kuntz et al., 2012; Thran et al., 2013; Kuntz et al., 2017; Rieche et al., 2018).

The region of location of this type of memory in the *Drosophila* brain could be identified using a structural mutant that affects the EB. While flies containing ablated MBs performed like wild-type flies, *ebo (ellipsoid body open)* mutants, containing a morphologically disrupted EB (Strauss and Heisenberg, 1993), showed a complete loss of detour memory, making the ring neurons of the EB, the primary region of interest for this memory formation. Another interesting observation was that *ignorant*$^{58/1}$, a null allele for *ignorant*, the gene coding for ribosomal protein S6 kinase 2 (RSKII) (Putz et al., 2004), could perfectly recognize the landmarks, but failed to remember their original heading direction once distracted. These mutants could be completely rescued when the *ign* transgene was expressed specifically in the R3 and R4 ring neurons. *ignorant* knock-downs also showed a phenotype similar to that of the mutants. Targeted silencing of these ring neurons using Tetanus Toxin (TNT) (Sweeney et al., 1995), in an adult-specific manner, also completely destroyed detour memory, confirming that these neurons are indeed the hub for this memory to exist and function (Neuser et al., 2008).

Hypomorphic mutants for *foraging (for),* a gene coding for Protein Kinase G (PKG) (Kalderon and Rubin, 1989), which is expressed abundantly in the EB ring neurons (Belay et al., 2007), also seemed to disrupt detour memory functioning. Rescue of these mutants using UAS-*for* transgene in different ring neurons proved that its expression is required specifically in the R3 ring neurons. While genetic interaction studies between *for* and *ign* revealed that the two proteins belong in the same signalling pathway that regulates this memory, rescue of *for* mutants using UAS-*ign* transgene expression in R3 neurons, showed that, *for* is required upstream of *ign* (Kuntz et al., 2012).

A recent study focussing on the characterization of *ebo*, revealed that when *ebo* is mutated, it leads to an accumulation of actin, since *ebo* codes for Exportin6,

an actin/profilin-binding protein, required for the export of monomeric actin from the nucleus. *ebo* mutants can thus experience increased availability of actin in the nucleus, which might potentially impair detour memory by negatively affecting the dMRTF/dSRF (*Drosophila* Myocardian-related Transcription Factor/Serum Response Factor) regulation complex (Thran et al., 2013). Since *ebo* could be rescued in all the ring neurons, it was suspected that there might be a diffusible second messenger in the form of a gasotransmitter that is involved in this type of memory functioning.

The scope of the gasotransmitters that could be regulated by this transcription complex was analysed in this next study where Nitric Oxide (NO) and Hydrogen Sulphide (H_2S) were explored for their roles in the functioning of detour memory (Kuntz et al., 2017). Kuntz and colleagues could prove that dMRTF/dSRF positively regulated CBS (cystathionine-β-synthase), which in turn led to the production of H_2S. This experimental endeavour ultimately revealed that these two gasotransmitters (H_2S and NO), control detour memory by regulating the cGMP levels in a shared pathway, ultimately leading to the activation of CREB protein, by increasing the levels of cGMP. The second, instructive role of NO signalling, was identified to facilitate a memory trace encoded by cGMP, which arises in the axons of the R3 neurons. As depicted in Figure 4, the visual input from the landmark, as well as the distractor, are conveyed to the R3 neurons by the R2/R4 neurons. Different wedges are activated in the EB for each of the visual inputs, where a cGMP-mediated memory trace (through NO) is formed for each of them, depending on their duration of exposure to the fly (Figure 4).

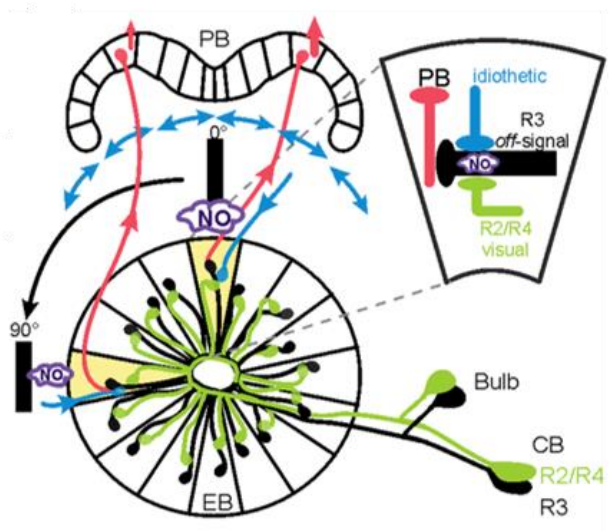

Figure 4: Schematic representation of the working model of detour memory in *Drosophila*

Visual information regarding the landmarks and the distractor is captured by the R2/R4 neurons (green) which is transferred to the R3 neurons (black). Different wedges of the EB are activated depending on the location of the landmark and a memory trace is formed for each of them through NOS-regulated cGMP. Once a differential calculation is done in the R3 neurons based on the strength of the memory trace, a decision is made, which is then communicated to the PB through the bridge neurons (red). The R2 neurons, and the idiothetic neurons (blue), coincidentally activate/inhibit the R3 neurons. Figure adapted from (Kuntz et al., 2017); copyright license attached in Appendix (section 8.4).

The fly makes a differential calculation between the individual memory traces in the R3 neurons, which is then put to use once all visual cues disappear. Since the memory trace representing the landmark would be stronger than that of the just briefly-seen distractor, the neurons connecting the EB to the bridge, aid in the steering of the fly towards the original landmark, which is ultimately perceived as the fly's "choice" (Kuntz et al., 2017).

Impact of ageing on detour memory

Ageing, is a process that affects all types of memory across species. While olfactory memory in wild-type flies has been shown to decline after 30-40 days of ageing (Mery, 2007; Yamazaki et al., 2007), not much had been discussed in regards to how ageing affects short-term visual orientation memory until 2018, in a study by Rieche and colleagues. This work focussed on comparing the memory performance of wild-type flies to those with an increased processing of APPL. The study revealed that normal processing of APPL (Amyloid Precursor Protein Like) by α, β, and γ secretases, leads to a decline in detour memory within 4-6 weeks in wild-type flies (Rieche et al., 2018). RNAi-mediated knock-down of *Appl*, as well as overexpression of the secretases that degrade the APPL protein in the R3 neurons, both led to severe defects in detour memory even in young flies. This phenotype was notably rescued by sdAPPL (secretion-defective APPL) in young, and ageing flies, but not by any of the APPL fragments produced after secretase-directed cleaving. This result reinforced the importance of full-length APPL (flAPPL) in the functioning of this memory (Rieche et al., 2018).

Immunohistochemistry studies using double-tagged APPL (N-terminal tagged with GFP, C-terminal tagged with RFP) revealed that both parts of the flAPPL were localised at the R3 axons, thereby supporting the inference from the behavioural results mentioned above. The paper also proposed FASII (Fasciclin II), to be a candidate gateway receptor through which APPL mediates the functioning of visual working memory because FASII is enriched in most of the ring neurons (Young and Armstrong, 2010b), and is known to interact with APPL at the *Drosophila* NMJs (Ashley et al., 2005). Their hypothesis was validated after the successful rescue of *FasII* mutants using UAS-*FasII* in the same R3 neurons where APPL is localised, providing a possibility for the two proteins to interact. Finally, genetic interaction

studies between *Appl* and *FasII* revealed that *FasII* is negatively regulated by *Appl* in the R3 neurons and is acting downstream of *Appl*.

Another protein that has been closely associated with the pathology of Alzheimer's disease is the Tau protein (Weingarten et al., 1975). First identified and characterized in *Drosophila* in the year 2001 (Heidary and Fortini, 2001), the role of Tau has been revealed to bind to microtubules to stabilize the axonal architecture. The reason why Tau is associated with neurodegenerative diseases such as AD and cerebral palsy (CP), is due to the presence of hyperphosphorylated Tau in the "neurofibrillary tangles" (NFT), that are observed in these pathologies in vertebrates. Albeit being associated with a number of dementias, the knowledge regarding Tau's influence on memory is limited. The few studies that do discuss this, are mostly related to olfactory learning and memory involving the MB neurons (Mershin et al., 2004; Beharry et al., 2013). Therefore, this dissertation aims to touch upon the role of Tau in visual working memory and determine if it is detrimental, or indispensable for detour memory, using knock-out mutants and variants of human *Tau* (section 3.3).

1.5 Protein Kinase A (PKA) and its functions in *Drosophila*

Protein Kinase A (PKA) in *Drosophila*, is a phosphorylating kinase that is dependent on its activation by cylic AMP (Adenosine Mono Phosphate), and is a key component of the cAMP/PKA cascade. PKA is a tetramer, consisting of two regulatory, and three catalytic subunits. When the regulatory subunits bind to cAMP, they disassociate from the catalytic subunits, allowing PKA to perform its phosphorylating function. In the absence of cAMP, the regulatory subunits bind to the catalytic subunits instead, and inhibit their catalytic activity (Coffino et al., 1976). Alterations in PKA activity are possible by manipulating the interaction between the different subunits. For example, PKA activity can be permanently inhibited using a mutated version of the regulatory subunit that can no longer bind to cAMP, because of which, the catalytic site of PKA can no longer be active (McKnight et al., 1988). On the flip side, the catalytic site of PKA can be constitutively activated by altering the catalytic subunit in such a way, that it can no longer bind to (and be inhibited) by the regulatory subunit (Li et al., 1995).

One of the earliest works that revealed the role of PKA in olfactory learning, was carried out by Drain and colleagues in the year 1991. They used PKI[1-31] (PKA inhibitor 1-31), a 75kDa protein, isolated from rabbit, which inhibits PKA activity by

competitively binding to the regulatory subunit, preventing its activation by cAMP (Walsh et al., 1971). The flies expressing the transgene for PKI, as well as those expressing the transgene for constitutively active *Pka* under a heat shock promoter, both led to disruptions in olfactory learning (Drain et al., 1991). As a result, this study could prove that the right amount of PKA activity is necessary for olfactory learning, because, lower or higher activity of PKA than the required threshold, both had a negative impact on learning. This study drew parallels between the results observed here to those observed in *rutabaga* and *dunce* mutants, where the cAMP levels are reduced or increased respectively, but have a similar behavioural output.

The next attempt at understanding the role of PKA, and its region of localisation in the *Drosophila* brain, was carried out using an antibody raised against DCO, the protein product of the *Dco* gene. *Dco* codes for one of the three catalytic subunits of PKA, which is required in the early stages of development (Kalderon and Rubin, 1988). It was observed that this antibody selectively bound to the MB lobes, calyces and peduncles, showing that PKA activity is required primarily in these neurons (Skoulakis et al., 1993). Dco^{581}, an enhancer trap line, was created by a P-element insertion in *MB581*, a gene preferentially expressed in the MB. Dco^{581} was partially able to complement the lethality exhibited by Dco^{B10}, a hypomorphic point mutant of the *Dco* gene. Despite being fertile and healthy, the flies carrying both these alleles $Dco^{B10}/Dc0^{581}$, had less than 20% of the cAMP activity usually recorded in wild-type controls. These heteroallelic flies also displayed a highly disrupted initial learning, and early olfactory memory, once again proving that PKA catalytic activity is required for this memory in the MB neurons (Skoulakis et al., 1993).

While the PKA catalytic subunit and *dnc* are expressed in the axonal and dendritic compartments of the MB, *rut* is expressed predominantly in the axonal region of the MB. Hence, researchers have remained curious over the years to understand how these three genes operate together in the overall functioning of olfactory learning and memory (Davis et al., 1995). Following up the previous study (Skoulakis et al., 1993), Li and colleagues manipulated the expression of DCO, the catalytic subunit of PKA, this time by using a mutant allele which is cold-sensitive (*DCOX4*). *DCOX4* hemizygotes displayed a reduced PKA activity at 18°C. These mutants also exhibited a significantly reduced initial olfactory learning and mid-term memory (Li et al., 1996).

The role of postsynaptic PKA in motor neurons has been explored by expressing a constitutively active PKA transgene in the *Drosophila* NMJs to identify that the quantal size was reduced in these neurons. On the flip side, expression of a mutated regulatory subunit, unfit for cAMP binding, exhibited a larger quantal size (Davis et al., 1998). This indicates that postsynaptic PKA is capable of regulating postsynaptic sensitivity to Glutamate, specifically through DGluRII (*Drosophila* Glutamate Receptor II), since the nature of synapses at the *Drosophila* NMJ bears ultrastructural similarities to the central synapses in vertebrates, which also happens to be glutamatergic (Atwood et al., 1993).

One of the earliest experiments performed to test whether cAMP is required for visual memory, was using the flight simulator, which is the classical method to observe a fly's visual flight orientation behaviour (Xia et al., 1997b). This study was carried out by feeding the flies caffeine, which significantly increased the cAMP levels and reduced the visual memory. This phenotype was compared to the gradual reduction of visual memory with age, since cAMP levels are also observed to increase with age (Wang et al., 1998). Thus, the inference of this study was that, a regulated mechanism to control the expression of cAMP, is required for the proper functioning of visual memory.

Although *dnc* and *rut* are heavily associated with olfactory learning and memory, an interesting development in regards to visual STM came about when the mutant form of these genes had a reduced response to visual objects in a novelty paradigm, and an optomotor paradigm (van Swinderen and Greenspan, 2003). The *dnc* mutants displayed a delayed optomotor responsiveness, whereas the *rut* mutants were unresponsive to the distractor, indicating subtle differences in their processing of visual information, which were both defective nonetheless. This pointed towards a lack of cAMP-dependent short-term plasticity, that is required for visual STM (van Swinderen, 2007). Continuing on the lines of PKA-related memory deficits, a noteworthy study from 2010 revealed that the inhibition of PKA activity at an old age, ameliorated age-related memory impairment (AMI) in *Drosophila*. The authors of this study state that this is not necessarily a direct result of PKA activity, but rather an effect of PKA-signalling, which is one step downstream to PKA itself (Yamazaki et al., 2010).

By the late 1990's and early 2000's, the function of cAMP in the regulation of synaptic vesicles was starting to gain attention. This was done using a fluorescent dye (FM1-43), which was originally characterized to study synaptic vesicle release in the NMJs of frogs (Betz and Bewick, 1992). This dye stains membranes in an activity-dependent manner, thereby being useful in identifying synaptic vesicle recycling and neurotransmitter release (Maistrenko et al., 2015). It was later used in *Drosophila* larvae which revealed the presence of two types of synaptic vesicle pools, the endo/exo cycling pool, and the reserve pool (Kuromi and Kidokoro, 1998). In the next particular study that was carried out in the year 2000, this dye was once again used to visually observe the recruitment of vesicles from the reserve pool in *dnc* and *rut* mutants, using external tetanic stimulation (Kuromi and Kidokoro, 2000). This study revealed that 10Hz stimulation of wild-type fies could lead to the initiation and continued recruitment of vesicles from the reserve pool for 10 seconds afterwards.

In contrast, the *rut* mutants did not have an initiation of vesicle recruitment, whereas the *dnc* mutants did not exhibit persisted recruitment of synaptic vesicles from the reserve pool, indicating that a regulated level of cAMP, is critical for the efficient recruitment and release of synaptic vesicles from the reserve pool. However, repeated tetanic stimulation and treatment with db-cAMP (a cyclic nucleotide derivative which mimics the action of endogenous cAMP), could lead to an increased recruitment of vesicles in *rut* mutants. It was also interesting to note that activation of cAMP and PKA, both led to the shifting of the dye from the centre, to the periphery of the boutons. However, the inhibition of cAMP and PKA led to a heightened loading of the dye in the vesicles in the reserve pool. These findings, together, hint that the cAMP/PKA cascade moderates the release of vesicles from the reserve pool to the recycling pool (Kuromi and Kidokoro, 2000).

When it comes to the release of synaptic vesicles from the reserve pool, one has to discuss the role of the synaptic vesicle protein "Synapsin", which exists as a family of phosphoproteins (SynapsinI(a&b) and II(a&b)) in vertebrates (Greengard et al., 1993), and as a singlular protein with multiple isoforms in *Drosophila* (Klagges et al., 1996). Synapsin is a major target of phosphorylation by PKA in mammals, and consists of multiple phosphorylation sites on different domains, depending on the Synapsin orthologue (Greengard et al., 1993). The function of Synapsin in maintaining the equilibrium between the vesicles in the reserve pool and recycling

pool, and consequently leading to the release of neurotransmitters stored in these vesicles, is conserved in vertebrates and invertebrates, although the exact mechanism by which this occurs in neurons, was unknown (Hilfiker et al., 1999).

The importance of Synapsin phosphorylation by PKA in invertebrates, was first identified in *Aplysia*, where the phylogenetically conserved PKA site-1 in the A domain on the N-terminal of the snail Synapsin protein was revealed (Fiumara et al., 2004). It was observed that when the PKA phosphorylation site on the A domain was mutated by substituting the serine with alanine, there was an absence of increased neurotransmitter release in comparison to that observed in wild-type *Aplysia* Synapsin (apSyn). The phosphorylation sites for PKA on the synapsin protein on the N and C terminal have been identified in *Drosophila* (Michels et al., 2005). The literature pertaining to the behaviour of *Synapsin* null mutants as well as *Syn* variants with respect to these phosphorylation sites, will be elaborated in the results section of this study. It should also be noted that PKA is not the only kinase that targets and phosphorylates the Synapsin protein at these recognition sites. *Drosophila* calcium-dependent calmodulin Kinase II (CaMKII), another widely observed kinase across species, also has a very interesting mechanism with which it coexists with PKA, and performs its phosphoryating function of Synapsin (Sadanandappa et al., 2013). This mechanism will also be addressed in detail in the results chapter of this thesis (see section 3.1.4).

To summarize the aspects of PKA-C1 in *Drosophila*, it is a phosphorylating kinase which is a part of the cAMP cascade and has been involved in a number of different learning and memory studies. While most of them have notably been related to olfactory associative learning and memory (Li et al., 1996; Tanaka et al., 2007; Volders et al., 2012; Zhao et al., 2013), there is limited evidence showing its relation to visual memory. In this doctoral dissertation, we aim to dissect the role of PKA in the context of visual short-term orientation memory, using hypomorphic mutant alleles, and transgenes that code for overexpression, as well as knock-downs of distinct subunits of the PKA tetramer in specific regions of the *Drosophila* brain. Throughout this study, we focus on not just PKA, but also the genes and proteins that regulate, and are regulated by this seemingly ubiquitous kinase, in order to design a novel model that can efficiently explain the functioning of this specific type of visual short-term orientation memory (see section 3.1).

1.6 Neurogenetic tools used in *Drosophila* behavioural studies

The GAL4-UAS system (Brand and Perrimon, 1993), has remained one of the most powerful methods to exercise targeted gene-expression in *Drosophila melanogaster* for nearly three decades. By directing the ectopic expression of genes that are of interest in a manner that is tissue specific, this method has expanded the field of *Drosophila* research, which was earlier dependent on either heat-shock promoters, or tissue-specific promoters to carry out the same function of targeted gene expression. However, these methods were accompanied by constraints in terms of temperature conditions, and limitations in availability of already characterized promoters.

This system comprises of two halves that cannot work independently of each other: 1) GAL4, a transcription activator protein isolated from yeast, and 2) an upstream activation sequence (UAS), which consists of five optimized GAL4 binding sites, followed by the gene of interest that needs to be expressed (Figure 5). Perrimon modified the original “enhancer detection technique“ in *Drosophila* (O'Kane and Gehring, 1987), by replacing lacZ with GAL4 so that the enhancer traps would now express GAL4. This mechanism utilized P-elements to study the expression of genes of interest. In addition, this work supported the previous observation pertaining to the importance of the strength of the enhancers of genes surrounding the exogenous gene in its expression, irrespective of its distance from the promoter (Rubin and Spradling, 1982).

“P-elements”, which are used as a means to generate transgenic *Drosophila* lines, consist of two aspects: 1) the “jumpstarter”, which codes for the transposase enzyme, and 2) the “mutator”, whose structure is viable for the cloning and insertion of exogenous DNA (Cooley et al., 1988). Oweing to the innate ability of the transposase enzyme to mobilize DNA, this system was extensively used in insertional mutagenesis in *Drosophila*.

In case of the GAL4/UAS system, the GAL4 activator was incorporated into the *Drosophila* genome using the enhancer detection vector pGawB, that was designed to contain the P-element carrying a sequence of inverted repeats (IR), and the GAL4 coding sequence, but not the P-transposase. Simultaneously, another “helper” plasmid was created which contains a defective version of the P-element, which can only code for the P-transposase enzyme, without transposing itself. Thus,

when both these plasmids are injected into the early embryo, only the plasmid containing the IRs is intergrated into the genome, and the random mobilisation of the P-element carrying the GAL4 activator sequence takes place. The strength of the GAL4 activator protein can also be varied, depending on the number, and nature of mutations made on the GAL4 transcription activator domain.

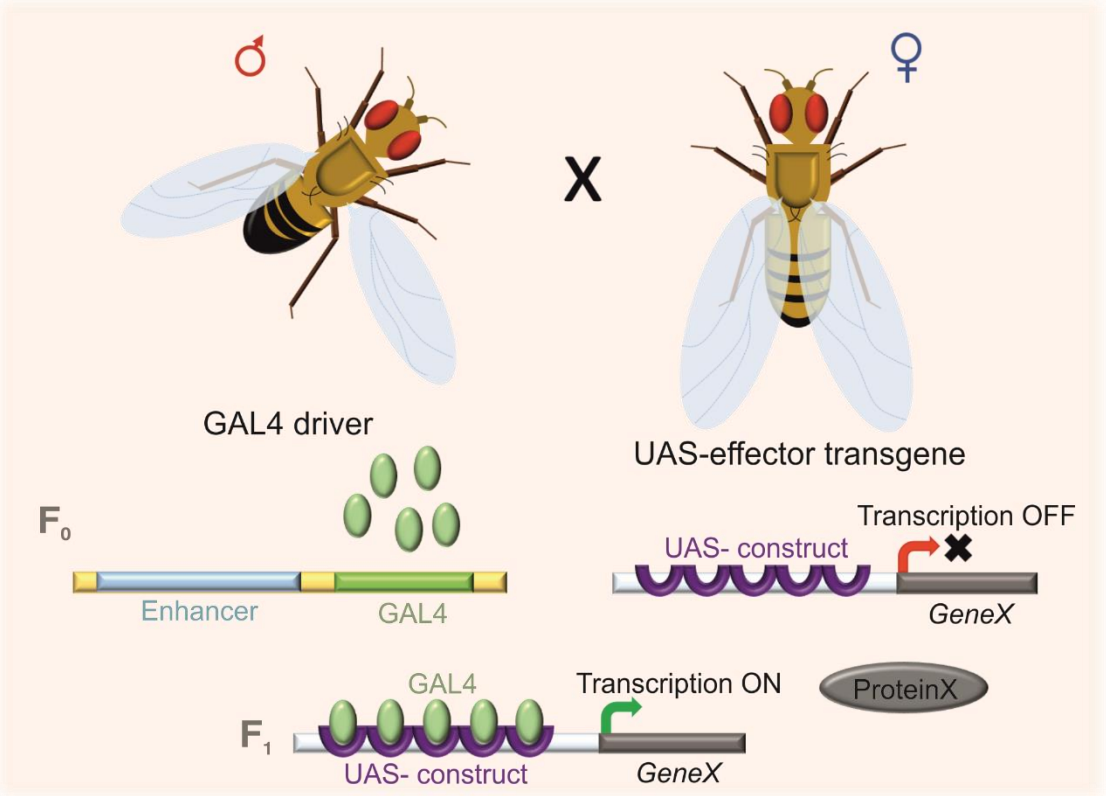

Figure 5: Functioning of the GAL4-UAS system in *Drosophila melanogaster*

The mechanism of GAL4/UAS system in *Drosophila* (Brand and Perrimon, 1993) consists of a minimal promoter, the GAL4 open reading frame (ORF) which is regulated by the nearest enhancer. The binding of the GAL4 proteins to the five distinct UAS-GAL4 binding sites, leads to the transcription of the transgene cloned next to the GAL binding domain. This transgene remains unexpressed until the binding of the GAL4 proteins. Thus, crossing a male carrying the GAL4-enhancer trap to a female containing the UAS-transgene construct, leads to the expression of the transgene in a cell/tissue specific manner in the fly belonging to the next (F1) generation, whose development and behaviour can be observed.

On the other hand, a pUAST plasmid was constructed, containing the UAS fragment behind which genes can be cloned. This fragment consisted of five GAL4 binding domains, a *hsp70* TATA box, and a transcription start sequence. When the GAL4 coding sequence, as well as the UAS construct containing the target gene are successfully integrated into the *Drosophila* genome, the binding of the GAL4 protein

to the UAS sequence, results in the cell/tissue-specific expression of the transgenes (Rubin and Spradling, 1982; Brand and Perrimon, 1993). Temperature-dependent repression of the GAL4 driver by $GAL80^{ts}$ between 18°C-30°C (McGuire et al., 2004), to enable the controlled expression of the UAS-transgene in an adult-specific manner without influencing the developmental process, is a modification of the classic GAL4/UAS system.

The specificity of the GAL4/UAS system has also been increased using the split-GAL4 system which divides the GAL4 activator domain into two parts, which can initiate the expression of the UAS-transgene only when present together within the same expression pattern in a fly (Luan et al., 2006).

The expression of the UAS-transgene can work in the context of overexpression as well as silencing of specific genes, in order to study their behavioural effects. This works in synergy with the principle of RNA interference (RNAi)/gene silencing. Originally discovered in *C. elegans*, RNAi involves the injection of double-stranded RNA hybrids containing both sense and anti-sense strands, where the RNA sequence was a part of the target gene homology (Fire et al., 1998).

In order to cater to cell/tissue specific silencing of genes in the *Drosophila* model, a comprehensive RNAi library has been created, comprising of a collection of 15,072 UAS-RNAi constructs, targeting 13,327 different genes (Dietzl et al., 2007; Ni et al., 2008), which can be addressed via the GAL4/UAS system. These UAS-IR constructs consisted of about 98.5% of the intended inverted repeats (IRs), which were predicted using e-PCR (electronic polymerase chain reaction), with a mean fragment length of 323bp, and matched the genes of interest. These palindromic fragments formed a dsRNA hairpin structure, which were then processed into smaller 19-mers by dicers. The same study (Dietzl et al., 2007), also uncovered the individual role of dicer-2 to be increasing the efficiency of the RNAi transgenic effect. Dicer-2 is also known for playing a critical role in siRNA formation (Lee et al., 2004).

In the year 2004, Groth and colleagues developed a very elegant method for mutagenesis using the phage ϕC31 (Groth et al., 2004). The site-specific integrase produced by phage ϕC31, mediates high frequency irreversible recombination between the *attB* and *attP* sequences, without requiring any co-factors. This ϕC31 system was incorporated into the *Drosophila* genome in this study by cloning two

individual plasmids into the *Drosophila* cells, where one contained the C31 integrase enzyme under the control of an antibiotic, while the other plasmid contained the LacZ gene flanked by attB and attP sequences. Staining with X-Gal revealed a recombination success rate of 47%. This method was highly useful for the insertion of a collection of exogenous genes at the same location within the *Drosophila* genome with the help of *attP* sites.

The latest development in the field of site-directed mutagenesis, is the prokaryotic system of the CRISPR/Cas9 (Jinek et al., 2012). The Cas9 enzyme, participates in the RNA processing using guide RNAs specific to the CRISPR (Clusterered Regularly Interspaced Short Palindromic Repeat) sequences which initiate a dsDNA break to mediate the deletion of endogenous DNA (Wiedenheft et al., 2012), and insertion of small exogenous DNA sequences when a repair ssDNA plasmid is present. This system has since then been tailored to suit the needs of mutatagenesis of the *Drosophila* genome *in vivo* (Lin et al., 2015; Xu et al., 2015).

The world of *Drosophila* neurogenetics was made even easier to access after the production of a vast collection of transgenic lines for *Drosophila*. Thousands of UAS-effector lines were created to observe gain-of-function phenotypes upon the expression of several transgenes (Rorth et al., 1998). In 2008, Pfeiffer and colleagues attempted to identify a large set of enhancers that could individually drive the expression of a reporter gene in a reproducible manner in a distinct population of cells in the adult CNS (Pfeiffer et al., 2008). 925 genes were identified to have expression in a subset of neurons in the adult *Drosophila* brain. Approximately 5200 test enhancer fragments were cloned, sequence verified, and fused with the GAL4 activator, using site-specific integration with the help of ϕC31 (Groth et al., 2004). UAS-GFP (Green Fluorescent Protein) was then used to observe the robustness of expression of each of these enhancers, and their ability to generate cell-specific expression patterns. This library was then expanded later in 2012, to include the expression patterns of all neurons within the *Drosophila* brain (Jenett et al., 2012).

Another binary system resembling the GAL4/UAS system, is the LexA/Lex_{op} system, where LexA, a dimer protein comprising of a DNA binding element, and a dimerization element, can bind to Lex_{op} (resembling the UAS), which has LexA DNA binding motifs, and is usually found upstream of the genes meant to be transcribed. Thus, fusion of LexA with GADd (GAL4 Activating Domain), or VP16, can facilitate in

the transcription of the genes with their respective promoters containing Lex_{op} motifs (Lai and Lee, 2006). Since 2010, an improvised LexA/Lex_{op} system was introduced by Pfeiffer and colleagues, where the GADd and VP16 were replaced with an extended GAL4 activating domain (GADfl) and P65, the human activation domain, along with a modified reporter that recognizes the LexA activity more efficiently (Pfeiffer et al., 2010).

One of the more recent developments in *Drosophila* genetics is the “Q system”, adapted from *Neurospora* (Potter et al., 2010). This binary system entails the mosaic labelling of transgenes whose expression occurs independently of the GAL4 system. It consists of 3 parts 1) A promoter driving the expression of an exogenous transcription factor QF, 2) the effector gene under the control of a promoter activated by QF, and 3) QS, the suppressor of QF, under the control of a ubiquitous tubulin promoter. All three components, while regulating each other, ultimately lead to the expression of the effector gene. This method improves the existing binary system in flies by preventing lethality due to direct interaction between the GAL4 and the effector lines, while increasing the efficiency of transcription of the effector gene due to the presence of a transcription factor. This technique was further improved in 2015 to include variants of the QF, such as Gal4QF, and LexAQF chimeric transcription factors (Riabinina et al., 2015), to rectify the lethality caused in the original method, where the QF was broadly expressed *in vivo*.

The most recent adaptation of the Q-System was applied in the trans-Tango method designed by Talay and colleagues in 2017. The trans-Tango design is based on the configuration of human glucagon. The membrane-tethered form of glucagon, which is fused to the presynaptic marker Neurexin, is the activator of this mechanism (labelled by myristilated GFP). The expression of the ligand, and the reporter 1 (UAS-myr::GFP), is GAL4 dependent. Another component of the pathway is the QF, which is coupled with a pan-neuronally expressed glucagon receptor, and controls the transcriptional activation of a second reporter (QUAS-tdTomato (mCherry)). Following the binding of the glucagon molecule to its receptor, QF is released, which binds to the QUAS, and leads to the transcription of mCherry. Thus, mCherry is expressed only in those neurons that are postsynaptic to the ones which contain the membrane bound glucagon, pre-determined by the GAL4 driver.

This highly used method, incorporates the reporters 1 and 2 along with the Q-system, in a single fly line. Crossing of these flies to the appropriate GAL4 driver, helps to visually reveal the presynaptic side, and postsynaptic partners of the neuronal subfamily addressed by the driver (Talay et al., 2017). Over the years, a number of fluorescent reporters have been used in synergy with the GAL4, Q, and LexA systems. In our study, we have extensively utilized the membrane-bound GFP (UAS-mCD8::GFP;(Lee and Luo, 1999)), to elucidate cell morphology. Recently, hexameric GFP, and mCherry constructs, have been created to increase the strength of fluorescence using the tandem fusion approach (Shearin et al., 2014). These reporters have aided in the visualisation of neuronal structures, as well as the connectome between different neuronal subtypes.

Analysis of neurotransmitters such as Dopamine, and Serotonin, has been done using activity measurement of enzyme decarboxylases (Livingstone and Tempel, 1983). A family of fluorescence sensors for Acetylcholine (GACh), which rely on GPCRs, have recently been employed to monitor the levels of ACh *in vivo* (Jing et al., 2018).

Activity measurement of neurons in *Drosophila* are currently being carried out using calcium indicators such as GCaMP3, which is a reader of action potentials (Tian et al., 2009). The voltage-gated sodium (Na) channel, termed as NaChBac, originally observed in prokaryotes (Ren et al., 2001) involving a depolarization-activated sodium channel, has also been adapted to study the excitability of neurons involved in the circadian rhythm, and other associated arrhythmic activity (Nitabach et al., 2006).

Selective activation of neurons is done through red light via the opening of the Chrimson channel (Klapoetke et al., 2014), and through temperature, via the activation of the TrpA1 channel protein (Rosenzweig et al., 2005). Selective inactivation of neurons by blocking the synaptic transmission with *shibire*^{ts1} (Kitamoto, 2002), and by repressing the cellular depolarization in the postsynaptic membrane using the *kir3.1* potassium channel (Paradis et al., 2001), are also performed regularly to manipulate *Drosophila* neurogenetics.

1.7 Objectives

This doctoral dissertation can be divided into three chapters with distinct objectives:

1). To understand, and elucidate the individual roles of Protein Kinase A (PKA) and Synapsin, in the functioning of short-term visual orientation memory (detour memory) in the R3 neurons of EB of *Drosophila melanogaster*. PKA, a cAMP-activated kinase, which is involved in a number of major pathways in *Drosophila*, can phosphorylate Synapsin at site-1, in the N terminal of the *Drosophila* Synapsin protein. The phosphorylated form of Synapsin (Syn-P1), eventually leads to the release of synaptic vesicles tethered to the cytoskeleton, leading to a shift between the reserve pool and recycling pool. These vesicles, filled with neurotransmitter molecules, would have a positive effect on detour memory functioning when allowed to be released. In addition to discovering the importance of PKA phosphorylation site-1 on the Synapsin protein, we also focus on the role of Rugose, an AKAP (A Kinase Anchoring Protein), that has been previously reported to function alongside PKA in the improvement short-term olfactory memory in *Drosophila* (Zhao et al., 2013).

2) Secondly, we aim to understand the role of each of the neuronal substructures belonging to the *Drosophila* central complex in the functioning of visual short-term orientation memory. This list includes the ring neurons (R1-R6) of the EB, the compass neurons (E-PG), the shift neurons (P-EN), and the newly characterized “non-canonical” ring neurons. This was done via temperature-sensitive activation and inactivation of these neurons. We also focussed on the relationship between the R3 neurons, and the compass neurons, and the potential synaptic connectivity between these two neuronal subfamilies that could govern this visual working memory.

3) Finally, we target the microtubule-associated protein “Tau”, which has been studied in the context of neurodegenerative diseases such as Alzheimer’s disease (AD), and fronto-temporal dementia and Parkinsonism associated with chromosome 17 (FTDP-17) in humans. In this study, we try to understand the importance of this protein in visual working memory using *dTau* knock-out/deletion, and point mutations for the human *Tau* gene after replacing the endogenous one.

2. Materials and methods

2.1 Fly stocks

Table 1: Fly catalogue

2.1 (a) A comprehensive catalogue of the flies used in this study along with their chromosome number, respective source and a published reference.

Strain	Chr.	Source	Reference
WT-CS		Prof. Dr. Roland Strauß, Institute of developmental biology and neurobiology (IDN)	(Benzer, 1967)
GAL4 drivers			
189Y-GAL4	II	Douglas Armstrong, University of Edinburgh, UK	(Renn et al., 1999)
EB1-GAL4	III	Douglas Armstrong	(Pan et al., 2009)
ftz-ng-GAL4/TM3,*Sb*	III	Bloomington Drsosophila Stock Centre (BDSC); BL 8767	(Pereanu et al., 2011)
R12D09-GAL4	III	BDSC; BL 48503	(Jenett et al., 2012)
R18A05-GAL4	III	BDSC; BL 48794	(Jenett et al., 2012)
R19C08-GAL4	III	BDSC; BL 48845	(Jenett et al., 2012)

R19G02-GAL4	III	BDSC; BL 48860	(Jenett et al., 2012)
R31A12-GAL4	III	BDSC; BL 49661	(Jenett et al., 2012)
R32A11-GAL4	III	BDSC; BL 62831	(Jenett et al., 2012)
R58H05-GAL4	III	BDSC BL 39198	(Jenett et al., 2012)
R75H04-GAL4	III	BDSC; BL 39909	(Jenett et al., 2012)
VT011965-GAL4	III	V.Hartenstein	(Kvon et al., 2014)
VT42759-GAL4	III	Vienna Drosophila Research Centre (VDRC) 202895	(Kvon et al., 2014)
LexA lines			
R54B05-LexA	II	BDSC; BL 54892	(Pfeiffer et al., 2010)
R60D05-LexA	III	BDSC; BL 52867	(Pfeiffer et al., 2010)
Mutant lines			
189Y-GAL4/*CyO*; *Syn*^{97}/TM3,*Sb*	II,III	Sara Kuntz	Sara Kuntz, PhD Thesis, Uni Mainz
Pka-C1^{H2}*/CyO*	II	BDSC; BL 4101	(Lane and Kalderon, 1993)
rgγ5	I	BDSC; BL 78792	(Shamloula et al., 2002)
Synapsin (Syn^{97}*)*	III	E. Buchner, University	(Godenschwege et al., 2004)

		Würzburg	
hTau^{WT}	III	D. Kretzschmar, OHSU- Portland, USA	Unpublished
hTau$^{K/I}$	III	D. Kretzschmar	Unpublished
hTau$^{P/L}$	III	D. Kretzschmar	Unpublished
hTau$^{V/M}$	III	D. Kretzschmar	Unpublished
Tau^{del}	III	D. Kretzschmar	Unpublished
Tau^{KO}	III	BDSC; BL 64782	(Burnouf et al., 2016)
Recombinant lines			
Pka-C1^{H2}189Y-GAL4/*CyO*	II	Burkhard Poeck	Unpublished
Pka-C1^{H2}UAS-*Pka-C1(Fl5.9)*/*CyO*	II	Burkhard Poeck	Unpublished
UAS-mCD8::GFP/FM7a;189Y-GAL4/*CyO*	I,II	Sara Kuntz	Sara Kuntz, PhD Thesis, Uni Mainz
VT42759>*UAS-Pka-C1Fl5.9*/TM3,*Sb*	III	Anjana Venkataramanan	Unpublished
UAS effector lines			
UAS-*Adar*^{RNAi}	III	BDSC; BL 28311	(Perkins et al., 2015)
UAS-Den(mCherry), Syt::GFP/*CyO*	II	BDSC; BL 33064	(Nicolai et al., 2010) (Zhang et al., 2002)
UAS-*CaMKII.T287D*	III	BDSC; BL 29665	(Park et al., 2002)
UAS-*CaMKII-I.Ala*	II	BDSC; BL 29666	(Griffith et al., 1993; Jin et al., 1998)
UAS-*CaMKII*^{RNAi}	III	BDSC; BL 29401	(Perkins et al., 2015)

UAS-mCD8::GFP/FM7a	I,II	BDSC; BL 5136	(Lee and Luo, 1999; Dubruille et al., 2002)
UAS-myrGFP,QUAS-mtdTomato(3XHA)(mCherry); trans-Tango	I,II	Gilad Barnea, Brown University-Providence, USA #2087	(Talay et al., 2017)
UAS-Nrx::GFP1-10/*CyO*; LexA(op)CD4::GFP11/TM6,*Tb*	II,III	Zipursky, UCLA-USA	(Chen et al., 2014)
UAS-*Pka-C1(Flag5.9)*/TM3,*Sb*	III	Kiger	(Kiger et al., 1999)
UAS-*Pka[mC*]*/TM3,*Sb*	III	Kiger	(Li et al., 1995)
UAS-*Pka-R1*^{RNAi}	III	BDSC; BL 27708	(Perkins et al., 2015)
UAS-*rg*/*CyO*	II	M. Schwärzel	(Volders et al., 2012)
UAS-*rg*^{RNAi}	II	BDSC; BL 57703	(Perkins et al., 2015)
UAS-*shi*^{ts1}	III	BDSC; BL 44222	(Waddell et al., 2000)
UAS-*Syn*(cDNA8); *Syn*^{97}	II,III	Erich Buchner	(Michels et al., 2011)
UAS-*Syn*(PKA1+2mutant), *Syn*^{97}/TM3,*Sb*	III	Erich Buchner	(Michels et al., 2011)
UAS-*Syn*(PKA1mut,PKA2wt), *Syn*^{97}/TM3,*Sb*	III	B.Gerber, LIN-Magdeberg BG#143 Erich Buchner	Unpublished
UAS-*Syn*(PKA1non-edit,PKA2mut),*Syn*^{97}	III	B.Gerber, LIN-Magdeberg Erich Buchner EB 1-12	Unpublished
UAS-*Syb*::spGFP1-10, LexA(op)CD4::spGFP11/*CyO*	II	BDSC; BL 64314	(Macpherson et al., 2015)
UAS-*TrpA1*/*CyO*	II	BDSC; BL 26263	(Rosenzweig et al., 2008)

2.1 (b) Source and generation of special fly lines

Synapsin mutant flies

All the strains containing the *Synapsin* gene and its variants, were graciously provided by our colleague E. Buchner (University Würzburg). The single mutations for individual PKA phosphorylation sites on Synapsin: UAS-*Syn*(Pka2 WT, Pka1 mut), and UAS-*Syn*(Pka1 non-edit, Pka2 mut), were originally generated in Bertram Gerber's group (LIN Magdeburg), and provided to us by E. Buchner. The flies mutant for the two PKA phosphorylation sites on *Synapsin* (UAS-*Syn*(Pka site 1+2 mut)), were created the same way it is described in previous literature (Michels et al., 2011).

Tau mutant flies

The *Tau* mutant and deletion ($dTau^{del}$) flies were generated in the D. Kretzschmar lab (OHSU, Portland OR; USA), using the CRISPR/Cas9 technique (Ren et al., 2014). The deletion covers all coding exons of *dTau*. For functional analysis of the human Tau protein in flies, a cDNA presenting one of the splice variants of the human *Tau* gene, encoding the 1N4R isoform, was integrated into the *Drosophila* genome, thereby deleting all coding exons of the *Drosophila* (*dTau*) gene (Figure 6A). The same cDNA was used to introduce point mutations associated with familial tauopathies (Alonso et al., 2004), by site-directed mutagenesis (Figure 6B). Again, the CRISPR/Cas9 technique was used to mediate homologous recombination into the endogenous *dTau* gene locus. The resultant transgenic lines were crossed into wild type Canton S (CS) background for behavioural analysis.

- Human ($hTau^{WT}$) → *hTau*-1N4R
- HumanTau^{K369I} ($hTau^{K/I}$) → Point mutation leading to missense in exon 12.
- HumanTau^{P301L} ($hTau^{P/L}$) → Point mutation leading to missense in exon 10.
- HumanTau^{V337M} ($hTau^{V/M}$) → Point mutation leading to missense in exon 12
- Tau^{del} → Deletion of the entire coding sequence of *Tau* gene.

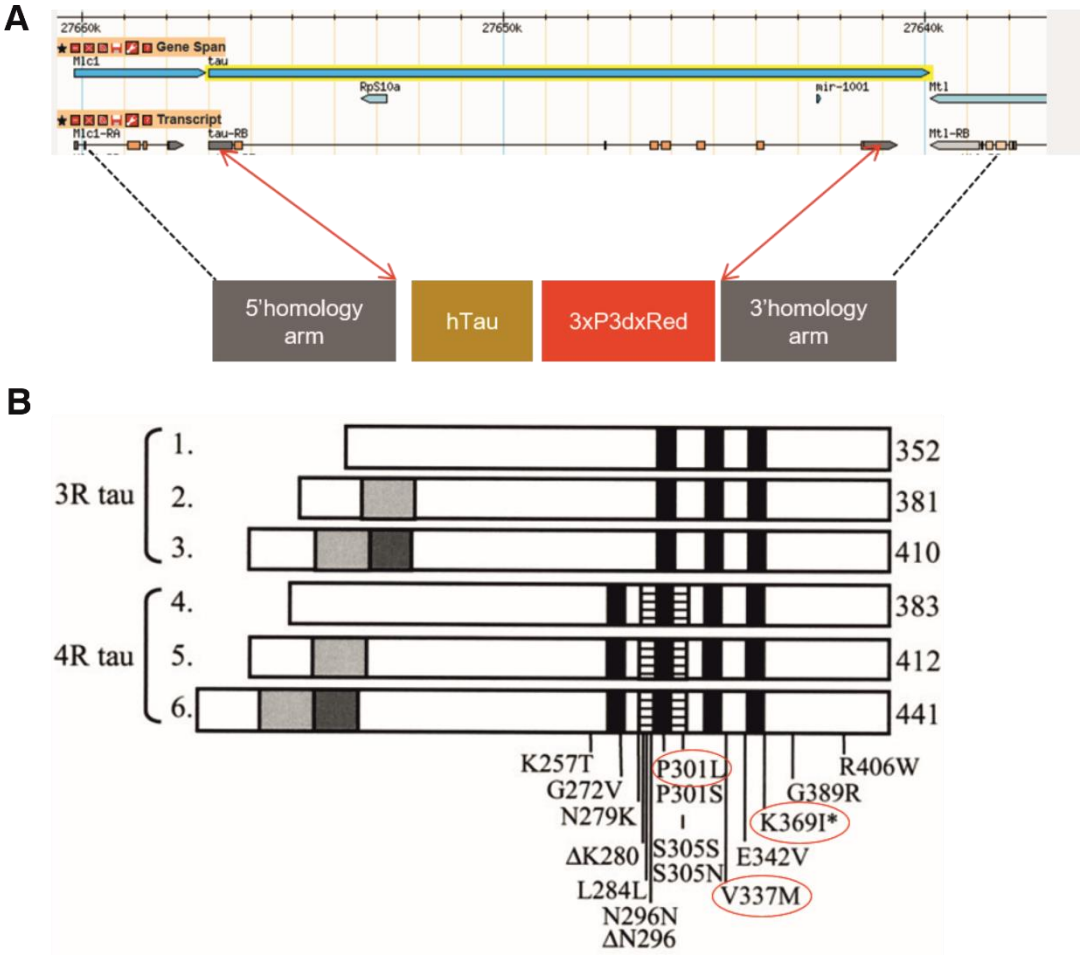

Figure 6: Deletion of *Drosophila Tau* and incorporation of human wild-type *Tau* and variants

(A) Deletion of the *Drosophila Tau* (*dTau*) gene using CRISPR/Cas9 to incorporate the human *Tau* (*hTau*) gene (Figure modified from (Marlène Cassar, 2020)). Guide-RNAs were designed to direct Cas9 to the first and last exon of the *dTau* gene (red arrows). The resultant deletion covers all coding regions of dTau. The human *Tau* cDNA was incorporated into the fly genome using the same guide-RNAs and a repair template containing a hTau cDNA and Pax3 driven DsRed as selectable marker.
(B) Six different Tau isoforms are expressed in the adult human brain. The gray, dark gray, and striped boxes represent the alternatively spliced exons 2,3 and 10 respectively. The black bars are indicative of the microtubule binding repeats (Neumann et al., 2001); copyright license attached in Appendix (section 8.4). Three of the sixteen missense mutations (circled in red) were induced into the *hTau* gene using CRISPR/Cas9, and incorporated into the *Drosophila* genome as shown in (A).

2.2 Fly raising and maintenance

All flies were raised and maintained on standard fly food under conditions of 60% humidity, and 25°C temperature. They were subjected to a 14:10 hr light/dark cycle (with the light cycle beginning at 07:00 hr). All the flies stored at 25°C were transferred to vials containing new food every three days to one week. Flies that were raised in the 18°C chamber were transferred to vials containing new food once in two weeks. The vials were transparent, with a total capacity of 80cc, and filled with nearly 20mL of standard fly food. Air-permissive foam stoppers were used in order to

contain the flies within the vials. The fly food consists of fixed concentrations of water, maize flour, malt extract, sugar beet syrup, yeast, soy flour, agar and nipagin.

2.2 (a) Drug treatment with tetracycline

For flies requiring special treatment with food containing tetracycline, Tetracycline Hydrochloride (from Carl Roth GmbH; Art. -Nr. HP63.1) was used. 1.5mL of tetracycline (10mg/mL), was added to 1L of the fly food and distributed amongst multiple vials. The food vials containing tetracycline were stored in the dark at 4ºC until use. Flies that underwent ageing on tetracycline food, were transferred to vials containing new food (with tetracycline) every three days.

2.2 (b) Raising of temperature-sensitive flies

The crosses involved in TrpA1 activation and Shibire inactivation studies (including GAL4 and UAS control crosses), were kept at 25°C for the first three days, and transferred to the 18°C chamber for the rest of the developmental stages until eclosion. The young F1 progeny males (1-3 day old) were then maintained at 18°C until testing in the detour arena.

2.3 Behavioural assay- the detour paradigm

2.3.1 Detour paradigm- apparatus

All behavioural experiments were carried out in the “detour arena” (Neuser et al., 2008) (Figure 7), encompassing an artificial environment for the flies to perform in. It is a cylindrical LED arena consisting of 180 columns, with 32 light-emitting diodes (LED), as shown in Figure 7.

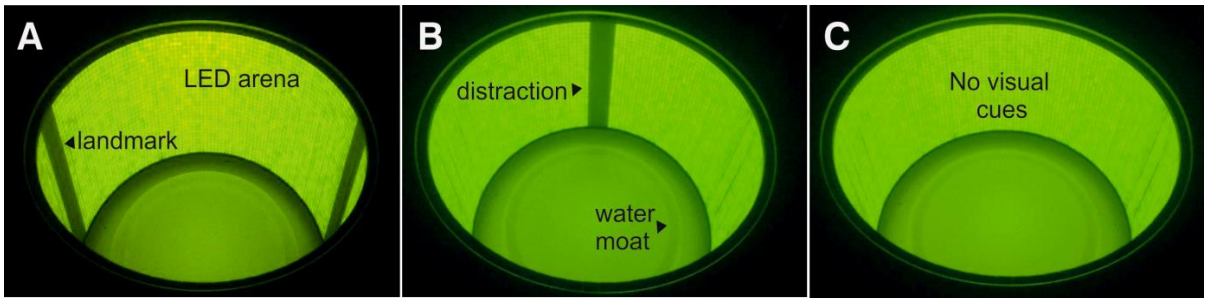

Figure 7: The detour paradigm apparatus

(A) The cylindrical LED screen shows two landmarks on either side, serving as the primary visual cues facing each other at 180º. **(B)** The distractor bar appears at an angle of 90º to both the landmarks and has an appearance similar to that of the landmark bars. **(C)** It disappears one second after the fly has turned to track the distractor, leaving the arena with no observable visual cues.

The diodes emit 5760 pixels (Figure 7), and each pixel has a 2º X 2º viewing angle when observed from the centre of the arena. The floor/platform of the arena spans 26cm in diameter, surrounded by a 2-cm-wide water moat and made of matted plexiglass (Figure 7). Landmarks (both landmarks and distractor) were created by turning off a section of the LED lights, to create the illusion of darkness/exit to the fly currently in the arena (contrast 0.94). They were at a distance of 20cm from the centre of the arena, and the distractor bar is exactly at an angle of 90º from the landmark bars (Figure 7) (Strauss et al., 1997).

All experiments were carried out at temperatures ranging between 23ºC-25ºC, to facilitate optimal behavioural output from the organism. The temperature in the room was regulated using an air-conditioner on hot days, and the heating system on the colder days. The room was also maintained to be dark, either by turning off any light sources, or by using the over-head red light on the ceiling (flies are blind to red light), to ensure that the flies being tested were exposed only to the visual inputs provided inside the arena and not to any external distractions.

2.3.2 Principle behind the detour arena

In the detour paradigm (Figure 8), a walking fly (3-5 days old) in a lit LED arena (Figure 7), shuttles between two dark vertical stripes (landmarks), perceiving them to be escape routes from the enclosed arena (Figure 8A). Just before crossing a virtual midline, it is distracted by switching the stripe to + or - 90°.

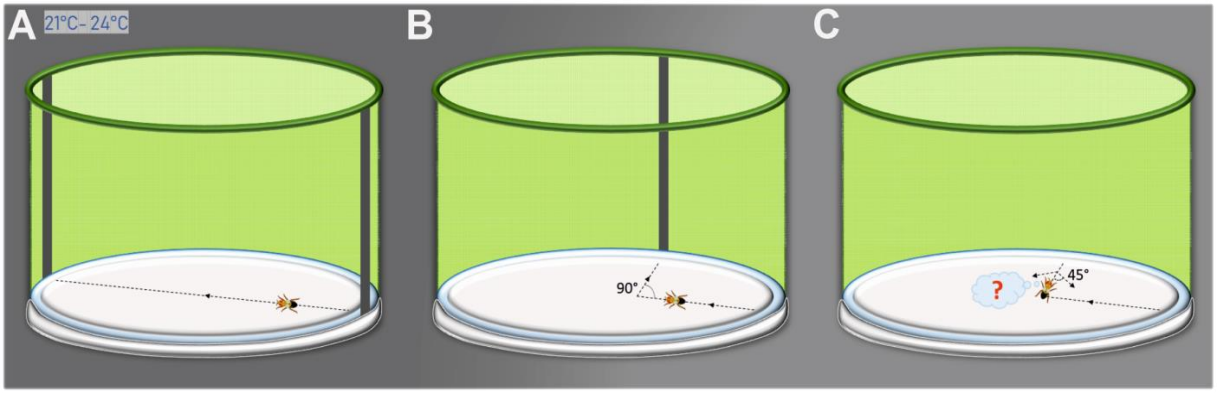

Figure 8: Functioning of the detour paradigm at a normal temperature range

(A) The test fly, follows the landmarks back and forth across the arena and is prevented from escaping by the water moat surrounding the floor of the arena. **(B)** The fly is shortly distracted by the distractor bar appearing at 90º to the landmarks and turns towards it as it approaches the centre of the arena. **(C)** After the disappearance of the distractor bar, the fly is facing the direction of the distractor before turning 45º to the initial direction of walking (positive choice) or turning 45º back towards the starting point (negative choice)

This distractor bar, albeit resembling the landmark in its shape, disappears 1 second after the fly has turned towards it (Figure 8B). Now, no visual cues remain, and the fly is expected to decide its direction of turning within the next 4 seconds (Figure 8C). Turns of more than 45° in the direction of the initial landmark the fly was walking towards, were counted as positive choices. Wild-type flies recall the position of their initial target in ~80% of the trials and turn to resume their walk towards the original direction even when the landmark is still invisible. While the mutant flies, which have undergone a manipulation in any of the genes regulating the orientation memory, fail to remember the original landmark within 4 seconds, leading to random choices. The random choice level (dashed line in all box plots in the results section), is at 58% due to the so-called turn compensation. This value was determined by analysing freely walking flies in an arena without any cues. During random search, a fly has a higher probability to perform a right turn after a previous left turn, and vice versa.

2-5-day-old flies were collected and tested in the detour arena one day after shortening their wings. Every fly was allowed to perform ten trails in the arena and their respective positive and negative choices were noted for comparative statistical analysis, where every positive choice accounted for 10% of the total score. For each genotype, approximately 20-25 flies were tested to build a reasonable sample size for further statistical analysis.

2.3.3 Temperature-sensitive behavioural experiments

The experiments requiring activation of certain proteins through increase of temperature, were performed using a red warming lamp[1] (220-230V, 100W) that was placed underneath the detour arena and connected to an external power supply. The activation of temperature-sensitive TrpA1 channel protein in flies, was done de-novo by increasing the temperature in the arena between 28°C - 30°C, using the red lamp, which was periodically switched ON (when the arena temperature went < 28°C), and OFF (when the temperature reached > 30°C) (Figure 9).

The same principle was followed for the activation of *shibire*^{ts1}, by increasing the temperature to range between 30°C - 32°C at the time of testing (Figure 9). The existing temperature in the arena was measured before the start of testing of each fly

[1]OSRAM SICCATHERM, 220-230V, 100W

using a temperature-measuring device[2], which was always pointed at the centre of the arena for accurate measurement.

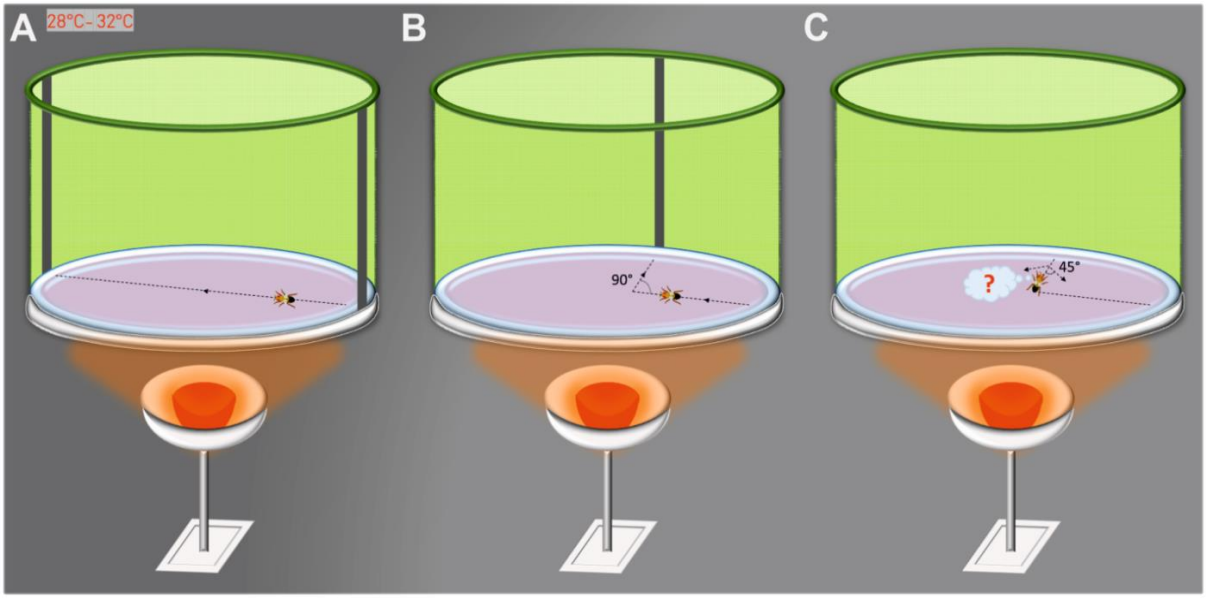

Figure 9: The set-up for the detour paradigm at elevated temperature range

(A&B) The functioning of the paradigm is similar to that observed in Figure 8, except that there is a red lamp placed beneath the arena which is switched ON to increase the temperature to the required range and then switched OFF when necessary, to avoid overheating. **(C)** In the absence of any visual cues, the performance of the fly in the arena may strictly depend on the type of protein that is being activated at the higher temperature range.

2.3.3.1 Temperature-sensitive activation of neurons by TRPA1 channel protein

dTRPA1 (*Drosophila* Transient Receptor Potential Ankyrin1), was originally detected in the anterior cell (AC), lateral cell (LC), and the ventral cell (VC) neurons of the *Drosophila* brain (Hamada et al., 2008). Compartmentalized knock-down studies revealed that the function of TRPA1 for thermotaxis was primarily located in the AC neurons since the knock-out of dTRPA1 in the other neurons, did not affect the original phenotype of warmth avoidance (Rosenzweig et al., 2005). The precise mechanism of thermospecific activation was uncovered using GCaMP, a fluorescent indicator of calcium. The study revealed a spike in GCaMP fluorescence in the AC neurons upon TRPA1 activation, accompanied by an absence of increase in Ca^{2+} in dTRPA1 mutants (Hamada et al., 2008). This confirmed that the increase in Ca^{2+} ions, was an effect of thermal responsiveness, and a crucial aspect of dTRPA1 activation mechanism (Hamada et al., 2008). The activation of dTRPA1 at higher

[2] FLUKE 62 Mini IR Thermometer

temperatures (>28ºC), leads to an increased Ca^{2+} influx through the cell membrane, thereby activating the neurons (Figure 10).

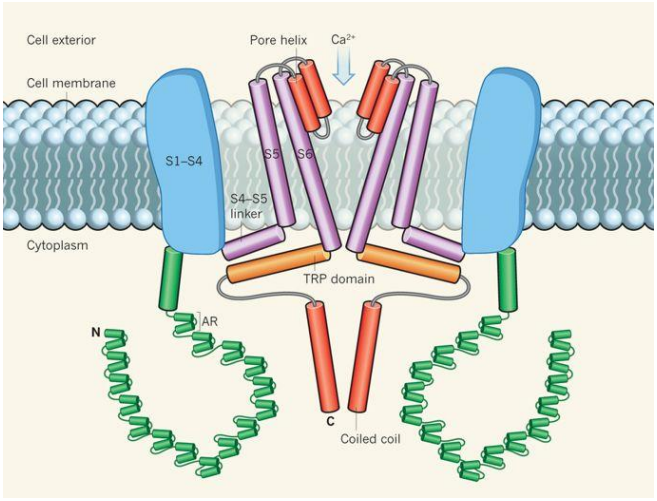

Figure 10: Structure and working of the TRPA1 channel protein

The TRPA1 channel which allows the influx of Ca^{2+} ions through the cell membrane based on temperature shift. The channel consists of 4 domains (2 shown here). There are 16 ankyrin repeats in the N (amino) terminal surrounding the coiled structure of the C (carboxy) terminal. This leads to an increase in its surface area. Figure adapted from (Clapham, 2015); copyright license attached in Appendix (section 8.4).

Using this channel protein as an effective tool, neuronal activation using GAL4-driver-specific expression in the brain was carried out by manipulating the temperature within the arena. Every fly belonging to the TrpA1 activation study (GAL4 control, UAS control and experimental group), was tested twice in the detour arena- once at 21°C (Figure 8) and another time at 29°C (Figure 9), with an intermediate gap of 15-30 minutes at room temperature (25°C). The flies were placed in mini vials, with one fly in each vial, in order for the behavioural test procedure to qualify for a pair-wise statistical analysis.

2.3.3.2 Temperature-based inactivation of neurons by UAS-*shibire^{ts1}*

In *Drosophila*, the *shibire* gene encodes for the protein “dynamin”, which regulates neurotransmission by regulating the synaptic vesicle recycling at nerve terminals (Kasuya et al., 2009). A particular mutant form of *shibire,* where a single amino acid is substituted in the GTP-ase domain, leads to the version of the dynamin protein that is no longer active at higher temperatures. Thus, these *shibire* mutants are called *shi^{ts1}* (*shibire temperature-sensitive1*), which code for the dominant negative form of the dynamin protein that is impaired at higher temperatures, but can be reversibly activated on returning to lower temperatures (Kosaka and Ikeda, 1983).

The inactivation of dynamin at higher temperatures leads to failure in synaptic vesicle recycling, leading to a deficit in the vesicles available at the nerve terminal (Figure 11). As a result, the neurotransmission is curbed, leading to a plethora of behavioural defects.

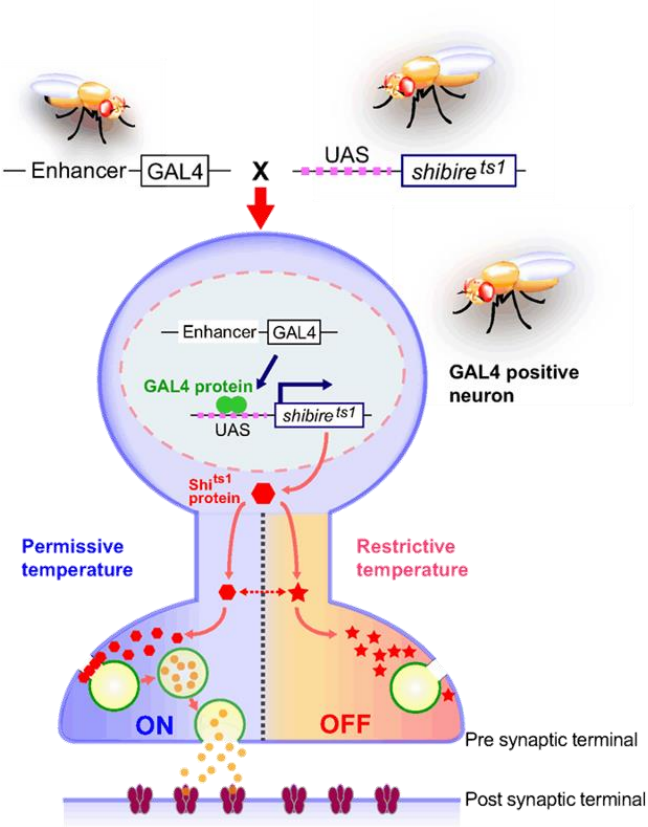

Figure 11: Schematic representation of the mechanism of UAS-*shibire*^{ts1} in *Drosophila*

The expression of UAS-*shi*^{ts1} in a neuron using the GAL4 enhancer trap, leads to two different outcomes in different scenarios depending on the temperature. At the permissive temperature (<30ºC), dynamin is allowed to function in synaptic vesicle recycling, leading to successful neurotransmission. On the other hand, in the restrictive temperature (>30ºC), the vesicle recycling is inhibited due to reversible deactivation of the dynamin protein, leading to an absence of neurotransmission and synaptic activity at the nerve terminal. Figure adapted from (Kasuya et al., 2009).

The UAS-*shi*^{ts1} transgene has so far been expressed in GAL4 drivers targeting excitatory cholinergic neurons, which led to paralysis at higher temperatures, but normal behaviour within 2 minutes of returning to the permissive temperature (Kitamoto, 2001). Expression of the UAS transgene in neurons involved with vision, for example, the photoreceptors, also led to temperature-dependent deficit in behaviours which are light-dependent. Thus, this mechanism has been proposed as a molecular switch to enable selective inactivation of neuronal subsets to study their impact on different behaviours.

For our study focussing primarily on the detour memory, this UAS-*shi*^{ts1} transgene was expressed using specific GAL4 drivers to enable neuronal inactivation of different subsets of the neurons in the *Drosophila* brain. This was carried out by manipulating the temperature within the detour arena to facilitate activation and inactivation of the dynamin protein. Every fly belonging to the inactivation study (GAL4 control group, UAS control group and experimental group), was tested twice in the detour arena, once at 24°C (Figure 8), and another time at 32°C (Figure 9) with an intermediate time gap of at least 15-30 min at room temperature (25°C). The flies were placed in mini vials with one fly in each vial in order for the behavioural test procedure to qualify for a pair-wise statistical analysis.

2.4 Statistical analysis of behavioural studies

All statistical analysis were carried out using STATISTICA 8.0. Shapiro-Wilk test was used to test for normality distribution where $p>0.05$ signifies a normally distributed data-set and $p<0.05$ indicates that a data-set is not normally distributed. Wilcoxon matched pair test was used for pair-wise analysis. Multiple comparison tests were done to compare three or more genotypes against one another using Kruskal-Wallis ANOVA (with in-built Bonferroni post-hoc). For non-parametric data, the Sign test was used to compare the genotypes against the chance level of 58% while the single-sample t-test was used for normally distributed/parametric data for the same comparison. A significant difference (indicated by *) was observed when the p values amongst groups ranged between $p<0.05$ (*), $p<0.01$(**), and $p<0.001$(***). The “n.s” denotes “not significant”. In all graphical representations, the whiskers indicate 5%/95% quantiles, while the boxes signify 25%/75% quantiles. Dashed line in graphs depicts the random chance level of 58%.

2.5 Immunohistochemistry

2.5.1 Standard staining protocol AG Strauß

Before beginning the dissection process, the flies were immobilized by placing them on ice shortly. Each fly was then transferred to a vial containing 70% ethanol to clean the fly from any form of superficial dirt for about 20-30 seconds, and then transferred to another vial containing 1X PBS (Phosphate Buffer Saline).The *Drosophila* heads were dissected out in a third vial (the dissection dish), also containing 1X PBS. Fixing of biological processes was done by treating the brains with 4% paraformaldehyde (PFA)/PBS for a total of 1 hour at room temperature (30 min in 4% PFA/PBS + 30 min in 4% PFA/0.2% PBTX). Subsequent washing steps were carried out using 0.5% Triton-X100/1X PBS at room temperature (4 times, 5 min each+ 3 times, 10 min each). A permeabilisation step was carried out to increase the receptiveness of the brain’s membrane to the primary antibodies by incubating them with 1% PBTX for 45 min at room temperature on a shaker[3]. Blocking step was performed to prevent cross-reactivity of proteins by treating the brains with 5% horse serum in 0.5% PBTX for 1 hour. The brains were then incubated with primary antibodies of dilutions 1:1000 (chicken anti-mouse antibody), 1:100 (mouse anti-FASII antibody), 1:200 (rat anti-FLAG antibody), 1:200 (goat anti-mCherry antibody)

[3] Mini-Rocker shaker from Johanness Gutenberg University

in blocking solution for 36-48 hours on the shaker, at 4°C. On the second day of immunohistochemistry treatment, 0.5% PBTX was used to wash away the primary antibodies (2 times, 5 min each + 6 times, 20 min each), followed by blocking with 5% horse serum in 0.5% PBTX for 30 minutes. Secondary antibodies (Table 3) were added in dilutions of 1:1000 (unless mentioned otherwise) in blocking solution, and incubated for 48-72 hours on the shaker, at 4°C. On day 3 of treatment, the secondary antibodies were washed out using 0.5% PBTX (2 times, 5 min each + 6 times, 20 min each), and the brains were stored in 50% glycerine/PBS at 4°C overnight to promote clarification, and aid in clearer visualization. The specimens were then transferred to fresh glass slides[4] containing a drop of VECTASHIELD® mounting medium (to aid in extending the longevity of the fluorophores and minimize fading), and secured with a cover slip[5]. The coverslip was sealed on all four sides using a transparent top-coat nail polish, and allowed to dry. Scanning and acquiring of images were done using a laser-scanning microscope (Leica TCS SP8), and the Leica LASX software respectively.

2.5.2 Staining protocol for phosphosyapsin-1 (Syn-P1)

The samples were dissected in 1X PBS, as mentioned in the previous section (section 2.5.1 Standard staining protocol AG Strauß). Fixing of biological processes was done by treating the brains with 4% PFA/PBS for a total of 1 hour at room temperature. Subsequent washing steps were carried out using 0.3% Triton-X100/1X PBS at room temperature (2 times, 5 min each + 3 times, 10 min each). A permeabilisation step was carried out to increase the receptiveness of the brain's membrane to the primary antibodies by incubating them with 1% PBTX for 45 min at room temperature. Blocking step was performed to prevent cross-reactivity of proteins by treating the brains with 5% goat serum in 0.3% PBTX for 1 hour. The brains were then incubated with primary antibodies of dilutions 1:1000 (chicken anti-GFP antibody), and 1:300 (rabbit anti-SYNP1 antibody, (Blanco-Redondo et al., 2019). On the second day of immunohistochemistry treatment, 0.3% PBTX was used to wash away the primary antibodies (2 times, 5 min each + 6 times, 20 min each) followed by, blocking with 5% goat serum in 0.3% PBTX for 30 minutes. Secondary antibodies (Table 3) were added in blocking solution, and incubated for 48-72 hours on the shaker, at 4°C. On day 3 of treatment, the secondary antibodies were washed

[4] Marienfield microscope slides 76x26x1mm
[5] Marienfeld Superior, Precision cover glasses thickness No. 1.5H (18 x 18 mm)

out using 0.3% PBTX (2 times, 5 min each + 6 times, 20 min each) and the brains were stored in 50% glycerine/PBS at 4°C overnight to promote clarification and aid in clearer visualization. Mounting on day 4 was done as described previously (section 2.5.1 Standard staining protocol AG Strauß).

2.5.3 Protocol from Wilson and Laurent., 2005

The brains were dissected out in 1X PBS (maintained in cold temperatures) and fixed in 5% PFA/PBS for 15 minutes at room temperature. The samples were then washed with 1X PBS (3 times, 20 minutes each) and incubated in the blocking solution (5% goat serum/0.2% PBTX) for 20 minutes. They were then incubated in the blocking solution containing the primary antibodies for 48 hours on the shaker, at 4°C. On day 2 of experiment, the primary antibodies were washed off using 0.2% PBTX (2 times, 5 min each + 3 times, 20 minutes each) and incubated with the secondary antibodies (Table 3), in 0.2% PBTX (in the absence of 5% goat serum) for 48-72 hours on the shaker, at 4°C. Finally, on day 3, the secondary antibodies were rinsed off from the samples using 0.2% PBTX (3 times, 10 min each), and briefly with 1X PBS before mounting them on the microscopic slides (Wilson and Laurent, 2005) as described previously (section 2.5.1 Standard staining protocol AG Strauß)

2.5.4 GRASP protocol from Pech et al., 2013

The preparation of samples was done at cold temperatures in Ringer solution (Table 5) and fixed for 2 hours on ice in 4% PFA/PBS. Following the fixation step, the samples were washed 3 times (20 minutes each) in 0.5% PBTX on the shaker. A pre-incubation step was carried out where the samples were placed in the blocking solution (0.1% BSA in 5% Goat serum/0.5% PBTX) for 2 hours at 4°C. They were then incubated in the blocking solution containing the primary antibodies (anti-GFP, mouse; anti-CD4, rabbit) overnight on the shaker, at 4°C. The next day, the washing steps were performed in 0.5% PBTX (3 times, 20 minutes each) to cleanse the samples off of the primary antibodies before incubating them with the blocking solution containing the secondary antibodies (Table 3), overnight on the shaker at 4°C. On day 3, the samples were washed once again in 0.5% PBTX (3 times, 20 minutes each) and stored in 1X PBS overnight on the shaker, at 4°C (Pech et al., 2013), before mounting them on day 4 as described previously (section 2.5.1 Standard staining protocol AG Strauß).

2.6 Antibodies used

Table 2: List of primary antibodies

Antibodies	Animal	Source	Identifier	Section	Dilution
α-CD4	rabbit	Sigma-Aldrich	HPA004252	3.2.3.3	1/100
α-FasciclinII	mouse	DHSB	Cat# 1D4 RRID:AB_528235	3.1.5	1/100
α-FLAG	rat	Novus Labs	NBP1-06712	3.1.5	1/200
α-GFP	chicken	Aves Labs	Cat# GFP-1020	3.1.2, 3.1.3r, 3.1.4, 3.2.3.2, 3.2.5.3	1/1000
α-GFP (GFP-20)	mouse	Sigma-Aldrich	G6539	3.2.3.3	1/200
α-mCherry	goat	SICGEN	AB0040-200	3.2.3.1, 3.2.3.2 3.2.5.3	1/200
α-Phospho-synapsin1	rabbit	(Blanco-Redondo et al., 2019)		3.1.2, 3.1.3 and 3.1.4	1/300

Table 3: List of secondary antibodies

Antibodies	Animal	Source	Identifier	Section	Dilution
α-chicken(A488)	goat	Invitrogen	A11039	3.1.2, 3.1.3, 3.1.4	1/1000
α-chicken(A488)	donkey	Sigma-Aldrich	SAB4600031	3.2.3.1, 3.2.3.2, 3.2.5.3	1/1000
α-goat(Cy3)	donkey	Dianova	705-165-147	3.2.3.1, 3.2.3.2, 3.2.5.3	1/1000
α-mouse(A488)	goat	Sigma-Aldrich	62197	3.1.5, 3.2.3.3	1/1000, 1/250
α-rabbit(Cy3)	goat	Dianova	111-165-003	3.1.2, 3.1.3, 3.1.4	1/1000
α-rat(Cy3)	donkey	Dianova	712-165-150	3.1.5	1/1000

2.7 Chemicals used

Table 4: Serums used in the IHC study and their source

Solutions	Source
Normal Horse Serum blocking solution	VECTOR laboratories (S-1000)
Normal Goat Serum blocking solution	VECTOR laboratories (S-2000)
VECTASHIELD® mounting medium	VECTOR laboratories (H-1000)

Table 5: Solutions used in the IHC study and their chemical components

Solutions	Chemical components
Fixing solution (4% PFA/PBS)	Paraformaldehyde
	ddH_2O (double-distilled water)
	1N NaOH (100µL to disolve at 60°C)
	1N HCl (100µL to neutralize thereafter)
	1/10 volume of 10X PBS
PBS	130mM NaCl
	7 mM Na2HPO4 x 2H2O
	3 mM NaH2PO4 x H2O
PBTX	10X PBS
	Triton-X (10%)
	ddH_2O
Ringer Solution	5 mM Hepes
	130 mM NaCl
	5 mM KCl
	2 mM MgCl2
	2 mM CaCl2

All standard chemicals were purchased from AppliChem or Roth GmbH

2.8 Scanning of samples using the laser scanning microscope

The LEICA laser-scanning microscope was used to scan the samples that underwent immunohistochemistry treatment in order to detect the fluorescence of the secondary antibodies attached to the target primary antibodies. The microscope includes two LASERS: 1) Argon (output power adjusted to 20%), and 2) a DPSS (Diode Pumped Solid State). Using the detectors PMT1 and PMT2, individual channels were visualized separately for the GFP signal using A488 (488nm), and Cy3 (580nm). The 10X lens (dry) was used for preliminary visualization of the samples and for further magnifications, 20X and 63X (immersion lenses) were used (as and when needed) after adding a drop of “Type G” solution on top of the coverslip. All samples were scanned with the default settings (size: 1024x1024 mm, speed: 600Hz, bidirectional, line average: 2 (or 3) and thickness: 0.75 microns (for 20X), 0.33 microns (for 63X) and 330/750nm focal depth. Processing of the images was done on Fiji (imageJ 64V5) (Schindelin et al., 2012), assembled using Photoshop (PS5 64 bit V5) and annotated with CorelDraw 2018.

2.9 Measuring of median intensity values using Fiji

Scanning of the samples was done using Leica TCS SP8 confocal microscope (equipped with the LASAF software for processing) in 63X water emulsion magnifications with identical settings. Intensity measurements were calculated using Fiji (ImageJ) (Schindelin et al., 2012). Every brain was examined for the staining pattern in the entire neuropil, as well as specifically in the EB. A “primary slice” was identified in each specimen which is most often the middle slice of the R3/EB neuropil, which is observed through the green channel (488nm). Once the primary slice containing the required staining pattern was identified based on quality of the control staining of a reference protein (ex: GFP, FASII) of the substructure (ex: R3 neurons, EB), a subsidiary stack from the original total stack was compiled using “Z-Project”, by assembling 5 slices above and below the primary slice (i.e. stack of 11 focal section =3.30µm), and selecting the “sum slices” function. Using this subsidiary stack as the template, a 2-dimensional circular outline representing the region of interest (ROI), was manually drawn around the specific structure of interest for every individual brain, and the cumulative ROI data was saved for future reference. Discrete median intensity of each channel was measured for the same ROI (using the ctrl+m operation on Fiji). This process was repeated for every brain until the

resultant “csv.” file containing all the pre-defined measurements (mean and median intensities, area, perimeter, etc.,) for the complete dataset was obtained for subsequent statistical analysis.

2.10 Statistical analysis of immunohistochemistry studies

The ratios of median intensities of individual samples were calculated using the data obtained from the consolidated csv file provided by Fiji. The ratios of median intensities between the variable protein (ex: PKA-C1[Fl], Syn-P1), and the reference protein (ex: GFP, FASII), were calculated individually. The resultant ratios of the control group were compared to those belonging to the experimental group using the Mann-Whitney U test (for comparison of two independent variable samples). $p<0.05$ between the control and the experimental groups indicate a (*) significant difference between the two while a $p<0.01$ indicates a highly significant difference (**), and $p<0.001$ indicates a very highly significant difference (***). In addition, the median intensities of only the reference protein were also compared between the control group and experimental group using the Mann-Whitney U test to ensure that there was no significant difference in the expression levels of the reference protein between the two groups for the protein to qualify as a reliable standard of reference.

3. Results

3.1 Roles of PKA and Synapsin in visual working memory in *Drosophila melanogaster*

3.1.1 Role of PKA-C1 in R3 neurons

The roles of cGMP and PKG in the formation and functioning of detour memory in *Drosophila*, were uncovered by Sara Kuntz in her PhD thesis. She could observe that manipulations in the cGMP/PKG cascade affected the performance of flies in the detour arena. Thus, she set out to test if the same was applicable to cAMP, and by association, cAMP-dependent protein kinase A (cAMP/PKA). By feeding the flies with inhibitors of PKA (Rp-cAMPs) in varying concentrations ranging from 10µM to 200µM, she could observe that the detour memory was significantly reduced in these flies in comparison to WT-CS (Wild-Type Canton Special) control flies (Kuntz, 2015).

She then proceeded to knock-down *Pka-C1* in the R3 neurons (189Y-GAL4; (Renn et al., 1999)) in an adult-specific manner using TubGAL80^{ts} (McGuire et al., 2004) to reveal that the visual orientation memory was once again, significantly reduced in these flies, compared to the WT-CS control group. In addition, when she tested flies heterozygous for the hypomorphic allele for *Pka-C1* (*Pka-C1*^{H2}/II; (Lane and Kalderon, 1993)), it was seen that the detour memory score was reduced to 70%, in comparison to the WT-CS group which had a memory score of 80% (Kuntz, 2015).

Subsequently, Kuntz also tested the *Synapsin* null mutant (*Syn*^{97}) flies, which lacked the Synapsin protein altogether and observed a complete loss of detour memory. She could rescue this loss of memory by expressing the UAS-*Syn*(cDNA8) (Michels et al., 2011) transgene specifically in the R3 neurons of the EB, showing that Synapsin is required in the R3 neurons for the functioning of visual working memory. To verify whether this result was related to PKA-C1 activity, she performed an interaction study between the hypomorphic *Pka-C1* allele (*Pka-C1*^{H2}), and the *Synapsin* null mutant (*Syn*^{97}), which showed a complete loss of memory in the double heterozygous mutants (*Pka-C1*^{H2}/II;*Syn*^{97}/III). In fact, the heterozygosity of *Syn*^{97} enhanced the phenotype of *Pka-C1*^{H2}/II, hinting that PKA and Synapsin belonged to

the same pathway that is required for the functioning of visual short-term orientation memory (Kuntz, 2015).

Thus, these preliminary results paved the way for our study, which focussed even more on the cAMP-dependent PKA and its role in the functioning of detour memory, along with the proteins it targets for phosphorylation, particularly Synapsin.

To understand the role of PKA in *Drosophila* visual orientation memory, it was important to test its relevance in the R3 ring neurons of the *Drosophila* EB. As described earlier, this visual working memory resides in the R3 neurons (Neuser et al., 2008; Kuntz et al., 2012). In order to prove that PKA has a functional role in this particular set of neurons, we used the strategy of targeted rescue experiments, designed to rescue the phenotype of *Pka-C1*^{H2}/II using UAS-*Pka-C1* in both R2 (EB1-GAL4; (Pan et al., 2009)), and R3 neurons (189Y-GAL4; (Omoto et al., 2018)).

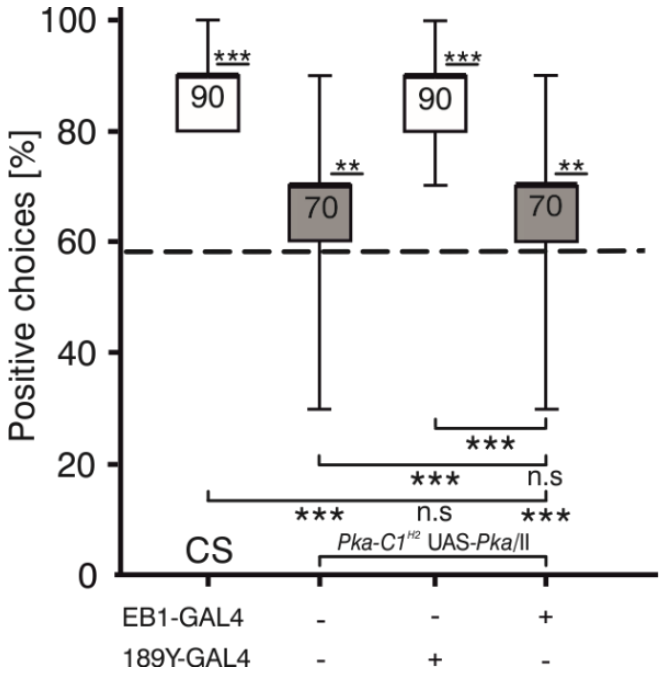

Figure 12: Rescue of *Pka-C1*^{H2}/II in R3 neurons

The heterozygous *Pka-C1*^{H2} hypomorphic allele (*Pka-C1*^{H2}/II, n=30) has a median of 70%. Its rescue using UAS-*Pka-C1* takes place only in the R3 neurons (189Y-GAL4, n=30) where the median value is at 90%, not significantly different from the WT-CS control group (n=29). The attempted rescue in R2 neurons (*Pka-C1*^{H2}/II;EB1-GAL4/III, n=30) is unsuccessful since the median remains at 70%. The whisker lengths of the *Pka-C1*^{H2}/II and the *Pka-C1*^{H2}/II;EB1-GAL4/III genotypes signify a larger distribution range of the memory scores.

Refer to **Table 7** in **Appendix** for statistical analysis for multiple comparison (Kruskal-Wallis test), normality distribution (Shapiro-Wilk test) and comparison against random chance level (58%) (Sign/t-test)

Since it was already proven that the R2 neurons are responsive to visual patterns (Pan et al., 2009), Kuntz hypothesized that these neurons may convey the visual information of the landmarks and the distractor to the R3 neurons, where the idiothetic memory is created. It was therefore necessary to screen for both these neuronal groups to effectively identify the ring in which *Pka-C1* is required. As shown here (Figure 12), the rescue was successful only in the R3 neurons, proving that PKA activity is necessary only in these neurons, for visual working memory functioning.

The aim of the next experiment, was to understand how increasing the levels of catalytic PKA, specifically in the R3 neurons, could improve the functioning of detour behaviour. For this, we were also keen on elucidating if the loss of function phenotype in visual working memory in *Pka-C1*^{H2}/II, can be rescued by silencing the regulatory subunit of the PKA complex (PKA-R1), using RNAi-mediated knock-down. This experiment was focussed on the importance of the catalytic activity of PKA-C1, simply by limiting the regulatory activity of PKA-R1, which is a different approach from overexpressing *Pka-C1* (as in Figure 12).

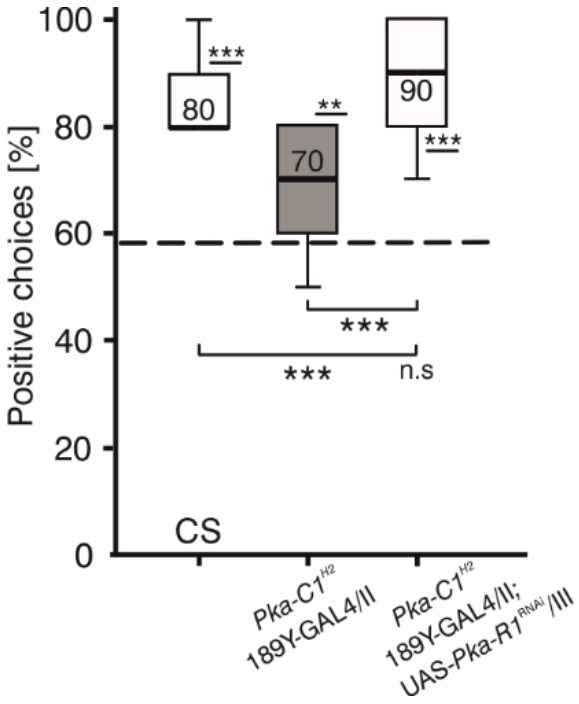

Figure 13: Rescue of *Pka-C1*^{H2}/II with *Pka-R1*^{RNAi} in R3 neurons

The heterozygous *Pka-C1*^{H2} mutant group (*Pka-C1*^{H2}/II, n=30) had a median score of 70%. The rescue of this genotype in the R3 neurons (189Y-GAL4) using RNAi-mediated knock-down of *Pka-R1* (n=22) was successful. The median score of the rescue was increased to 90%, comparable to that of the WT-CS control group (n=25) and highly significantly different from the chance level (58%).

Refer to **Table 8** in **Appendix** for statistical analysis for multiple comparison (Kruskal-Wallis test), normality distribution (Shapiro-Wilk test) and comparison against random chance level (58%) (Sign/t-test)

As observed in Figure 13, the rescue is successful, thereby re-establishing the notion that PKA, in its catalytic form, is required in the R3 neurons for the functioning of visual working memory.

3.1.2 Relationship between PKA and Synapsin

Synapsin, a synaptic vesicle (SV) associated protein, is a part of a number of processes such as, regulating synaptic plasticity (Rosahl et al., 1995), maintaining neuronal development and neurite outgrowth (Ferreira et al., 1994), as well as in synaptogenesis (Ferreira and Rapoport, 2002). Synapsin can exist in different states of phosphorylation, as well as in an unphosphorylated state (Niewalda et al., 2015). In its unphosphorylated form, it helps in the tethering of the SVs to the cytoskeleton, due to its affinity for vesicle binding, thereby curtailing them to remain as a part of the reserve pool. Once phosphorylated by PKA, or another kinase, Synapsin can now

allow the transfer of these vesicles from the reserve pool to the readily releasable pool, thereby increasing their propensity to release the neurotransmitters (Fiumara et al., 2004).

The *Drosophila* homolog for the vertebrate *Synapsin* gene was identified in 1996 (Klagges et al., 1996). At least six different isoforms of the Synapsin protein have been discovered in *Drosophila*. Each of these isoforms contain three of the domains: A,C, and E which are conserved across phyla. While the A, and C domains belong to the N terminus, which is highly homologous, the C-terminal domain (domain E), is relatively variable in its amino acid sequence (Cesca et al., 2010). A generalised homology study between the human and invertebrate Synapsin revealed that the C domain is the largest, and most conserved across phyla. When it comes to *Drosophila* Synapsin specifically, it bears a 50% homology to the C domain of the human Synapsin. Domain A, on the other hand, contains the phosphorylation sites for kinases such as PKA and CaMKII. Site-1, the major phosphorylation site, is conserved among vertebrates, as well as invertebrates, and is responsible for the reversible association with SVs in vertebrates (Hosaka et al., 1999). These findings support the notion that the underlying mechanisms of synaptic transmission and regulation, have been conserved in both vertebrates and invertebrates during evolution.

In *Drosophila*, this function of tethering the SVs to the cytoskeleton is performed by the Synapsin protein, encoded from a single *Syn* gene. Based on the functions of the Synapsin protein enlisted above, one would expect that the absence of this 143kDa protein would cause significant damage to memory, and other associated functions. This was investigated by Godenschwege and colleagues using the null mutant for *Synapsin (Syn^{97})*. Using P-element remobilization (Tower et al., 1993), combined with jump-out mutagenesis, a number of deletion mutants were created for the Synapsin protein, one of which is *Syn^{97}*. This *Syn^{97}* mutant contained a deletion of 1397bp, effectively lacking half of the first exon as well as major chunks of the regulatory regions required for the functioning of the protein. Thus, these mutants do not possess a detectable Synapsin protein, as confirmed by Western blot studies (Godenschwege et al., 2004).

To begin with, the adult flies homozygous for *Syn^{97}*, appeared to be healthy, with no discrepencies in the anatomy of the brain, and its surrounding structures.

They also did not show any defect in synaptogenesis in the muscles scaffolding the body wall of the fly. After showing no significant difference to the wild-type controls in terms of the excitatory junction potential (EJP), it was deduced that these mutants have normally functioning synaptic activity. However, *Drosophila* larval research showed that these *Synapsin* null mutants had considerable defects in terms of olfactory associative learning. The data published by Michels and colleagues states that although stimuli recognition, habituation, and satiation remained unchanged, the associative learning was reduced by half (50%) in Syn^{97} larvae, in comparison to the wild-type control group (Michels et al., 2005). This phenotype was later reproduced by RNAi-mediated knock-down of *Synapsin*, which was carried out pan-neuronally in *Drosophila* larvae (Michels et al., 2011). In 2015, Niewalda and colleagues showed for the first time, that Synapsin is required for associative olfactory memory in adult *Drosophila*, by rescuing *Syn* null mutants through the expression of UAS-*Synapsin* in the MB in an adult-specific manner (Niewalda et al., 2015).

Sara Kuntz published in her PhD thesis that flies homozygous for Syn^{97}, showed a complete loss of memory in the detour paradigm since these flies performed with a memory score similar to random chance level (58%). Their median memory score was also highly significantly different from the memory score of wild-type CS control group. She thus concluded that the availability of Synapsin is necessary for the functioning of visual orientation memory. In *Drosophila*, PKA is one of the major kinases targeting Synapsin for the purpose of phosphorylating it (Diegelmann et al., 2006). There exists two recognition sites for PKA on the Synapsin protein - one in the A domain on the N terminal, and another adjacent to the E domain closer to the C terminal. These two sites are comprised of specific amino acid sequences, where the “RRFS” motif, specific to the PKA phosphorylation site-1 on the A domain, is widely conserved across all known forms of Synapsin (Kao et al., 1999), whereas the PKA recognition site-2 “RRDS” on the E domain, is not.

In 2011, Michels and colleagues generated a version of the *Drosophila* Synapsin cDNA, where the two sites for PKA recognition were altered using site-directed mutagenesis (Figure 14). The phosphorylation sites 1 and 2 were mutated so that the final protein product contains alanine instead of serine in the sixth positions of PKA recognition site 1 (RRFS→RRFA), and site 2 (RRDS→RRDA), rendering these sites unphosphorylatable (Michels et al., 2011). The Synapsin

transgenes (Syn$^{Pka\text{-}AlaAla}$), were then cloned into the pUAST plasmid vector (Brand and Perrimon, 1993), and transformed into *E. coli*, which was subsequently transformed into *w1118;Syn^{97}* to generate UAS-*Syn$^{Pka\text{-}AlaAla}$*, *Syn^{97}*.

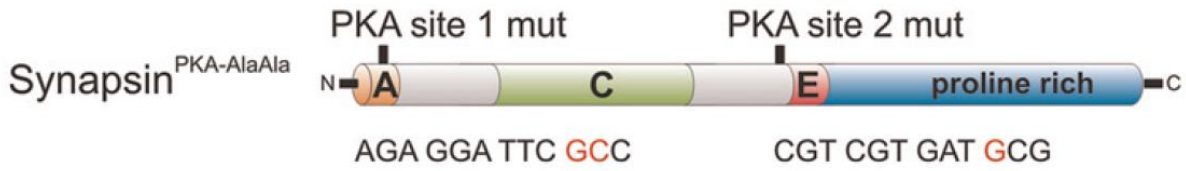

Figure 14: Mutated PKA phosphorylation sites on *Drosophila* Synapsin protein

Mutated PKA-sites 1 and 2 where the serine in the 6th position is replaced with alanine (PKA-AlaAla) giving rise to RRFA and RRDA. Figure modified from (Michels et al., 2011) and reproduced under the creative common license CC BY-NC 4.0 https://creativecommons.org/licenses/by-nc/4.0/

In addition to these transgenes defective for the Synapsin protein, a rescue line was also generated, containing UAS-*Syn*;*Syn^{97}*, based on earlier literature (Lohr et al., 2002). Expressing UAS-*Syn*;*Syn^{97}* pan-neuronally (elav-GAL4), as well as in the mushroom body (MB247-GAL4) neurons, led to a rescue of associative olfactory learning in *Drosophila* larvae (Michels et al., 2011). The rescue attempt was not successful with UAS-*Syn$^{Pka\text{-}AlaAla}$Syn^{97}*, indicating that the phosphorylation of Synapsin by PKA, is vital for larval olfactory learning (Michels et al., 2011). This also led to the generation of the single-site mutant variants by Gerber and colleagues, where each of the PKA recognition sites were individually mutated by replacing the serine in the 6th position (S^6) with alanine.

In our study, we attempted to rescue the visual working memory phenotypes of double-heterozygous *Pka-C1^{H2}*/II;*Syn^{97}*/III and homozygous *Syn^{97}* mutants using the UAS-*Syn* transgene, along with its variants (the single and double site-variants for the PKA phosphorylation sites), in the R3 neurons (189Y-GAL4; (Renn et al., 1999)). Performing these experiments would help solidify our notion that the reason PKA-C1 is important for this memory, is due to its function of phosphorylating Synapsin. In addition, we would also be able to identify whether both the recognition sites for PKA on the Synapsin protein are required for the functioning of visual short-term orientation memory. In order to finalize which site is more important for the functioning of detour memory, it was decided that both sites would be used as targets for the rescue experiments.

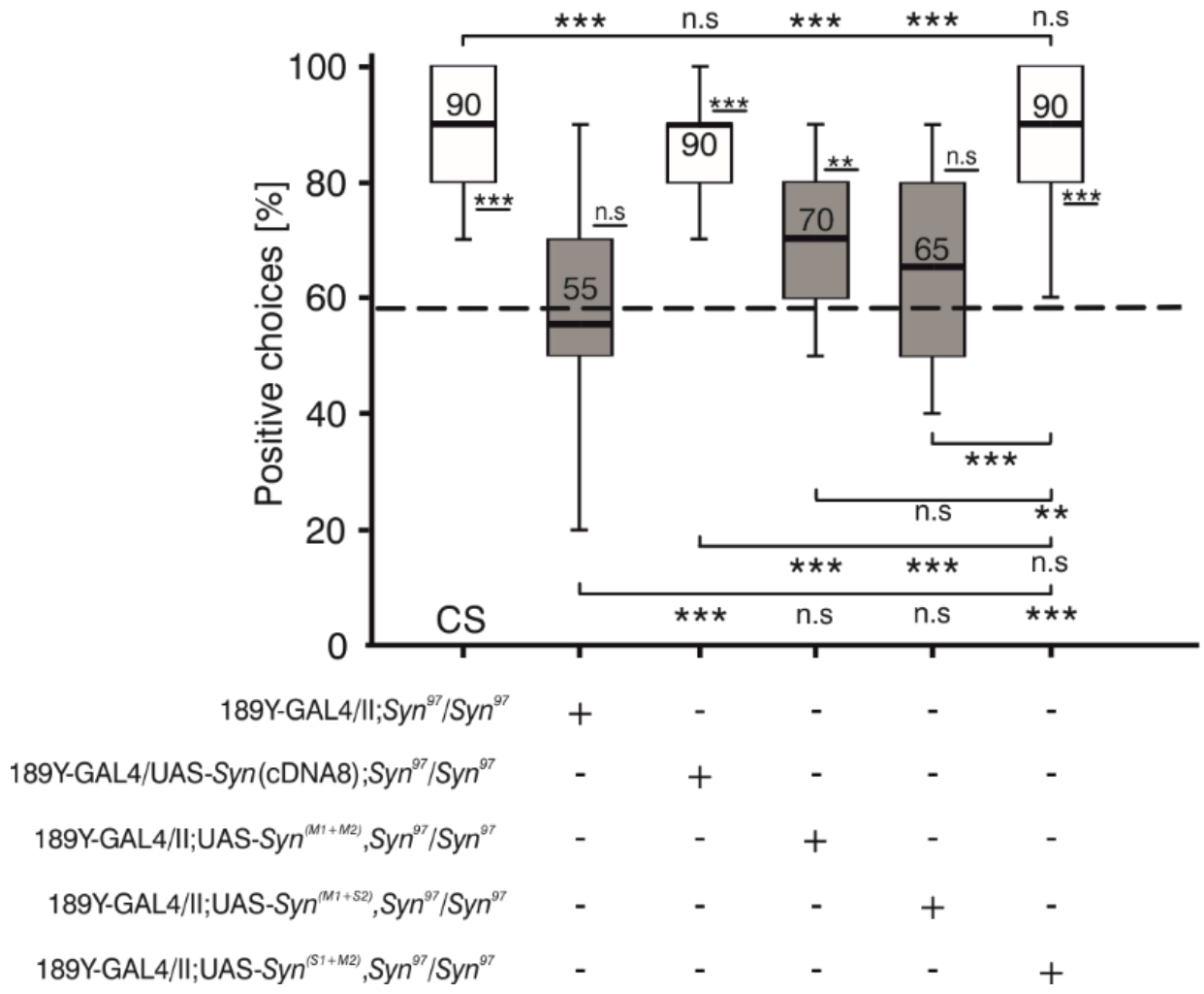

<u>Figure 15</u>: Rescue of *Syn^{97}* with UAS-*Syn* (and variants) in R3 neurons

Homozygous *Synapsin* null mutants (*Syn^{97}*, n=20) exhibited a detour memory median score of 55% which was not significantly different from chance level (58%). Rescue of this phenotype using UAS-*Syn*(cDNA8), n=25) in R3 neurons was successful and increased the median score to 90%, comparable to the WT-CS group (n=23).and highly significantly different from chance level (58%). Rescue attempt using UAS-*Syn* (M1+M2), n=25) where both the sites for PKA phosphorylation on the Synapsin protein were mutated, did not elicit a rescue and the memory score was at 70%, significantly different from the WT-CS control group and the rescue with UAS-*Syn*(cDNA8). The Synapsin variant containing a mutated site-1 but an intact site-2 for PKA phosphorylation (UAS-*Syn* (M1+S2), n=26) was used for an attempted rescue of the *Syn^{97}* phenotype, which proved to be unsuccessful. The memory score remained at 65%, highly significantly different from the WT-CS control group and the UAS-*Syn* rescue group and not significantly different from the chance level (58%). When the Synapsin variant containing a non-edited site-1 but a mutated site-2 for PKA phosphorylation (UAS-*Syn* (S1+M2), n=25) was used to rescue *Syn^{97}* phenotype, the memory score increased to 90%, comparable to that of the WT-CS control group and the initial rescue using UAS-*Syn* (cDNA8). It was also highly significantly different from chance level (58%).

Refer to **Table 9** in **Appendix** for statistical analysis for multiple comparison (Kruskal-Wallis test), normality distribution (Shapiro-Wilk test) and comparison against random chance level (58%) (Sign/t-test).

As shown in Figure 15, this venture was successful, as UAS-*Syn*(cDNA8) could rescue the memory deficit caused by *Syn^{97}* when expressed in the R3 neurons,

proving that the Synapsin protein is required in these neurons. The subsequent step was to identify which PKA phosphorylation site was required more than the other, or if both were required equally. Thus, the following variants of the UAS-*Syn* transgenes were used, where the PKA phosphorylation sites were mutated individually for site-1 (UAS-*Syn*(M1+S2),*Syn*^{97}), site-2 (UAS-*Syn*(S1+M2),*Syn*^{97}), and together (UAS-*Syn*(M1+M2),*Syn*^{97}). It is observed that mutating both sites for PKA phosphorylation, impairs the memory to a level that was not significantly different from the phenotype observed in *Syn*^{97}, but was also significantly different from the chance level (Figure 15). This proves that phosphorylation of Synapsin by PKA-C1, or any other kinase, is a requirement for detour memory functioning, either through site 1, or site 2, or both.

Following this result, the rescue experiment was continued for the same homozygous *Syn*^{97} mutants using UAS-*Syn* transgene with a mutated site 1 and a wild-type site 2 (UAS-*Syn*(M1+S2),*Syn*^{97}). It is apparent that the rescue was unsuccessful and the flies exhibited an impaired working memory with the median at 65% (Figure 15). This was the first indication that phosphorylation of Synapsin by PKA at site-1 is a paramount requirement for the functioning of visual short-term orientation memory. When the same procedure was carried out using the UAS-*Syn* variant carrying a mutated site 2 but an intact, non-edited site 1 (UAS-*Syn*(S1+M2),*Syn*^{97}), the rescue was successful. As shown here (Figure 15), the median for detour memory was once again comparable to that of the wild-type CS flies, hence proving that site-2 (RRDS^{6}) is dispensable for detour memory functioning as long as site-1 (RRFS^{6}) remains non-mutated.

Sara Kuntz showed that the detour memory phenotype of the *Pka-C1*^{H2}/II mutants was enhanced in the double heterozygous mutants (*Pka-C1*^{H2}/II;*Syn*^{97}/III). This brings along the hypothesis that the loss of memory in the latter, could be a result of PKA not being able to target and phosphorylate Synapsin. Thus, an experiment to rescue *Pka-C1*^{H2}/II;*Syn*^{97}/III using the expression of UAS-*Syn* and its variants in R3 neurons was designed to prove that Synapsin is an important target of PKA that is required for the functioning of detour memory. Figure 16 shows that the heterozygous *Pka-C1*^{H2} allele displayed a reduced detour memory with a median of 70%, which was made slightly worse in the double-heterozygous (*Pka-C1*^{H2}/II; *Syn*^{97}/III) situation, albeit not being significantly different from the former.

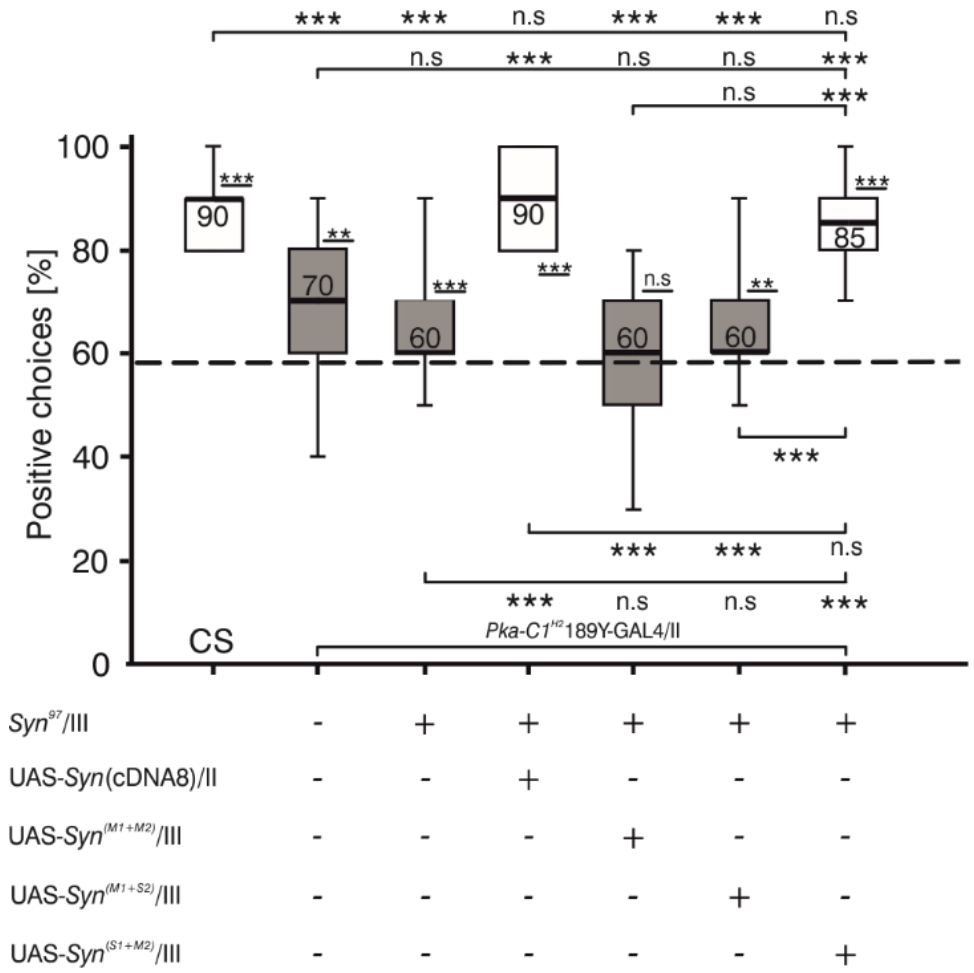

<u>Figure 16</u>: Rescue of *Pka-C1*^{H2}/II;*Syn*^{97}/III with UAS-*Syn* (and variants) in R3 neurons

Heterozygous hypomorphic mutants for *Pka-C1* (*PkaC1*^{H2}/II, n=30) displayed a detour memory score of 70% while double-heterozygous mutants carrying the hypomorphic *Pka-C1* allele and the *Synapsin* null allele (*Pka-C1*^{H2}/II;*Syn*^{97}/III, n=23) exhibited a detour memory median score of 60% which was not significantly different from chance level (58%). Rescue of this phenotype using UAS-*Syn* (cDNA8) (n=29) in the R3 neurons was successful and increased the median score to 90%, comparable to that of the WT-CS group (n=30) and highly significantly different from chance level. Rescue attempt using UAS-*Syn* (M1+M2), n=30) where both the sites for PKA phosphorylation on the Synapsin protein were mutated, was unsuccessful. The memory score was at 60%, significantly different from the WT-CS control group and the UAS-*Syn*(cDNA8) rescue and not significantly different from the chance level (58%). The Synapsin variant containing a mutated site-1 but an intact site-2 for PKA phosphorylation (UAS-*Syn* (M1+S2), n=27) was used for an attempted rescue of the *Pka-C1*^{H2}/II;*Syn*^{97}/III phenotype, which proved to be unsuccessful. The memory score remained at 60%, highly significantly different from the WT-CS control group and the UAS-*Syn* rescue group. When the *Synapsin* variant containing a non-edited site-1 but a mutated site-2 for PKA phosphorylation (UAS-*Syn* (S1+M2), n=28) was used to rescue the *Pka-C1*^{H2}/II;*Syn*^{97}/III phenotype, the memory score increased to 85%, comparable to that of the WT-CS control group and the initial rescue using UAS-*Syn* (cDNA8). It was also highly significantly different from chance level (58%).

Refer to **Table 10** in **Appendix** for statistical analysis for multiple comparison (Kruskal-Wallis test), normality distribution (Shapiro-Wilk test) and comparison against random chance level (58%) (Sign/t-test)

Rescue of *Pka-C1*^{H2}/II; *Syn*^{97}/III the using UAS-*Syn*(cDNA8) was successful, thereby increasing the median value from 60% to 90%, making it comparable to the memory score of wild-type CS flies (Figure 16). It is also noticed that UAS-*Syn* containing mutations in both PKA sites 1 and 2, failed to rescue the phenotype, similar to the observations made previously (Figure 15). In addition, mutating site-1 and hindering the phosphorylation of Synapsin by PKA-C1 at this site, proves to be detrimental to the functioning of this type of visual memory. This defective phenotype was absent when site-2 was mutated, showing once again, that the non-conserved site-2 is dispensible for the function of Synapsin in R3-neuons.

Collectively, Figure 15 and Figure 16 prove that the phosphorylation of Synapsin by PKA-C1 at the site-1 in the A domain on the N terminal of the protein, is imperative for the seamless functioning of short-term visual orientation memory in *Drosophila*. Apart from behavioural experiments, it was also necessary to prove the importance of site-1 for PKA phosphorylation of Synapsin in a manner that was capable of visualization, as well as quantification. To achieve this goal, we decided to carry out immunohistochemistry experiments in the R3 neurons using a specific antiserum raised against the phosphorylated Synapsin protein obtained from phosphorylation site-1 at the serine in the 6th position (anti-PSyn(S6); (Blanco-Redondo et al., 2019)).

At the time, it was an antibody predominantly used in Western blot studies (Sadanandappa et al., 2013) and not in immunohistochemistry analysis. Here, we wanted to stain for the distribution of phosphorylated Synapsin from site-1, when Pka is consitutively actively expressed (using *Pka*(mC*);(Li et al., 1995)). It is also important to address the question of editing of the Synapsin protein. In contrast to Diegelmann et al., who claimed that all cDNA are edited (Diegelmann et al., 2006), Niewalda and colleagues, showed through a proteomic approach that at least equal amounts of both isoforms are present in the *Drosophila* brain (Niewalda et al., 2015). Hence, our aim was to discover the extent of non-edited Synapsin in the R3 neurons. If Niewalda et al. was right, then the expression of PKA(mC*) should potentially increase the labelling by anti-PSyn(S6) serum.

In addition, when the anti-Syn-P1 antibody (anti-PSyn(S6)) was used in the recent Blanco-Redondo study, it was shown that there was no colocalisation of Syn-P1 in the R3 neurons (189Y-GAL4) (Blanco-Redondo et al., 2019). However, our

behavioural results have shown that PKA phosphorylation site-1 on the Synapsin protein is essential for visual working memory. Thus, we compared the levels of Syn-P1 in the control group to those expressing UAS-*Pka(mC*)* in R3 (189Y-GAL4).

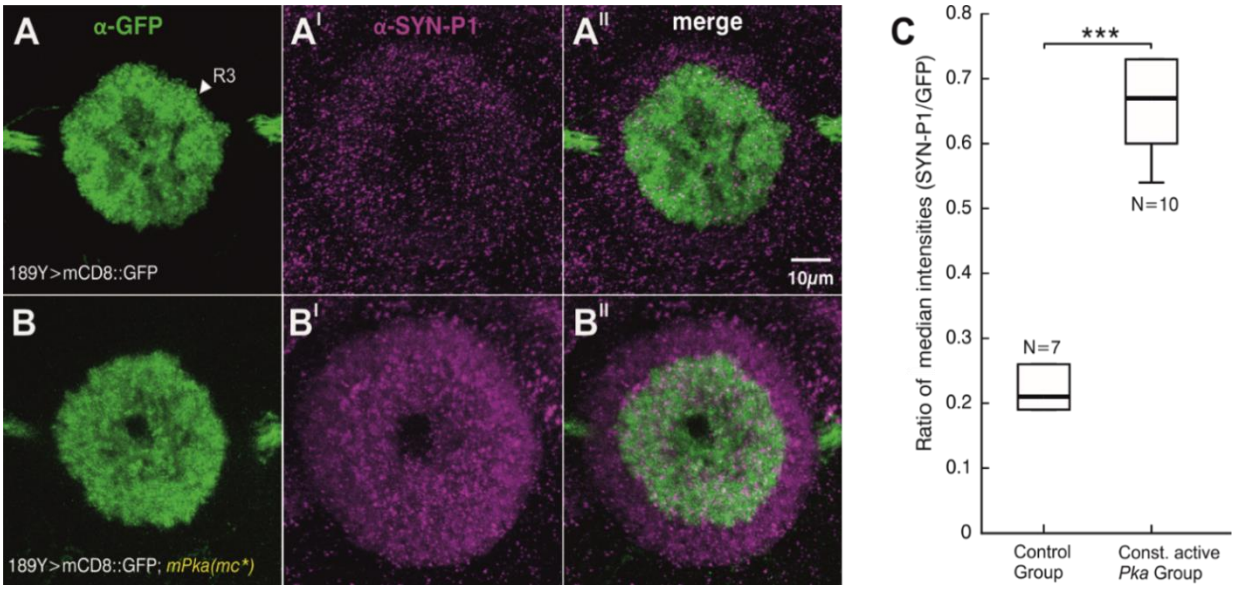

<u>Figure 17</u>: Phosphorylation of Synapsin on site-1 when constitutively active *Pka-C1* is expressed in R3 neurons

All samples were scanned under 63X magnification with 0.33μm thickness of each slice.
31 slices were stacked for the images and 11 slices were stacked for the intensity measurements.

(A-A'') Control brain (A) R3 neurons (189Y-GAL4>mCD8::GFP) stained in green (A') minimal distribution of the phosphorylated Synapsin (Syn-P1) protein (magenta) (A'') The merged version where the green staining overpowers the magenta with little to no colocalisation.
(B-B'') Brain expressing constitutively active PKA-C1 (UAS-*Pka(mc*)*) (B) R3 neurons stained in green (189Y-GAL4>GFP). (B') The distribution level of the (Syn-P1) protein was visibly increased in the regions of the R3 axons and its surroundings (B'') In the merged scenario, the co-distribution of GFP and Syn-P1 is more profound than that found in the control group with endogenous PKA-C1 activity.
(C) Quantitative analysis of the ratio of median intensities (using Mann-Whitney U test) between Syn-P1 and GFP for the control group and the group with constitutively active Pka-C1, showed a very highly significant difference between the two. The latter group had a significantly higher distribution of Syn-P1 in the R3 neurons (Syn-P1/GFP ratio ~0.66) compared to that in the control group (Syn-P1/GFP ratio ~0.21).

Refer to **Table 11** in **Appendix** for statistical analysis for two independent variable samples (Mann-Whitney U test) to compare the median intensity ratios between the control and the experimental group. Refer to **Table 2** for the primary antibodies and **Table 3** for the secondary antibodies used in the experiment.

The immunohistochemistry result shown in Figure 17, consists of the control panel (Figure 17A-A"), addressing the R3 neurons (189Y-GAL4), labelled using membrane-bound GFP (UAS-mCD8::GFP) (Figure 17A). These neurons appear to contain a sparse local distribution of phosphorylated Synapsin (magenta) from site 1 (Syn-P1), in the R3 neurons (Figure 17A'), which is barely visible in the merged situation (Figure 17A"). Moving on to the experimental group with the expression of

constitutively active mouse Pka (UAS-*Pka*(mc*)) (Figure 17B-B”), the strength of the membrane-bound GFP labelling the R3 neurons (Figure 17B) was seen to be comparable to that of the control group (Figure 17A). However, it is clearly apparent that there is a significant increase in the levels of phosphorylated Synapsin from site-1 in this case (Figure 17B’), in comparison to the minimal levels observed in the control panel (Figure 17A’). The merging of the two channels in the experimental group, also suggests an overall higher level of Syn-P1 in the R3 neurons, along with the regions surrounding it (Figure 17B”).

Using the intensity measurements obtained using Fiji™ software for the two individual channels, we decided to build a set of ratios between the phosphorylated Synapsin 1 and membrane-bound GFP for the two groups (control group and constitutively active PKA group) with the ultimate aim of comparing them against each other to look for a significant difference. However, before comparing the Syn-P1/GFP ratios for the two groups, the median values for GFP were first compared between the two, to ensure that there was no change in GFP expression when PKA was expressed in a constitutively active manner. This statistical analysis revealed that there was no significant difference in the distribution of GFP between the two groups (see Table 11 in Appendix). This allowed us to use GFP as a valid denominator to calculate the quantifiable difference in Syn-P1 levels between the groups.

The comparison of median intensity ratios between phosphorylated Synapsin from site-1, and membrane-bound GFP, between the two groups, revealed a very highly significant increase in phosphosynapsin1 (Syn-P1), when PKA-C1 was constantly allowed to perform its catalytic activity of phosphorylating Synapsin (Figure 17C). This was the first visual proof that helped support the previously obtained behavioural data, which showcased the effect of silencing the regulatory subunit of Pka (*Pka-R1*), and as a result, freeing the protein to fully function as a catalytic entity in the R3 neurons (Figure 13). Albeit this result being circumstantial, this finding confirmed that this particular antiserum is specific for the phosphorylated Synapsin arising from the site-1. It was also curious to observe that the expression of constitutively active PKA in the R3 neurons, somehow triggered increased Syn-P1 levels in the surrounding R2/R4 neurons as well (Figure 17B’). In addition, this result is also an indication of the existence of non-edited Synapsin protein, that is capable

of being phosphorylated by PKA in the canonical site 1, when PKA is allowed to be constitutively actively expressed in the R3 neurons.

3.1.3 Post-transcriptional mRNA editing of Synapsin by ADAR

By now, the structure of the Synapsin protein with respect to the phosphorylation sites it contains for PKA, has been described several times in this study. We have successfully managed to identify that site-1 on the “A” domain, is the site that is necessary to carry out the visual working memory in *Drosophila*. It is postulated at this stage, that the phosphorylation of Synapsin by PKA on site-1, increases the number of readily releasable vesicles available to partake in the release of neurotransmitters.

However, as it was briefly mentioned in the previous section, Diegelmann and colleagues proved that this site-1 has been edited in all known cDNA at the time, and in those sequenced after RT-PCR (Diegelmann et al., 2006). This pre-mRNA editing is carried out by ADAR (adenosine deaminase acting on RNA), an RNA editing enzyme (Bass et al., 1997). It replaces the adenosine group to an inosine group in a number of target genes in vertebrates and invertebrates alike. In this particular case of editing, the arginine group in the second position of the original PKA site-1 (RRFS) is changed to glycine (RGFS), making the site presumably unrecognizable to PKA (Diegelmann et al., 2006), and subsequently preventing it from phosphorylating Synapsin at this site (Figure 18).

cDNA translation and amino acid sequencing have revealed that the PKA-site 1 is edited out in majority of the Synapsin protein isolated from the *Drosophila* heads (Diegelmann et al., 2006). Most of the targets of ADAR are known to require rapid chemical neurotransmission (Hoopengardner et al., 2003). When it comes to the function of endogenous ADAR in *Drosophila*, the most recent study by Khan and colleagues showed that *Adar* null mutants (*Adar*^{5G1}), experienced severe impairment of locomotor functions and neurodegeneration. The authors of this paper speculate that one of the roles of ADAR must be to regulate aberrant synaptic vesicle clustering and accumulation, by editing Synapsin at PKA site-1 (Khan et al., 2020).

Predictions have been made regarding what makes a sequence eligible to be edited. These sequences usually contain a defective RNA duplex formed between the adenosine group that is meant to be edited and a non-coding intron that follows

the adenosine group. This non-coding intron called an ECS (editing site complementary sequence), acts as a partner sequence to the original adenosine sequence, and can span from several hundred to thousand nucleotides in length (Higuchi et al., 1993). In case of the Synapsin protein, this ECS region was discovered 90bp downstream of the edited arginine codon on site-1, and was 15bp in length (Diegelmann et al., 2006).

Despite what we know about the editing of PKA site-1 on the Synapsin protein, our immunohistochemistry experiments have shown an increased Syn-P1 level when constitutively active *Pka-C1* was expressed. This might indicate that Synapsin can exist in its non-edited form as well, and that PKA activity is the rate limiting step. This made us question how the editing of Synapsin at this particular site 1 would affect the detour memory in R3 neurons in the context of PKA, and its function of phosphorylating Synapsin, and if simply using non-edited Synapsin can rescue the *Pka-C1*^{H2}/II phenotype.

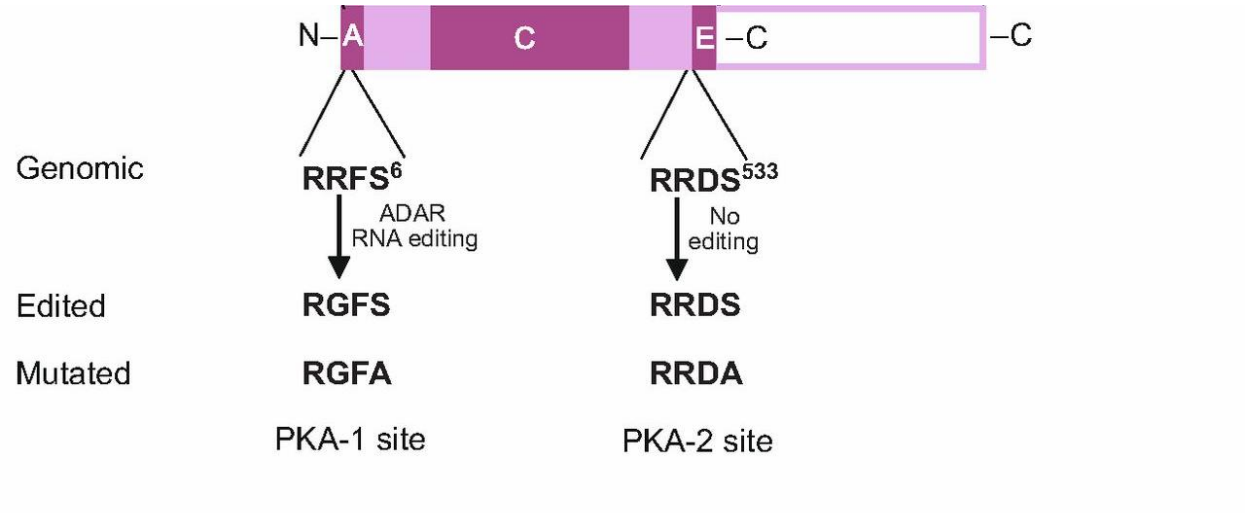

Figure 18: Editing of PKA-site 1 on the *Drosophila* Synapsin protein by ADAR

The editing of PKA site-1 by ADAR at the A domain in the N terminal of the Synapsin protein involves the replacement of the arginine (adenosine group) on the second position of "RRFS" to glycine (inosine group), making it "RGFS" The site-2 in the E domain is not edited and remains as "RRDS": In case of the mutated versions of both the sites, the serine on the sixth position is changed to alanine, resulting in the transition of the PKA-sites 1 and 2 to "RGFA" and "RRDA", respectively. Figure adapted from (Diegelmann et al., 2013); copyright license attached in Appendix (section 8.4).

With an objective to answer this question, we set out to observe the consequence of *Adar* expression being reduced in the R3 neurons, through an RNAi-mediated knock-down (UAS-*Adar*^{RNAi}; (Diegelmann et al., 2006)). This was designed

in the form of a rescue experiment, where the heterozygous form of the *Pka-C1* hypomorph (*Pka-C1*^{H2}/II), was rescued by RNAi-mediated knock-down of *Adar* in the R3 neurons. The hypomorphic allele, as always, showcased a reduced detour memory, with a median score of 70%, as shown in Figure 19A.

Silencing the *Adar* gene using the classical RNAi technique in the R3 neurons, proved to be useful in rescuing the memory score back to 90% in this group (*Pka-C1*^{H2}189Y-GAL4/II;UAS-*Adar*^{RNAi}/III), and statistically similar to the behaviour of the WT-CS control group (Figure 19A). This was the first clue in identifying that under circumstances where PKA-C1 activity is limited (as in *Pka-C1*^{H2}/II), a rescue of memory is possible by preventing the editing of the Synapsin protein at site-1 by reducing the activity of ADAR.

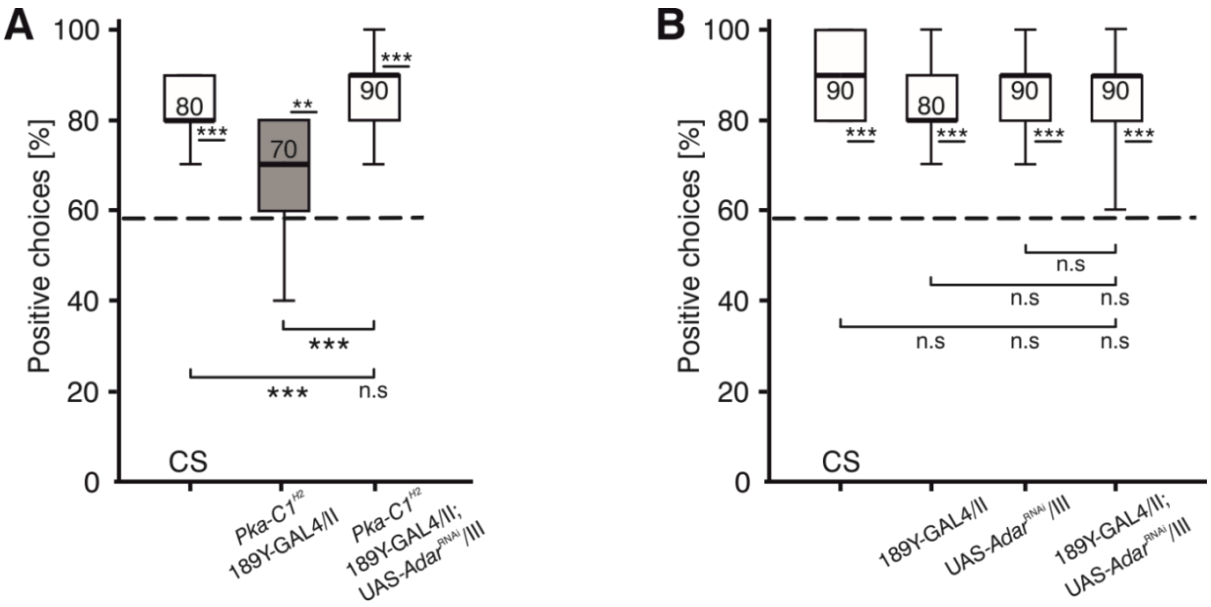

Figure 19: Behavioural effect of RNAi-mediated knock-down of *Adar* in R3 neurons

(A) The heterozygous hypomorphic *Pka-C1* allele (*Pka-C1*^{H2}189Y-GAL4/II, n=30) exhibited a reduced detour memory score of 70% which was highly significantly different from the WT-CS control group (n=17) which had a median memory score of 80%. The former detour memory phenotype was rescued by RNAi-mediated silencing of *Adar* in R3 neurons (*Pka-C1*^{H2}189Y-GAL4/II; UAS-*Adar*^{RNAi}/III, n=24) which increased the memory score to 90% which was comparable to the control group and highly significantly different from the random chance level (58%). **(B)** RNAi-mediated silencing of *Adar* in the R3 neurons (189Y/II; UAS-*Adar*^{RNAi}/III, n=25) did not elicit any significant difference in detour memory median score in comparison to the individual GAL4 control group (189Y-GAL4/II, n=25), UAS control group (UAS-*Adar*^{RNAi}/III, n=25) as well as the WT-CS control group (n=21)

Refer to **Table 12** and **Table 13** in **Appendix** for statistical analysis for multiple comparison (Kruskal-Wallis test), normality distribution (Shapiro-Wilk test) and comparison against random chance level (58%) (Sign/t-test)

An additional behavioural experiment was carried out to observe the effect of expressing the *Adar* knock-down in the R3 neurons, in a wild-type background. It was interesting to note that the absence of *Adar* functioning, did not elicit any defect in detour behaviour, as the flies continued to have wild-type like memory, which was also comparable to the respective GAL4 and UAS control groups (Figure 19B).

Following the rescue (Figure 19A), the next logical step was to visualize the levels of Syn-P1 in the R3 neurons using the same antibody that was used previously in this study (Figure 17). This was performed to further probe the effects of allowing Synapsin to be phosphorylated by PKA at site-1 after silencing *Adar*, because most of the cells undergo pre-mRNA editing.

By carrying out a similar procedure as in the previous experiment (Figure 17), the R3 neurons were addressed specifically using the 189Y-GAL4 driver expressing the membrane-bound GFP in the axons, dendrites, and cell bodies of the R3 neurons (Figure 20). The anti-P-Syn(S6) antibody on the other hand (magenta), stained only for the localised distribution of phosphorylated Synapsin from site-1 (Syn-P1) at the presynapse. The control group, as always, seemed to host a very scarce amount of Syn-P1 in the EB (Figure 20A'), which was also reflected in the merged version, where the signal from the mCD8::GFP overpowered the strength of the Syn-P1 staining (Figure 20A'').

Interestingly enough, silencing of *Adar* in the experimental group (Figure 20B-B"), led to a very highly significant increase in Syn-P1 levels in the R3 neurons, and its surrounding regions (Figure 20B'). The GFP levels (Figure 20B) were similar to that observed in the control group (Figure 20A) (see Table 14 in Appendix). The merged situation could elucidate the distribution pattern of the Syn-P1 amidst the axons of the R3 neurons (Figure 20B").

In addition to being visually self-explanatory, the results were also quantifiable, where the ratios of median intensities between Syn-P1 and GFP were calculated for the two groups, and then compared between each other. The comparison revealed a statistically highly significant increase of Syn-P1 in the R3 neurons, when *Adar* was silenced (Figure 20C). This information, combined with the rescue obtained earlier (Figure 19A), is evidence that absence of ADAR activity in the R3 neurons, leads to the following two things:

1) Increasing the amount of non-edited Syn, supresses the memory deficit in *Pka-C1*^{H2}/II flies, and

2) It leads to a significant increase in the levels of Syn-P1, proving again that PKA-mediated phosphorylation of Synapsin at site-1, is required for visual working memory functioning in the R3 neurons.

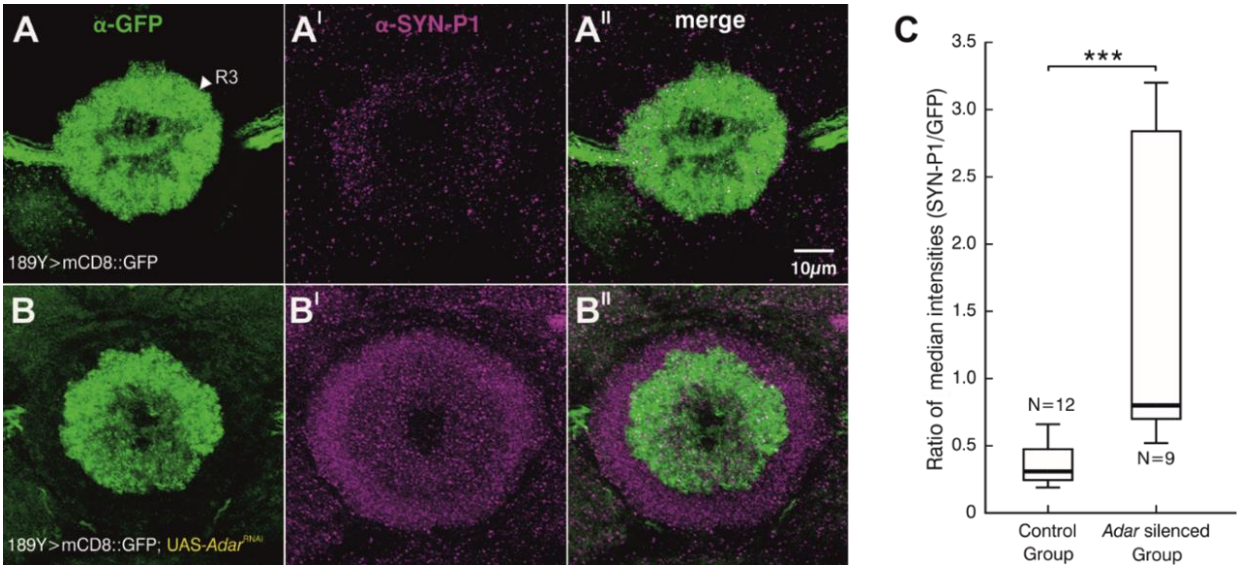

Figure 20: Phosphorylation of Synapsin on site-1 when *Adar* is silenced using RNAi-mediated knock-down in R3 neurons

All samples were scanned under 63X magnification with 0.33μm thickness of each slice.
31 slices were stacked for the images and 11 slices were stacked for the intensity measurements.

(A-A'') Control brain (A) R3 neurons (189Y-GAL4>GFP) stained in green (A') Minimal level of the Syn-P1 protein (magenta) (A'') The merged version where the green staining overpowers the magenta with little to no colocalisation.
(B-B'') Brain expressing RNAi-mediated knock-down of *Adar* (UAS-*Adar*^{RNAi}) (B) R3 neurons (189Y-GAL4>mCD8::GFP) stained in green. (B') The levels of the Syn-P1 protein was visibly increased. (B') In the merged scenario, the co-distribution of GFP and Syn-P1 is more profound than that found in the control group with endogenous ADAR activity.
(C) Quantitative analysis of the ratio of median intensities (using Mann-Whitney U test) between Syn-P1 and GFP for the control group and the group with RNAi-mediated knock-down of *Adar*, showed a very highly significant difference between the two. The latter group had a significantly higher levels of Syn-P1 in the R3 neurons (Syn-P1/GFP ratio ~0.75) compared to that in the control group (Syn-P1/GFP ratio ~0.25).

Refer to **Table 14** in **Appendix** for statistical analysis for two independent variable samples (Mann-Whitney U test) to compare the median intensity ratios between the control and the experimental group. Refer to **Table 2** for the primary antibodies and **Table 3** for the secondary antibodies used in the experiment.

To further support our finding that the phosphorylation of Synapsin by PKA in site-1 is necessary for detour memory, a new rescue experiment was set up. We already knew that the heterozygous *Pka-C1*^{H2} hypomorphic allele (*Pka-C1*^{H2}/II) is capable of causing memory reduction in flies, while the heterozygous *Synapsin* null

mutants (*Syn*^{97}/III) perform like wild-type flies. We therefore generated double-heterozygous mutants (*Pka-C1*^{H2}/II *Syn*^{97}/III) to observe whether they showed memory deficits in the detour paradigm, and if this phenotype can be rescued by RNAi-mediated knock-down of *Adar*. A successful rescue would indicate that simply allowing the remaining 50% of Synapsin protein to be phosphorylated at site-1, can compensate for the limited availability/activity of PKA.

As anticipated, these flies exhibited a severe impairment in detour memory, as they scored a median of 60%, which was highly significantly different from the score of WT-CS control flies (Figure 21). The attempt to rescue this phenotype by silencing the *Adar* gene in the R3 neurons (UAS-*Adar*^{RNAi}), proved to be successful, as the median score now improved to 90%, making these flies perform with the visual working memory resembling that of the WT-CS control group.

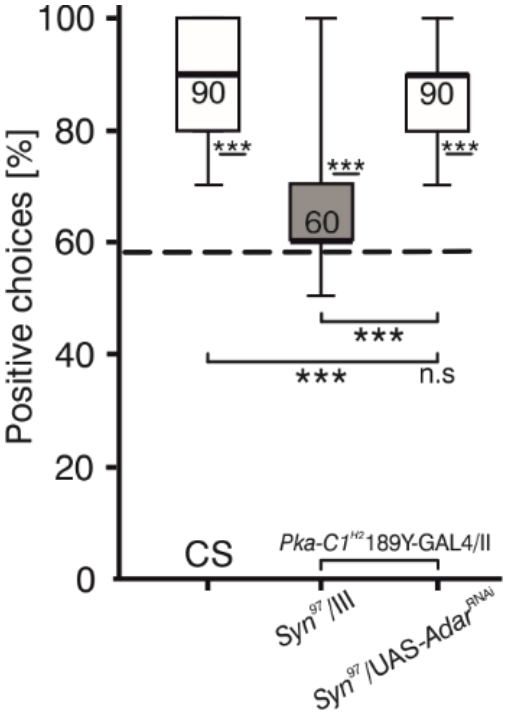

Figure 21: Rescue of *Pka-C1*^{H2}/II;*Syn*^{97}/III using RNAi-mediated knock-down of *Adar*

The double heterozygous group (*Pka-C1*^{H2}/II; *Syn*^{97}/III, n=25), displayed a highly significantly reduced detour memory score (60%) in comparison to that of the WT-CS control group (n=25) which had a high median score of 90%. Rescue of this phenotype using RNAi-mediated knock-down of *Adar* (UAS-*Adar*^{RNAi}/III, n=25) improved the score back to 90% which was comparable to the score of the WT-CS control group and highly significantly different from the random chance level (58%).

Refer to **Table 15** in **Appendix** for statistical analysis for multiple comparison (Kruskal-Wallis test), normality distribution (Shapiro-Wilk test) and comparison against random chance level (58%) (Sign/t-test).

It should be noted that the rescuing of this double-heterozygous genotype (Figure 21) occurred without the overexpression of the *Synapsin* transgene, and only by simply knocking-down the *Adar* gene. Hence, this result solidifies our hypothesis that PKA-C1 activity is undoubtedly required for the phosphorylation of Synapsin in the R3 neurons, specifically through PKA recognition and phosphorylation of site-1.

However, the question remains as to what happens in those flies, where endogenous *Adar* is still intact. Flies belonging to the WT-CS control group

themselves, have undergone pre-mRNA editing of the site-1 of the Synapsin protein, and are able to function with a normal visual working memory. If we divert our attention back to the earlier results (Figure 15 and Figure 16), we notice that the rescue of the defective phenotypes of homozygous *Syn*^{97} phenotype (Figure 15), and double heterozygous *Pka-C1*^{H2}/II;*Syn*^{97}/III phenotype (Figure 16), were done using UAS-*Syn*(cDNA8), which was presumably edited on the site-1 by the ADAR enzyme. This raises the question of how these rescues were successful.

A hypothesis would be that there is a chance of another kinase, capable of phosphorylating Synapsin at site-1, in addition to PKA-C1. This kinase must then have less selectivity for the amino acid sequence of site-1, that despite the editing of this site by ADAR in the fourth position, where arginine (RRFS) is altered to glycine (RGFS), the phosphorylation of Synapsin by this alternative kinase is still successful.

Thus, our quest began, to understand the role of CaMKII in the functioning of visual short-term orientation memory in *Drosophila* as a potential alternative kinase. We already knew from literature that the phosphorylation of Synapsin by CaMKII in the local circuit interneurons (LN1), is required for short-term olfactory habituation (STH) in *Drosophila* (Sadanandappa et al., 2013). We wondered whether it would play a similar role in the R3 neurons, in service of visual working memory. Thus, the aim of the next section of this chapter, was to elucidate how CaMKII takes on the role of phosphorylating Synapsin in a scenario where PKA-C1 might either be unavailable to perform its function due to reduced catalytic activity (as in the case of *Pka-C1*^{H2} hypomorphic allele), or inefficient in phosphorylating Synapsin at site-1 (due to pre-mRNA editing by ADAR).

3.1.4 Relationship between CaMKII and Synapsin

Drosophila calcium-dependent calmodulin kinase II (CaMKII), a 50kDa protein, was first identified to be involved in long-term adaptational processes in the neural tissues of *Drosophila* (Mitschulat, 1989).

The phosphorylating function of CaMKII, was first elucidated in 1981, in a study, as one of the two specific kinases phosphorylating the “Protein I” (a synaptic vesicle associated protein), in rat brains (Kennedy and Greengard, 1981). By using a kinase assay, this study was able to prove that the purified Protein I, could be phosphorylated, simply by the addition of Ca^{2+} ions to the homogenate, which

initiated, and maintained the phosphorylation rate of the substrate effectively. When this activity was abolished by the addition of Trifuroperazine, which has been known to bind to calmodulin in a calcium-dependent manner (Levin and Weiss, 1976). Thus, it was discovered that the dependence on calcium was mediated by calmodulin, giving rise to the term “calcium-dependent calmodulin kinase (CaMK)”.

Following this primary finding, several more mammalian studies involving CaMKII, and its phosphorylation of the Synapsin protein were recorded. One of the important ones, was the comparison of CaMKII to the cAMP-dependent Protein Kinase A (PKA), and how the two kinases operate differently to perform a seemingly similar function (Huttner et al., 1981). Huttner and colleagues demonstrated that the specificity of these kinases towards the multiple phosphorylation sites on the mammalian synaptic vesicle Protein I, was different, as a result of which, the regulation of their phosphorylating nature also varies. Further characterization of the kinase protein with respect to its nature of phosphorylating mammalian synaptic vesicle Protein I, along with its innate tendency for autophosphorylation, has also been done (Kennedy et al., 1983).

On the behavioural front, the function of CaMKII in phosphorylating Synapsin, and its role in short-term olfactory habituation (STH), was first addressed in *Drosophila* in 2013. The study focussed on the importance of the phosphorylation sites on the Synapsin protein, using fly lines mutated for Synapsin, generated by an earlier method, where the serine in the 6th position of both the phosphorylation sites was replaced with alanine (Michels et al., 2011). Western blot analysis were done to estimate the level of phosphorylated Synapsin in these mutants using an antibody that was specifically raised against the Synapsin protein phosphorylated at the serine (anti-PSyn(S6); the same antibody used in Figure 17 & Figure 20). The analysis revealed a complete absence of phosphoylated Synapsin in these mutants, which was comparable to that observed in the *Synapsin* null mutants (Syn^{97}), which served as a negative control (Sadanandappa et al., 2013).

Pan-neuronal, conditional, and targeted expression of a peptide inhibitor against CaMKII (*CaMKII-I.Ala*), all had a negative impact on olfactory short-term memory in *Drosophila* (Griffith et al., 1993). In Western blot analysis, pan-neuronal expression of the inhibitor also led to a significantly reduced level of phosphorylated

Synapsin (PSyn(S6)), indicating that CaMKII phosphorylation of Synapsin, is important for olfactory memory (Sadanandappa et al., 2013).

Although both PKA and CaMKII phosphorylate the site-1 in the A domain on the Synapsin protein, they differ in their sequence of recognition. As we had explained in the previous section, a post-transcriptional mRNA editing of the site-1 occurs in the *Drosophila* Synapsin (Diegelmann et al., 2006). Interestingly, this editing process does not impact the phosphorylation of this site by CaMKII, as much as it does PKA. The mammalian Synapsin, is phosphorylated by CaMKII in the conserved A domain, at ser^{553} (Kao et al., 1999), which corresponds to the ser^{6} in the RRFS of the *Drosophila* Synapsin. Based on this correlation, it could be deduced that the serine in the 6^{th} position is more crucial than the glycine in the second position, for the recognition and phosphorylation of Synapsin by CaMKII.

Thus, based on the literature enlisted above, we decided to consider the possibility that CaMKII phosphorylates Synapsin at site-1 in the cells that undergo mRNA editing by ADAR. The behavioural results in the earlier part of the study (Figure 15 & Figure 16), showed that a rescue of homozygous Syn^{97} and double-heterozygous $Pka\text{-}C1^{H2}$/II;Syn^{97}/III, was possible with the UAS-*Synapsin* transgene, which presumably underwent ADAR editing. A reasonable explanation for this, would be that the phosphorylating activity of CaMKII, can potentially allow the functioning of visual working memory.

We began with the question of what would happen in the absence of CaMKII activity in the R3 neurons. Thus, we went ahead and expressed the RNAi-mediated knock-down of *CaMKII* (UAS-$CaMKII^{RNAi}$; (Perkins et al., 2015)) in the R3 neurons in a wild-type background, simply to reveal the effect it has on detour memory. It is seen in Figure 22A that it leads to a significant reduction in visual working memory, in comparison to the GAL4, UAS, and WT-CS control groups, clearly elucidating the importance of CaMKII activity in the R3 neurons.

As an additional experiment, we expressed the peptide inhibitor for CaMKII (Griffith et al., 1993) which carries an alanine in place of the threonine (UAS-*CaMKII-I.Ala*), which is usually autophosphorylated. The phenotype elicited by expressing the inhibitory peptide in the R3 neurons, is arguably stronger than the one observed in the knock-down of *CaMKII* (Figure 22A), and led to a significant loss of visual working memory in comparison to the respective GAL4 and UAS control groups (Figure 22B).

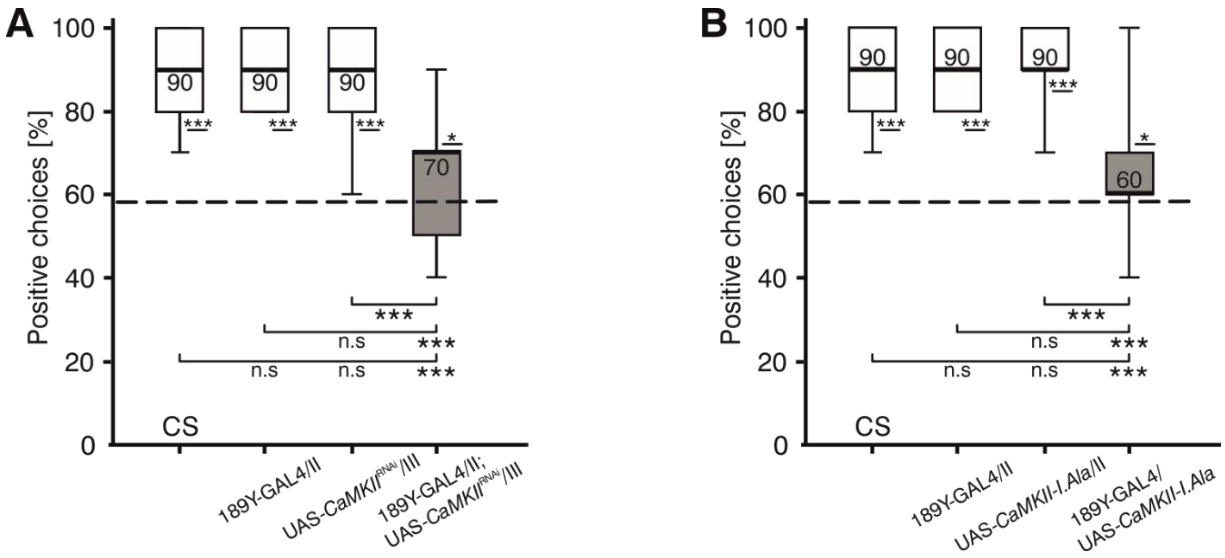

Figure 22: Behavioural effect of RNAi-mediated knock-down and inhibition of *CaMKII* in R3 neurons

(A) RNAi-mediated knock-down of *CaMKII* in R3 neurons (189Y/II; UAS-*CaMKII*^{RNAi}/III, n=25) elicited a severe impairment of the working memory score in the detour paradigm. With a median of 70%, the experimental group was very highly significantly different from the respective GAL4 control (189Y-GAL4/II, n=25), UAS control (UAS-*CaMKII*^{RNAi}/III, n=25) and the WT-CS group (n=25). The experimental group was also significantly different from random chance level (58%).
(B) The inhibition of CaMKII activity using inhibitory peptide in R3 neurons (189Y/UAS-*CaMKII-I.Ala*, n=25) reduced the median memory score to 60% which was very highly significantly different to the respective GAL4 control (189Y-GAL4/II, n=25), UAS control (UAS-*CaMKII-I.Ala*/II, n=25), and the WT-CS group (n=25). The experimental group was also significantly different from random chance level (58%).

Refer to **Table 16** and **Table 17** in **Appendix** for statistical analysis for multiple comparison (Kruskal-Wallis test), normality distribution (Shapiro-Wilk test) and comparison against random chance level (58%) (Sign/t-test)

Following the above findings, we set up a complementary rescue experiment to improve the detour memory deficit caused by the heterozygous hypomorphic *Pka-C1* allele (*Pka-C1*^{H2}/II), by expressing the constitutively active UAS-*CaMKII*^{T287D} (Park et al., 2002) transgene in the R3 neurons. As observed in Figure 23, the rescue was successful, and the memory score was increased to 90%, comparable to that of the WT-CS control group. This proves that CaMKII activity can compensate for the memory deficits caused by the reduction in the level, and catalytic activity of the hypomorphic *Pka-C1* allele. However, in case of a wild-type brain with fully functioning PKA, as well as CaMKII, there is a possibility that both PKA, as well as CaMKII can phosphorylate the Synapsin protein at site-1, depending on the isoforms that have been edited, and those that have not.

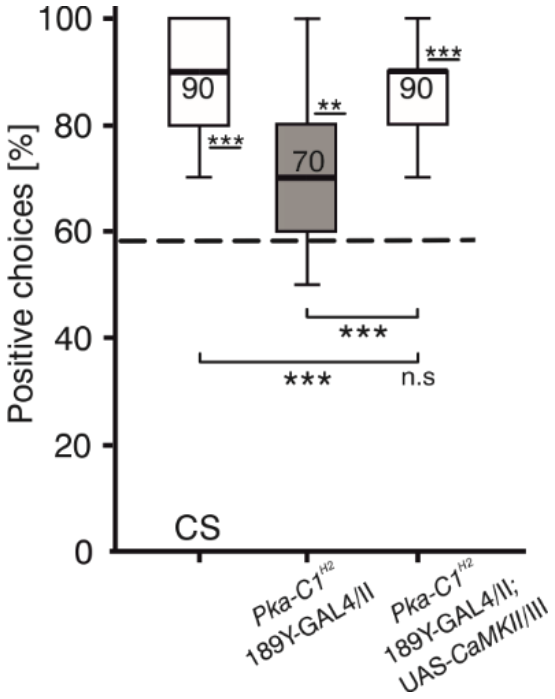

Figure 23: Rescue of *Pka-C1^{H2}*/II with UAS-*CaMKII^{T287D}*

The heterozygous hypomorphic allele for *Pka-C1* (*Pka-C1^{H2}*189Y-GAL4/II, n=25) had a median score of 70% in the detour paradigm which was highly significantly different from that of the WT-CS control group (n=25) with a median score of 90%. Rescue of the former phenotype was possible with constitutive active expression of *CaMKII* (UAS-*CaMKII^{T287D}*/III, n=25) in the R3 neurons, which raised the median memory score to 90%, comparable to that of the WT-CS control group.

Refer to **Table 18** in **Appendix** for statistical analysis for multiple comparison (Kruskal-Wallis test), normality distribution (Shapiro-Wilk test) and comparison against random chance level (58%) (Sign/t-test).

The next plan of action, was to visualize whether this constitutive active expression of *CaMKII* does indeed lead to increased levels of phosphorylated Synapsin on site-1. We resorted to immunohistochemistry once again, to specifically label phosphosynapsin-1 (Syn-P1) with the anti-SynP1 antibody used in the earlier experiments (Figure 17 & Figure 20).

Not unlike in the previous cases, the brains belonging to the control group labelling the R3 neurons with membrane-bound GFP (Figure 24A) displayed a bare-minimum level of phosphosynapsin1 in R3 neurons (Figure 24.A-A') The group expressing constitutively active UAS-*CaMKII^{T287D}* on the other hand, showed a highly significant increase in Syn-P1 (Figure 24B'), despite having GFP levels comparable to that of the control group. (Figure 24B, see Table 19 in Appendix). The merged version (Figure 24B"), also shows relatively increased levels of Syn-P1 in the R3 neurons, in comparison to the merged version of the control group (Figure 24A"), which predominantly showed a GFP staining of the R3 neurons, with little to no phosphosynapsin1 (Syn-P1) protein (magenta).

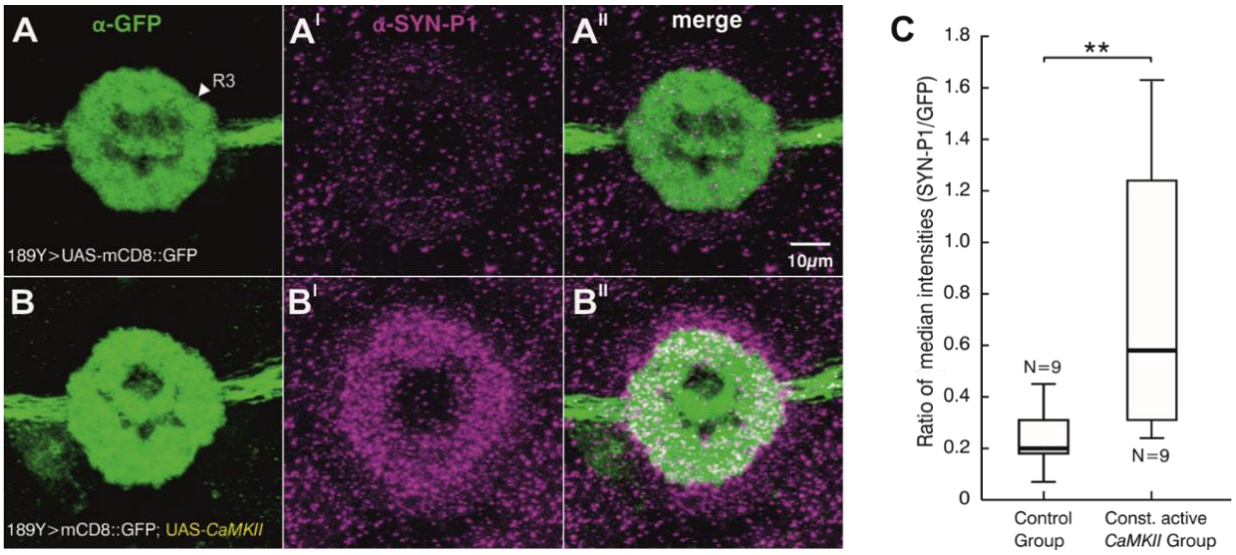

<u>Figure 24</u>: Phosphorylation of Synapsin on site-1 when constitutively active *CaMKII* is expressed in R3 neurons

All samples were scanned under 63X magnification with 0.33μm thickness of each slice.
31 slices were stacked for the images and 11 slices were stacked for the intensity measurements.

(A-A'') Control brain (A) R3 neurons (189Y-GAL4>GFP) stained in green. (A') minimal distribution of Syn-P1 (magenta). (A'') merged version where the green staining overpowers the magenta with little to no colocalisation.
(B-B'') Brain expressing constitutively active *CaMKII* (UAS-*CaMKII*^{287D}) (B) R3 neurons (189Y-GAL4>GFP) stained in green. (B') The level of the phosphorylated Synapsin-1 (Syn-P1) protein was visibly increased in the R3 neurons as well as in the surrounding neuropil. (B'') In the merged scenario, the co-distribution of GFP and Syn-P1 is more profound than that found in the control group with endogenous CaMKII activity.
(C) Quantitative analysis of the ratio of median intensities (using Mann-Whitney U test) between Syn-P1 and GFP for the control group and the group with constitutively active *CaMKII*, showed a very highly significant difference between the two. The latter group had a significantly higher distribution of Syn-P1 in the R3 neurons (Syn-P1/GFP ratio ~0.58) compared to that in the control group (Syn-P1/GFP ratio ~0.2)

Refer to **Table 19** in **Appendix** for statistical analysis for two independent variable samples (Mann-Whitney U test) to compare the median intensity ratios between the control and the experimental group. Refer to **Table 2** for the primary antibodies and **Table 3** for the secondary antibodies used in the experiment.

In addition to visual proof, statistical comparison of the ratio of median intensities (Syn-P1/GFP) between the two groups also showed a significant difference between each other. There was a highly significant increase in the level of phosphosynapsin-1 (Syn-P1) in R3 neurons when constitutively active *CaMKII* was expressed, in comparison to the control group with endogenous *CaMKII* expression (Figure 24C).

The above results, together, show that CaMKII is capable of phosphorylating Synapsin at site-1, thereby increasing the level of Syn-P1 in R3 neurons, which could

eventually lead to the release of the cytoskeleton-tethered synaptic vesicles. CaMKII also has the potential to act as the less-specific kinase alternative for PKA-C1, that can recognize site-1, despite the editing of the adenosine group to an inosine group by ADAR, since CaMKII relies more on the serine in the sixth position for its phosphorylating function.

3.1.5 Relationship between Rugose and PKA

During his master thesis, Dennis Lalotra (Lalotra, 2014), performed an enhancer suppression to identify proteins interacting with PKA, by crossing the lines carrying X-chomosomal deletions into the heterozygous *Pka-C1*^{H2}/II background. One of the deletions, which covered the *rugose* (*rg*) gene, could rescue the reduced visual working memory of *Pka-C1*^{H2}/II flies, indicating that the reduced activity of Rugose is compensating for the limited PKA activity.

The *rugose* gene in *Drosophila,* codes for the *Drosophila* AKAP550 (A Kinase Anchoring Protein 550), and interacts with members of the Notch-mediated signalling pathway (Shamloula et al., 2002). Due to this reason, *rugose* has been suspected to have a role in cell-fate determination. One of the first phenotypes identified in *rugose* mutant flies, was the “rough eye”, indicating that Rugose is necessary for the correct retinal pattern formation. An important function of AKAPs, in general, is to bind to kinases such as PKA, in order to target them towards specific substrates that the kinase phosphorylates (Rubin, 1994). Several studies have come out analysing nature of interaction of a variety of AKAP proteins with the individual regulatory subunits of PKA, such as PKA-R1 (Angelo and Rubin, 1998), PKA-R2 (Herberg et al., 2000), and both (Huang et al., 1997b; Huang et al., 1997a).

In the context of learning and memory, the above mentioned AKAP-PKA-R2 interaction was manipulated using the eCORP2 (endogenous competitor of PKA-R2) in *Drosophila*, to understand its role in anesthesia-sensitive memory (Schwaerzel et al., 2007). This study revealed that the AKAP-PKA-R2 interaction is more important for a distinct anesthesia-sensitive memory (ASM) phase after aversive conditioning, rather than the actual association process that takes place in odour memory. This was also the first piece of research that revealed that this type of memory is localised in the same Mushroom Body (MB) neurons, where cAMP-dependent short-term memory also resides.

rugose has also been termed the functional homologue of the mammalian gene *Neurobeachin (Nbea)*, which is a multidomain scaffolding protein, and modulates the vesicle sorting and secretion in presynapses of mice. Using an antiserum for Rugose, and the cis-Golgi marker GM130, Volders and colleagues demonstrated that the RG protein localises in and around the Golgi complex (Volders et al., 2012). Additional results in this study, using *rg* hypomorphic alleles such as rg^{1} and $rg^{\gamma 5}$, also strengthened the earlier findings that Rugose is required for olfactory associative learning (both aversive and appetitive), and that these processes are confined to the MB Kenyon cells. Immunohistochemistry studies using MB-specific GAL4 drivers expressing UAS-mCD8::GFP, also revealed aberrations in overall MB development in *rg* mutants (except in rg^{1}), hinting that Rugose is critical for the effective formation of the MB lobes (Volders et al., 2012).

It was later revealed that *Drosophila* Rugose impacts only the olfactory STM formation when interacting with PKA, while not affecting the types of LTM that require consolidation (Zhao et al., 2013). Interaction between hypomorphic alleles of *Pka* ($Pka\text{-}C1^{H2}$) and *rugose* (rg^{1}), led to an additive effect in the loss of olfactory STM, indicating that *rugose* interacts positively with *Pka*. An explanation for this behaviour was that, Rugose might spatiotemporally restrict the subcellular distribution of PKA near the region that requires PKA activity, thereby facilitating its targeting and phosphorylating of the proteins that are required for olfactory STM.

Thus, with the above observations in mind, we approached our behavioural paradigm pertaining to visual working memory, to understand how Rugose interacts with PKA in this memory. We decided to use the same hypomorphic allele for *rugose* ($rg^{\gamma 5}$) that was used in a previous study (Volders et al., 2012), to observe how it impacts the phenotype exhibited by the hypomorphic *Pka-C1* allele ($Pka\text{-}C1^{H2}$), that we have regularly used in our study. The heterozygous hypomorphic *Pka-C1* allele ($Pka\text{-}C1^{H2}$/II), performed poorly, with a reduced detour memory as always, with a median of 70%, which was highly significantly different from the WT-CS control group (Figure 25).

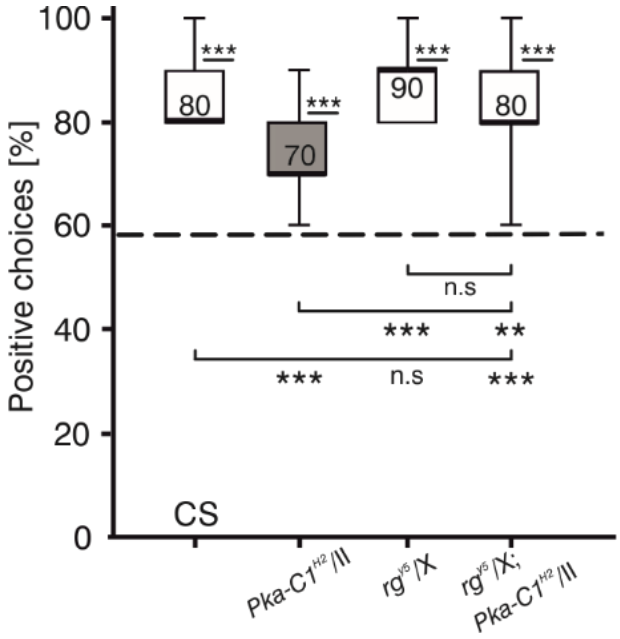

<u>Figure 25</u>: Genetic interaction study between *Pka-C1* and *rugose*

The heterozygous hypomorphic *Pka-C1* allele (*Pka-C1^{H2}*/II, n=30) displayed a median detour memory score of 70% which was highly significantly different from that of the WT-CS control group (n=30) which had a score of 90%. The heterozygous hypomorphic rugose allele (*rg^{γ5}*/X, n=30) group performed similar to the WT-CS control group with a median of 90%. The impaired detour memory phenotype of the *Pka-C1^{H2}*/II group was rescued by the hypomorphic rugose allele in the double heterozygous mutant group (*rg^{γ5}*/X;*Pka-C1^{H2}*/II, n=30) where the median score was increased to 80% which was statistically not significantly different from the WT-CS group and highly significantly different from random chance level (58%).

Refer to **Table 20** in **Appendix** for statistical analysis for multiple comparison (Kruskal-Wallis test), normality distribution (Shapiro-Wilk test) and comparison against random chance level (58%) (Sign/t-test)

Individually, the *rugose* hypomorphic allele (*rg^{γ5}*) did not elicit a phenotype in the detour paradigm, and the flies behaved like wild-type control fies, indicating that lowering the levels of Rugose does not hamper the functioning of this type of short-term memory. Interestingly, double-heterozygous flies containing the hypomorphic alleles for both the genes, displayed a wild-type-like phenotype, where the memory deficit of *Pka-C1^{H2}*/II was compensated for by the *rg^{γ5}*/X allele (Figure 25).

This was the first clear-cut proof that *Pka* and *rugose* do interact in *Drosophila* during the functioning of visual working memory in a way that has not been witnessed in olfactory memory. After zoning in on *rugose* as a potential antogonist of *Pka* in the functioning of detour memory, the next step was to design rescue experiments for the phenotype of *Pka-C1^{H2}*/II, by altering the levels of Rugose in the R3 neurons, where visual working memory is formed. Flies heterozygous for *Pka-C1^{H2}*/II, displayed an impaired memory score of 70%, which was significantly lower than that of WT-CS flies (Figure 26). When the UAS-*rg* transgene was overexpressed in the R3 neurons in a *Pka* mutant background, the memory score failed to improve. In fact, the phenotype of *Pka-C1^{H2}*/II was made slightly, but not significantly worse, upon *rugose* overexpression, hinting that the overexpression of *rugose*, worsens detour memory, when PKA levels are already reduced.

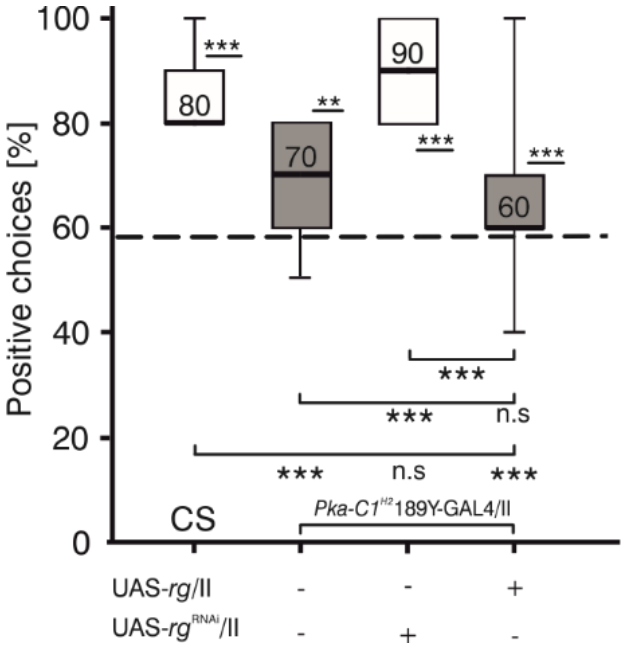

<u>Figure 26</u>: Modulation of *Pka-C1^{H2}* phenotype by RNAi-mediated knock-down and overexpression of *rugose* in R3 neurons

The heterozygous *Pka-C1* hypomorphic (*Pka-C1^{H2}*189Y-GAL4/II, n=30) group exhibited a median detour memory score of 70% which was highly significantly different from the WT-CS control group (n=25) with a median of 80%. The memory score of the former group was rescued to 90% with the RNAi-mediated silencing of *rugose* in R3 neurons (*Pka-C1^{H2}*189Y/UAS-*rg*^{RNAi}, n=30) which was highly significantly different from the *Pka-C1^{H2}*/II group and not significantly different from the WT-CS control group. Over-expression of rugose in R3 neurons (*Pka-C1^{H2}*189Y/UAS-*rg*, n=24) did not rescue the memory phenotype of *Pka-C1^{H2}*/II and was highly significantly different from the WT-CS group.

Refer to **Table 21** in **Appendix** for statistical analysis for multiple comparison (Kruskal-Wallis test), normality distribution (Shapiro-Wilk test) and comparison against random chance level (58%) (Sign/t-test)

On the other hand, silencing of *rugose* using an RNAi-mediated knock-down, led to a full rescue of detour memory where the memory score in these flies was increased up to 90%, making it statistically similar to the score of the WT-CS control group.

Following the evidence provided by the behavioural experiments, it was safe to presume that the reduced levels of Rugose in the R3 neurons, either due to a hypomorphic allele (Figure 25), or through RNAi-mediated silencing (Figure 26), benefitted the detour memory functioning. In order to conclude that this effect was due to the direct influence Rugose has in the distribution of PKA in the axons of the R3 neurons, immunohistochemistry experiments were set up. We hypothesized that reducing the levels of Rugose, would result in an increase in PKA localisation in the R3 axons, while *rg* overexpression would elicit the opposite effect of reduced PKA levels at the presynapse, by sequestering PKA to the Golgi in the cell soma.

Since there are no antibodies available that directly address PKA-C1, we made use of the fluorescent tag (FLAG) technique, where the FLAG epitope, a polypeptide protein tag, can be attached to any given protein (example: PKA) using

recombinant DNA technology (Hopp et al., 1988). A mono/polyclonal antibody raised against this FLAG tag, can then be considered as a primary antibody for this protein. In our case, we expressed the UAS-*Pka-C1* transgene (used in a previous rescue experiment (Figure 12) and contains the FLAG tag) in the R3 neurons (VT42759-GAL4), and utilized the anti-FLAG antibody to carry out the immunohistochemistry experiments. We replaced 189Y-GAL4 with VT42759-GAL4 to drive expression in the R3 neurons, since VT42759-GAL4 lies on the third chromosome, making it possible to recombine this driver with UAS-*Pka-C1* (also on chromosome 3).

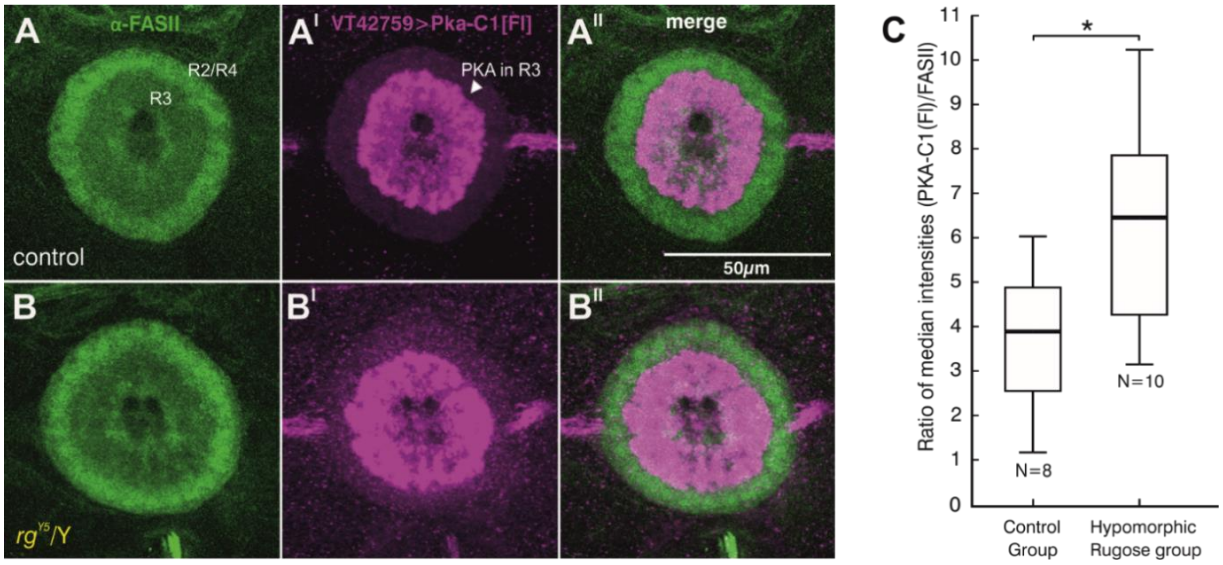

Figure 27: Distribution of PKA-C1 in R3 neurons in a hypomorphic *rugose* mutant background

All samples were scanned under 63X magnification with 0.33μm thickness of each slice.
31 slices were stacked for the images and 11 slices were stacked for the intensity measurements.

(A-A'') Control brain (A) FASII (stained in green) showcasing the entire EB.(A') Localisation of PKA-C1 in the R3 neuronal axons projecting into the EB (VT42759>UAS-*Pka-C1*) (magenta) (A'') merged version showing the distribution of PKA-C1 in R3 neurons (magenta) with respect to the entire EB (green).
(B-B'') Hypomorphic *rugose* mutant brain (rg^{Y5}/Y). (B) FASII staining for the entire EB (green) (B') Visible increase in the localisation of the PKA-C1 in the axons of the R3 neurons projecting into the EB. (B'') merged version showing the increased distribution of PKA-C1 in R3 neurons (magenta) with respect to the entire EB (green).
(C) Quantitative analysis of the ratio of median intensities (using Mann-Whitney U test) between PKA-C1 and FASII for the control group and the *rg* hypomorph (rg^{Y5}/Y), showed a significant difference between the two. The latter group had a significantly increased distribution of PKA-C1 in the R3 neurons projecting into the EB (PKA-C1/FASII ratio ~ 6.5) compared to that in the control group (PKA-C1/FASII ratio ~ 3.9).

Refer to **Table 22** in **Appendix** for statistical analysis for two independent variable samples (Mann-Whitney U test) to compare the median intensity ratios between the control and the experimental group. Refer to **Table 2** for the primary antibodies and **Table 3** for the secondary antibodies used in the experiment.

The immunohistochemistry experiment included a wild-type control group (with endogenous rugose expression), and an experimental group, hemizygous for the hypomorphic allele for the rugose gene (rg^{Y5}/Y). The EB in both groups were labelled using anti-Fasciclin II (green), as the counter stain (Figure 27A and B). The FASII protein seemed to be unaffected by the altered levels of Rugose in the *Drosophila* brain, based on the median intensity values of FASII in both the groups, which were statistically indistinguishable from each other (see Table 22 in Appendix).

As observed in Figure 27, the PKA-C1[Fl] was localised in the axons of the R3 neurons (Figure 27A'), and the merge represents its distribution pattern in the R3 neurons with respect to the FASII staining of the entire EB (Figure 27A"). Moving on to the experimental group (Figure 27B-B"), the FASII counter staining (Figure 27B), appears to be visually similar to that of the control group (Figure 27A). Nonetheless, there is an apparent increase in the intensity of the PKA-C1[Fl] staining (Figure 27B'), in comparison to that of the control group (Figure 27A'), which was also reflected in the merge (Figure 27B").

Quantification of the ratios of median intensities (PKA-C1[Fl]/FASII) between the two groups was done to analyze any potential differences between them. The region of interest (ROI) was selected to be the circumference of the entire EB, based on the FASII staining, where the EB appeared the most complete (approximately the middle slice of the EB neuropil). There was a statistically significant increase in the levels of of PKA-C1 in the axons of the R3 neurons of the rg^{Y5}/Y mutant group (Figure 27C), suggesting that more PKA is transported into the axons of the R3 neurons since hypomorphic Rugose has reduced ability to sequester PKA to the Golgi.

Earlier behavioural experiments showed that the overexpression of *rugose* in a hypomorphic *Pka-C1* mutant background made the visual working memory worse, albeit not significantly (Figure 26). Whereas, reducing the endogenous expression levels of *rugose*, proved to be beneficial in rescuing this phenotype (Figure 25 and Figure 26). Our next mission, was to understand what happens when the UAS-*rg* transgene is overexpressed specifically in R3 neurons, in an otherwise wild-type background. This resulted in a reduction of detour memory in the experimental group,

which was highly significantly different from the GAL4 and UAS control groups as well as the WT-CS flies (Figure 28). The reduction in median score to 70%, was an indication that increasing the levels of *rugose* expression in the R3 neurons, affects the activity of endogenous PKA at the presynapse of R3 neurons in these flies, leading to a reduction in visual working memory.

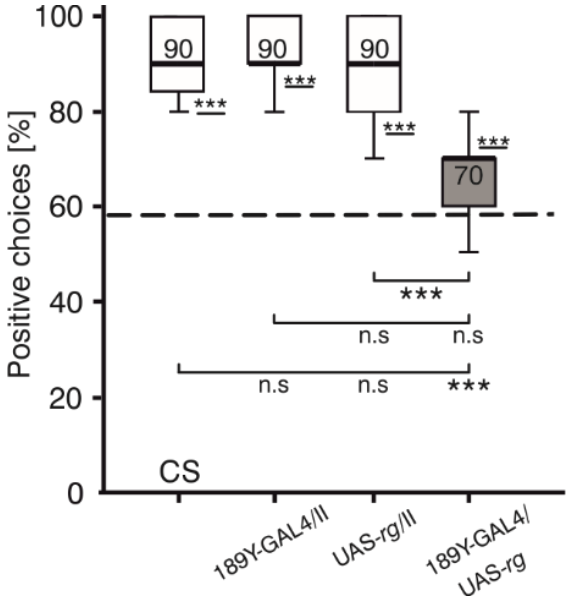

<u>Figure 28</u>: Behavioural effect of over-expressing *rugose* in R3 neurons

Overexpression of the *rugose* transgene in R3 neurons (189Y-GAL4/UAS-*rg*, n=29) exhibited a defective detour memory phenotype. It had a median memory score of 70% which was very highly significantly different from the individual GAL4 controls (189Y-GAL4/II, n=30), UAS controls (UAS-*rg*/II, n=30) and the WT-CS group (n=28) where the control groups all displayed a median score of 90%. The experimental group was also highly significantly different from the random chance level (58%).

Refer to **Table 23** in **Appendix** for statistical analysis for multiple comparison (Kruskal-Wallis test), normality distribution (Shapiro-Wilk test) and comparison against random chance level (58%) (Sign/t-test)

Finally, to claim that Rugose overexpression directly affects the sub-cellular distribution levels of PKA-C1 in the presynaptic site of the R3 neurons, an immunohistochemistry experiment was designed to obtain visual proof supporting the aforementioned hypothesis. The anti-Flag-tag antibody which was used in the earlier experiment (Figure 27), was once again utilized to stain for the PKA-C1 Flag-tag fusion protein. The control group of flies which possessed intact (and functioning) endogenous Rugose, was compared against the group with overexpression of *rugose* in the R3 neurons. FASII was once again used as the common counter staining for both groups (see Table 24 in Appendix) to visualize the entire EB (Figure 29A and B). In case of the control group (Figure 29A-A”), PKA-C1 was stained in magenta (Figure 29A’), and was found to be localised in the region of the axons of the R3 neurons (Figure 29 A”). The experimental group, in contrast, exhibited an obvious decrease in the levels of Pka-C1[Fl] in the axons of the R3 neurons (Figure 29B’), proving that an increase in Rugose levels, leads to sequestering of more PKA to the Golgi, and reduced axonal transport of PKA into the EB.

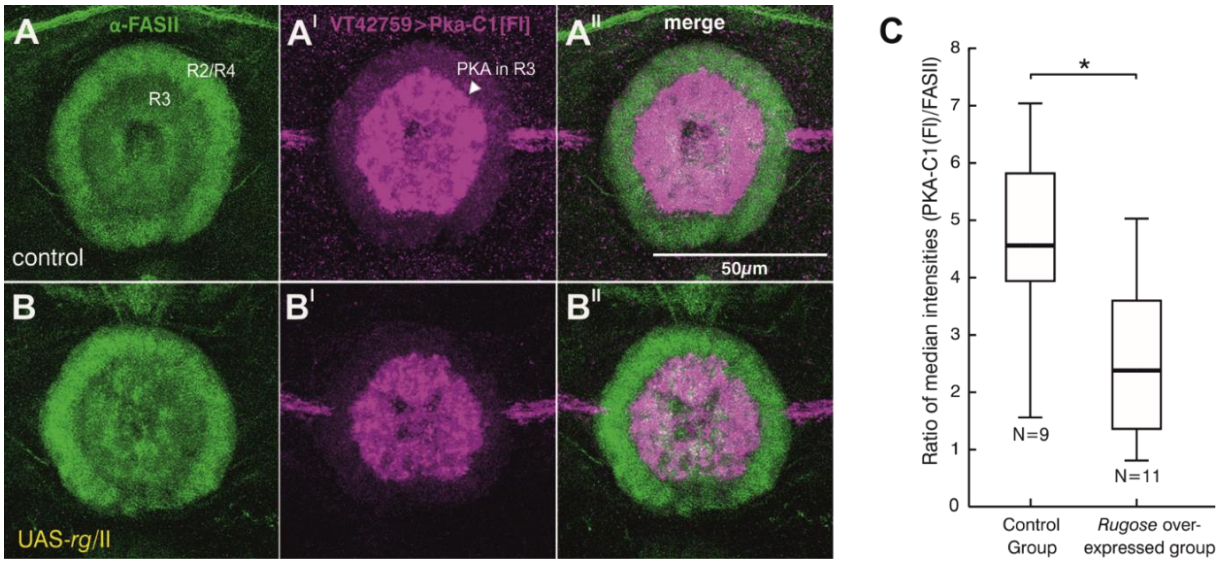

Figure 29: Distribution of PKA-C1 in R3 neurons in a *rugose*-overexpressed background

All samples were scanned under 63X magnification with 0.33μm thickness of each slice.
31 slices were stacked for the images and 11 slices were stacked for the intensity measurements.

(A-A'') Control brain (A) FASII (stained in green) showcasing the entire EB (A') The distribution of PKA-C1 in the axons of the R3 neurons (VT42759>UAS-*Pka-C1*) (magenta) (A'') merged version showing the distribution of PKA-C1 driven in the R3 neurons (magenta) with respect to the entire EB (green).
(B-B'') Brain overexpressing *rugose* transgene in the R3 neurons (VT42759>UAS-*rg*) (B) FASII staining for the entire EB (green) in (B') Visible decrease in the localisation of the PKA-C1 in the R3 neurons. (B'') merged version showing the reduced distribution of PKA-C1 in R3 neurons (magenta) with respect to the entire EB (green).
(C) Quantitative analysis of the ratio of median intensities (using Mann-Whitney U test) between PKA-C1 and FASII for the control group and the group with overexpression of *rg*, showed a significant difference between the two. The latter group had a significantly reduced distribution of PKA-C1 in the axons (PKA-C1/FASII ratio ~2.4) compared to that in the control group (PKA-C1/FASII ratio ~ 4.5).

Refer to **Table 24** in **Appendix** for the statistical analysis of two independent variable samples (Mann-Whitney U test) to compare the median intensity ratios between the control and the experimental group. Refer to **Table 2** for the primary antibodies and **Table 3** for the secondary antibodies used in the experiment.

The merged version of the experimental group, also showed reduced PKA in the R3 region of the EB (Figure 29B"), in comparison to the merged version of the control group, which filled up the whole R3 region of the EB (Figure 29A"). The region of interest (ROI) was selected to be the circumference of the entire EB, based on the FASII staining, where the EB appeared to be most complete (approximately the middle slice of the EB neuropil), and a stack of 11 slices with 3.63μM total thickness was built. Ratio of median intensities between the two groups for PKA vs FASII, mirrored the visual observation. The experimental group had nearly half of the levels of PKA-C1 in the axons of the R3 neurons, in comparison to that of the control group

(Figure 29C). This difference was statistically significant after calculating the values for a reasonable sample size for both groups.

In conclusion, Rugose has a direct role to play, when it comes to the distribution of PKA-C1 to the presynaptic site of the R3 neurons. This interaction is primarily antagonistic in nature, which differs from their relationship in regards to olfactory short-term memory in the Kenyon cells of the MB. Rugose's function of preventing PKA from being available at the presynaptic site of the R3 neurons, could be the reason for the deficit in detour memory in flies overexpressing the UAS-*rg* transgene (Figure 26 and Figure 28). And by association, it can be assumed that in case of olfactory memory functioning in flies, PKA activity is possibly required in the cell body, and dendrites of the MB neurons, rather than at the presynapse.

3.2 Network analysis of the *Drosophila* central complex

Existing literature and the previous section of our study have both shown that the R3 ring neurons of the EB play a pivitol role in visual working memory. The EB on the whole, contains six classes of ring neurons (R neurons), which have synaptic partners within the EB, as well as in other regions of the CC. The CC contains multiple substructures, all of which are presumably interconnected to each other in unique ways.

According to the model presented by Sara Kuntz for the functioning of detour memory, synergistic activation of a particular axonal branch of the R3 neurons due to the visual input from the R2/R4 neurons, and the spatial information from the "idiothetic neurons", resulted in the elevated levels of NOS in the R3 neurons. Increase in NOS levels was predicted to lead, in turn, to cGMP induction, followed by cGMP-mediated opening of cyclic nucleotide-gated (CNG) ion channels. This mechanism eventually results in Ca^{2+} influx in the R3 neurons (Kuntz et al., 2017).

Going by the aforementioned hypothesis, it would mean that external influx of Ca^{2+}, would understandably exceed the exisiting threshold of the calcium levels in the R3 neurons. Since the formation of the memory traces for the landmarks and the distractor are dependent on the cGMP-mediated Ca^{2+} influx, this sudden surge in calcium levels, following the activation of UAS-*TrpA1*, might understandably hinder this mechanism. We predicted that TrpA1 activation of the R3 neurons, might lead to

the potential activation of multiple axonal wedges, opening the door to the possibility that the fly visually perceives multiple landmarks in the detour arena, in addition to the original landmarks, making it difficult for the fly to differentiate between the landmarks and the distractor. In our detour arena, we aimed to observe the effect of increased firing of action potentials, upon the activation of dTrpA1 at 29ºC. We hypothesized that the TrpA1 activation of the neurons involved in detour memory, would have a counter-productive effect on its execution, and can thus be used as an effective method to screen for the different neuronal subclasses of the CC, for their involvement in the functioning of visual working memory.

3.2.1 TRPA1 activation of neurons

As mentioned earlier, TrpA1, a channel protein, performs the function of allowing increased influx of Ca^{2+} ions, when allowed to be opened at temperatures higher than 28°C (Rosenzweig et al., 2005). The detour memory of a fly functions based on the functioning of NOS, which is the chemical currency of this pathway, conveying the information regarding the visual input of the landmarks, and the distractor from the R2/R4 neurons to the R3 neurons, where the idiothetic memory is formed (Kuntz et al., 2017). Needless to state, the pathway relies on a delicate balance of NOS and Ca^{2+} availability in the presynaptic region of the R3 neurons. However, this system has the potential to hamper the functioning of detour memory in any neuronal subtype that is necessary for its functioning. Thus, we proceeded to use the activation of TrpA1 as a method to reveal the ring neurons, in addition to the R2 and R3 neurons that might have a role to play in visual working memory.

3.2.1 (a) TRPA1 activation of ring neurons

The EB is the most important region of the CC that is associated with visual orientation, and this substructure comprises of the ring neurons. Most of the ring neurons presumably have synaptic connections with each other (Omoto et al., 2018). According to Neuser and colleagues, adult-specific silencing of different ring-neuron subfamilies (R1,R3,R3/R4d), using UAS-TNT, severely affected visual working memory (Neuser et al., 2008). However, complete silencing of these neurons with TNT expression, is considerably different from a more streamlined, thermogenetic approach. Thus, we were curious to identify the importance of each of these ring neuronal subfamilies in detour memory, by overactivating them individually, using GAL4-specific expression of UAS-*TrpA1*.

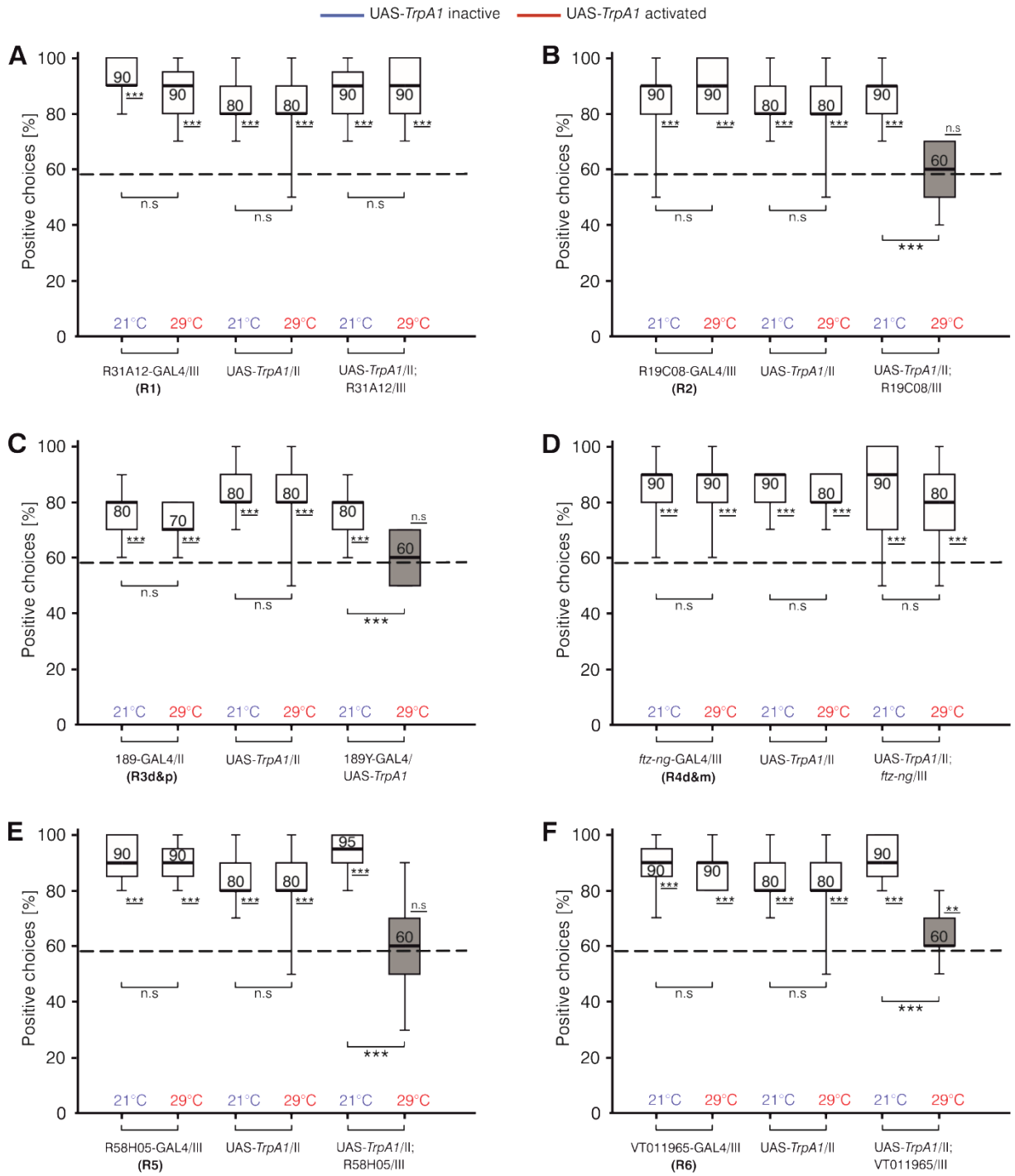

Figure 30: TrpA1 activation of ring-neuron subtypes

(A) UAS-*TrpA1* activation of R1 (R31A12-GAL4, n=24) ring neurons did not elicit any defect in detour memory (median 90%) and was highly significantly different from the chance level (58%). **(B&C)** Over-activation of R2 (R19C08-GAL4, n=25) and R3 (189Y-GAL4, n=21) neurons at 29°C led to a complete loss of memory (median=60%) which was not significantly different from the chance level. **(D)** R4 neurons (*ftz-ng*-GAL4, n=30) did not have an effect in detour memory when activated using UAS-*TrpA1* at 29°C (median=80%) and was highly significantly different from chance level. **(E)** UAS-*TrpA1* activation of R5 (R58H05-GAL4, n=24) neurons led to a complete loss of memory (median=60%) and **(F)** Activation of R6 (VT011965-GAL4, n=24) neurons led to a loss of memory where the memory score (median=60%) was highly significantly different from the same group at 21°C but also significantly different from the chance level.

Refer to **Table 25-Table 30** in **Appendix** for statistical analysis for paired-test (Wilcoxon matched-pair test), normality distribution (Shapiro-Wilk test) and comparison against chance level (58%) (Sign/t-test).

Overactivation of R1 neurons (R31A12-GAL4) (Omoto et al., 2018), using UAS-*TrpA1* (29ºC) did not elicit any significant difference in detour memory in comparison to the inactivated state (21ºC) (Figure 30A). The experimental group had a median of 90% correct decisions at both temperatures. The GAL4 and UAS controls behaved like WT-CS flies at both temperatures with a median of 90% and 80% respectively, indicating that the control groups were reliable.

On the other hand, overactivation of the R2 neurons (R19C08-GAL4; (Omoto et al., 2017)), led to a complete loss of memory when tested at 29ºC, where the flies had a median memory score that was not significantly different from chance level (Figure 30B). The score was very highly significantly different from the median score of the same group when tested at 21ºC, indicating that overactivation of these neurons had a detrimental effect in detour memory.

Similarly, UAS-*TrpA1* activation of R3 neurons (189Y-GAL4; R3d&p) (Renn et al., 1999; Omoto et al., 2018), also led to the loss of visual working memory at 29ºC, where the median memory score was not significantly different from the chance level and was very highly significantly different from the same group of flies which were not activated by UAS-*TrpA1* at 21ºC (Figure 30C).

On the contrary, R4 (d&m) neurons (*ftz-ng*-GAL4) (Pereanu et al., 2011) did not affect visual working memory whether UAS-*TrpA1* was activated (at 29ºC), or not (at 21ºC), where the test group had a median memory scores of 90% and 80% respectively. It was also highly significantly different from the chance level, further proving that hyperactivation of the R4 neurons did not directly or indirectly impact detour memory (Figure 30D).

The R5 (R58H05-GAL4; (Omoto et al., 2017)), and R6 (VT011965-GAL4) neurons that have recently been published (Omoto et al., 2018), were also overactivated using UAS-*TrpA1*, to identify if they also had a part in the functioning of detour memory. As observed (Figure 30E), over-activation of the R5 neurons showed a complete loss of visual working memory, which was significantly different from the memory score of the same group at the lower temperature (at 21ºC), and not significantly different from the chance level. The over-activation of R6 neurons on the other hand, also elicited a deficit in detour memory, where the memory score was highly significantly different from chance level while also being significantly different from the median score of the same group at 21ºC (Figure 30F).

3.2.1 (b) TRPA1 activation of compass and shift neurons

The activation of different ring neurons using UAS-*TrpA1*, proved to be an effective way to discern the neurons which take part in the functioning of detour memory, from those which did not. Thus, using the same mechanism, we next decided to test the compass neurons (also known as the E-PG neurons), which are the ones responsible for heading representation and orientation in *Drosophila*. From our hypothesis, it is understood that although the memory is formed in the R3 neurons, this information needs to be conveyed to the PB for the turning process to occur. One of the potential candidates connecting the EB with the PB, and the gall, is the compass neurons (Wolff et al., 2015).

Thus, we pursued activating these neurons by driving UAS-*TrpA1* with the R19G02-GAL4 driver (Wolff et al., 2015). As observed below (Figure 31A), there was a complete loss of detour memory, where the median memory score of the activated group was very highly significantly different from that of the same group in the inactivated scenario (Figure 31A).

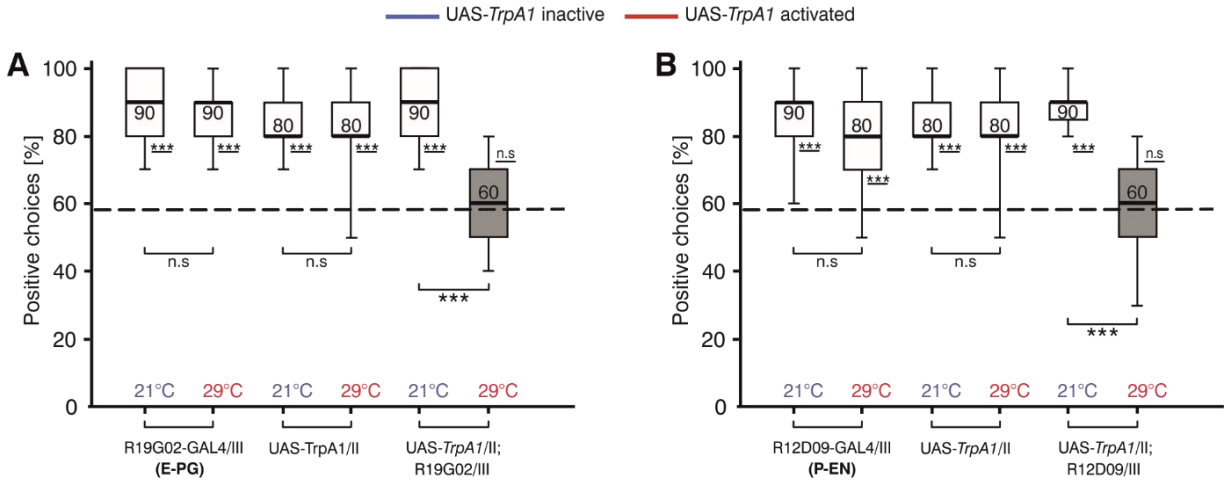

Figure 31: TrpA1 activation of compass and shift neurons

(A) Overactivation of compass neurons using TrpA1 (UAS-*TrpA1*/II; R19G02/III, n=23) led to a complete loss of memory at 29°C (median=60%) which was very highly significantly different from the median memory score of the same group at 21°C (median=90%). The GAL4 (R19G02-GAL4/III, n=25) and UAS (UAS-*TrpA1*/II, n=24) control groups exhibited memory scores of 90% and 80% respectively at both temperatures. **(B)** TrpA1 activation of the shift neurons (UAS-*TrpA1*/II; R12D09/III, n=24) led to a complete memory loss (median=60) which was very highly significantly different from the memory score of the same group (median=90) at 21°C. The GAL4 (R12D09-GAL4/III, n=18) and UAS (UAS-*TrpA1*/II, n=24) control groups behaved like wild-type flies with median memory scores ranging between 80-90% in both temperature conditions.

Refer to **Table 35** and **Table 36** in **Appendix** for statistical analysis for paired-test (Wilcoxon matched-pair test), normality distribution (Shapiro-Wilk test) and comparison against random chance level (58%) (Sign/t-test).

The GAL4 (R19G02-GAL4/III) and UAS controls (UAS-*TrpA1*/II), performed like WT-CS flies with median memory scores at 90% and 80%, which were very highly significantly different from the chance level.

Next, we decided to address the "shift" neurons (also known as the P-EN neurons), which are responsible for moving/shifting the dendritic calcium bump of the E-PG neurons, along the wedges of the EB (Turner-Evans et al., 2017). R12D09-GAL4 (Wolff et al., 2015), was used to drive UAS-*TrpA1* in these neurons, where the visual working memory was completely lost at 29ºC, while the same group of flies displayed wild-type like memory at 21ºC. The latter exhibited a memory score of 90% that was very highly significantly different from the chance level. The GAL4 (R12D09-GAL4/III) and UAS control (UAS-*TrpA1*/II) groups behaved like wild-type flies, with high memory scores that were very highly significantly different from chance level as well.

3.2.2 Shibire^{ts1} inactivation study

The temperature-sensitive mutant for the *shibire* gene (*shibire^{ts1}*) has been shown to code for the defective dynamin protein, which has a temperature-dependent deficit in synaptic vesicle recycling. Expression of UAS-*shi^{ts1}* in the Kenyon cells of the MB, has been performed by researchers to examine the importance of different MB lobes in olfactory memory (Kasuya et al., 2009). Here, we decided to implement the same mechanism in the neurons of the CC, as a screen to identify the ones required for visual working memory.

3.2.2 (a) Shibire^{ts1} inactivation of ring neurons

The inactivation of different ring neurons followed the same principle as that of the activation of neurons using UAS-*TrpA1*, except in this case, instead of manipulating their function using a sudden influx of Ca^{2+} ions, these neurons were prevented from having chemical synaptic transmission. The driver lines used for this study were the same as those used in the activation study to address the different ring-neuron types. Starting with the R1 (R31A12-GAL4) driver, UAS-*shi^{ts1}* inactivation of these neurons at 32ºC, did not impact the median memory score, as it remained as high as 80%, similar to WT-CS memory. It was not significantly different from the median memory score of the same group at 24ºC, when *shi^{ts1}* did not inactivate these neurons. The GAL4 (R31A12-GAL4/III), and UAS (UAS-*shi^{ts1}*/III) control groups performed like wild-type flies at both temperatures as well (Figure 32A).

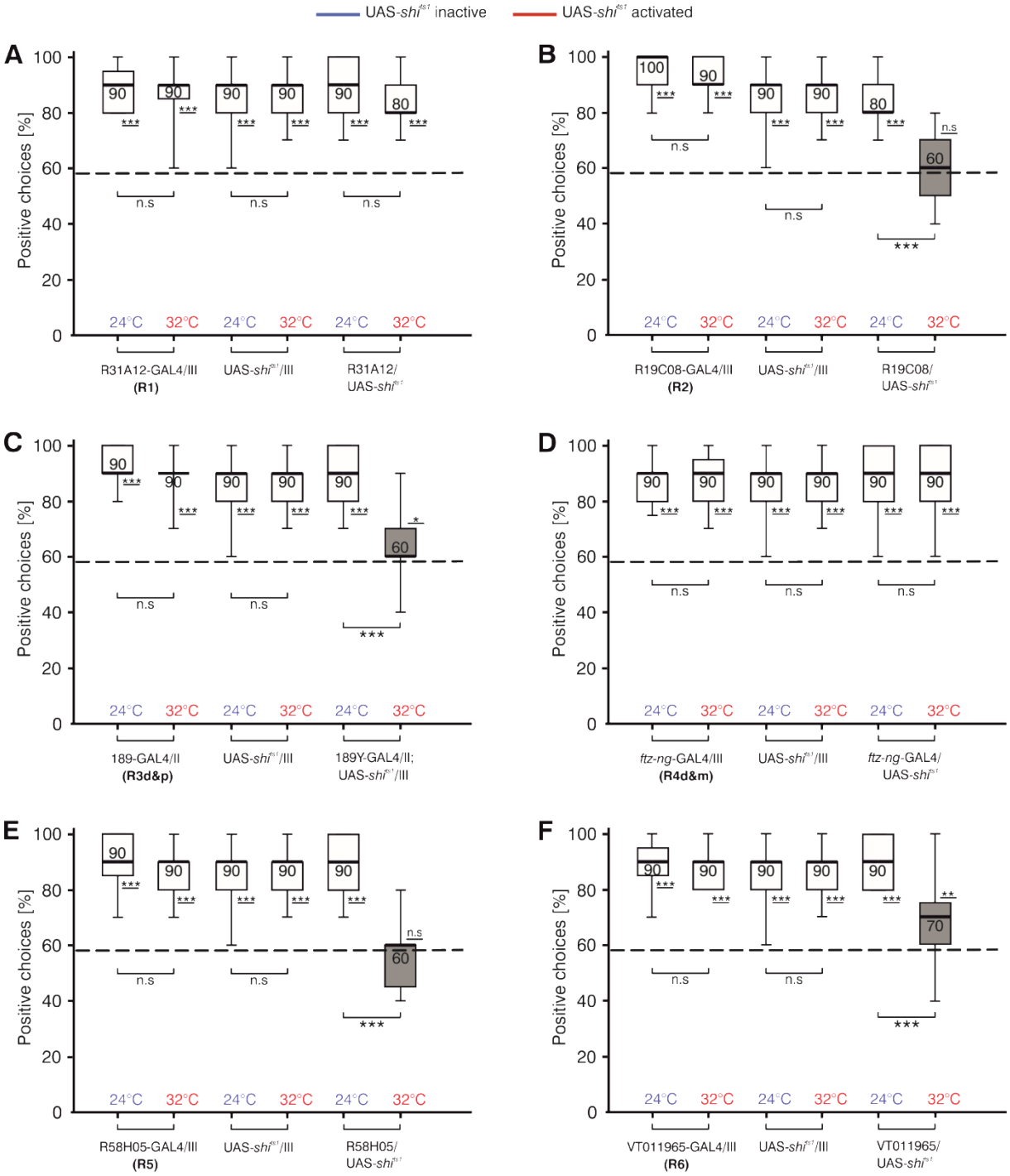

Figure 32: shi^{ts1} inactivation of ring-neuron subtypes

(A) UAS-*shi*^{ts1} inactivation of R1 (R31A12-GAL4, n=25) ring neurons did not elicit any defect in detour memory (median=80%) and was highly significantly different from the chance level (58%). **(B&C)** Inactivation of the R2 (R19C08-GAL4, n=25) and R3 (189Y-GAL4, n=25) neurons at 32°C led to a complete loss of memory (median=60%) which was not significantly different from the chance level. **(D)** R4 neurons (*ftz-ng*-GAL4, n=25) did not have an effect in detour memory when inactivated using UAS-*shi*^{ts1} at 29°C (median=90%) and was highly significantly different from chance level. **(E)** UAS-*shi*^{ts1} inactivation of R5 (R58H05-GAL4, n=24) neurons led to a complete loss of memory (median=60%). **(F)** inactivation of R6 (VT011965-GAL4, n=24) neurons led to loss of memory where the memory score (median=70%) was very highly significantly different from the same group at 24°C but also highly significantly different from the chance level.

Refer to **Table 42-Table 47** in **Appendix** for statistical analysis for paired-test (Wilcoxon matched-pair test), normality distribution (Shapiro-Wilk test) and comparison against chance level (58%) (Sign/t-test).

The R2 (R19C08-GAL4) ring neurons on the other hand, which are responsible for visual object recognition, severely affected the detour memory when inactivated at 32ºC. The median memory score in this case, was reduced to 60%, which was very highly significantly different from the memory score (median=80%) of the same group of flies at 24ºC. The memory score of the former indicates a complete loss of memory, since it was not significantly different from chance level (58%), indicating that the choices made by these flies, were mostly random, than by using their idiothetic memory (Figure 32B). The individual GAL4 (R19C08-GAL4/III), and UAS (UAS-*shi*^{ts1}/III) controls performed like WT-CS flies at both temperatures, with median memory scores that were very highly significantly different from chance level, indicating that they are reliable controls that could be used in this study.

Inactivation of the R3 neurons, the home of this type of idiothetic memory, was anticipated to have a major effect on detour memory. As expected, activation of UAS-*shi*^{ts1} at 32ºC in these neurons, severely affected the memory score down to 60% which was very highly significantly different from the memory score of the same group of flies (median=90%) at 24ºC. High memory scores were displayed by the respective GAL4 (189Y-GAL4/III) and UAS (UAS-*shi*^{ts1}/III) controls, reinforcing that the memory score of the experimental group at 32ºC is due to the *shibire*^{ts1} inactivation of these neurons (Figure 32C).

ftz-ng-GAL4 addressing the R4(d&m) neurons, did not affect detour memory when inactivated using *shibire*^{ts1} at 32ºC. These flies had a median memory score of 90%, which was statistically comparable to the memory score of the same group at 24ºC when *shibire*^{ts1} was not inactivating these neurons. The median memory scores of the experimental group in both temperatures, were highly significantly different from the chance level (58%). The GAL4 (*ftz-ng*-GAL4/III), and UAS (UAS-*shi*^{ts1}/III) controls performed like WT-CS flies, with all of them having a median memory score of 90%, and were highly significantly different from chance level (Figure 32D).

In contrast, inactivation of the recently discovered R5 (R58H05-GAL4) neurons, and R6 (VT011965-GAL4) neurons, led to a significant decrease in detour memory. In case of the R5 neurons, activation using UAS-*shi*^{ts1} at 32ºC, leads to a complete loss of memory, where the median score is reduced to 60%, and is significantly lower than the memory score of the same group at 24ºC (median=90%). The GAL4 (R58H05-GAL4/III), and UAS (UAS-*shi*^{ts1}/III) control groups, once again,

exhibited a wild-type like memory with a median memory score of 90% at both temperatures (Figure 32E).

In the R6 neurons, by activating UAS-*shi*^{ts1} at 32ºC, the median memory score was reduced to 70% from the memory score of 90%, when the same group was tested at 24ºC. These two groups were thus highly significantly different from each other. However, the former group was still highly significantly different from the chance level, indicating that the memory was not completely lost to the point of random behaviour. The GAL4 (VT011956-GAL4/III), and UAS (UAS-*shi*^{ts1}/III) control groups had high median memory scores of 90%, and were very highly significantly different from the chance level (58%) (Figure 32F).

3.2.2 (b) Shibire^{ts1} inactivation of compass and shift neurons

After observing the effect of over-activation of the compass and shift neurons using the temperature-regulated expression of UAS-*TrpA1*, we decided to approach the importance of these neurons using the opposite mechanism. Temperature-regulated inactivation of compass neurons and shift neurons using *shibire*^{ts1} seemed to be effective, since we already observed the effect of inactivating ring neurons, and the impact they had on detour memory.

For the compass/E-PG neurons, R19G02-GAL4 (Wolff et al., 2015), was used, so as to remain consistent with the TrpA1 activation study. As observed (Figure 33A), the inactivation of E-PG neurons at 32ºC, led to a complete loss of short-term visual orientation memory. The memory score was not significantly different from chance level, where the entire box seems to range between 50% and 70%, indicating an overall low memory score for the dataset. The GAL4 and UAS control groups on the other hand, did not show this behaviour, and behaved like wild-type control groups, indicating that there was no leaky expression.

This result is consistent with what was observed in the TrpA1 activation study of these neurons, where allowing the sudden influx of Ca^{2+} ions into these neurons at 29ºC, greatly perturbed the short-term visual orientation memory (Figure 31A). Together, these results strongly suggest that the compass neurons play an important role in the functioning of visual working memory.

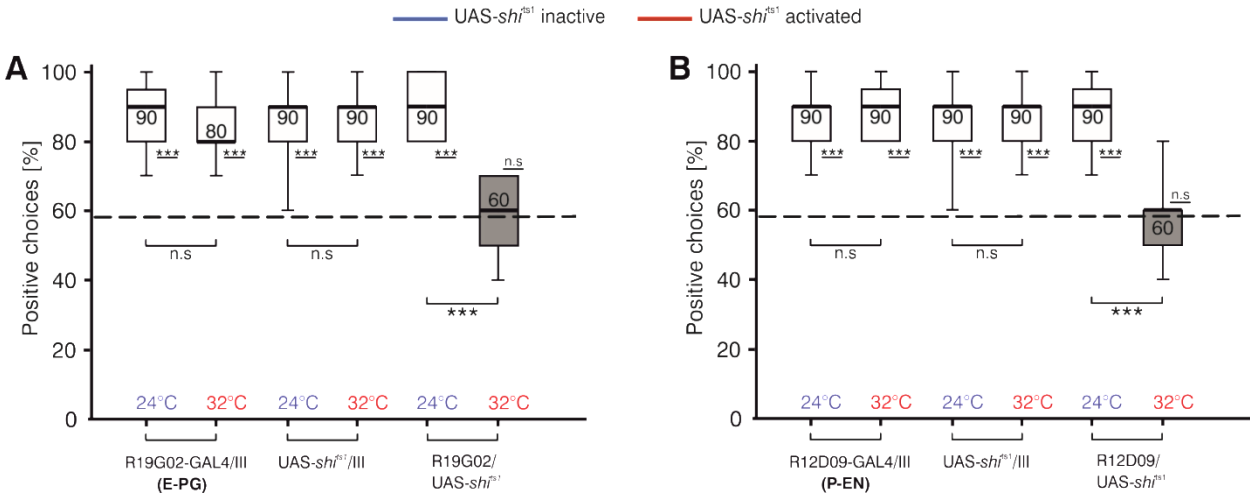

Figure 33: shi^{ts1} inactivation of compass and shift neurons

(A) Inactivation of compass neurons using UAS-*shi*^{ts1} (R19G02/UAS-*shi*^{ts1}, n=23) led to a complete loss of memory at 32°C (median=60%) which was very highly significantly different from the median memory score of the same group at 24°C (median=90%). The GAL4 (R19G02-GAL4/III, n=24) and UAS (UAS-*shi*^{ts1}/III, n=25) control groups exhibited memory scores ranging between 80% and 90% at both temperatures. **(B)** shi^{ts1} inactivation of the shift neurons (R12D09/UAS-*shi*^{ts1}, n=24) led to a complete memory loss (median=60) at 32°C which was very highly significantly different from the memory score of the same group (median=90, n=24) at 24°C. The GAL4 (R12D09-GAL4/III, n=24) and UAS (UAS-*shi*^{ts1}/III, n=25) control groups behaved like wild-type flies with median memory scores of both groups at 90% in both temperature conditions.

Refer to **Table 48** and **Table 49** in **Appendix** for statistical analysis for paired-test (Wilcoxon matched-pair test), normality distribution (Shapiro-Wilk test) and comparison against random chance level (58%) (Sign/t-test).

The other family of neurons having their axons and dendrites in an orientation opposite to that of the E-PG neurons, are the P-EN neurons. Since they have their axons in the EB, and dendrites in the bridge, these neurons would be expected to have a negative effect on detour memory when inactivated using UAS-*shi*^{ts1} at 32ºC.

The driver line used to address these neurons was R12D09-GAL4 (Wolff et al., 2015), which was used to drive the UAS-*shi*^{ts1}, and showed wild-type like memory, when tested for the median memory score at 24ºC (Figure 33B). Whereas, inactivation of these neurons with *shibire*^{ts1} at 32ºC led to a complete loss of memory. The GAL4 and UAS controls did not mimic this behaviour, as they performed like wild-type controls at both temperatures. This finding resembles the one observed earlier, where TrpA1 was used to activate these neurons at 29ºC (Figure 31B).

Together, these results indicate that P-EN neurons play a vital role in the overall functioning of detour memory in addition ot the E-PG neurons.

The temperature-based experiments served as a useful candidate analysis. Situational activation and inactivation of the aforementioned neuronal groups provided a valuable insight on the different prospective neurons that could be considered for further connectome analysis in the context of detour behaviour.

After re-evaluating the individual roles of R3, and the compass neurons, we decided to probe further into their potential synaptic interaction and the possibility of them being each other's pre/postsynaptic partners.

3.2.3 Connectivity between R3 neurons and the compass neurons

Literature states that the E-PG neurons extend their axonal projections into the glomeruli of the bridge, while having dendritic arborizations in the wedges of the EB (Wolff et al., 2015). Since the ring neurons of the EB contain their axons in these doughnut-shaped structures of the CC, we were curious to identify if there were any synaptic interactions between these two neuronal subfamilies. On the behavioural front, both R3 neurons and the E-PG neurons, seem to affect visual working memory profusely, where activation and inactivation of these neurons led to complete loss of detour memory. Since we already know that the memory is formed in the R3 neurons, it seemed apt for us to probe whether the R3 neurons, and E-PG neurons transmit synaptic input to each other, or whether the connectivity was unidirectional, with the E-PG neurons strictly being the postsynaptic partners of R3 neurons, as literature might suggest. We thus began with a simple DenMark-Synaptotagmin (DenSyt) (Zhang et al., 2002; Nicolai et al., 2010) staining, to visualise the expression pattern of the pre- and postsynaptic parts of these neurons.

3.2.3.1 DenMark-Synaptotagmin studies

3.2.3.1 (a) Dendritic projections of R3 neurons

With the TrpA1 and shibire^{ts1} temperature-sensitive experiments, we could confirm the importance of R3 neurons, and discover the significance of the compass neurons in the functioning of visual short-term orientation memory. However, before beginning with the experiments addressing their synaptic connectivity, we decided to study the individual nature of their innervation pattern of the R3 neurons (VT42759-GAL4), using a simple DenSyt staining approach. As it is widely known, DenMark, a dendritic marker, is a proficient tool that helps label not only the existing but also the growing, and upcoming dendrites of the specific neuronal type (Nicolai et al., 2010).

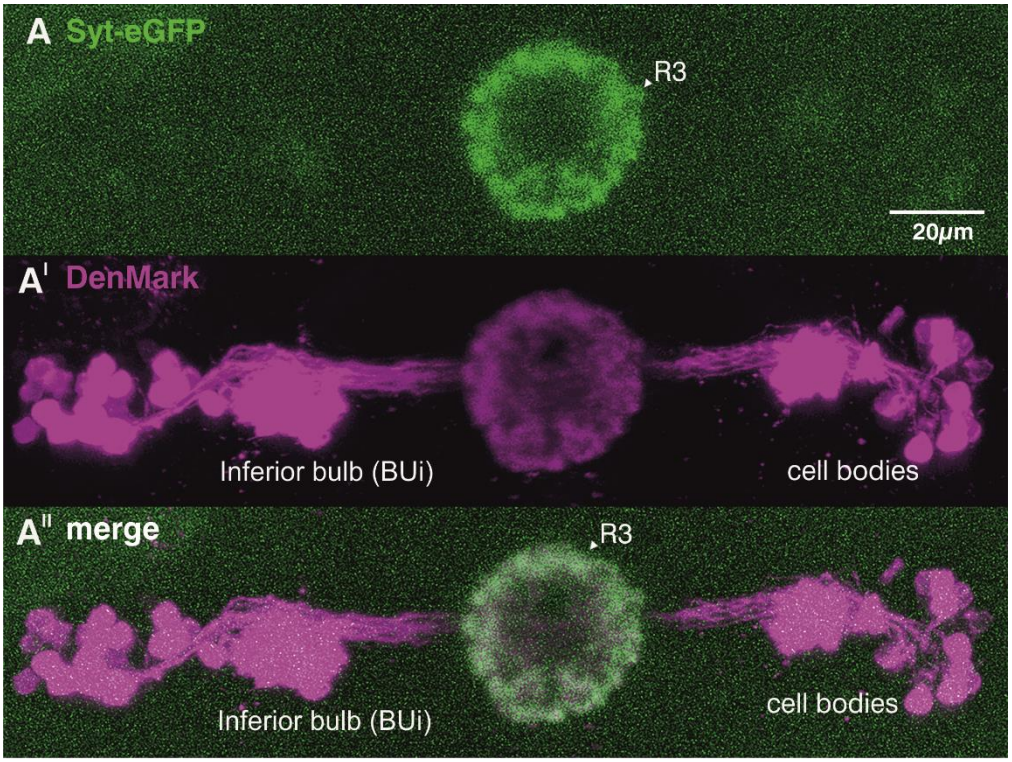

Figure 34: Study of dendritic projections of R3 neurons

(A-A'') Expression pattern of VT42759-GAL4 in the ellipsoid body (EB) **(A)** The presynaptic part of the R3 neurons (VT42759-GAL4>DenSyt) stained in green with Synaptotagmin-GFP (Syt::eGFP) is specifically located in the axonal part of the R3 neurons in the EB. **(A')** The dendritic projections of the R3 neurons stained in magenta using mCherry (DenMark::mCherry) arise from 15-20 cell bodies on both hemispheres innervating the the inferior bulb regions projecting into the EB. **(A'')** the merged version of both the presynaptic and postsynaptic expression patterns.

Refer to **Table 2** for the primary antibodies and **Table 3** for the secondary antibodies used in the experiment.

In this case, DenMark was fused with mCherry, an excellent visual marker that aids in efficient visualization. To separate the presynaptic part of the neurons from their postsynaptic counterparts, Synaptotagmin was used as the other half of the DenSyt construct, which is known for specifically labelling the presynaptic zone of neurons, due to its association with synaptic vesicles (Zhang et al., 2002). In this construct, it was fused with GFP that aids in its visualization.

To specifically address the R3 neurons, we made use of the VT42759-GAL4 driver that predominantly drives the expression of transgenes in these neurons without any off-target labelling in the rest of the brain. The R3 neurons stained in green (Figure 34A), represent their presynaptic region, which resides in the EB with no presynaptic signal in the bulb region. The dendritic branching of these neurons seem to extend out from the cell bodies on either hemisphere towards the inferior

region of the bulb (BUi), where the dendrites appear to be grouped into bundles formed out of microglomeruli, before projecting out into the EB region, which is also stained by DenMark (Figure 34A'). The DenMark expression found in the EB region, indicates that the R3 neurons not only have axons arborizing in the EB, but also dendritic projections in this region, hinting that they could not only transmit, but also potentially receive synaptic input from other neurons, which have their axons projecting into the EB.

The merged version shows a bright green presynaptic signal in the axons pertaining to the R3 region of the EB, and postsynaptic signals specifically in the bulb regions and the cell bodies (Figure 34A''). This coincides with the original classification of the location of pre- and postsynaptic parts of the ring neurons (Omoto et al., 2017). The next part of the study was therefore to understand the projection pattern of E-PG neurons, using the same DenSyt-staining experimental procedure.

3.2.3.1 (b) Dendritic projections of compass neurons

The compass neurons, aptly named in synchronization with their function, are also known as E-PG neurons. They have been proposed to have their axons in the protocerebral bridge (P), and the gall (G), with dendrites branching into the EB (E) (Wolff et al., 2015). Thus, these neurons are thought to have no presynaptic input into the EB, thus limited to only receiving information from the EB, due to their postsynaptic dendrites extending into the various ring neurons.

To confirm whether this statement is indeed accurate, we decided to perform a DenSyt staining to mark the presynaptic and postsynaptic parts of these neurons using Synaptotagmin and DenMark, respectively. To address the E-PG neurons, we used the the R19G02-GAL4 driver (Wolff et al., 2015), to drive the UAS-*DenSyt* transgene.

Interestingly, the presynaptic region of these neurons, stained with GFP, consists of the EB (Figure 35A), along with the gall and the PB (Figure 35B). The intensity of the GFP signal in the EB appears to be equally strong, as it is in the PB, which leads us to believe that the E-PG neurons do have their axonal projections within the EB region, despite literature suggesting that their projections in the EB are strictly dendritic (Wolff et al., 2015). This would indicate that they are capable of

sending out synaptic input to other neurons extending their dendrites into the EB region.

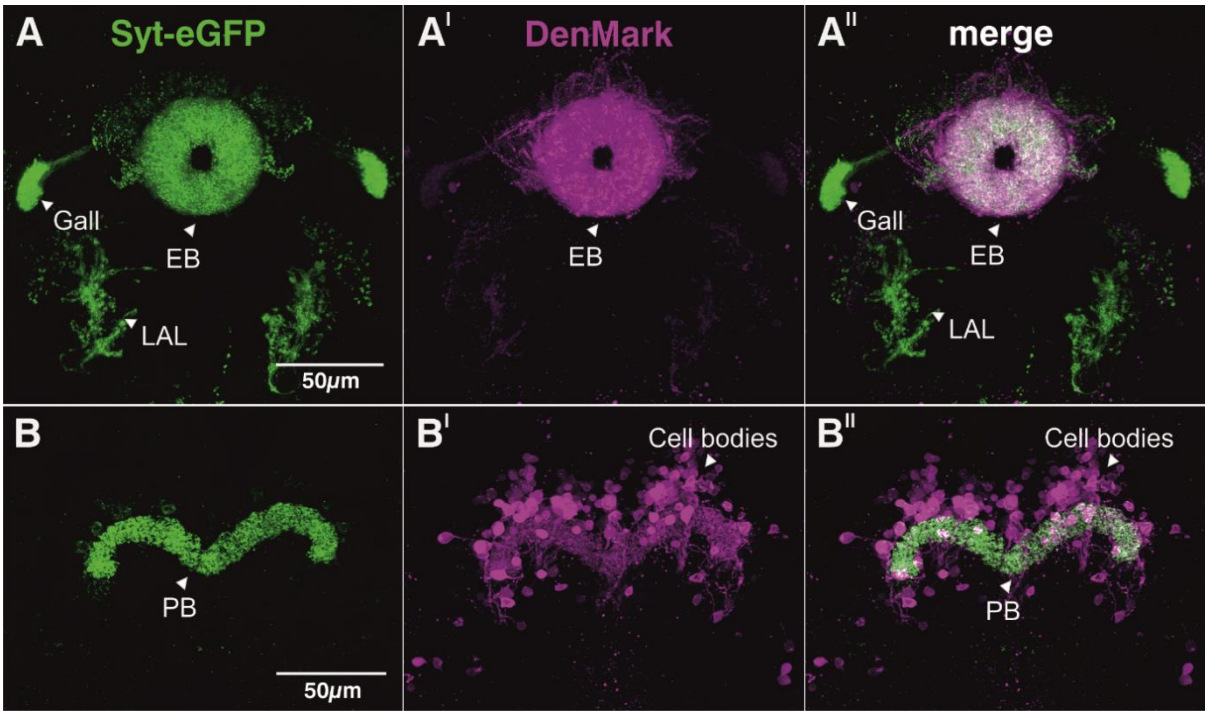

Figure 35: Study of dendritic projections of compass (E-PG) neurons

(A-A") Expression pattern of R19G02-GAL4 in the ellipsoid body (EB). **(A)** The presynaptic part of the E-PG neurons (R19G02-GAL4>DenSyt) stained in green with Synaptotagmin-GFP (Syt::eGFP) is specifically expressed in the entire EB and the gall. **(A')** The dendritic projections of the E-PG neurons stained in magenta using mCherry (DenMark::mCherry) which seem to be expressed only in EB. **(A'')** The merged version of both the presynaptic and postsynaptic expression patterns.
(B-B") Expression pattern of R19G02-GAL4 in the protocerebral bridge. **(B)** A strong GFP signal is observed in the protocerebral bridge region and **(B')** a faint staining of the protocerebral bridge along with many postsynaptic cell bodies stained in magenta (DenMark::mCherry). **(B'')** Merged version of the presynaptic and postsynaptic expression patterns.

Refer to **Table 2** for the primary antibodies and **Table 3** for the secondary antibodies used in the experiment.

The postsynaptic parts of these neurons seem to be marked specifically in the EB (Figure 35A'), without any projections in the gall. The merged version shows a clear distinction between the presynaptic, and postsynaptic parts of this neuronal family in the context of the EB and the gall (Figure 35A"), proving that the E-PG neurons do have presynapses within the EB.

The PB, which has always been suggested to contain the axons of these neurons, was also stained in green, confirming that it indeed belongs to the presynaptic side of the E-PG neurons (Figure 35B). The postsynaptic part of these neurons had a faint magenta staining in PB that was marked with DenMark, and

extended into cell bodies stained in magenta (Figure 35B'), showing that the E-PG neurons have limited dendrites in the PB. The merged version shows the discernible difference between the presynaptic part (PB), and the postsynaptic regions (PB and cell bodies), of the E-PG neurons in the context of the PB (Figure 35B"). Now that the projection pattern of both compass, and R3 neurons have been uncovered, we were curious to visualize the postsynaptic partners of E-PG neurons to observe whether the previous result regarding them having presynaptic inputs into the EB (Figure 35A), would have an effect on their synaptic interaction with the EB ring neurons.

3.2.3.2. trans-Tango study- postsynaptic partners of compass neurons

We set out to effectively stain for the postsynaptic partners of the E-PG neurons, mainly to verify if they indeed do not have any presynaptic inputs into the EB region. For this reason, we used the trans-Tango technique (Talay et al., 2017). We used the R19G02-GAL4 driver described in recent literature (Wolff et al., 2015), to address the E-PG neurons as previously used in the DenSyt experiment of this study (Figure 35). The trans-Tango flies consist of a UAS-myrGFP (myristilated GFP), designed to address the expression pattern of the GAL4 line, thereby labelling the entire E-PG neurons. The postsynaptic partners of these neurons, are expected to be red in colour, owing to the tdTomato (mCherry), tagged with the QUAS part of the construct. The postsynaptic part is expressed once the QF binds to the promoter of the respective GAL4 line after its release, following the synaptic interaction between the pre- and postsynaptic neurons.

In the following figure (Figure 36), it is seen that the GFP labels the whole cell, which in this case, spans across the EB and gall (Figure 36A), the FB (Figure 36B) and the PB (Figure 36C). Moving on to the postsynaptic partners of each substructure of the neuropil, postsynaptic mCherry signal was observed in the middle region of the EB, loosely resembling the axonal projection pattern of the R3a ring neurons (Omoto et al., 2018), although it could not be ascertained. There was also a shadow of postsynaptic staining observed in the outer rings (R2/R4m) of the EB (Figure 36A'). Thus, the trans-Tango technique failed to identify any ring neurons of the EB as direct synaptic partners of the E-PG neurons. Moving on to the FB, we observed postsynaptic projections in the lower layer of the FB, which extended into the paired NO. This projection from the FB and the NO, were seen to be arising from cell bodies located above the PB.

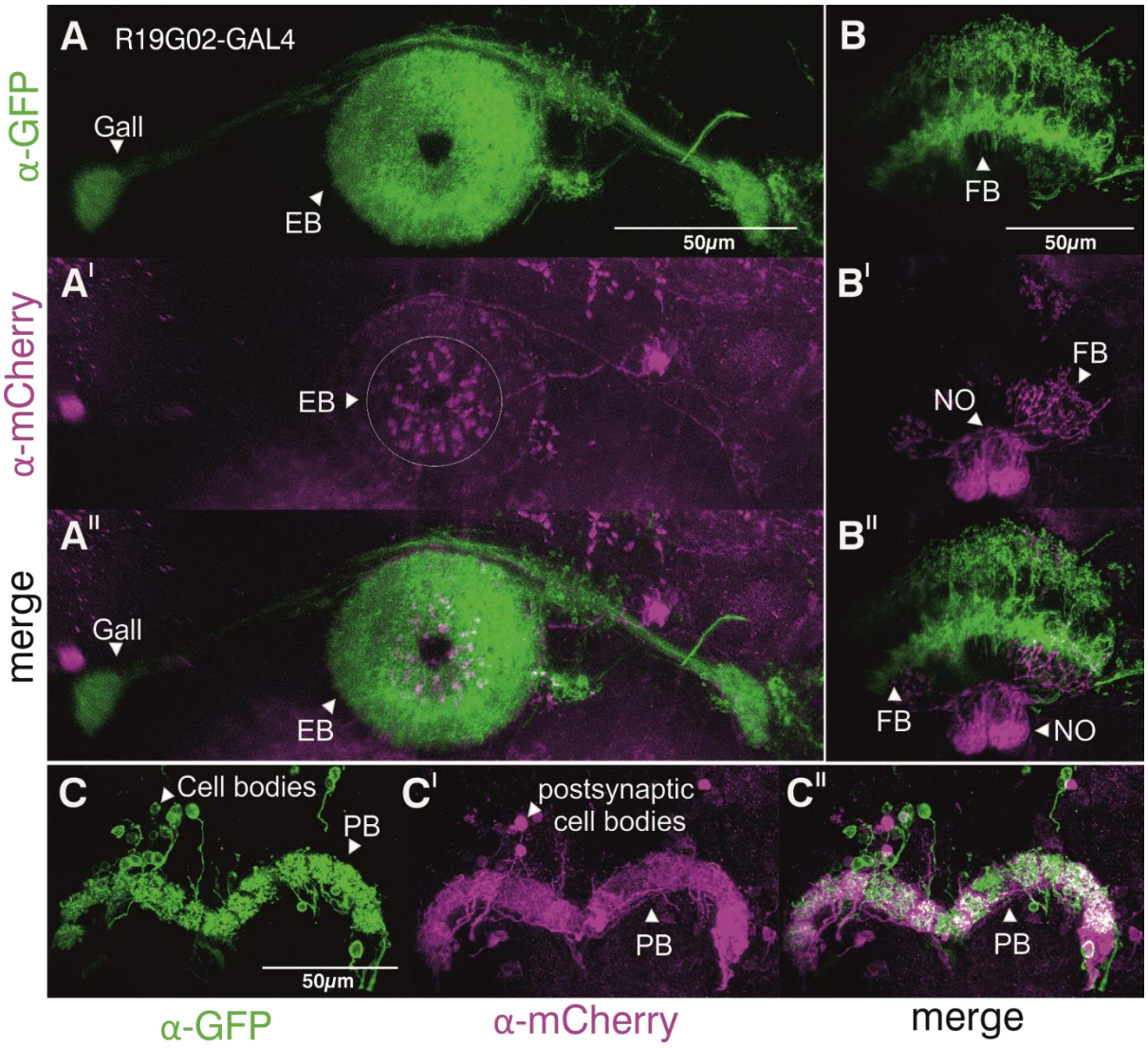

Figure 36: Analysis of postsynaptic partners of compass (E-PG) neurons

Visualisation of the expression pattern of E-PG neurons (R19G02-GAL4) using UAS-myrGFP,QUAS-tdTomato(mCherry);trans-Tango was performed by following the protocol in section **2.5.1** where the whole cell is stained with anti-GFP (in green) and the postsynaptic partners are revealed using anti-mCherry (in magenta). Refer to **Table 2** for the primary antibodies and **Table 3** for the secondary antibodies used in this experiment. Magnification: 63X. Step size: 0.33µm.

(A-A'') Expression pattern of R19G02-GAL4 in the EB and gall **(A)** The entire EB along with the gall on either hemisphere is stained with GFP as the presynaptic partner. **(A')** The postsynaptic partner comprises of the R3a ring neurons connected to a single postsynaptic cell body. **(A'')** Merged version of the above two expression patterns.
(B-B'') Expression pattern of R19G02-GAL4 in the FB **(B)** The E-PG neurons which are the presynaptic partners included the FB stained with GFP **(B')** The postsynaptic partner included the NO with visible postsynaptic connections arising from the FB to the NO. **(B'')** Merged version of the above two expression patterns.
(C-C'') Expression pattern of R19G02-GAL4 in the PB **(C)** The presynaptic partner included the entire PB along with a number of cell bodies. **(C')** The PB along with multiple postsynaptic cell bodies were stained with mCherry. **(C'')** Overlap of the above two expression patterns.

The bridge was also stained as a part of the postsynaptic neurons, belonging to the same network as the FB and the NO. This made us question whether a subtype of the P-FN (PB-to-FB-and-NO) neurons, defined by Wolff and colleagues (Wolff et al., 2015), could be a potential postsynaptic partner of E-PG neurons.

Thus, we decided to build a stack of the entire neuropil, to obtain an overview of the substructures addressed by this driver (R19G02-GAL4), for the E-PG neurons. This also led to us being able to visualize multiple postsynaptic partners in a single image. According to Wolff and colleagues, there exists five different types of P-FN neurons, which arborize in different layers of the noduli (Wolff et al., 2015). The postsynaptic cells which we observe in our trans-Tango experiment, presumably aroborize in most ventrally located Noduli (NO_3), which we speculated based on their size (Figure 37A'). Thus, if these neurons indeed arborize in NO_3, there are once again three different subtypes of P-FN neurons which have axonal projections in this substructure, depending on their arborisation in the medial, posterior and anterior noduli (PBG2–9.s-FB‘1.b-NO3P.b, PBG2–9.s-FB‘1.b-NO3M.b and PBG2–9.s-FB‘2.b-NO3A.b). Thus, we could not confirm the exact subtype of P-FN neurons that are postsynaptic to the E-PG neurons, simply based on this one trans-Tango experiment. A way to pursue this, would be to perform individual GRASP experiments between the E-PG neurons and the different P-FN neurons, to truly identify the family of P-FN neurons seen in Figure 37A'.

Alongside the P-FN neurons, we also observed approximately three Δ7 neurons on either hemisphere, stained as a postsynaptic partner (Figure 37A'). These lateral neurons of the PB, have spiny arbours in all of the PB glomeruli. The activation of cAMP/PKA cascade, and dCREB2 in these neurons, have been proven to create an ever-lasting body-size memory in flies (Krause et al., 2019). However, these Δ7 neurons have not been shown to play a role in visual working memory. It is possible that these neurons are a part of a loop of executing neurons that govern detour memory. Therefore, it would be interesting to perform temperature-shift experiments using TrpA1 and *shibire*^{ts1} in the P-FN neurons, as well as Δ7 neurons, to answer this question.

Nonetheless, the trans-Tango method has not served us in identifying any postsynaptic partners in the ring neurons of the EB. However, we decided to investigate the synaptic partners of these neurons using other, more classical

methods that have been well established. One of these methods, was by using the GFP reconstitution across synaptic partners (GRASP) for these two families of neurons. Thus, we proceeded to perform the following experiments.

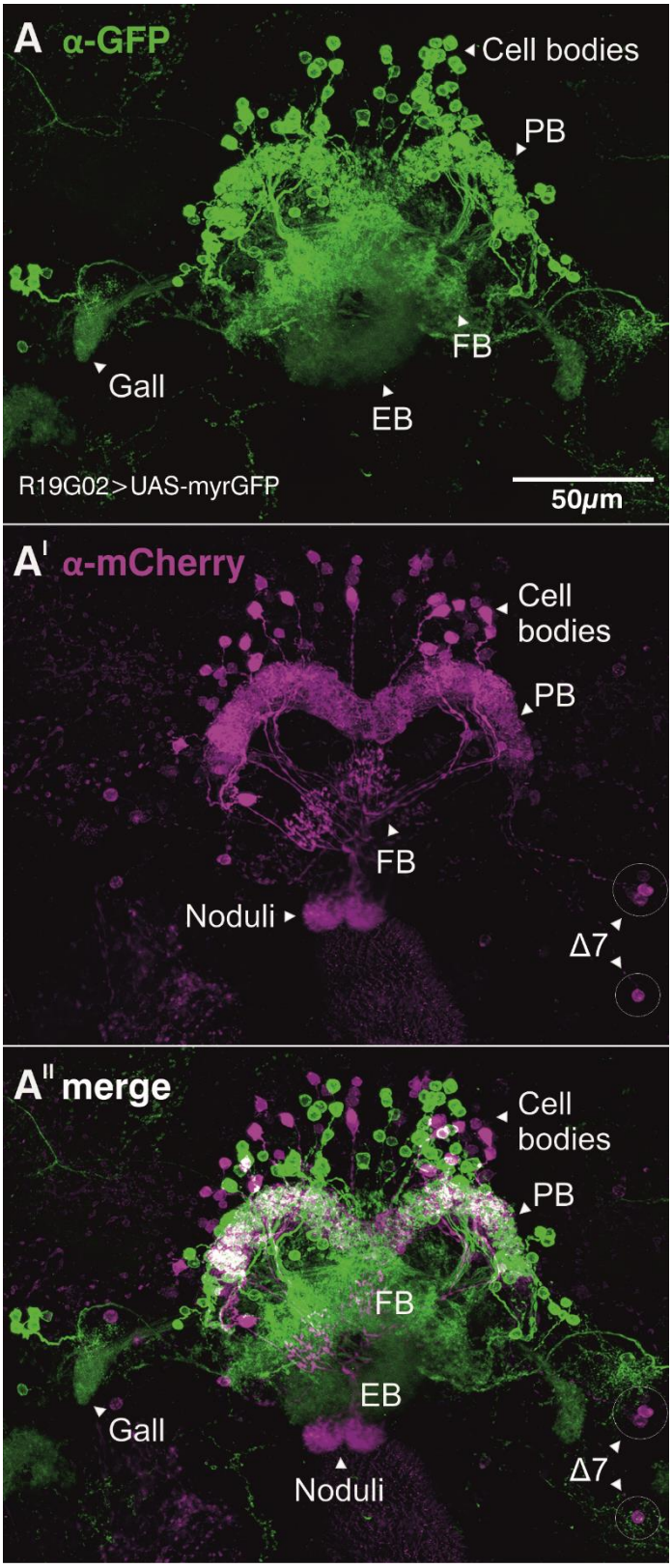

Figure 37: P-FN neurons and Δ7 neurons marked as potential postsynaptic partners of E-PG neurons

Visualisation of the expression pattern of E-PG neurons (R19G02-GAL4) using UAS-myrGFP,QUAS-tdTomato(mCherry); trans-Tango was performed by following the protocol in section **2.5.1** where the whole neuron is stained with anti-GFP (in green) and the postsynaptic partners are revealed using anti-mCherry (in magenta). Refer to **Table 2** for the primary antibodies and **Table 3** for the secondary antibodies used in this experiment. Magnification: 63X. Step size: 0.33μm. Stack size: 417 slices.

(A) Expression pattern of the entire E-PG neurons (R19G02-GAL4) labelled by UAS-myrGFP. The presynaptic signal covers the neurons located above the PB which arborize into the glomeruli of the bridge and into the FB which projects into the EB and the gall.
(A') Postsynaptic partners of the E-PG neurons (R19G02-GAL4) stained with mCherry. A subtype of P-FN neurons located above the bridge with their projections in the bridge, the lower layer of the FB and the ventral most noduli (NO_3). Three Δ7 neurons lateral to the bridge were also observed to be postsynaptic partners and have their arborizations in the PB.
(A'') Overlap of the above two expression patterns.

3.2.3.3 GRASP analysis of R3 and compass neurons

When it comes to unravelling the synaptic connectivity between two neurons, GRASP has always remained as one of the most reliable systems to evaluate it. Originally described in literature as a split GFP method (Feinberg et al., 2008), the system works by splitting the GFP protein into two parts, where one belongs to the presumed presynaptic region, and the other to the post. The resultant GFP signal can be obtained and visualized only if there exists a synaptic connectivity between the two sets of neurons.

With the above information in mind, we decided to first test the direction of synaptic transmission that has already been speculated in literature (Wolff et al., 2015) i.e., the rings of the EB (in part, R3), acting as the presynaptic partner, transmitting information to the postsynaptic partner, presumably the E-PG neurons, since literature suggests that they only have dendrites in the EB region. This would mean that the E-PG neurons receiving synaptic inputs from the R3 neurons, would be the only direction possible, and not the other way around. However, the work by Xie and colleagues (Xie et al., 2017), identified synaptic connectivity between the dendrites of the E-PG neurons, and the axons of several ring neuronal subfamilies (R1,R2,R3,R4d/m), using GRASP. Thus, we decided to proceed with the directional GRASP analysis between the R3 and E-PG neurons using GFP_{1-10} and GFP_{11} fragments.

For this particular GRASP experiment in our study, we selected Synaptobrevin (Syb) (Macpherson et al., 2015), as the marker for the presynaptic region. Syb is localised in the lumen of the synaptic vesicles, hence the strength of the GRASP signal is highly dependent on the neuronal activity. Syb was fused with the GFP_{1-10} part of the whole GFP protein, and designed as a UAS-*Syb*::GFP_{1-10} construct, so that, it could be driven by the GAL4 line that acts as the presynaptic part. Hence, in this case, the R3 neurons, driven by VT42759-GAL4 driver was the presynaptic part.

The presumed postsynaptic neuron was marked with CD4 (Cluster of Differentiation 4), a transmembrane protein which can address the entire cell, and can be visualized with the anti-CD4 antibody. CD4 is fused with the other part of the GFP protein i.e., GFP_{11}, which is designed as a Lex(op)-CD4::GFP_{11} construct. This transgene expression can be driven in the postsynaptic region using a specific LexA driver addressing these E-PG neurons (R60D05-LexA; (Kottler et al., 2019)).

VT42759-GAL4>UAS-Syb::spGFP$_{1-10}$,
R60D05-LexA>LexA(op)-CD4::spGFP$_{11}$

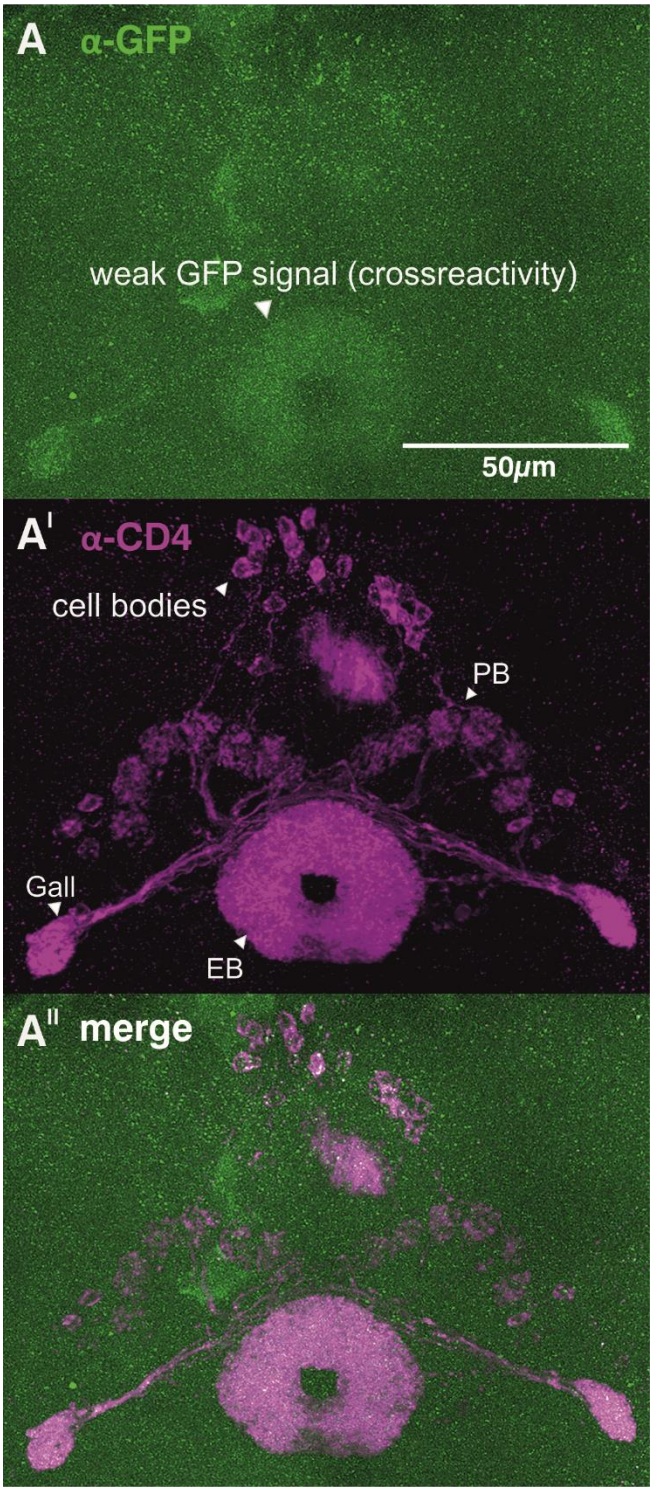

Figure 38: Split-GFP GRASP study of presynaptic R3 neurons and postsynaptic E-PG neurons (I)

The split-GFP system was used to visualise the synaptic connectivity between the presynaptic side determined to be the R3 neurons (VT42759-GAL4) using UAS-Synaptobrevin::spGFP$_{1-10}$ with Synaptobrevin as the presynaptic marker and the postsynaptic side determined to be the E-PG neurons (R60D05-LexA) using Lex$_{op}$-CD4::spGFP$_{11}$ with anti-CD4 as the whole-cell marker. The reconstituted GFP signal (stained with anti-GFP) reveals a synaptic connection in the pre-determined direction. The presumed postsynaptic neuron was labelled using the anti-CD4 antibody as a control staining. Refer to **Table 2** for the primary antibodies and **Table 3** for the secondary antibodies used in this protocol mentioned in **2.5.3**. Magnification: 63X. Step size: 0.33µm. Stack size: 160 slices.

(A) A faint GFP signal can be observed in the region of the EB and the Gall.
(A') The E-PG neurons (postsynaptic) were revealed using anti-CD4 (magenta), and include the entire EB along with the gall, the shells (glomeruli) of the PB and the respective cell bodies.
(A'') Overlap of the above two expression patterns.

The postsynaptic part, stained with anti-CD4 antibody in magenta (Figure 38A'), reveals the expression pattern of this E-PG neuron LexA driver (R60D05-LexA), consisting of the EB, the PB, and its respective cell bodies, similar to the expression pattern of the R19G02-GAL4 driver that was used earlier in this study

(Figure 35) to target these neurons. This ensures that their expression patterns do not differ largely and hence, could be used interchangeably for behaviour and immunohistochemistry studies.

When we took a look at the GFP signal, it was observed that the faint signal observed in the EB, and the gall (Figure 38A), were not a result of reconstituted GFP, but rather directly corresponds to the CD4 signal. We came to this conclusion because, the GFP signal was observed with equal strength in the EB and the gall. R3 neurons do not innervate the gall, therefore, there is no possibility for synaptic interaction in this region. Thus, the GFP signal observed in Figure 38A cannot be considered as a legitimate GRASP signal. This could be due to a possibility that the mouse anti-GFP antibody individually detects the GFP_{11} instead of strictly targeting the reconstituted GFP, as a result of which, the E-PG neuropil has been stained.

Moving on to the other direction of this GRASP study, the GAL4 and LexA lines now had to be interchanged to address the neurons in the opposite direction of synaptic connectivity. For this purpose, we used the R54B05-LexA (Xie et al., 2017) driver to specifically target R3 neurons as a postsynaptic partner. The same Lex(op)-CD4::GFP_{11} construct as in the previous experiment was used to drive the expression of the second part of the GFP protein. R19G02-GAL4 was used to drive the expression of UAS-Syb::GFP_{1-10} in the E-PG neurons.

The result that followed, was completely unexpected. As observed in Figure 39, there is a significantly strong GFP signal (Figure 39A). In this scenario, the R3 neurons act as the postsynaptic partners, which are on the receiving end of synaptic transmission from the E-PG neurons, which are supposedly presynaptic. This result was surprising for two reasons: 1) According to literature, there are no presynaptic projections belonging to the E-PG neurons that reside on the EB region (Wolff et al., 2015), and 2) R3 neurons, so far, are not known to have any presynaptic partners other than R2 neurons (Omoto et al., 2018), and other subtypes of the R3 neurons.

For the aforementioned reasons, this result was both interesting and intriguing. If the E-PG neurons indeed have only dendrites innervating the EB, this strong GRASP signal (Figure 39A) could not have been achievable. It is also worth mentioning that the intensity of the GFP signal obtained here, is much stronger than the one observed previously when the direction of synaptic connectivity was reversed (Figure 38A).

R19G02-GAL4>UAS-Syb::spGFP$_{1-10}$, R54B05-LexA>LexA(op)-CD4::spGFP$_{11}$

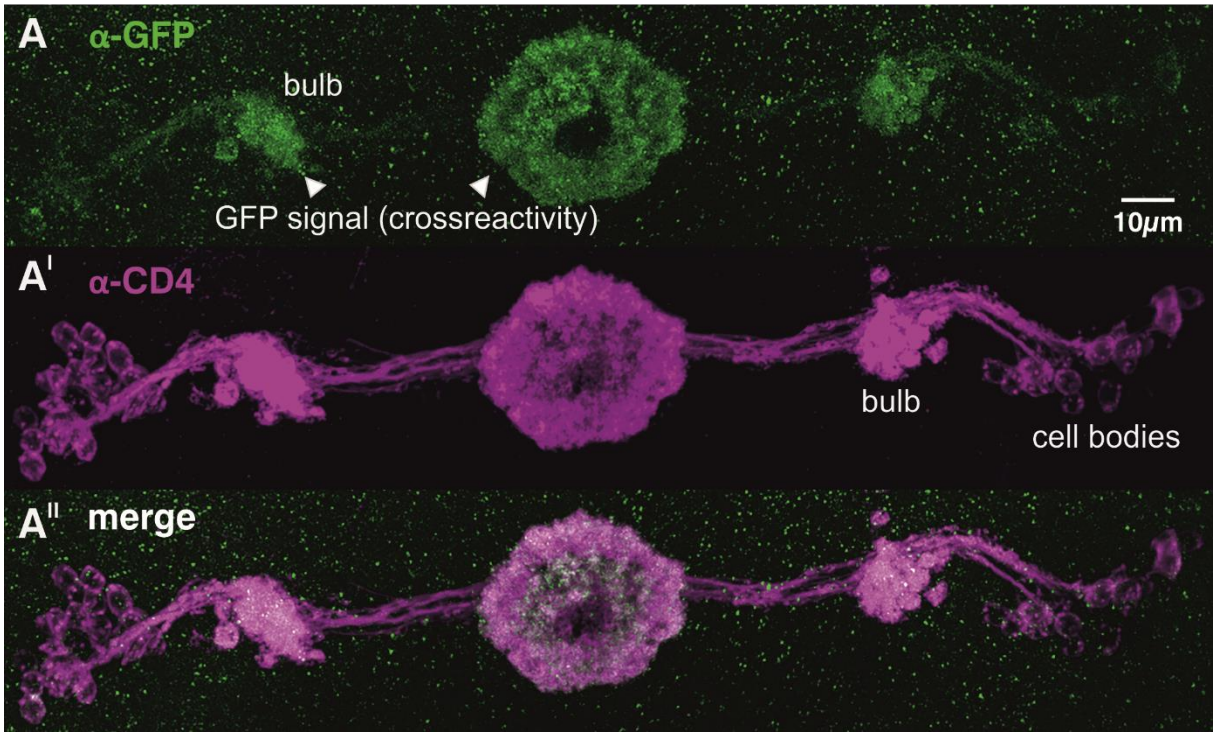

Figure 39: Split-GFP GRASP study of presynaptic E-PG neurons and postsynaptic R3 neurons (I)

The split-GFP system was used to visualise the synaptic connectivity between the presynaptic side determined to be the E-PG neurons (R19G02-GAL4) using UAS-Synaptobrevin::spGFP$_{1-10}$ with Synaptobrevin as the presynaptic marker and the postsynaptic side determined to be the E-PG neurons (R60D05-LexA) using Lex$_{op}$-CD4::spGFP$_{11}$ with CD4 as the whole-cell marker. The reconstituted GFP signal (stained with anti-GFP) reveals a synaptic connection in the pre-determined direction. The postsynaptic side was labelled using the anti-CD4 antibody as a control staining. Refer to **Table 2** for the primary antibodies and **Table 3** for the secondary antibodies used in this protocol mentioned in **2.5.3**. Magnification: 63X. Step size: 0.33μm. Stack size: 139 slices.

(A) A strong GFP signal was observed in the R3 neurons and in the bulb regions (cross-reactivity).
(A') The R3 neurons (postsynaptic) were revealed using anti-CD4 (magenta) which include the axons in the EB and dendritic projections into the bulb and cell bodies on either hemisphere.
(A'') Overlap of the above two expression patterns.

This would allude to the notion that the hypothesis laid out in literature so far, may not be entirely true, and that there might be synaptic input from both these neurons in both the directions. They have the potential of being each other's pre- as well as postsynaptic partners The anti-CD4 labelling of the R3 neurons (Figure 39A'), reveals the axonal regions of these neurons in the EB, and the dendrites bundled together in the bulbar regions, which eventually lead up to their individual cell bodies. It should be noted here that in Figure 39A, the GRASP signal is found not only in the EB neuropil, but also in the bulb regions. This is a contradiction to the concept of GRASP, since E-PG neurons do not have any innervation in the bulb region.

Thus, the GRASP signal in the bulb as well as in the R3 axons, must once again be a result of the anti-GFP antibody recognizing the GFP_{11}. Thus, the GFP signal observed in Figure 39A, can also not be considered as a legitimate GRASP signal. One of the ways to verify the validity of this GFP signal is by using an anti-GFP mouse antibody that specifically addresses GFP_{11}, which can then reveal whether the GFP signal observed in these GRASP experiments is the entire postsynaptic part, instead of the reconstituted GFP signal between the synaptic partners.

Oweing to the confusion created regarding the working of the anti-GFP antibody, we deemed the results obtained so far in this regard (Figure 38 and Figure 39), as questionable. Thereby, we took another approach, and decided to redo these experiments with a different presynaptic marker to verify whether our hypothesis that the R3 neurons and E-PG neurons have synaptic interaction, is indeed valid.

Neurexin, a marker of the presynaptic region (Ushkaryov et al., 1994), has been extremely useful in the realms of immunohistochemistry. Unlike Synaptobrevin, Neurexin is not acitivity-dependent and is located on the surface of the synaptic vesicle, thereby enabling a more readily visible GRASP signal. Thus, we decided to use a construct, where the Neurexin gene has been fused with GFP_{1-10}, in the form of a UAS transgene, capable of being expressed under the control of the respective GAL4 driver. Anti-CD4 was retained as the reliable whole-cell marker, and fused with the other part of the GFP (GFP_{11}), in the form of a Lex(op) construct, to maintain consistency across the GRASP experiments.

The direction of synaptic connectivity to be tested first, was with the R3 neurons as the presynaptic side, and the E-PG neurons as their postsynaptic partners. The driver lines used for these individual neurons, were the same as the ones used in the previous study (Figure 38). In contrast to the GFP signal observed in the previous complementary study (Figure 38A), where the signal was found all over the EB as a result of cross-reactivity of the anti-GFP antibody, the GRASP signal observed in Figure 40A was much stronger. The GRASP signal here, was also more specifically located in the region of the R3 axons, thereby leaving less room for an element of doubt about whether the synaptic interaction between these two neuronal groups exists. Thus, we can visually witness that the direction of synaptic

connectivity from the R3 neurons to the E-PG neurons definitely exists, as suggested in literature (Wolff et al., 2015).

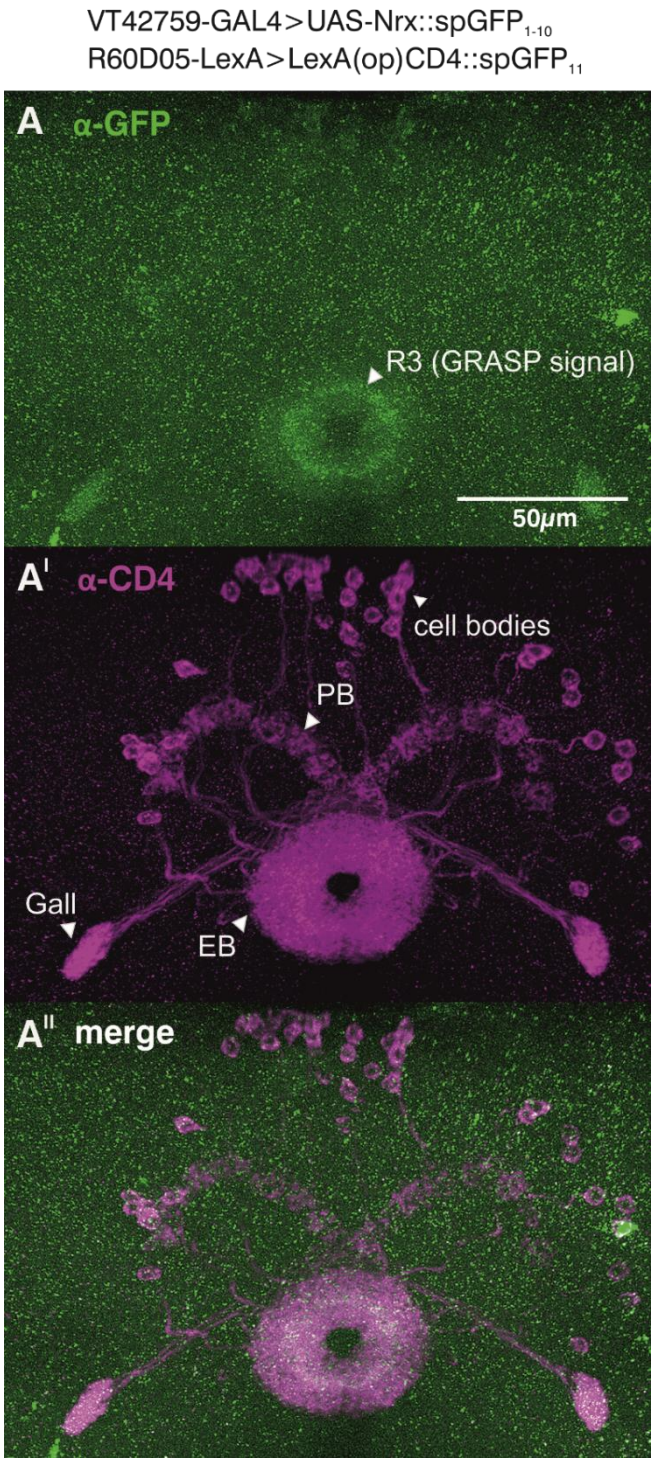

Figure 40: Split-GFP GRASP study of presynaptic R3 neurons and postsynaptic E-PG neurons (II)

The split-GFP system was used to visualise the synaptic connectivity between the presynaptic side determined to be the R3 neurons (VT42759-GAL4) using UAS-Neurexin::spGFP$_{1-10}$ with Neurexin as the presynaptic marker and the postsynaptic side determined to be the E-PG neurons (R60D05-LexA) using Lex$_{op}$-CD4::spGFP$_{11}$ with CD4 as the whole-cell marker. The reconstituted GFP signal (stained with anti-GFP) reveals a synaptic connection in the pre-determined direction. The postsynaptic side was labelled using the anti-CD4 antibody as a control staining. Refer to **Table 2** for the primary antibodies and **Table 3** for the secondary antibodies used in this protocol mentioned in **2.5.3**. Magnification: 63X. Step size: 0.33µm. Stack size: 275 slices.

(A) A fairly strong reconsitituted GFP signal can be observed in the region of the R3 region of the EB and also in the gall (crossreactivity).
(A') The E-PG neurons (postsynaptic) were revealed using anti-CD4 (magenta) include the entire EB along with the gall, the shells (glomeruli) of the PB and the respective cell bodies.
(A'') Overlap of the above two expression patterns where the region of the R3 neurons appears to have a higher intensity of the GFP signal than the rest of the EB.

The anti-CD4 signal representing the whole cell of the postsynaptic partner, on the other hand (Figure 40A'), is comparable to the previous experiment with the same control staining (Figure 38A'). Thus, the anti-CD4 staining could be counted as a reliable control staining when it comes to comparing Neurexin and Synaptobrevin

as effective presynaptic markers. The specificity of the GRASP signal being localised in the R3 neurons, is even more apparent in the merged version (Figure 40A"), where the GRASP signal overlaps with the inner layer of the anti-CD4 staining occupying the entire EB. Finally, to confirm the synaptic connectivity between R3 and the compass neurons, the experiment was repeated in the opposite direction, with R3 neurons (R54B05-LexA) as the postsynaptic partner, receiving input from the E-PG neurons (R19G02-GAL4), which were pre-determined to be presynaptic in this case.

The resultant GFP staining (Figure 41), was different from the one that was obtained the previous time with Syb as the presynaptic marker (Figure 39). To address each aspect of the staining individually, the GRASP signal obtained here (Figure 41A), was much brighter, with little to no background, proving the presence and legitimacy of the signal. The anti-CD4 signal representing the R3 ring neurons (Figure 41A'), stains for the inferior regions of the bulb (BUi), and the middle region of the EB neuropil, which is where the R3 neurons are located. This result solidifies the hypothesis that the R3 neurons are potential postsynaptic partners of the E-PG neurons, irrespective of what has been hypothesized so far regarding the direction of interaction between the two neuronal subtypes.

However, if we took a closer look at Figure 41A, it would be apparent that the GRASP signal is also observed in regions of the bulb in both hemispheres, a part of the CC not addressed by the E-PG neurons. This could once again be explained as a tendency of the GFP antibody's off-target staining pattern. Nonetheless, it should be acknowledged that the staining of the bulb region in this experiment (Figure 41A), has been highly significantly reduced in comparison to the previous case with Synaptobrevin as the presynaptic marker (Figure 39A). This might be because Neurexin is activity-independent, leading to a significantly stronger GRASP signal in the EB neuropil.

Thus, to summarize this section, it can be concluded that the trans-Tango experiments from Omoto and colleagues (Omoto et al., 2018), showed limited input from R3 to E-PG neurons, while our own showed no input from the E-PG neurons to the R3 neurons. Nonetheless, our GRASP experiments using Neurexin, showed that there is a strong input from the E-PG neurons to the R3 neurons, suggesting that trans-Tango potentially has its functional limitations when it comes to effectively addressing the EB neuropil.

R19G02-GAL4>UAS-Nrx::spGFP$_{1-10}$, R54B05-LexA>LexA(op)CD4::spGFP$_{11}$

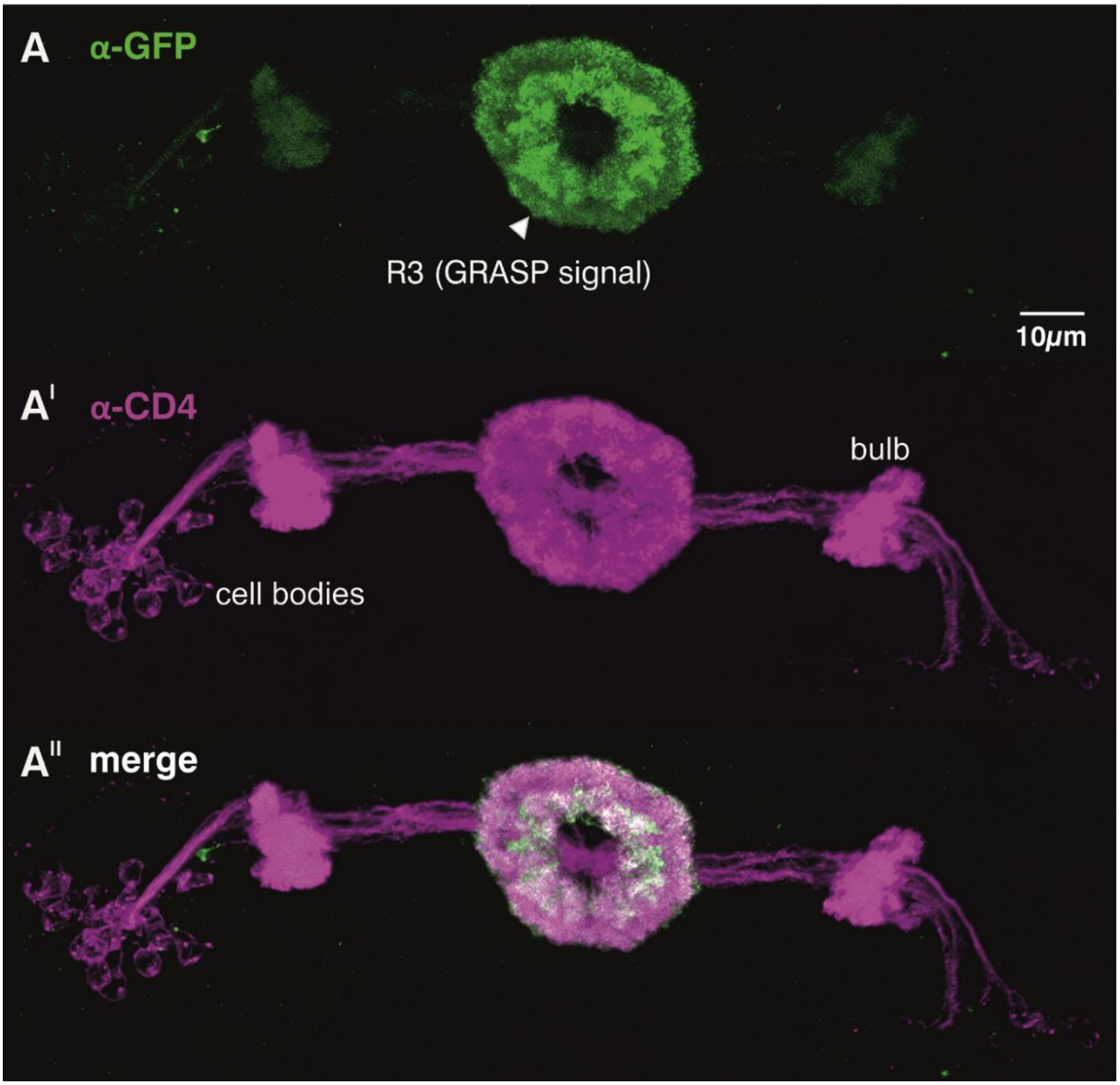

Figure 41: Split-GFP GRASP study of presynaptic E-PG neurons and postsynaptic R3 neurons (II)

The split-GFP system was used to visualise the synaptic connectivity between the presynaptic side determined to be the E-PG neurons (R19G02-GAL4) using UAS-Neurexin::spGFP$_{1-10}$ with Neurexin as the presynaptic marker and the postsynaptic side determined to be the R3 neurons (R54B05-LexA) using Lex$_{op}$-CD4::spGFP$_{11}$ with CD4 as the whole-cell marker. The reconstituted GFP signal (stained with anti-GFP) reveals a synaptic connection in the pre-determined direction. The postsynaptic side was labelled using the anti-CD4 antibody as a control staining. Refer to **Table 2** for the primary antibodies and **Table 3** for the secondary antibodies used in this protocol mentioned in **2.5.3**. Magnification: 63X. Step size: 0.33μm. Stack size: 133 slices.

(A) A strong reconstituted GFP signal was observed in the R3 neurons.
(A') The R3 neurons (postsynaptic) were revealed using anti-CD4 (magenta) which include the axons in the EB and dendritic projections into the bulb and cell bodies on either hemisphere.
(A'') Overlap of the above two expression patterns indicating a highly visible GFP signal in the R3 neurons of the EB.

3.2.4 Analysis of non-canonical ring neurons

Following the connectome analysis of the classical ring neurons, compass neurons, and shift neurons using TRPA1 activation and shibire^{ts1} inactivation studies, we were curious to address the recently discovered non-canonical ring neurons (Franconville et al., 2018). These neurons, which are one of the newer entries to the realm of the *Drosophila* CC, have been classified to have a GABAergic (inhibitory) input into the EB, which ultimately target the compass neurons (Franconville et al., 2018).

The results obtained in the earlier chapters of this study indicate that some of the ring neurons of the EB (Figure 30 and Figure 32), along with the compass neurons (Figure 31 and Figure 33), are both required for the functioning of detour memory in *Drosophila*. With that in mind, we proceeded to test each type of these non-canonical ring neurons, arising predominantly from the LAL, and the gall (GB) viz., 1). L-Ei (LAL to the EB inner region), 2) L-Em (LAL to the EB middle region), and 3) GB-Eo (Gall to the EB outer region) in the detour paradigm. Both activation, and inactivation experiments were performed for the aforementioned neurons as effective screening methods for connectome analysis.

3.2.4.1 TrpA1 activation of non-canonical ring neurons

As described in the previous sections, activation of neurons using TrpA1 by temperature modifications, has a potential effect in the perceiving of visual landmarks by the fly, oweing to the sudden increase in Ca^{2+} levels. Thus, each of the non-canonical ring neurons were tested using this method to identify if all, or none of them are required for the functioning of short-term visual orientation memory.

As depicted in Figure 42A, the L-Ei neurons (R75H04-GAL4), which innervate the LAL, and the inner region of the EB, seem to have an impact on detour memory when UAS-*TrpA1* is activating these neurons. This is interesting, since the inner region of the EB might contain both the R1, and the R3a (R3 anterior) neurons. If the L-Ei neurons innervate the inner region of the EB, then there is a possibility that they have synaptic connectivity with the ring neurons in this region. This result, hence, has to be verified using *shibire^{ts1}* inactivation studies, as well as through immunohistochemistry to identify the exact EB region targeted by this specific driver.

In addition, the GAL4 and UAS controls seem to behave like wild-type flies at both temperatures with very high median memory scores (Figure 42A).

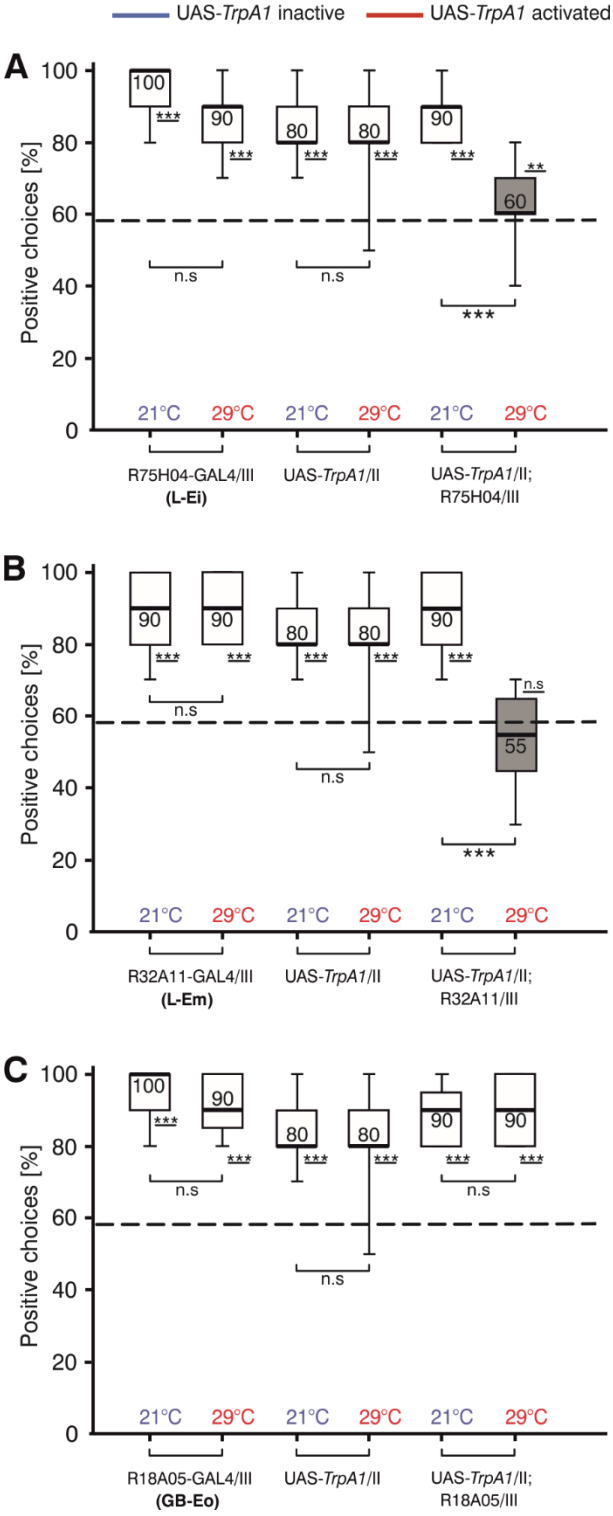

Figure 42: TrpA1 activation of non-canonical ring neurons

(A) The GAL4 control group (R75H04-GAL4/III, n=23) for the L-Ei neurons behaved like wild-type controls at both 21ºC (median=100%) and 29ºC (median=90%). The median memory scores of the flies in both temperatures were highly significantly different from the random chance level (58%) and not significantly different from each other. The UAS-control group (UAS-*TrpA1*/II, n=24) also showed a high memory score in both temperature conditions (median=80%) with the whiskers ranging between 50% and 100% when tested at 29ºC. The experimental group (UAS-*TrpA1*//II; R75H04-GAL4/III, n=24) had a wild-type like memory at 21ºC (median=90%) while the memory score reduced to 60% when tested at 29ºC and was highly significantly different from the chance level (58%) as well as the memory score of the same group tested at 21ºC.
(B) The GAL4 control group (R32A11-GAL4/III, n=24) of the L-Em neurons displayed wild-type like memory (median=90%) at both temperatures. The UAS control group was the same as described above. The experimental group (UAS-*TrpA1*//II; R32A11-GAL4/III, n=24) had a very highly significant difference between the memory scores when tested at 21ºC (median=90%) and at 29ºC (median=55%) where the latter was not significantly different from chance level.
(C) The GB-Eo neurons did not elicit a deficit in detour memory when UAS-*TrpA1* was activated at 29ºC (UAS-*TrpA1*//II; R18A05-GAL4/III, n=24) where the memory score (median=90%) was not significantly different from that of the same group at 21ºC. The experimental group also behaved similarly to the GAL4 control group (R18A05-GAL4/III, n=24) and the UAS control group (UAS-*TrpA1*/II, n=24) where the median memory scores of all the groups were highly significantly different from the chance level at both 21ºC and 29ºC.

Refer to **Table 39**, **Table 40**, and **Table 41** in **Appendix** for statistical analysis for paired-test (Wilcoxon matched-pair test), normality distribution (Shapiro-Wilk test) and comparison against random chance level (58%) (Sign/t-test).

The next set of neurons to be tested was the L-Em neurons (R32A11-GAL4), which was more interesting to us since the middle region of the EB is where the R3 neurons are located. Recent studies have shown that there is more than one subtype

of R3 neurons (Omoto et al., 2018). However, it would be telling to identify precisely which middle region of the EB is addressed by this L-Em driver (R32A11-GAL4), to speculate on the canonical ring neurons that might be innervating the same region. There is a complete loss of visual orientation memory when these neurons are activated using UAS-*TrpA1*, while the same flies perform like wild-type controls at 21°C when TrpA1 is not activating the neurons (Figure 42B). Thus, there was a highly significant difference in the memory score between the two groups. The individual GAL4, and UAS control groups behaved like wild-type flies with high median scores at both the temperatures, indicating that they were reliable controls with no leaky expression (Figure 42B).

Finally, the last group of non-canonical ring neurons to be tested using TrpA1 activation was the GB-Eo (R18A05-GAL4) neurons, addressing the outer regions of the EB, receiving inputs from the gall. The outer regions of the EB include the R2 neurons, the R4d (R4 distal), and R4m (R4 medial) neurons. Thus, if these neurons innervate the same regions as the canonical R2 or R4 neurons, they could have potential synaptic interactions with R2 and/or R4, which might have an effect on visual working memory, when manipulated with TrpA1.

However, the behavioural result observed here depicts that the activation of these neurons using TrpA1 did not cause any change in detour behaviour, compared to the memory of the same flies when tested at 21°C (Figure 42C). In the absence of TrpA1 activation, the flies behaved wild-type-like in both cases, indicating that the neurons addressed here might potentially interact with the R4 neurons, since the activation of both these neuronal subtypes did not affect visual working memory. The respective GAL4, and UAS controls behaved like wild-type flies as well, with high median memory scores, that were not significantly different from each other at both temperatures (Figure 42C). It is also intriguing that the activation of these neurons with TrpA1 did not elicit a negative effect on visual working memory since these neurons have been classified to have an inhibitory input into the E-PG neurons. Activation of these neurons should presumably lead to a more pronounced inhibition of the E-PG neurons, which have been shown to be necessary for visual working memory in both TrpA1 activation (Figure 31A) and shibire^{ts1} inactivation (Figure 33A) experiments.

3.2.4.2 Shibire^{ts1} inactivation of non-canonical ring neurons

Inactivation of the non-canonical ring neurons using temperature-sensitive *shibire^{ts1}* led to some interesting results, which supported the previously performed activation experiments using UAS-*TrpA1*. Inactivation of the L-Ei neurons (R75H04-GAL4) at 32ºC seemed to result in a reduction in detour memory (Figure 43A).

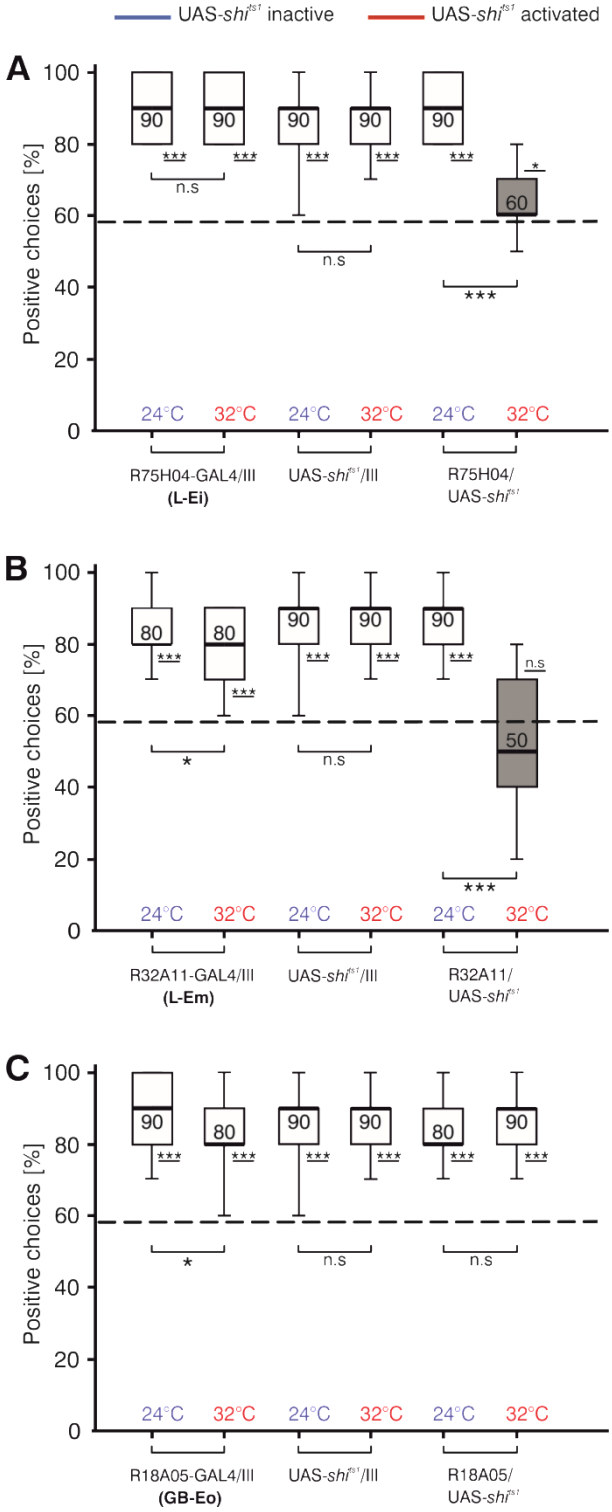

Figure 43: shibire^{ts1} inactivation of non-canonical ring neurons

(A) The GAL4 control group (R75H04-GAL4/III, n=23) for the L-Ei neurons behaved like wild-type controls at both 24ºC (median=100%) and 32ºC (median=90%). The median memory scores of the flies in both temperatures were highly significantly different from the random chance level (58%) and not significantly different between each other. The UAS-control group (UAS-*shi^{ts1}*/III, n=25) also showed a high memory score in both temperature conditions (median=90%) with the whiskers ranging between 60% and 100% when tested at 32ºC. The experimental group (R75H04-GAL4/UAS-*shi^{ts1}*, n=23) had a wild-type like memory at 24ºC (median=90%) while the memory score reduced to 60% when tested at 32ºC and was highly significantly different from the chance level (58%) as well as the memory score of the same group tested at 24ºC.
(B) The GAL4 control group (R32A11-GAL4/III, n=24) of the L-Em neurons displayed wild-type like memory (median=80%) at both 24ºC and 29ºC. The UAS control group was the same as described above. The experimental group (R32A11-GAL4/UAS-*shi^{ts1}*, n=25) had a very highly significant difference between the memory scores when tested at 24ºC (median=90%) and at 32ºC (median=50%) where the latter was not significantly different from chance level.
(C) The GB-Eo neurons did not elicit a deficit in detour memory when UAS-*shi^{ts1}* was activated at 32ºC (R18A05-GAL4/UAS-*shi^{ts1}*, n=26) where the memory score (median=90%) was not significantly different from that of the same group at 24ºC. The experimental group also behaved similarly to the GAL4 control group (R18A05-GAL4/III, n=26) and the UAS control group (UAS-*shi^{ts1}*/III, n=25) where the median memory scores of all the groups were highly significantly different from the chance level at both 24ºC and 32ºC.

Refer to **Table 50**, **Table 51** and **Table 52** in **Appendix** for statistical analysis for paired-test (Wilcoxon matched-pair test), normality distribution (Shapiro-Wilk test) and comparison against random chance level (58%) (Sign/t-test).

The GAL4 and UAS controls, on the other hand, exhibited wild-type like memory at both temperatures (Figure 43A), showing that there is no leaky expression of the UAS construct or off-target effect of the GAL4 driver. The inner region of the EB may include the R1 ring neurons, along with the anterior region of R3. Further probing using immunohistochemistry techniques is required to visualize the exact ring neuron system interacting with the L-Ei neurons addressed by this driver.

The L-Em neurons (R32A11-GAL4), innervating the middle region of the EB, when inactivated using *shibire*^{ts1} at 32°C, led to complete loss of short-term visual orientation memory, while performing like wild-type flies at 24°C (Figure 43B). The memory score of the flies, when these neurons were inactivated, was not significantly different from the random chance level (58%), while being highly significantly different from the score of the same group of flies when tested at 24°C. The GAL4, and UAS control groups performed like WT-CS flies, with high memory scores of 80%, and 90%, respectively. These EB middle neurons might possibly interact with one, or more subclasses of the R3 ring neurons. Immunohistochemistry studies should elucidate the location, and projection pattern of these neurons.

Finally, the GB-Eo neurons (R18A05-GAL4), arriving from the gall and into the outer regions of the EB, did not affect the visual working memory when inactivated at 32°C (Figure 43C). The memory scores were around 80%-90%, when these neurons were allowed to have regular synaptic transmission, and then inactivated using UAS-*shibire*^{ts1}. The GAL4 and UAS control scores remained high as well, indicating that the controls were reliable, and that these neurons are dispensable for the functioning of visual working memory.

3.2.4.3 Postsynaptic partners of non-canonical ring neurons

Two-thirds of the non-canonical ring neurons seemed to be of importance for the functioning of detour memory. In order to understand their exact location and projection pattern within the *Drosophila* brain, we decided to reveal their postsynaptic partners through the trans-Tango technique (Talay et al., 2017), which has already been used in our study to address the postsynaptic partners of compass neurons (Figure 36). We were also curious to visually observe whether the E-PG neurons are indeed the postsynaptic partners of these non-canonical neurons, as suggested by Franconville and colleagues (Franconville et al., 2018).

3.2.4.3 (a) L-Ei neurons

We decided to first target the L-Ei neurons, where the innervation pattern was presumed to be in the inner region of the EB, and the LAL. The whole cell of this extrinsic ring neuron (R75H04-GAL4), labelled with GFP (Figure 44A), came as a surprise to us for a number of reasons. The first one being the staining pattern observed in the EB, where, in addition to the inner region, the rings occupying the middle and outer regions were also addressed.

Secondly, it was unexpected that these neurons would have projections in the bulb regions, since their description clearly excludes any innervation in this site (Franconville et al., 2018), and strictly limits their projection arising from the LAL straight to the EB inner region. However, there is a bright GFP staining pattern in the microglomeruli of both the superior, and inferior bulbs (Figure 44A). Aside from these two puzzling elements, the presynaptic region was as expected, where cell bodies on either hemisphere branch their connections to the LAL, which extends its projections into the inner region of the EB, which then spreads out to the middle and outer regions (Figure 44A).

As for the postsynaptic partner stained with mCherry, the innervation pattern in the EB was specifically found in the middle region of the EB, where the axons of the R3d/p and R3m neurons are situated (Figure 44A'). The dendrites of these neurons were found specifically in the inferior bulb region (Figure 44A'), reinforcing the notion that the postsynaptic part potentially consists of a combination of R3d/p/m neurons. The cell bodies belonging to the postsynaptic neurons ranged from 15-20 in number on either hemisphere. The merged version (Figure 44A'), depicts how the postsynaptic region fits perfectly into the middle region of the EB, while being surrounded by the presynaptic part innervating almost the entire EB (stained with GFP). The above observation perfectly correlates with the deficit in detour memory when the L-Ei neurons were hyper-activated using *TrpA1* (Figure 42A) or inactivated using *shibire*^{ts1} (Figure 43A), since both these approaches potentially negatively affected the functioning of the R3 neurons, which are critical for this working memory. A DenSyt staining of these L-Ei neurons to discern between their presynaptic and postsynaptic regions, would answer more questions about its degree of similarity with the classical ring neurons.

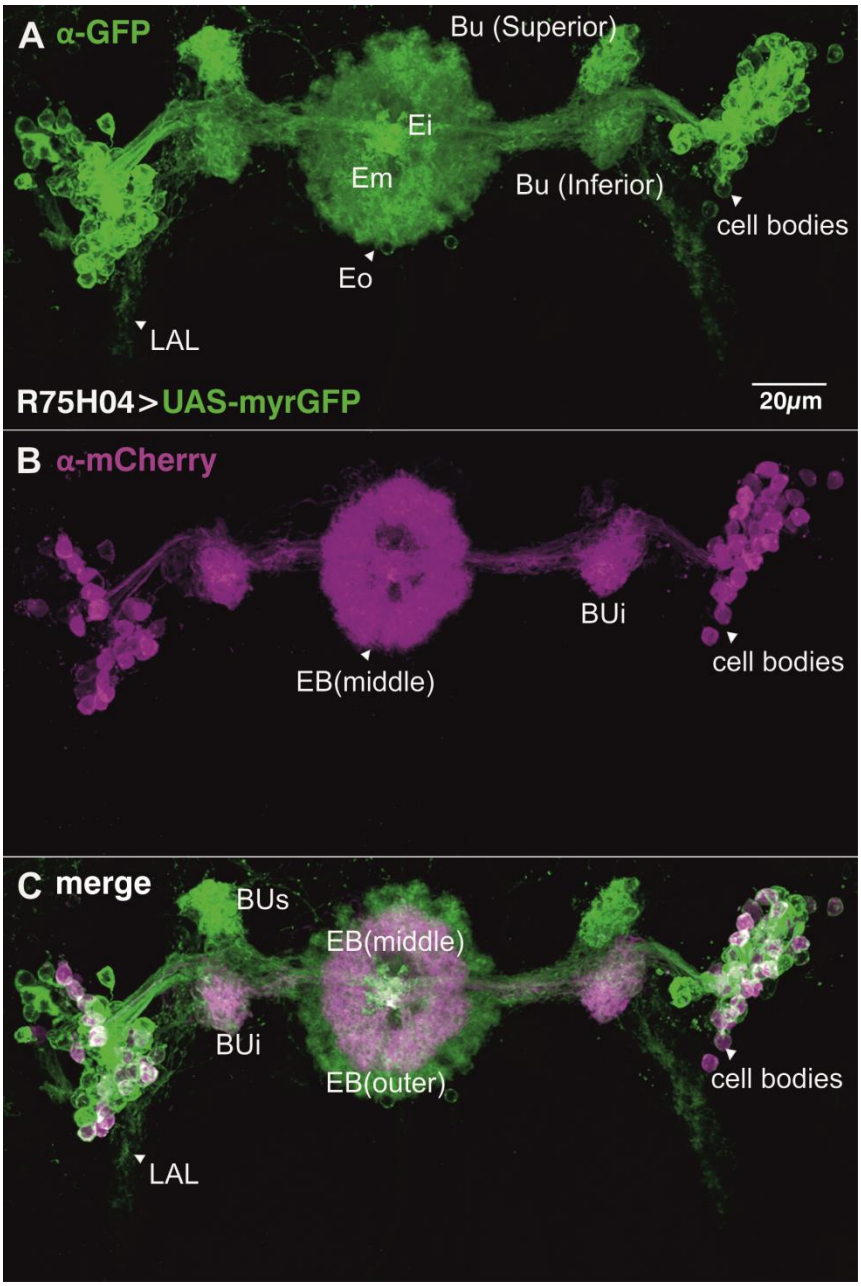

Figure 44: Analysis of postsynaptic partners of the L-Ei neurons

Visualisation of the expression pattern of L-Ei neurons (R75H04-GAL4) using UAS-myrGFP,QUAS-tdTomato(mCherry); trans-Tango was performed by following the protocol in section **2.5.1** where the whole cell is stained with anti-GFP (in green) and the postsynaptic partners are revealed using anti-mCherry (in magenta). Refer to **Table 2** for the primary antibodies and **Table 3** for the secondary antibodies used in this experiment. Magnification: 63X. Step size: 0.33µm. Stack size: 230 slices.

(A) The whole cell of the L-Ei neurons stained in green (anti-GFP) included 20-30 cell bodies on each hemisphere which extended its projections to the lateral accessory lobe (LAL), ellipsoid body inner (Ei), ellipsoid body middle (Em) and the ellipsoid body outer (Eo). The superior (BUs) and inferior bulb (BUi) regions also belonged to the presynaptic partner.
(B) The postsynaptic partner of L-Ei neurons were revealed to be approximately 20 cell bodies on each hemispehere which projected into the middle region of the EB, specifically in the region of the R3 neurons with the postsynaptic extensions into the region of the BUi.
(C) The merged version of the above two expression patterns revealing the location of the postsynaptic partner in the middle region of the EB in comparison to the presynaptic partner expressed in the entire EB.

3.2.4.3 (b) L-Em Neurons

Subsequently, we moved on to the set of non-canonical ring neurons where the inputs from the LAL are targeted towards the middle region of the EB (Franconville et al., 2018). The original literature describing these L-Em neurons did not address their postsynaptic partners or the neurons potentially targeted by these neurons. Hence, we were curious to uncover what their potential postsynaptic partners might be, especially since both hyper-activation with *TrpA1* (Figure 42B) and inactivation with *shibire*^{ts1} of these neurons (Figure 43B) led to severe impairment of the functioning of visual short-term orientation memory.

The whole cell (R32A11-GAL4) stained with GFP, consisted of presumably dendritic aroborizations in the LAL and extending their axons into the EB middle region (Figure 45A). The GFP signal in the EB resembles the axons of R1 and R3a neurons (Figure 45B) described in recent literature (Omoto et al., 2018). The most important aspect is that there are no innervations in the bulb, as mentioned in literature. They eventually converge into the cell bodies, which are approximately 15-20 in number on each hemisphere. We decided to look at the different parts of the neuropil separately to facilitate better analysis of the postsynaptic partners of these neurons (labelled with mCherry). In the EB middle region, a faint shadow of the magenta staining was observed (Figure 45B'). More interestingly, a single microglomerulus, presumably stained with mCherry was present in the inferior bulb region and had connections to the EBm region (Figure 45B'). This postsynaptic connection from the EB to the single BUi microglomerulus was seen arising from a single postsynaptic cell body (Figure 45C'). In addition to this exclusive postsynaptic cell, other postsynaptic cell bodies were also found, which overlapped with the presynaptic cell bodies that were stained with GFP on either hemisphere.

This hints that the L-Em neurons might indeed be their own potential synaptic partners, with no known targets outside of themselves (Franconville et al., 2018). Additionally, it would also explain the extreme deterring of detour memory in termperature-shift experiments (Figure 42B & Figure 43B), since both the presynaptic and postsynaptic parts of these neurons, potentially innervate the same regions in the EB, in proximity to the canonical R3 neurons, where this working memory essentially resides. This result therefore warrants a DenSyt staining to discern between the location of the presynaptic and postsynaptic regions of these neurons.

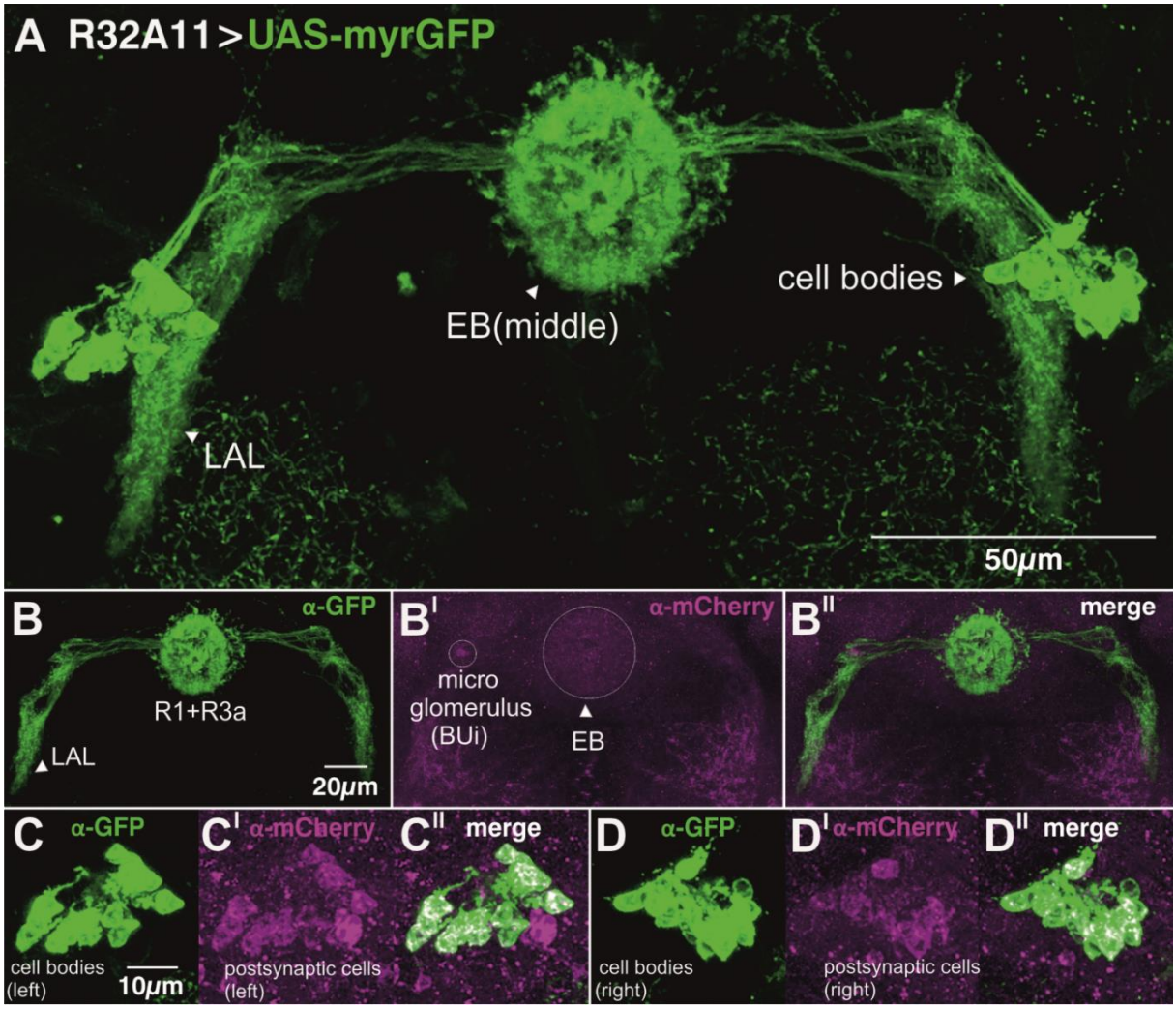

Figure 45: Analysis of postsynaptic partners of the L-Em neurons

Visualisation of the expression pattern of L-Em neurons (R32A11-GAL4) using UAS-myrGFP,QUAS-tdTomato(mCherry); trans-Tango was performed by following the protocol in section **2.5.1** where the whole cell is stained with anti-GFP (in green) and the postsynaptic partners are revealed using anti-mCherry (in magenta). Refer to **Table 2** for the primary antibodies and **Table 3** for the secondary antibodies used in this experiment. Magnification: 63X: Step size: 0.33μm. Stack size: 300 slices.

(A) The expression pattern of the whole cell of the L-Em neurons stained in green (anti-GFP), which included approximately 15 cell bodies on each hemisphere and the lateral accessory lobe (LAL) projecting into the middle region of the ellipsoid body (EB).
(B-B'') Expression pattern of L-Em neurons in the LAL and EB region. **(B)** The presynaptic partner appears to include the LAL along with innervations in the region of the R1 and R3a ring neuron families. **(B')** A faint shadow of mCherry staining was observed in the region pertaining to the middle region of the EB along with the staining of a single microglomerulus in the inferior bulb (BUi) region that seemed to have postsynaptic connections with the EB region. **(B'')** Overlap of the above two expression patterns.
(C-C'') Expression pattern of L-Em neurons in the cell bodies (left). **(C)** Approximately 15 cell bodies observed as those belonging to the presynaptic partner on the left hemisphere. (C') Approximately 10 cell bodies belonging to the postsynaptic partner with one cell body exclusively postsynaptic. (C'') Overlap of the above two expression patterns.
(D-D') Expression pattern of L-Em neurons in the cell bodies (right). **(D)** Approximately 15 cell bodies observed as those belonging to the presynaptic partner on the right hemisphere **(D')** Approximately 10 cell bodies belonging to the postsynaptic partner. **(D')** Overlap of the above two expression patterns.

3.2.4.3 (c) GB-Eo Neurons

The final group of non-canonical ring neurons described in recent literature (Franconville et al., 2018), are the GB-Eo (gall-ellipsoid body outer) neurons, where the input from the gall innervates the outer region of the EB. The inhibitory input is GABA-ergic and does not pertain to the bulb region. The outer region of the EB contains multiple families of ring neurons, including R2, R4(d&m), R5 and R6 neurons. Thus, we were curious to identify which part of the EB these neurons innervate, since literature suggests that they have inhibitory input into the E-PG neurons. From Figure 46A, it is seen that the whole cell (R18A05-GAL4) of these neurons (anti-GFP) consisted of two cell bodies on either hemisphere, which projected into the gall and the outer region of the EB. There was also presynaptic signal observed in the LAL region.

The postsynaptic partners of these neurons (anti-mCherry), did not involve any substructure of the CC, except for a faint shadow of the FB. The MB lobes also appeared to be stained with mCherry, albeit without any observable cell bodies pertaining to these structures (Figure 46B). This was reflected in the merged version (Figure 46C), where the presynaptic and postsynaptic partners were distinguishable from each other with no postsynaptic partners visible in the neuropil associated with the CC. This was an interesting result, as it potentially supports the behavioural result observed in the detour paradigm, where *TrpA1* activation (Figure 42C), and *shibire*^{ts1} inactivation (Figure 43C) of these neurons, proved to cause no defective detour memory phenotype.

It is imperative to mention that there were no E-PG neurons labelled by mCherry, which might once again insinuate that the trans-Tango technique is not entirely efficient when it comes to targeting the synaptic partners of neurons innervating the EB. A DenSyt staining of these neurons would reveal their respective pre/postsynaptic parts within the CC. Individual directional GRASP experiments with other specific neuronal subfamilies belonging to the CC, would presumably shed more light on the synaptic partners of these neurons.

In conclusion, the trans-Tango analysis of the non-canonical ring neurons (L-Ei, L-Em and GB-Eo) were not entirely conclusive, and would need further, more specific immunohistochemistry studies to reveal why some of them affect visual working memory in *Drosophila*, while others do not.

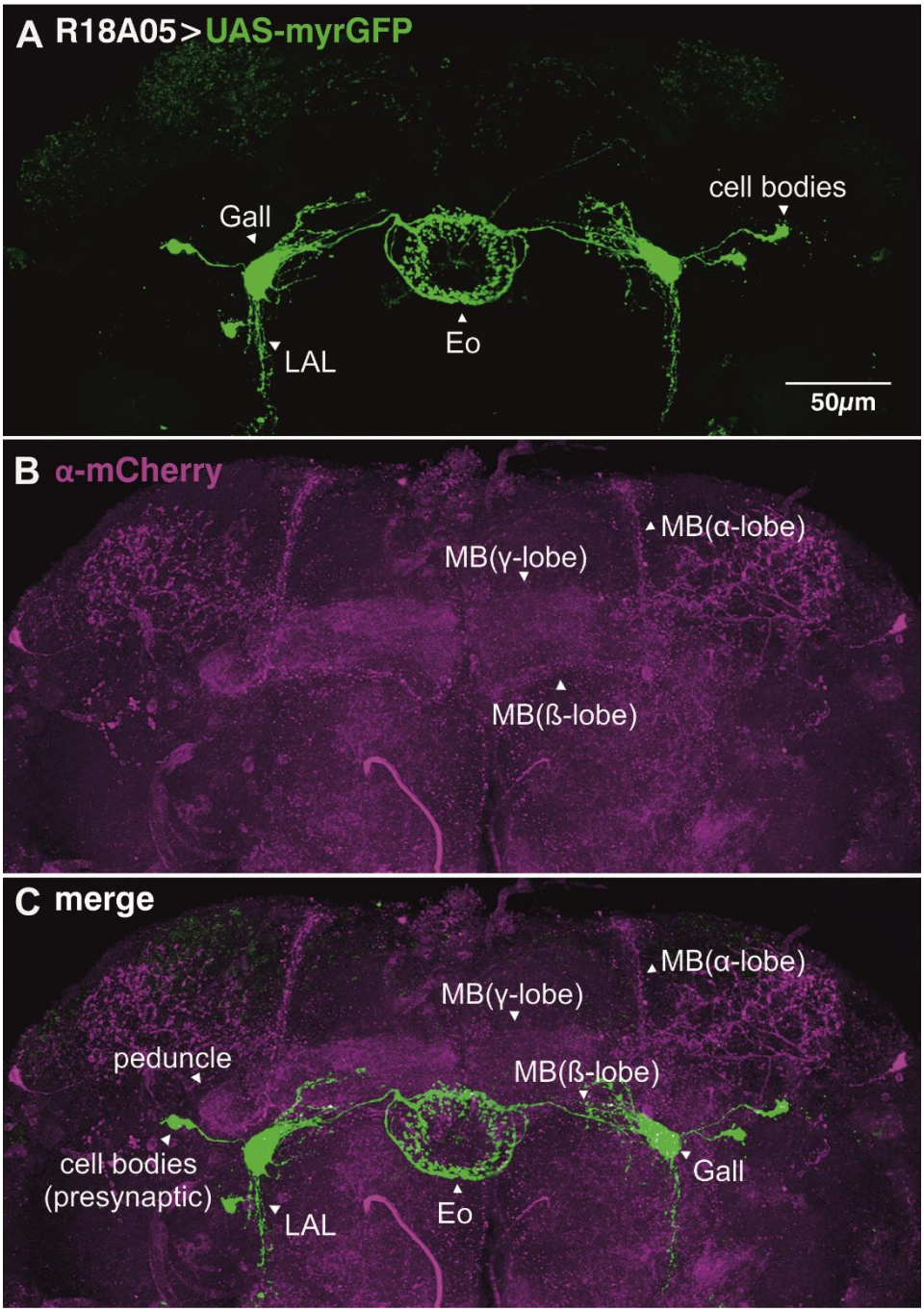

Figure 46: Analysis of postsynaptic partners of the GB-Eo neurons

Visualisation of the expression pattern of GB-Eo neurons (R18A05-GAL4) using UAS-myrGFP,QUAS-tdTomato(mCherry); trans-Tango was performed by following the protocol in section **2.5.1** where the whole cell is stained with anti-GFP (in green) and the postsynaptic partners are revealed using anti-mCherry (in magenta). Refer to **Table 2** for the primary antibodies and **Table 3** for the secondary antibodies used in this experiment. Magnification: 20X: Step size: 1.05µm. Stack size: 100 slices.

(A) Expression pattern of the GB-Eo neurons stained in green (anti-GFP) addressing 2 cell bodies on each hemisphere projecting into the LAL, gall and outer region of the ellipsoid body (EB). **(B)** No observable postsynaptic partners observed in the region of the central complex neuropil. Innervations observed in the Mushroom Body (MB) lobes. **(C)** Overlap of the above two expression patterns.

3.3 Importance of Tau protein in the functioning of short-term visual orientation memory in young and ageing flies

3.3.1 *Tau* in *Drosophila*

Recent literature in *Drosophila*, has shed light on the importance of APPL in visual working memory (Rieche et al., 2018). It is known that APPL and Tau are two of the key players of the pathology associated with AD. This made us question whether dTau also has a significant role to play in visual working memory.

Tau, a protein originally isolated from porcine brain, was recongized for its function of regulating microtubule assembly, by binding to tubulin dimers, and initiating their polymerization process to eventually form microtubules (Weingarten et al., 1975). Ever since the isolation of the Tau cDNA (Lee et al., 1988), its protein version, has been included in the family of microtubule-associated proteins (MAP), and the C terminal of the protein (known as the assemble domain), is crucial for its binding to microtubules (Lee et al., 1989). The specific repeat sequence on the Tau protein, which binds to tubulin, contains a ser^{262}, which, when hyperphosphorylated, can no longer efficiently bind to tubulin, ultimately leading to axonal destabilization, and collapsing of the cytoskeleton network (Biernat et al., 1993; Iijima et al., 2010).

Hyperphosphorylation of Tau, can also result in the formation of “neurofibrillary tangles” (NFT) (Alonso et al., 1996), which is a prime indicator or AD, along with the accumulation of amyloid beta (Aβ) peptide plaques in the brain. Thus, Tau has been given high importance in the realm of AD research, where pathologies involving the hyperphosphorylation of Tau, come under an umbrella of diseases collectively known as “Tauopathies”. Several kinases such as mitogen-activated protein kinase (MAPK) (Drewes et al., 1992), glycogen synthase kinase (GSK-3) (Mandelkow et al., 1992), and cyclin-dependent kinases (cdk) (Baumann et al., 1993), have been discovered to take part in the abnormal Alzheimer-like phosphorylation of Tau, leading to paired helical filaments (PHF) in the brains of patients suffering from AD.

Moving on to the role of Tau in *Drosophila* learning and memory, the earliest study expressing wild-type human and *Drosophila* Tau in the MB, revealed that the accumulation of both phosphorylated and unphosphorylated forms of Tau in the MB neurons, led to deficits in olfactory associative memory, and compromised

behavioural plasticity, without causing any morphological defects, or degeneration of the MB (Mershin et al., 2004). The studies following this one, had varied approaches towards Tau-related learning deficits, such as, the importance of sequential phosphorylation of ser on the Tau protein (Kosmidis et al., 2010; Papanikolopoulou and Skoulakis, 2015; Higham et al., 2019). Pseudophosphorylated Tau, also seemed to have severe detrimental effects on olfactory memory (Beharry et al., 2013). In another study, an interaction study between flies expressing mutant forms of *Ank2* (orthologue of human *Ank1*, usually methylated in patients with AD), and *Tau*, together, resulted in significantly reduced olfactory memory and degeneration of the photoreceptor neurons (Higham et al., 2019).

There have been conflicting schools of thought regarding the relevance of Tau protein in *Drosophila*. While some claim that the absence, or deletion of endogenous Tau causes no detrimental effects in flies (Burnouf et al., 2016), others have argued that RNAi-mediated knock-down of *Tau* can affect vision, oweing to the loss of photoreceptors, accompanied by an onset of neurodegeneration in *Drosophila* (Bolkan and Kretzschmar, 2014). Over the years, several studies have come to light, defending the requirement of Tau in *Drosophila*, by focussing on the importance of Tau-mediated microtubule and actin-cytoskeleton stabilization (Nam, 2016; Talmat-Amar et al., 2018; Papanikolopoulou et al., 2019). Thus, with the knowledge that we have gathered about Tau in regards to learning, memory, and vision, we decided to apply it in our own detour paradigm, to discover how Tau may, or may not affect visual working memory in young and aged flies.

3.3.2 Effect of *Tau* Knock-outs on visual working memory in *Drosophila*

One of the preliminary tests we performed, was to test for the effect of eliminating Tau activity in young flies. We achieved this by using flies with the *Tau* gene knocked-out using the classical recombination technique ($dTau^{KO}$ (Burnouf et al., 2016)), and compared their performance to those flies in which the *Tau* gene has been deleted using the latest CRISPR/Cas9 technique ($dTau^{del}$; D.Kretzschmar lab). It should also be mentioned that although created in very different backgrounds, both these mutants were crossed into WT-CS (white plus) backgrounds for our experiments. The WT-CS flies were always used as the control group. The $dTau^{KO}$ flies have been reported to have no phenotype when it comes to lifespan, and climbing behaviour (Burnouf et al., 2016).

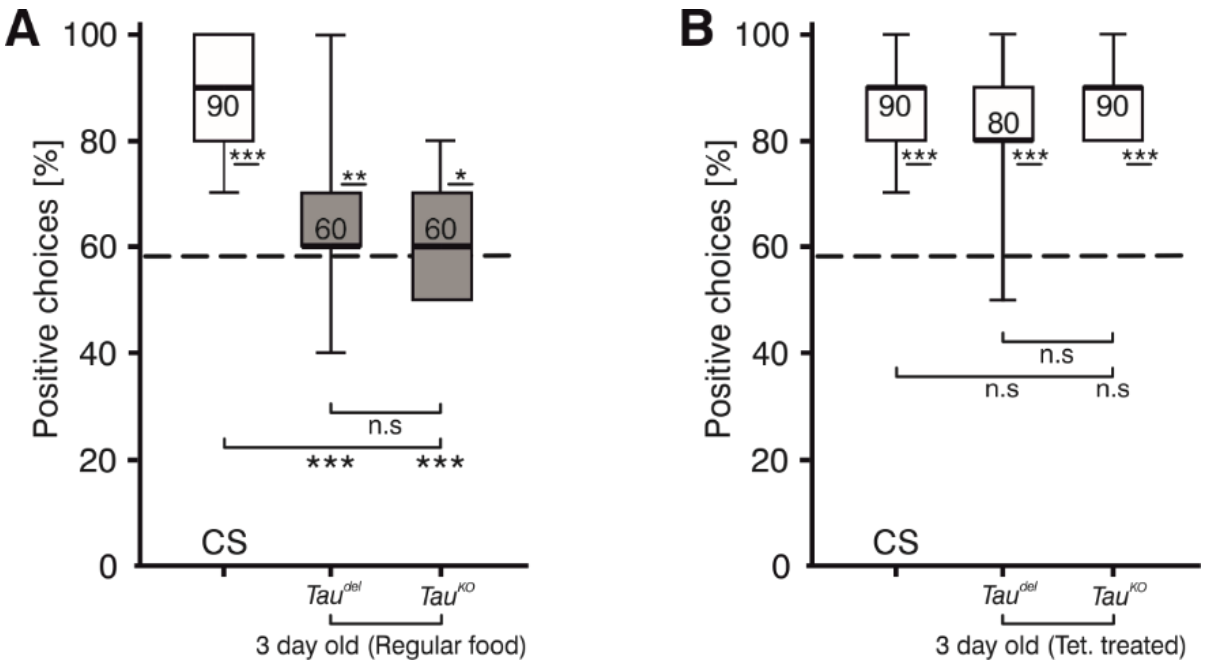

Figure 47: Short-term visual orientation memory in young homozygous *Tau* deletion/knock-out mutants

(A) Regular food: Homozygous deletion (*Tau*^{del}, n=25*)* and knocking-out of *Tau* (*Tau*^{KO}, n=25) led to a complete loss of detour memory where both mutant groups (3 day old) had a median memory score of 60% that was not significantly different from random chance level (58%). They were also very significantly different from the WT-CS control group (n=25) which displayed a high memory score (median=90%) that was very highly significantly different from chancel level (58%). **(B) Tetracycline-treated food:** The 3-day-old mutant flies raised on tetracycline food exhibited a memory that was comparable to that of the wild-type control group (n=25). The homozygous *Tau* deletion mutant (*Tau*^{del}, tet. Treated, n=25) had a median memory score of 80% while the homozygous *Tau* knock-out mutant (*Tau*^{KO}, tet. Treated, n=25) had a memory score of 90%. Both mutant groups performed very highly significantly differently from the chance level (58%).

Refer to **Table 53** and **Table 54** in **Appendix** for statistical analysis for multiple comparison (Kruskal-Wallis test), normality distribution (Shapiro-Wilk test) and comparison against random chance level (58%) (Sign/t-test).

However, as observed here (Figure 47A), both, the homozygous *Tau* knock-outs, as well as the deletion mutants that were raised on regular food, and tested three days after eclosion, displayed a median memory score that was significantly lower than the control group (Figure 47A). This was a surprise because, we did not expect the Tau protein to have such a pronounced effect on the visual working memory of young flies, since Burnouf and colleagues stated in their work that the loss of Tau protein has no detrimental effects in flies. Hence, we pondered whether this could be the effect of an infection or deficiency plaguing these flies, thereby hampering their behavioural output.

One of lines of treatments for infections that has been found to be effective across all species (including *Drosophila*), is the usage of tetracycline (Chopra and Roberts, 2001). When the same genotypes seen in Figure 47A were raised on food containing a stipulated concentration of tetracycline, and the male offsprings from the F1 generation were tested three days after eclosion, the results were astonishing. The median memory scores for the *Tau* knock-outs as well as the deletion mutants were increased to a level, comparable to that of the WT-CS control group (Figure 47B).

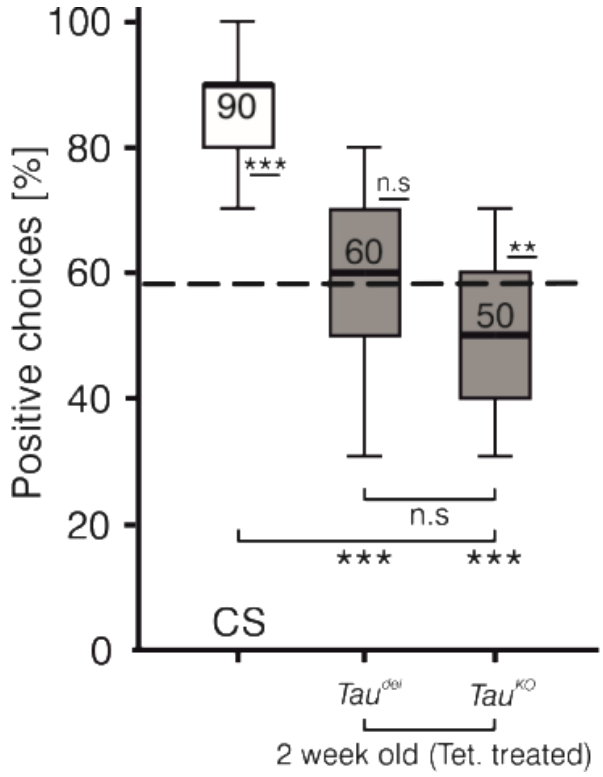

<u>Figure 48</u>: Short-term visual orientation memory in 2-week-old homozygous *Tau* deletion/knock-out mutants

Homozygous *Tau* deletion mutant flies (Tau^{del}, tet. treated, n=25) had a complete loss of detour memory (median=60%) after 2 weeks of ageing on tetracycline-containing food. The memory score was not significantly different from chance level. The homozygous *Tau* knock-out mutants (Tau^{KO}, tet. treated, n=25) also displayed a complete loss of visual orientation memory as well as turn compensation (median=50%). The memory score was highly significantly lower than the chance level (58%). Both the mutant groups were highly significantly different from the 2-week-old WT-CS control group (n=25) with a high median memory score of 90% which was highly significantly different from chance level (58%).

Refer to **Table 55** in **Appendix** for statistical analysis for multiple comparison (Kruskal-Wallis test), normality distribution (Shapiro-Wilk test) and comparison against random chance level (58%) (Sign/t-test).

Since the tetracycline treatment had a huge impact on the working memory of these flies, all the ageing studies pertaining to these flies (Tau^{KO} and Tau^{del}), from this point onwards, were carried out on food containing tetracycline, to observe whether the memory was impaired in these flies in the later stages of their life. To our surprise, the loss of Tau severely impaired the functioning of visual working memory in the two-week-old, homozygous *Tau* knock-out (Tau^{KO}), and deletion (Tau^{del}) mutants, that were raised on tetracycline food throughout their life. Their median memory scores were highly significantly different from the WT-CS control group, but not significantly different from random chance level. In fact, the knock-out flies that

were generated using homologous recombination (Burnouf et al., 2016), appeared to have lost even their turn compensation (Figure 48). This reveals that despite the treatment with tetracycline, the flies lacking the whole Tau protein, tend to experience a complete loss of memory with ageing, which in this case, was after 14 days of ageing after eclosion.

After discovering that homozygous *Tau* knock-out flies suffered severely in terms of visual working memory after a period of 14 days, we were determined to examine if the same effect would be true for the heterozygous mutants. Since heterozygous mutants would have half the amount of functional Tau protein remaining, we were interested to know how their memory would be impaired with ageing.

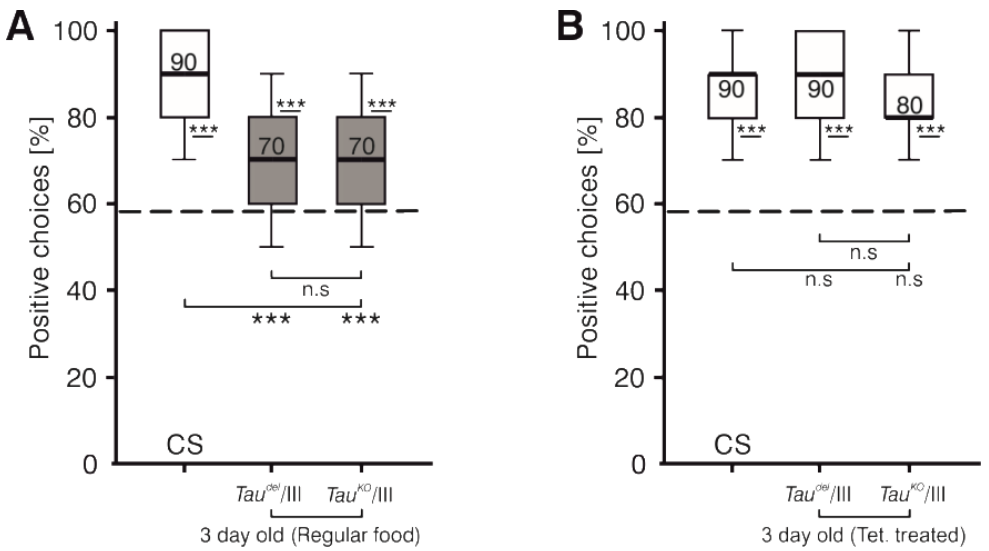

<u>Figure 49</u>: Short-term visual orientation memory in young heterozygous *Tau* deletion/knock-out mutants

(A) Regular food: The detour memory of 3-day old heterozygous *Tau* deletion flies (Tau^{del}/III, n=25) had a partial loss of detour memory (median=70%). The median was very highly significantly different from the chancel level as well as the 3-day-old WT-CS control group (n=25) which had a high memory score of 90% which was also very highly significantly different from the chance level (58%). The 3-day old heterozygous *Tau* knock-out mutants (Tau^{KO}/III, n=25) also performed similarly (median=70%) where the memory score was very highly significantly different from the WT-CS control group as well as the chance level. **(B) Tetracycline-treated food:** 3-day-old heterozygous *Tau* mutant flies had a wild-type like memory where both groups were very highly significantly different from the chance level (58%). The *Tau* deletion mutants (Tau^{del}/III, tet. treated, n=25) had a median memory score of 90% and the *Tau* knock-out mutants (Tau^{KO}/III, tet. treated, n=25) had a memory score of 80% and were both comparable to the memory score of the WT-CS control group (n=25).

Refer to **Table 56** and **Table 57** in **Appendix** for statistical analysis for multiple comparison (Kruskal-Wallis test), normality distribution (Shapiro-Wilk test) and comparison against chance level (58%) (Sign/t-test).

In addition, we were curious to observe whether tetracycline has similar effects in heterozygous *Tau* knock-out flies as well. As seen here (Figure 49A), the young heterozygous *Tau* knock-out flies (both Tau^{KO}/III and Tau^{del}/III), raised on regular food, performed poorly in the detour arena, exhibiting a definite deficit in visual working memory, in comparison to the WT-CS control group. In parallel, the heterozygous mutants from the F1 progeny of parents that were crossed and maintained on tetracycline food, exhibited a detour memory similar to that of the WT-CS control group (Figure 49B). Once again, tetracycline proved to have an effect in improving their detour memory, and was thus incorporated in the food on which these heterozygous *Tau* mutants were aged.

We carried on with the ageing process of the heterozygous *Tau* knock-out flies on tetracycline food and tested their detour memory once again, after a period of two weeks. As shown here (Figure 50A), both the heterozygous groups (Tau^{del}/III and Tau^{KO}/III) seemed to have lost their visual working memory, in comparison to when they were three days old. However, their memories were not completely lost, despite their median memory scores ranging around 70% (Tau^{del}/III), and 60% (Tau^{KO}/III), as they were still significantly different from the random chance level of 58%.

Thus, we decided to age these flies for a week more to investigate whether any further deterioration could be observed in visual working memory. Sure enough, after twenty-one days (3 weeks) of ageing, the heterozygous *Tau* knock-out flies had completely lost their visual working memory, and were now making choices in the detour arena as a result of random behavior (Figure 50B). Additionally, the flies where the *Tau* gene was knocked-out as a result of homologous recombination (Tau^{KO}/III), even lost their turn compensation since their median memory score was now reduced to 50%.

In summary, complete (homozygous knock-outs) or partial (heterozygous knock-outs) loss of Tau protein, leads to the loss of short-term visual orientation memory in *Drosophila*. And although tetracycline could ameliorate this effect in young flies, the process of ageing eventually caught up with these Tau deficient flies, leading to significant loss of memory (Figure 50), and in some cases, even turn compensation (Figure 50B). Following this lead, our next objective, was to examine whether mutant forms of the *Tau* gene in the form of splice variants would have the same effect as the *Tau* knock-outs on visual working memory in *Drosophila*.

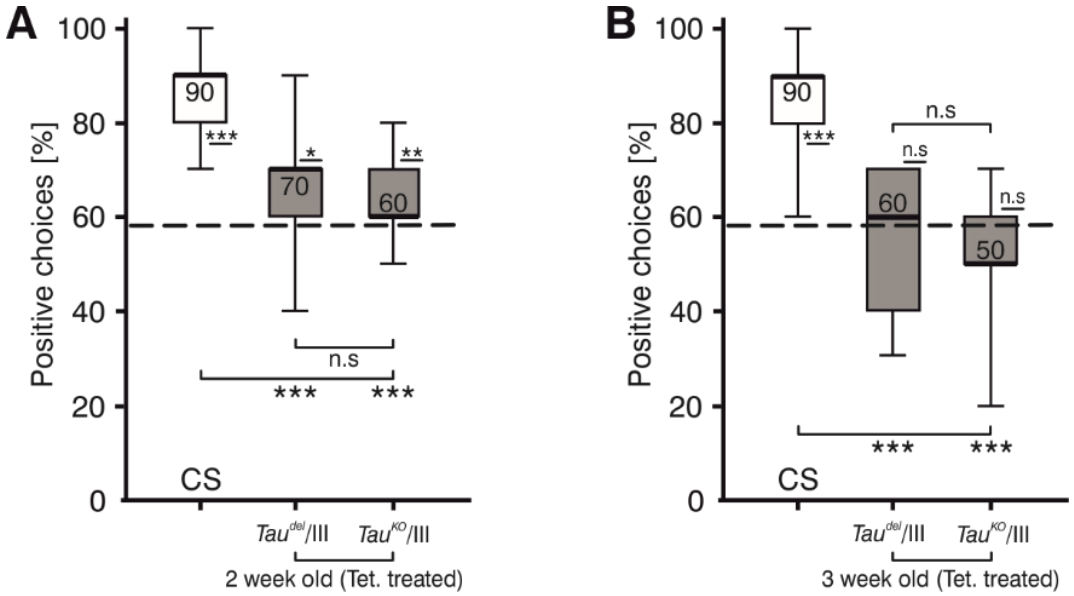

Figure 50: Short-term visual orientation memory in aged heterozygous *Tau* deletion/knock-out mutants

(A) The detour memory of 2-week-old heterozygous *Tau* deletion flies (Tau^{del}/III, tet. treated, n=25) had a partial loss of detour memory (median=70%). The memory score was significantly different from the chancel level as well as the memory of 2-week-old WT-CS-control group (n=25) which had a high memory score of 90% that was very highly significantly different from the chance level (58%). The 2-week-old heterozygous Tau knock-out mutants (Tau^{KO}/III, tet. treated, n=25) also performed similarly (median=60%) where the memory score was significantly different from the WT-CS control group as well as the chance level. **(B)** 3-week-old heterozygous *Tau* mutant flies had a complete loss of detour memory where they both had no statistically significant difference from the chance level (58%). The *Tau* deletion mutants (Tau^{del}/III, tet. treated, n=25) had a median memory score of 60% and the *Tau* knock-out mutants (Tau^{KO}/III, tet. treated, n=25) had a memory score of 50% and were both very highly significantly different from the WT-CS group (n=25).

Refer to **Table 58** and **Table 59** in **Appendix** for statistical analysis for multiple comparison (Kruskal-Wallis test), normality distribution (Shapiro-Wilk test) and comparison against random chance level (58%) (Sign/t-test).

3.3.3 Effect of *Tau* variants on visual working memory in *Drosophila*.

Aberrant Tau protein aggregation has been associated with a number of neurodegenerative disorders, one of them being fronto-temporal dementia and parkinsonism linked to chromosome 17 (FTDP-17). After genetic linkage analysis revealed that the *hTau* gene was related to this disease (Clark et al., 1998), it was demonstrated that missense mutations in *hTau*, created differential impairments of the Tau protein (Hong et al., 1998).

There have been six variants of the human Tau protein that have been observed as a result of alternative mRNA splicing of one gene (Goedert et al., 1989). These mutations, mostly occurring in exons 10 and 12, lead to an increase in the ratio of four-repeat *Tau* isoforms (4R), which have been previously associated with

reduced ability for microtubule binding. In this study, we will be addressing three of them (*hTau*^{K269I}, *hTau*^{P301L} and *hTau*^{V337M}), which have all been found to elicit detrimental effects in the context of microtubule assembly and toxicity. *hTau*$^{K/I}$ leads to reduction in microtubule assembly (Neumann et al., 2001), *hTau*$^{P/L}$ has been shown to increase beta sheet formation and aggregate-mediated toxicity *in vitro* (von Bergen et al., 2001), and *hTau*$^{V/M}$ has exhibited heightened hyperphosphorylation of Tau, eventually leading to Tau-related dementias (Alonso et al., 2004).

After observing the effects of loss of Tau in the functioning of short-term visual orientation memory in the previous section, we decided to test one of the various splice forms of human *Tau* (*hTau1N4R* ie., *hTau*^{WT}) in *Drosophila*, generated using the CRISPR/Cas technique (Lin et al., 2015). In this line, the same strategy was employed, as in case of the *dTau*^{del} mutant, but a construct offering the human cDNA for homologous end repair, was added. Thus, the endogenous *dTau* gene was replaced with the *hTau1N4R* in case of the wild-type control, and the variant mutants were created by inserting hTau1N4R with respective mutations into the fly genome in place of the *dTau* gene, and replacing coding exons with the respective cDNAs. All of the *hTau* variants were compared against *hTau*^{WT}, and an additional WT-CS control group.

We decided to first study their effect on detour memory in young flies (3-day old), homozygous for their respective splice forms. They were raised in parallel on regular and tetracycline food, oweing to the disparity in results that was observed in the *Tau* knock-out and deletion mutants.

In case of the flies raised on regular food, the WT-CS, and the *hTau*^{WT} flies, both showed a high detour memory score, statistically indistinguishable from each other (Figure 51A). The mutant variants on the other hand, showed memory deficits even at a young age, reflecting the hypothesis that the Tau protein might be required for the functioning of detour memory early on in *Drosophila* (Figure 51A). It is also worth noting that in one of the splice variants, the memory score was not significantly different from random chance level, hinting at a complete loss of memory in the flies (*hTau*$^{K/I}$). To our surprise, the homozygous *Tau* variants that were treated with tetracycline, also displayed a loss of memory, that was very highly significantly different from that of the *hTau*^{WT} and the WT-CS control groups (Figure 51B).

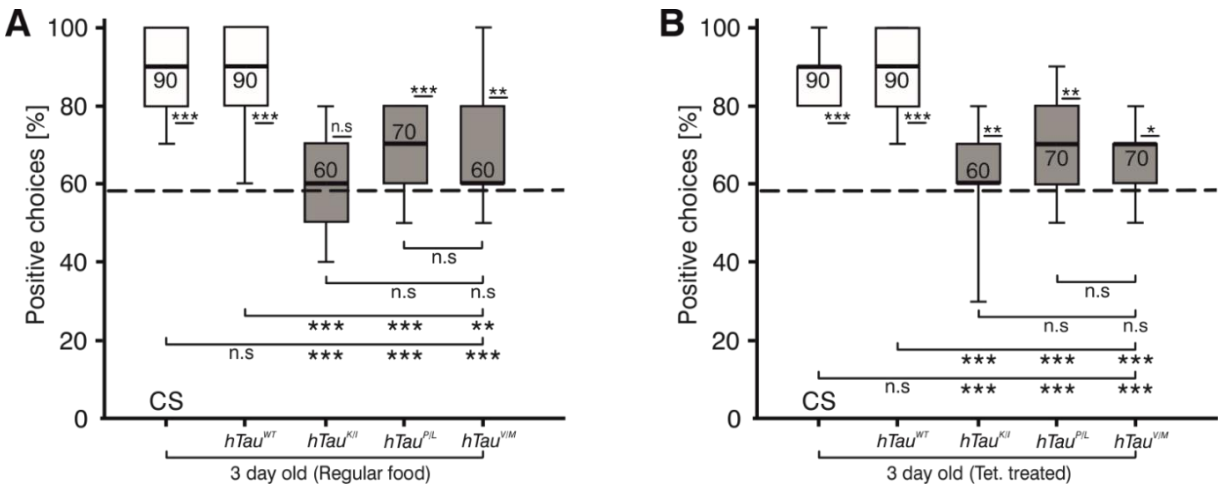

Figure 51: Short-term visual orientation memory in young homozygous CRISPR/Cas-generated *Tau* variants

(A) Regular food: The 3-day-old homozygous *Tau* variant flies displayed defective detour memory in comparison to the WT-CS (n=25) control group as well as the $hTau^{WT}$.(n=25) group where both groups had a high median memory score of 90% and were highly significantly different from chance level (58%). The $hTau^{K/I}$ (n=25) appeared to be the most affected genotype with a complete loss of memory phenotype (median=60%) where the memory score was not significantly different from the random chance level. The $hTau^{P/L}$ (n=25) variant exhibited an intermediate memory phenotype (median=70%) where the memory score was highly significantly different from the chance level as well as the control groups. The $hTau^{V/M}$ variant (n=25) also exhibited intermediate memory (median=60%) where the memory score was highly significantly different from the control groups as well as the chance level.
(B) Tetracycline-treated food: the 3-day-old homozygous *Tau* variants (including the $hTau^{WT}$ control group) led to similar results as that observed when they were raised and maintained on regular food. WT-CS (tet. treated, n=25) and $hTau^{WT}$ (tet. treated, n=25) both behaved wild-type like with a high median memory score of 90% and were highly significantly different from the random chance level (58%). The memory score (median=60%) of $hTau^{K/I}$ (tet. treated, n=25) was highly significantly different from the control groups as well as the chance level where the whiskers spanned across a wider range (30%-80%) of positive choices. The $hTau^{P/L}$ (tet. treated, n=25) also performed with intermediate memory (median=70%) where the box was spread across a range of 60-80% of positive memory choices. This led to the memory score being highly significantly different from the chance level and the control groups alike. The median memory score of $hTau^{V/M}$ (tet. treated, n=23) was at 70%, significantly different from the chance level and very highly significantly different from the WT-CS and $hTau^{WT}$ control groups.

Refer to **Table 60** and **Table 61** in **Appendix** for statistical analysis for multiple comparison (Kruskal-Wallis test), normality distribution (Shapiro-Wilk test) and comparison against random chance level (58%) (Sign/t-test).

The median memory scores of the variants ranged between 60-70%, which is a definite indicator of a loss of memory phenotype. This was proof that tetracycline does not interfere with the function of Tau in the *Tau* variants in the same way that it did in the *Tau* knock-out and deletion mutants in terms of visual working memory.

Since FTDP-17 is a dominant trait, we decided to carry out the remaining experiments with the heterozygous *Tau* variants, by raising them on regular food. As observed in Figure 52, the heterozygous *Tau* variants were able to perform with a memory as high as that of the WT-CS and the heterozygous human wild-type *Tau*

(*hTau*^{WT}/III) control groups. The *hTau*$^{K/I}$/III and *hTau*$^{P/L}$/III groups had a median of 90%, which was highly significantly different from random chance level.

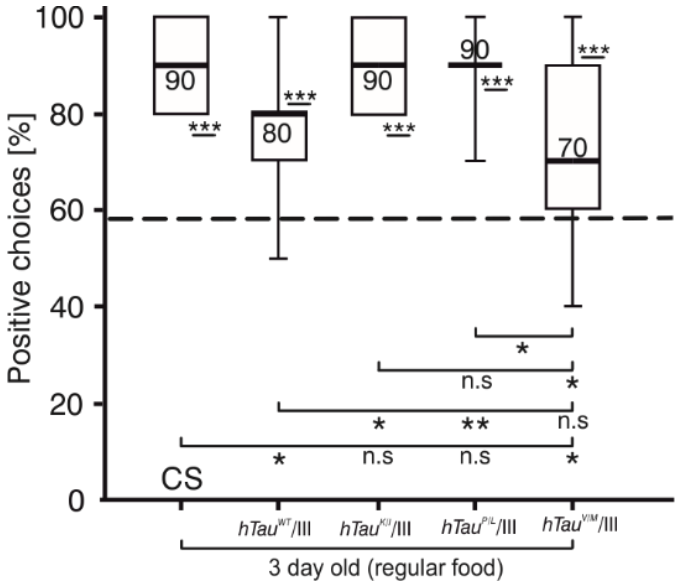

<u>Figure 52</u>: Detour memory in young heterozygous CRISPR/Cas-generated *Tau* variants

The 3-day-old heterozygous *Tau* variants *hTau*$^{K/I}$/III (n=25) and *hTau*$^{P/L}$/III (n=25) performed like wild-type flies with both having a median memory score of 90% that was not significantly different from the WT-CS (n=25) control group (median=90%). The *hTau*^{WT}/III (n=25) had a memory score (median=80%) that was significantly different from WT-CS memory score and very highly significantly different from the chance level (58%) albeit having whiskers that ranged between 50%-100%. The *hTau*$^{V/M}$/III (n=25) had an intermediate memory score (median=70%) which was significantly different from the WT-CS as well as the chance level with the box ranging between 60%-95% positive choices.

Refer to **Table 62** in **Appendix** for statistical analysis for multiple comparison (Kruskal-Wallis test), normality distribution (Shapiro-Wilk test) and comparison against random chance level (58%) (Sign/t-test).

The *hTau*$^{V/M}$/III group on the other hand, showed a slightly reduced median score of 70%, which was significantly different from the WT-CS group, but not the *hTau*^{WT}/III group. Thus, V/M was the only variant, which revealed an early dominant phenotype. The same group (*hTau*$^{V/M}$/III), was also highly significantly different from random chance level, indicating that the working memory of these flies was still existent, and that their choices in the detour paradigm were not entirely random.

Altogether, this result (Figure 52) reveals that half the amount of functional dTau protein that is present in heterozygous *Tau* variants, is sufficient to allow the normal functioning of the visual working memory in case of the young (3-day-old) flies. This interpretation is similar to the one derived from Figure 51B, where the heterozygous *Tau* knock-out flies were able to perform with wild-type-like visual working memory when treated with tetracycline-containing food on a daily basis. This made us question whether these heterozygous mutants can also exhibit FTDP-17 in *Drosophila*, and if this phenotype gets worse with ageing, as it does in humans. Hence, the next part of the study was to test how these heterozygous *Tau* mutant

flies will behave when they are allowed to age. We were also interested to know whether there were any significant differences between the splice variants and the control groups in the context of ageing. After 2 weeks of ageing, the heterozygous *Tau* variants started losing their visual working memory (Figure 53A). The *hTau*^{WT}/III group retained its working memory, with a median memory score of 90%, which was similar to the memory score of the 2-week-old WT-CS control group, but significantly different from each of the mutant variants.

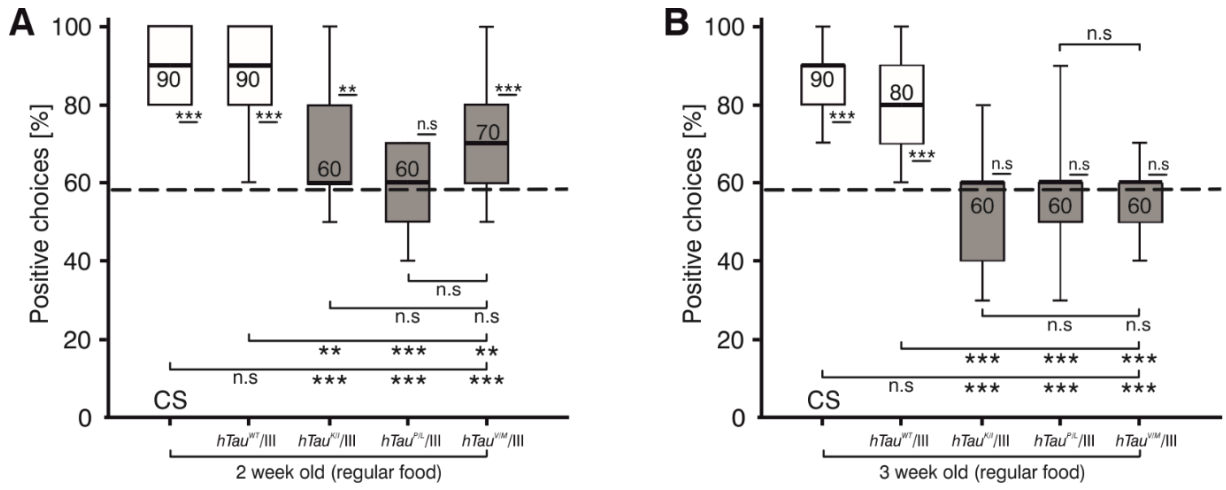

Figure 53: Short-term visual orientation memory in aged heterozygous CRISPR/Cas-generated *Tau* variants

(A) The 2-week-old heterozygous *Tau* variant flies displayed defective detour memory in comparison to the 2-week-old WT-CS (n=25) control group as well as the *hTau*^{WT}/III (n=25) group where both groups had a high median memory score of 90% and were very highly significantly different from chance level (58%). The *hTau*$^{K/I}$/III (n=25) appeared to have an intermediate memory phenotype (median=60%) where the box was distributed between 60%-80% positive choices and memory score was highly significantly different from the random chance level as well as the control groups. The aged *hTau*$^{P/L}$/III (n=25) variant exhibited a complete loss of memory (median=60%) where the memory score was not significantly different from the chance level and highly significantly different from the aged control groups. The aged *hTau*$^{V/M}$/III variant (n=25) exhibited intermediate memory (median=70%) where the box was distributed between 60%-80% positive choices and the memory score was very highly significantly different from the control groups as well as the chance level.
(B) The 3-week-old heterozygous *Tau* variants behaved similarly to that observed when they were aged until 2 weeks. The aged WT-CS (n=25) control group and *hTau*^{WT}/III (n=22) both behaved wild-type like with high median memory scores of 90% and 80% respectively and were very highly significantly different from the random chance level (58%). All the heterozygous *Tau* variants appeared to have completely lost their short-term visual orientation memory after 3 weeks of ageing. The *hTau*$^{K/I}$/III (n=17) group had a memory score (median=60%) which was not statistically different from the chance level and the box was spread between 40%-60% positive choices with the whiskers extending between 30%-80%. The *hTau*$^{P/L}$/III (n=25) and the *hTau*$^{V/M}$/III (n=25) variants both had a median memory score of 60% and were highly significantly different from the control groups while not being statistically different from the chance level. The *hTau*$^{P/L}$/III group had whiskers ranging between 30%-90% positive memory choices.

Refer to **Table 63** and **Table 64** in **Appendix** for statistical analysis for multiple comparison (Kruskal-Wallis test), normality distribution (Shapiro-Wilk test) and comparison against random chance level (58%) (Sign/t-test).

This signifies that *Tau* variants induce a phenotype in *Drosophila*, which is age-dependent, and is similar to what is observed in humans. However, the visual working memory of the heterozygous *hTau* variants, were significantly different from chance level, except in the case of $hTau^{P/L}$/III group, which had completely lost its visual working memory after two weeks of ageing.

The ageing process of the mutant variants, as well as the control groups were allowed to go on for one more week until they were twenty-one days (3 weeks) old. Testing of these 3-week-old heterozygous flies (along with the aged WT-CS group), revealed that all three of the mutant variants had completely lost their visual working memory (Figure 53B). The WT-CS and the $hTau^{WT}$/III control groups continued to have high median memory scores of 90% and 80% respectively, proving that the visual working memory becomes increasingly worse with age in the flies containing *hTau* variants.

In conclusion, this chapter details to us through several behavioural findings, that the loss of Tau protein drastically affects visual working memory in *Drosophila*, especially in ageing flies, and is thus an integral part of this memory functioning. This phenomenon was observed in *Tau* deletion/knock-out mutants, as well as in mutant variants of human *Tau* incorporated in *Drosophila*.

4. Discussion

4.1 Roles of PKA and Synapsin in *Drosophila* detour memory

Visual short-term orientation memory, also known as “detour memory”, is a type of visual working memory that allows a fly to remember its path, despite being distracted along the way, and is operative within a span of 4 seconds (Neuser et al., 2008). Earlier doctoral dissertations and publications have focussed on how this memory works, and the key ingredient that is needed for the memory trace has been shown to be NOS-mediated cGMP (Kuntz et al., 2017). This memory has also been shown to reside in the R3 ring neurons of the EB, a doughnut-shaped substructure of the *Drosophila* CC (Kuntz et al., 2012).

In this doctoral dissertation, we continued to focus on the functioning of this memory. However, instead of the already unravelled cGMP pathway, we decided to address here, the cAMP-dependent PKA pathway, and its effects on visual short-term orientation memory. We zoned in on the catalytic activity of PKA-C1 (Lane and Kalderon, 1993), by assessing the effect of its phosphorylation of the *Drosophila* Synapsin (Klagges et al., 1996), a synaptic vesicle protein which tethers synaptic vesicles to the cytoskeleton. We also addressed the differential role played by Rugose (Shamloula et al., 2002), an AKAP, and how its interaction with PKA-C1 in visual working memory might be contrasting to that documented in olfactory memory. Later in this chapter, we attempt to include Rugose, PKA and Synapsin in a single pathway that governs visual working memory in *Drosophila*.

4.1 (a) PKA, CaMKII and Synapsin regulate detour memory functioning

The importance of cAMP in the context of memory, has been well established for nearly four decades now (Dudai et al., 1986). Learning mutants of the *dunce* (Byers et al., 1981) or *rutabaga* (Livingstone et al., 1984) genes, which have dysregulated cAMP levels, have both been intensively examined in the realm of olfactory memory, and to some extent, in visual memory. But when it comes to visual orientation memory (also known as detour memory), these mutants were either wild-type like (*dunce*^{1}), or unfit to be tested in the detour arena due to their inability to recognize landmarks (*rutabaga*^{1}), revealing that cAMP levels impact detour memory differently in different mutants.

Protein Kinase A (PKA), is one of the key regulators of the cAMP cascade, and indirectly regulates several signal transduction pathways which are directly influenced by cAMP (Dhallan et al., 1990; Delgado et al., 1991). When it comes to the role of PKA in memory, one of the first studies in flies demonstrated that the catalytic subunit of PKA was selectively expressed in the MB neurons, and was also seen to have an effect on olfactory associative learning and memory (Skoulakis et al., 1993). Decreasing the activity levels of PKA-C1, specifically in the MB, has also proven to negatively affect olfactory learning and memory (Yin et al., 1994).

This dissertation revolves around one of the catalytic subunits of PKA (PKA-C1). A hypomorphic allele for *Pka-C1* (*Pka-C1*^{H2}) was utilized, which carries a point mutation in the third exon of the catalytic subunit (Lane and Kalderon, 1993), and has a 40% reduction in activity. With the help of this allele, we have shown that the catalytic activity of PKA-C1 in the R3 neurons, is indeed necessary for the functioning short-term visual orientation memory (Figure 12). This result also verifies that the requirement of PKA-C1 for visual working memory, is only in the R3 neurons, and not in the R2 neurons, since our hypothesis indicates that the visual information regarding the landmarks and the distractor is potentially captured by the R2 neurons, despite the memory being formed in R3 (Kuntz et al., 2017).

Structural characterization of the PKA protein in *Drosophila* reveals that it has three catalytic, along with two regulatory subunits which exist together as a tetramer. The regulatory subunit has a cAMP-binding domain (Coffino et al., 1976) and inhibits the catalytic activity of PKA. This mechanism seems to have been put in place, to avoid the hyperphosphorylation of certain substrates such as Complexin, and Synapsin that are targeted by PKA (Diegelmann et al., 2006; Cho et al., 2015). This theory prompts us to speculate that the controlled catalytic activity of PKA is necessary to avoid unregulated neurotransmitter release at the presynapse, as this can potentially lead to altered synaptic plasticity.

When we used the approach of silencing one of the regulatory subunits (*Pka-R1*^{RNAi}) to rescue the phenotype of *Pka-C1*^{H2}/II in the detour paradigm, it was seen that the memory of the flies improved back to wild-type range (Figure 13). This showed us that, more than simply increasing the levels of PKA-C1, it was necessary to allow its catalytic activity to function. This activity could be a part of a bigger

pathway involving one of the targets of PKA for phosphorylation i.e., Synapsin, which is potentially important for the detour memory functioning in *Drosophila*.

The structure and functions of the synaptic vesicle protein “Synapsin”, was first studied and understood in vertebrates. There are ten homologues of Synapsin proteins found in mammals (Syn I(a-b), Syn II(a-b), Syn III(a-f)). The different isoforms are a product of the alternative splicing of three different genes: SYN I, SYN II and SYN III (Sudhof et al., 1989; Sudhof, 1990). It was discovered that the domain C, a shared centrally located region, shows extensive homology across the various members of the family (Cesca et al., 2010). This domain was postulated to take part in the positioning of the synaptic vesicles (SVs) onto the nerve terminal based on its interaction with the SV phospholipids (Benfenati et al., 1993), and actin filaments (Bahler and Greengard, 1987). Several studies have suggested that the phosphorylation of Synapsin leads to the release of SVs from the actin cytoskeleton at the pre-synapse (Bahler et al., 1990; Benfenati et al., 1991).

Moving on to invertebrates, the central C domain was found to be conserved in the *Drosophila* homolog of the Synapsin protein, opening the door for studies to test whether the functions of this domain would also mimic those that are found in mammals (Klagges et al., 1996). Years later, studies in *Aplysia* revealed that the Protein Kinase A (PKA), is a potential phosphorylating kinase of Synapsin, which results in the transfer of the SVs from the reserve pool to the readily releasable pool, thereby facilitating neurotransmitter release (Fiumara et al., 2004). In terms of *Drosophila*, the site-1 in the A domain, is conserved from mammals, and represents the PKA phosphorylation site for Synapsin, but is edited (Diegelmann et al., 2006). In 2011, for the first time, this site was proven to be the location of CaMKII phosphorylation of the Synapsin protein in *Drosophila* (Sadanandappa et al., 2013).

Sara Kuntz, in her doctoral dissertation, proved that Synapsin is required for visual working memory specifically in the R3 neurons, through rescue experiments. She could also show that there was an interaction between *Pka-C1* and *Syn*. However, the phosphorylation aspect of the Synapsin protein had not yet been considered as a necessity for the functioning of detour memory until our study. For this reason, we decided to focus on the importance of each PKA phosphorylation site on the Synapsin protein using flies containing mutated versions of each site, individually, and together (Michels et al., 2011). When the serine on the sixth position

of both of these sites was replaced by alanine, it rendered them incapable of being phosphorylated by PKA, or any other kinase that might recognize these sites.

As it turns out, the PKA phosphorylation site-1, is the site important for the functioning of visual working memory. The defective detour memory of *Syn*^{97} was rescued by expressing the *Synapsin* transgene in the R3 neurons when the site-2 was mutated and the site-1 was maintained unedited (UAS-*Syn* (S1 unedited+M2) *Syn*^{97}/III) as seen in Figure 15. However, mutation of site-1 on the *Synapsin* transgene while retaining the site-2 intact (UAS-S*yn* (M1+S2) *Syn*^{97}/III), did not improve the detour memory of the *Syn*^{97} mutants, proving that the site-1 in the A domain, which is conserved across species, is important for detour memory, whereas the non-conserved putative second site does not seem to play a role.

Additionally, a behavioural rescue of *Pka-C1*^{H2}/II;*Syn*^{97}/III was also obtained with the UAS-*Syn* expression in R3 neurons when site-1 was unedited (UAS-*Syn*(S1 unedited+M2) *Syn*^{97}/III) (Figure 16). Thus, along with the existing proof that both Synapsin and PKA-C1 regulate detour behaviour (Sara Kuntz, PhD thesis (2015)), these results were the first clear-cut proof that the phosphorylation of Synapsin by PKA-C1, specifically in the conserved site-1 in the A domain, is necessary for the detour memory to function.

In order to specifically address the phosphorylated Synapsin in this conserved site, an antibody raised against the Synapsin phosphorylated at the serine in the 6th position (RRFS^{6}), was used (Sadanandappa et al., 2013). In the original study, this antibody was characterized using a Western blot assay, where the levels of P-Syn(S6) were quantifiably decreased when a CaMKII inhibitor was expressed pan-neuronally. A very recent study utilized this same antibody for Western blot assay as well as in immunohistochemistry analysis. The Western blot revealed that, out of the 21 different isoforms of Synapsin found in *Drosophila*, only some of them are phosphorylated at the serine^{6} on site-1 in the A domain (Blanco-Redondo et al., 2019), thereby hinting at some potential differences between the isoforms of the *Drosophila* Synapsin in regards to the individual roles they might play in vesicle binding and release.

The immunohistochemistry results of the same study (Blanco-Redondo et al., 2019), showcased the localisation pattern of Synapsin (Syn), as well as phosphorylated Synapsin (P-Syn(S6)). While the Synapsin protein was seen to have

a homogenous distribution throughout the brain, the anti-P-Syn(S6) antibody was specifically localised in the EB region of the CC. Nonetheless, the authors of this study declared that phosphorylated Synapsin did not colocalise with any of the R1-R4 ring neurons, and that further investigation was required to prove which ring contained the subcellular distribution of the P-Syn(S6).

In our study, the anti-P-Syn(S6) antibody (referred to as Syn-P1 in our study), was found sparsely in the R3 neurons of the control group, but tremendously increased in its distribution levels when constitutively active *Pka-C1* was expressed in the R3 neurons (Figure 17A). The comparable levels of GFP expression in the R3 neurons of the control, and the experimental group (see Table 11 in Appendix), also prove that the statistically very highly significantly increased Syn-P1 distribution (Figure 17B), was dependent on the continual PKA-C1 expression in the latter. This shows that Synapsin is phosphorylatable at site-1 by PKA, and that this antibody specifically detects and labels the phosphorylated Synapsin from this particular site (Syn-P1). However, the site-1 of PKA phosphorylation has been known to undergo selective mRNA editing at the fourth amino acid position of the sequence where the “RRFS” is changed to “RGFS” (Diegelmann et al., 2006). This specific editing of the PKA phosphorylation site-1 (while site-2 remains intact), is intriguing, since this site appears to be significant for the functioning of the visual working memory.

The shift of the adenosine (arginine) to an inosine (glycine), is the work of an editing enzyme termed as adenosine deaminase acting on RNA (ADAR) (Bass et al., 1997). These enzymes span across metazoan species, right from *Drosophila* to human. Higher metazoan organisms such as humans, have 3 ADARS (ADAR1, ADAR2 and ADAR3), and some of these enzymes have been predicted to form complexes with other proteins *in vivo*, thereby adding complexity and diversity to the existing genome (Bass, 2002). Lower metazoan organisms on the other hand, such as *Drosophila*, contains only one dADAR (*Drosophila* ADAR) enzyme, and was found to be specifically expressed in the nervous system of *Drosophila* embryos (Palladino et al., 2000).

In our study, RNA-mediated interference of *Adar* to allow PKA to phosphorylate Synapsin in the conserved site-1, led to a very highly significant increase in the subcellular distribution of Syn-P1 in the region of the R3 neurons (Figure 20A), which was statistically significantly different from the control group with

functioning endogenous ADAR (Figure 20B). If the ADAR protein is responsible for gene regulation, and for the maintenance of the nervous system in mammals, we pondered whether knock-down of *Adar* would lead to any behavioural defects in flies. Surprisingly, the visual working memory of flies in which *Adar* was knocked-down specifically in the R3 neurons, was wild-type-like (Figure 19B). In fact, the defective detour phenotype observed in flies with the hypomorphic *Pka-C1* allele (*Pka-C1*^{H2}/II), and double-heterozygous mutants (*Pka-C1*^{H2}/II;*Syn*^{97}/III), could both be rescued by knocking-down *Adar* in the R3 neurons, where the visual working memory of these flies was increased to resemble that of the wild-type phenotype (Figure 19A & Figure 21). These experiments revealed that the absence of *Adar* expression in R3 neurons, is beneficial for the functioning of visual working memory in *Drosophila*, as a result of allowing PKA-C1 to phosphorylate Synapsin at the canonical site-1.

In our study, the rescue of homozygous *Syn*^{97} (Figure 15) and double heterozygous *Pka-C1*^{H2}/II*;Syn*^{97}/III (Figure 16) mutants in the detour paradigm with the UAS-*Synapsin* transgene were the key results that showed us that Synapsin, and by means of which, PKA, are both vital for *Drosophila* visual working memory. The *Synapsin*(cDNA8) transgene that was used for the rescue in these cases, also presumably underwent endogenous ADAR editing, disallowing the phosphorylation of Synapsin by PKA at site-1. Hence, we were compelled to follow this line of study to identify the alternative kinases that could potentially phosphorylate this site when PKA is unable to. One of the primary candidates was CaMKII (calcium-dependent calmodulin Kinase II).

CaMKII was originally characterized as one of the two kinases phosphorylating “Protein I”, that was isolated and purified from rat brains (Huttner et al., 1981; Kennedy and Greengard, 1981). By that time, there was already some curiosity surrounding its role in the phosphorylation of major proteins, whose state of phosphorylation was observed to impact the nervous system in vertebrates (Ueda et al., 1973). In vertebrates, at that time, the primary candidates for phosphorylating this Protein I was either cAMP-dependent protein kinase A (PKA), or the calcium-dependent calmodulin kinase (CaMK). However, their approach towards regulating, and phosphorylating the multiple phosphorylation sites on this specific Protein I, was shown to be different from each other (Huttner et al., 1981).

In mice, CaMKII had long been established to affect a number of associative memories by mediating the signalling of NMDA (N-methyl D-aspartate) receptors which are involved in synaptic plasticity (Miller and Kennedy, 1986; Silva et al., 1992; Wang et al., 2008a). In *Drosophila*, there was a dearth of knowledge in this regard, until a study by Griffith and colleagues showed that the loss of CaMKII protein by peptide inhibition, resulted in aberrant behavioural plasticity that is related to associative learning in courtship behaviour (Griffith et al., 1993). In another study, pan-neuronal expression of the same inhibitor, showed a reduction in phosphorylated Synapsin (PSYN(S6)) in Western blot analysis, as well as a defective short-term habituation (STH) (Sadanandappa et al., 2013).

When we decided to express the same peptide inhibitor (UAS-*CaMKII-I.Ala*) in the R3 neurons, there was a near complete loss of visual working memory in these flies, in comparison to the control groups (Figure 22B), hinting at the importance of CaMKII activity in these neurons. RNAi-mediated knock-down of *CaMKII* in the R3 neurons, also led to a similar loss of memory phenotype in the detour paradigm, once again reinforcing the significance of the CaMKII protein for visual working memory (Figure 22A).

Over the years, a number of studies have analysed the role of CaMKII in different types of learning and memory. These studies have capitalised on the ability of CaMKII to undergo autophosphorylation in order to regulate its kinase activity. A Ca^{2+}/calmodulin (CaM)-associated serine kinase (CASK), has been shown to interact with CaMKII in order to mediate neuronal growth, Ca^{2+} signalling, and memory (Gillespie and Hodge, 2013). The experiments in this study focused on the principle of autophosphorylation of the threonine in the 287th position of the *Drosophila* CaMKII (CaMKII.T287D), which leads to the conversion of CaMKII from calcium-dependent to independent, allowing it to be consitutively actively expressed (Park et al., 2002).

When we applied the concept of autophosphorylation of CaMKII in *Drosophila* visual working memory, there was a complete rescue of the *Pka-C1*^{H2}/II phenotype when consitutively active UAS-*CaMKII* (*CaMKII.T287D*) transgene was expressed in the R3 neurons (Figure 23). This result indicates that CaMKII can step in as a substitute for PKA in visual working memory. This theory was also proven using an immunohistochemistry study, where the expression of UAS-*CaMKII*^{T287D} transgene, led to a very highly significant increase of phosphorylated Synapsin from site-1 (Syn-

P1), compared to the control group with regulated CaMKII expression (Figure 24A&B). Both groups were also confirmed to have comparable levels of GFP staining intensity.

This ability of CaMKII to phosphorylate Synapsin, despite the editing of phosphorylation site-1 by ADAR, could be a result of its specificity towards the serine in the 6th position of the site-1 (RRFS), rather than the arginine in the second position (which is the site that is edited to glycine (RGFS)). This was addressed by Sadanandappa and colleagues, where the mutation of both phosphorylation sites on the Synapsin protein by replacing the serine in the 6th position with alanine (Michels et al., 2011), led to a complete lack of phosphorylated Synapsin (Sadanandappa et al., 2013). This proves that when the serine at the 6th position is replaced with any other amino acid, neither PKA nor CaMKII are able to phosphorylate Synapsin at site-1.

These findings suggest that it is only logical to deduce that the site-1 on the *Drosophila* Synapsin protein is dually regulated by PKA and CaMKII in the R3 neurons, where PKA is unable to phosphorylate Synapsin at site-1, because it underwent pre-mRNA editing by ADAR. CaMKII, with its reduced specificity for the edited site, can still manage to phosphorylate Synapsin at the serine^{6}, thereby allowing for the functioning of visual working memory.

4.1 (b) Rugose negatively regulates PKA activity in visual working memory

Rugose, an AKAP (A Kinase Anchoring Protein) (Rubin, 1994), codes for the *Drosophila* AKAP550 (DAKAP550) (Shamloula et al., 2002). The general function of AKAPs is to modulate the specificity of kinases such as PKA by means of targeting, and compartmentalizing the kinase to specific subcellular structures. Hence, several studies have come out in an attempt to elucidate the nature of interaction between AKAPs, and the regulatory subunits of kinases such as PKA (Huang et al., 1997b; Herberg et al., 2000). In addition to binding with kinases, AKAPs have also been seen to function as signal integrators by interacting with scaffold signalling molecules, and membrane receptor proteins. A specific AKAP79/150 has been implicated in postsynaptic structure and signalling, where its recruitment of PKA is differentially regulated by the activation of NMDARs, and AMPARs in the context of long-term depression (LTD) in vertebrates (Dell'Acqua et al., 2006).

Mutant forms of *rugose* have given rise to morphological defects in the MB lobes, as well as a deficit in odour learning, albeit the two processes occurring independently of each other (Volders et al., 2012). Thus, it was surprising to us when we saw a defective visual working memory, upon expressing the UAS-*rugose* transgene in the R3 neurons (Figure 28), indicating that Rugose might be detrimental for this memory, and that its function in the R3 neurons of the EB might differ from how it operates in the Kenyon cells of the MB. The role of *rugose*, specifically in olfactory STM, was addressed in another study, where LTM consolidation remained unaffected in *rugose* mutant flies, as well as in flies expressing pan-neuronal knock-down of *rugose* in an adult-specific manner (Zhao et al., 2013). This study also explored the relationship between PKA-C1 and Rugose, where the flies with the hypomorphic alleles for both *Pka-C1* and *rugose* (rg^{1}/X;$Pka\text{-}C1^{H2}$/II), had a reduced STM, while the LTM remained unaffected, indicating that Rugose interacts in a positive manner with PKA in olfactory STM.

One of the more recent studies in *Drosophila* models for ASD (Autism Spectrum Disorders), revealed that the fragile X mental retardation protein (FMRP) positively translates Rugose in the MB Kenyon cells, by directly binding to the *rugose* mRNA. FMRP and Rugose, together, were shown to increase the activity of PKA in the MB Kenyon cells (Sears et al., 2019). A reason for this might be that the requirement of PKA lies in the postsynaptic part of the MB neurons, rather than in the presynaptic side, oweing to the localisation of Rugose protein in the cortex and its close association with the Golgi.

When we applied a similar principle to study the visual working memory using a genetic interaction study between *Pka-C1* and *rg*, it was revealed that the heterozygous hypomorphic rugose allele ($rg^{\gamma 5}$/X), could in fact rescue the defective detour memory phenotype found in heterozygous *Pka-C1* mutants ($Pka\text{-}C1^{H2}$/II). This indicates that the production of less Rugose is beneficial for detour memory, since the reduced PKA-C1 activity could be compensated for in these double heterozygous mutant flies ($rg^{\gamma 5}$/X;$Pka\text{-}C1^{H2}$/II). The flies heterozygous for the hypomorphic rugose allele ($rg^{\gamma 5}$/X), on the other hand, had a wild-type-like memory (Figure 25). This is contrasting to the deficit of olfactory STM observed in *rugose* null mutants, and knock-downs, once again proving that Rugose functions differently in olfactory memory and visual working memory.

In addition to genetic interaction studies, alleles hypomorphic for *rg* (Figure 25), as well as RNAi-mediated knock-down of *rg* in the R3 neurons (Figure 26), led to the rescue of defective detour memory phenotype of *Pka-C1*^{H2}/II flies, showing that reducing the *rg* expression in the R3 neurons could improve the memory back to wild-type range. Contrastingly, overexpression of the *rg* transgene in the R3 neurons, led to a reduced detour memory score, which was not significantly different from that seen in *Pka-C1*^{H2}/II flies. Together, these results display that the reduction of Rugose in the R3 neurons is beneficial for detour memory functioning in a cAMP/PKA-dependent manner (Figure 26).

We were interested in understanding how Rugose impacts the functioning of PKA-C1, and if this was by modulating the subcellular distribution of PKA-C1 in the R3 neurons. Immunolabelling of PKA-C1 through a specific anti-FLAG (fluorescent tag) antibody revealed that the localisation of PKA-C1 in R3 neurons was significantly increased in *rg*^{y5} flies in comparison to control flies with endogenous Rugose activity (Figure 27A). Comparable staining of the FASII protein between the control group and the experimental group showed that the significant increase in the levels of PKA-C1 (Figure 27B), was because of the genetic manipulation of Rugose levels, and not due to any procedural mishandling. The reverse was observed in the scenario in which *rg* was overexpressed in the R3 neurons, where the subcellular distribution of PKA-C1 was significantly reduced in the region of the R3 axons (Figure 29), supporting the hypothesis that the AKAP Rugose negatively impacts detour memory functioning by disallowing PKA-C1 to perform its phosphorylating function at the presynapse of the R3 neurons.

4.1 (c) Summary of the model for visual working memory functioning

Our model for the visual working memory in *Drosophila* revolves around the function of PKA, which is to phosphorylate Synapsin at the presynapse of the R3 neurons. As we had reiterated several times throughout this study, this phosphorylation process is required to be carried out at the conserved site-1, located at the A domain on the N terminal of the Synapsin protein. This site is edited out exclusively in *Drosophila* by the mRNA-editing enzyme ADAR, which usually recognizes precursor mRNA duplexes of its target proteins. Here, ADAR acts on the the Synapsin protein sequence in order to lead to a shift in amino acid group from an

adenosine to an inosine group in such a way that PKA can no longer recognize or phosphorylate the Synapsin protein at this canonical site.

In the absence of PKA-C1 performing its phosphorylating function, CaMKII takes over this role and manages to phosphorylate Synapsin at the 6th serine position, even when ADAR editing of site-1 at the second position from arginine to glycine (RRFS→RGFS), takes place. This phosphorylation process will now allow for the normal functioning of visual working memory, even in wild-type flies, where a fraction of the cells undergo pre-mRNA ADAR editing. This mechanism occurs in parallel with the functioning of NOS, which through cGMP, creates the memory trace for the landmarks and the distractor in the R3 neurons. An important function of cGMP is the regulation of ion channels at the presynapse (Kuntz et al., 2017). By interacting with the cyclic nucleotide-gated channel subunits (CngA and CngL), cGMP could potentially lead to the influx of Ca^{2+} ions, which in turn could activate CaMKII that phosphorylates Synapsin at site-1.

In light of the results brought forward by Niewalda and colleagues in their proteomics study, approximately 64% of the Synapsin protein is non-edited, while only 26% is edited (Niewalda et al., 2015). This would indicate that majority of the times, when the Synapsin protein is unedited, PKA can phosphorylate it at site-1 by means of activation from cAMP. Whereas in the cells where Synapsin undergoes editing, Ca^{2+} activation of CaMKII, can facilitate the phosphorylation of Synapsin. Thus, the release of SVs from the cytoskeleton membrane at the presynapse, is regulated by both cAMP/PKA as well as Ca^{2+}/CaMKII signalling cascades. In addition, PKA-C1 activity is regulated by the AKAP Rugose, which seems to negatively impact the functioning of PKA-C1 in visual working memory, especially when overexpressed in the R3 neurons of the EB. The localisation of Rugose in the *Drosophila* brain has been found to be in, or near the Golgi complex, since the anti-RG antibody appeared to disperse in a granular fashion resembling that of the Golgi network, and colocalised with the *cis*-Golgi marker (GM130) (Volders et al., 2012).

Thus, our model predicts that Rugose helps in the tethering of PKA to the Golgi when endogenous Rugose is allowed to function regularly. This prevents PKA from being available at the presynapse of the R3 neurons, where it is required to perform its phosphorylating function. When the endogenous Rugose levels are negatively regulated, either by a hypomorphic allele of *rugose* (rg^{V5}), or through the

expression of an RNAi-mediated knock-down, Rugose is not present at its optimum level, thereby allowing more PKA molecules to be present at the presynapse of the R3 neurons (Figure 54). A reduction in Rugose levels, facilitates the phosphorylation of Synapsin by PKA in order to mediate the employment of SVs filled with neurotransmitters from the reserve pool to the readily releasable pool. Since the phosphorylation of CREB in the cell soma is carried out by Ign, PKA may not be required to perform this particular function for detour memory functioning, and can be freely available at the presynapse to phosphorylate Synapsin, leading to the release of SVs from the reserve pool (Figure 54).

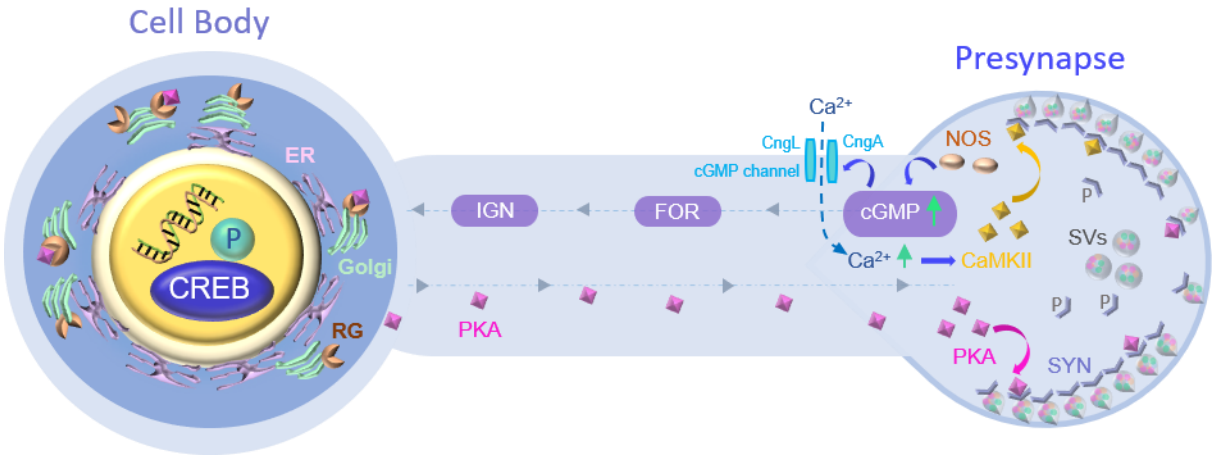

Figure 54: Schematic representation of the roles of PKA, CaMKII and Syn in the R3 neurons

In the cell soma of the R3 neuron, Rugose is localised near the Golgi network and tethers the PKA complex to the Golgi. The freely available PKA molecules travel towards the presynapse where they phosphorylate Synapsin, the synaptic vesicle protein that has an affinity to bind the vesicles to the cytoskeleton. In addition, cGMP interacts with the cyclic nucleotide-gated (CNG) channel subunits (CngA and CngL), potentially leading to the increased influx of Ca^{2+} ions, which in turn can activate CaMKII, that also phosphorylates Synapsin when site-1 is edited.Upon phosphorylation of Synapsin, the vesicles in the reserve pool are now deployed into the readily releasable pool, where they can now participate in vesicle recycling. These vesicles are filled with neurotransmitters, which upon their release, can facilitate the functioning of visual working memory. In the R3 cells, the phosphorylation of CREB takes place by Ignorant (RSKII), operating downstream of Foraging (For) whose levels have been increased by NOS-mediated cGMP. Since Ign performs this phosphorylating function predominantly, the need for PKA to be present in the cell soma is reduced, allowing it to migrate towards the presynapse of the R3 neurons.

The eventual release of tethered vesicles filled with neurotransmitters, creates a shift between the reserve and the recyclable pool, presumably leading to the functioning of visual working memory in *Drosophila* (Figure 54). It is apparent that this mechanism of phosphorylation of Synapsin by PKA at the R3 neurons' presynaptic region, is tightly regulated by ADAR editing at PKA site-1, as well as by Rugose, which potentially tethers PKA to the Golgi network at the cell soma (Figure 54). A

reason for this might be, to avoid the depletion of SVs in the reserve pool due to the extensive phosphorylation by PKA, which is normally found in abundance in all organisms. The requirement of phosphorylation of Synapsin for visual working memory might indicate that this memory requires the freeing of SVs from the reserve pool, which is usually observed in neurons which are frequently stimulated. It raises the question whether R3 neurons are more often stimulated than we might have predicted, and should be investigated in future studies.

4.2 Connectivity between neuronal subfamilies of the central complex which are involved in *Drosophila* visual working memory

Different substructures of the CC, primarily the EB, and the PB have been implicated in spatial orientation and memory. Although the location of the visual working memory in *Drosophila* has been established to be the R3 neurons of the EB (Kuntz et al., 2012), there is still a lack of information regarding the other neurons belonging to the CC, that could potentially interact with R3 in order for this working memory to function. An effective way to screen for these neurons, would be to modulate them through temperature-sensitive experiments in order to observe the read-out of the behaviour in the detour paradigm. Originally characterized in anterior cell (AC) neurons, *Drosophila* TrpA1 is a channel protein with the temperature-sensitive ability to allow variable Ca^{2+} influx into the cell (Hamada et al., 2008). Behavioural assays have demonstrated that the neurons expressing UAS-*TrpA1*, play essential roles in temperature cycle entrainment by controlling locomotor activity in a clock-independent manner (Lee, 2013).

When we decided to apply the mechanism of TrpA1 neuronal activation to identify the role of different ring neurons in detour memory, we had in mind the model presented by Kuntz and colleagues. According to their hypothesis, the influx of Ca^{2+} can form a memory trace based on the cGMP-mediated opening of CNG (cyclic nucleotide-gated) channels (Kuntz et al., 2017). If this were the case, then excessive influx of Ca^{2+} ions is bound to cause a disruption in the formation of memory traces for the landmarks and the distractor, hence hindering the visual working memory in these neurons. In addition to R3 neurons, which are the regions for this memory formation, their study discussed the distinct roles of R2/R4 neurons in the functioning of this memory with individual R2/R4 neurons representing visual objects in a topographic manner. Thus, TrpA1 activation of R2/R4 neurons would disrupt

information regarding the landmark or distractor. However, this network is not used by the fly when the landmarks are still present. This is the reason why Buridan behaviour is not affected by overactivating the R2/R4 neurons. In our study, we decided to pursue the individual roles of all the ring neuron subclasses, which might be presynaptic to R3 neurons, in order to clearly identify which ones are indispensable for detour memory functioning. This was carried out by inducing Ca^{2+} influx in these neurons with TrpA1 during a part of the behavioural experiment. As for the inactivation of the same neurons with *shibire*^{ts1}, we aimed to disrupt their synaptic transmission and silence them individually using UAS-*shi*^{ts1} in order to screen for the neurons which are truly necessary for the functioning of detour memory.

4.2 (a) Role of ring neurons and compass (E-PG) neurons in *detour* memory

We decided to classify the ring neurons based on their requirement of detour memory functioning, as observed in Table 6.

Table 6: Classification of ring neurons required for visual working memory

Ring neurons required for visual working memory	Ring neurons <u>not</u> required for visual working memory
R2 (R19C08-GAL4) R3d & R3p (189Y-GAL4) R3m (R28D01-GAL4) R5 (R58H05-GAL4) R6 (VT011965-GAL4)	R1 (R31A12-GAL4) R4d & R4m (*ftz-ng*-GAL4)

From Table 6, it is visible that R1 and R4 ring neurons were not required for visual working memory in the temperature-shift experiments. Beginning with the R1 neurons, there has been some degree of confusion until recently as to which driver specifically addresses these neurons. The driver line published by Ofstad and colleagues (R28D01-GAL4; (Ofstad et al., 2011)), in their work pertaining to place learning in flies, has now been characterized to address the R3m subtype (Omoto et al., 2018). Overactivation, as well as inactivation of the newly identified driver for R1 (R31A12-GAL4 (Omoto et al., 2018)), led to no significant impairment in visual working memory (Figure 30A). Despite there being no published evidence (as of yet) that proves that this new R1 driver is involved in place learning/memory in flies, this result is intriguing for a few reasons. It has recently been shown that the R3p

(posterior) neurons and the E-PG neurons are potential postsynaptic partners of the R1 neurons (Omoto et al., 2018). This made us wonder whether the information regarding the place/location of the fly, with respect to the landmarks within the arena, could possibly be communicated to the R3p and the E-PG neurons. As for the R1 and R3p neuronal connectivity, in the previous chapters, we made use of the 189Y-GAL4 driver to address the R3 neurons as a whole, which has now been categorized as a more specific driver that only addresses the R3d & R3p subsets (Omoto et al., 2018). If R3p is indeed a postsynaptic partner of the R1 neurons, and manipulating the activity of R1 has no effect in visual working memory, then it leads us to believe that this specific connectivity between R1 and R3p is unnecessary for visual working memory functioning.

As for the R4 neurons, literature would lead us to believe that it is an important participant in visual pattern memory (Pan et al., 2009), as well as in visual orientation conditioning (Guo et al., 2014). On the other hand, R2 neurons also play a key role in the recognition of visual objects, and have already been proven to be important in visual working memory. Thus, we were curious to discover whether R4 neurons work in synergy with the R2 neurons in the functioning of this memory, or if the R2 neurons can independently govern this behaviour. Through the *ftz-ng*-GAL4 driver (Pereanu et al., 2011), which addresses both R4d&m subtypes, we uncovered that the overactivation of these neurons, had no impact on the detour memory of flies (Figure 30D). This gave us an impression that the visual input pertaining to the landmarks and the distractor were not necessarily captured by the R4 neurons, and were single-handedly managed by the R2 neurons. The above mentioned behavioural result was intriguing, since it has been shown that the R4d, and R3d neurons are postsynaptic partners of each other. This might indicate that the synaptic inputs received by the R3d neurons from the R4 neurons, are not necessary for the formation of visual working memory, and are instead possibly overshadowed by the input received from the R2 neurons to the R3d neurons. Another interesting observation made by Omoto and colleagues, is the labelling of the the E-PG neurons as a strong postsynaptic partner of the R4m neurons. This synaptic transmission is presumably inhibitory, meaning that silencing of R4 neurons with *shibire*^{ts1}, could potentially decrease the inhibitory input received by the E-PG neurons, which positively affects visual working memory (Figure 32D).

The R2 (R19C08-GAL4; (Omoto et al., 2017)) ring neurons, when activated, led to a complete memory loss in the detour arena (Figure 30B). This was expected by us, since this ring neuron subclass has been postulated to respond to visual objects. According to our hypothesis, TrpA1 activation of the R2 neurons, might result in multiple R2 neurons (that are not representative of the landmark or distractor), sending out a signal through their axons. This can potentially lead to aberrant memory formation in the R3 neurons. On the other hand, inactivation of the R2 neurons, also led to a complete memory loss (Figure 32B).

The blocking of synaptic transmission within the R2 neurons using UAS-*shibire*^{ts1} could have resulted in two things: 1) the inability of R2 to capture the visual input from the landmarks and the distractor, and 2) the absence of communication of visual input from R2 to R3 neurons. Both these possibilities might have contributed to the memory loss that was observed here (Figure 32B). When it comes to the interaction of R2 neurons with other neurons of the CC, it has been shown that the R4d and R3d ring neuron subsets are potential postsynaptic partners of R2 neurons, in addition to other R2 neurons (Omoto et al., 2018). This finding was further proof that the visual working memory functions might be based on the visual input from the R2 to the R3d neurons. However, this synaptic transmission is potentially inhibitory, once again making us wonder how the visual information would be communicated to the R3 neurons. In addition, it has been shown in the same study (Omoto et al., 2018), that the E-PG neurons are an additional postsynaptic partner of the R2 neurons. This is not very surprising, since it has already been shown that the E-PG neurons extend their dendrites into the EB (Wolff et al., 2015), making it convenient to receive inputs from the axons of the ring neurons, some of which can potentially belong to the R2 neurons. The synaptic connectivity between the R2 neurons and E-PG neurons was further confirmed by Kottler and colleagues, where a GRASP signal was visible in both directions of synaptic connectivity, indicating that the E-PG, and R2 neurons are postsynaptic partners of each other (Kottler et al., 2019).

Fisher and colleagues have come up with a study addressing a mixture of EB ring neurons which declares that ring neurons (except R1 and R3a), mostly have inhibitory inputs into the E-PG neurons (Fisher et al., 2019). The authors of this study have shown through optogenetic studies that the R2/R4 neurons, which are stimulated by visual input, lead to the hyperpolarization of the E-PG neurons, which is

an inhibitory effect (Fisher et al., 2019). However, some of the E-PG neurons might be strongly inhibited, while the others are inhibited relatively weakly. This study proved that the input from the ring neurons to the E-PG neurons, is effectively plastic, and that the visual world can vary between individuals. This plasticity enables the representation of the visual world to change unpredictably within an individual. A recent study by Kim and colleagues also reiterated the importance of this plasticity since the orientation of the fly towards a part of a novel environment can be converted from a partial heading representation to a complete one, thereby enabling flexible navigation behaviour during exploration (Kim et al., 2019).

In relation to the R3 neurons, we used the 189Y-GAL4 (R3d&R3p; (Omoto et al., 2018)) to activate the R3 neurons using UAS-*TrpA1*. Since this ring neuronal subtype has been known to be the region of detour-memory formation, we expected the hyper influx of Ca^{2+} to cause disruptions in detour memory by virtue of activation of all wedges in the R3 neurons. In the detour paradigm at 28°C, this aberrant activation might result in the R3 neurons forming a memory for a non-existent landmark which was perceived by the fly due to the activation of multiple R3 wedges. This can potentially result in a complete loss of memory, which is what we observed in this case (Figure 30C). Complete inactivation of the R3(d&p) neurons, led to a significantly reduced visual working memory, albeit the flies not losing their memory completely (Figure 32C). A reason why this result is slightly different from the *TrpA1* activation of these neurons, might simply be due to the presumably decreased effectiveness of *shibire*^{ts1} in silencing these neurons. Thus, even a few R3 neurons that were not successfully silenced by *shibire*^{ts1} could have inadvertently gone on to allow the visual working memory to function, thereby preventing the complete loss of memory in this group of flies. It should also be considered that we now have multiple subtypes of the R3 neurons. Therefore, it would be useful to perform these activation and inactivation experiments in each of the R3 neuronal subtypes to identify which ones are truly necessary for the formation of visual working memory. The synaptic connectivity of the R3 (and its subtypes), with the other regions of the CC, was extensively analysed by Omoto and colleagues, once again with the aid of the trans-Tango technique (Talay et al., 2017). According to their observations, the R3w (wide), R3a (anterior), R3m (medial) and R3p (posterior), all have the compass neurons as their postsynaptic partners, in addition to the other R3 subtypes.

Moving on to our own experiments exploring the connectivity between the R3 and E-PG neurons, the steering of the fly after the decision making process in the detour paradigm must ostensibly be mediated by the bridge. Thus, we predicted that the E-PG neurons might be one of the potential candidates which communicates the idiothetic memory formed in the R3 neurons to the PB. The E-PG neurons, now known as “compass neurons”, were originally characterized under the term “EBw.s” neurons, and were proposed to be functionally comparable to the “head direction cells” observed in vertebrates (Seelig and Jayaraman, 2015). For the first time, an activity bump was observed in the dendrites of these EBw.s neurons, as the tethered fly turned on a rotating ball, following the movement of the single visual stripe. This activity bump was recognized to be the representation of the fly’s orientation with respect to a visual object and the movement of the fly, and could last for at least 30 seconds after the disappearance of the object. In the detour paradigm, there are two visual cues- landmark and distractor, which would activate the dendrites of the E-PG neurons in two different wedges of the EB. Thus, we decided to first test their impact on detour memory before exploring their synaptic connectivity to the R3 neurons.

Hyperactivation of E-PG neurons, led to a complete loss of visual working memory (Figure 31A), proving that these neurons are a positive candidate impacting this behaviour. The reasoning behind this result could be based on the function of the E-PG neurons, which have the potential to receive inputs from the EB, oweing to their dendritic projections, and then transmit them to the PB. The dendritic calcium bump of the E-PG neurons, is representative of a response to visual cues. When these neurons are hyperactivated with UAS-*TrpA1*, it is only expected that multiple activity bumps in different wedges of the EB are created, in addition to the legitimate bumps representing the landmarks and the distractor. Silencing of these neurons also caused complete loss of visual working memory (Figure 33A), presumably due to the reduced ability of these neurons to form an activity bump that is responsive to the shifting of the landmarks and the distractor in the visual field. Since the visual working memory has been proven to be formed in the R3 neurons, we hypothesized that there has to be a direct/indirect connection between the E-PG and the R3 neurons, for the E-PG neurons to effectively regulate visual working memory. Thus, we postulated that it is unlikely for the E-PG to only receive inputs from the ring neurons while having no presynaptic input into them. In order to test our hypothesis that the R3 neurons could be the potential postsynaptic partners of the E-PG neurons, it was

first essential to prove that the E-PG neurons not only extend their dendrites, but also have axonal arborizations within the EB.

The DenSyt staining which we performed to reconfirm whether the E-PG neurons extend only their dendrites in the EB, revealed an intense synaptotagmin-GFP signal in the entire EB (Figure 35A). Thus, this finding challenged the exisiting theory that there are no presynaptic parts of these neurons existing within the EB. This would suggest that the E-PG neurons not only receive inputs, but also have the scope of being a presynaptic partner to the EB ring neurons. However, the trans-Tango staining of the E-PG neurons revealed no R3 neurons to be their postsynaptic partners, despite these neurons having postsynaptic innervations in the EB middle region (Figure 36A'). Instead, a subtype of the P-FN neurons, presumably P-F_1N_3 according to the connectomics drawn by (Franconville et al., 2018), showed up as a potential postsynaptic partner of the E-PG neurons, although the specific P-FN subtype can only be discerned by performing a GRASP study between the E-PG neurons and the individual subfamilies of the P-FN neurons (Figure 37B). Three of the eight Δ7 lateral neurons on either hemisphere were also marked to be postsynaptic to E-PG neurons (Figure 37B). This connection between the E-PG neurons and the Δ7 neurons were classified to be excitatory, according to the physiology experiments conducted by Franconville et al (Franconville et al., 2018). Overall, this trans-Tango result was not useful in terms of establishing the potential postsynaptic partners of the E-PG neurons within the EB, and also highlighted the suspected inefficiencies of trans-Tango when it comes to the EB neuropil.

Interestingly, there is literature evidence showing that a synaptic connection exists between the dendrites of compass neurons (R19G02-LexA), and the axons of several ring neuronal subfamilies: viz., R2/R4m (EB1-GAL4) and R1/R3/R4d (R15B07-GAL4) (Xie et al., 2017). However, In our GRASP study, we were particular about understanding the synaptic connectivity purely between the R3 neurons and the E-PG neurons. Using the LexA driver for the E-PG neurons (R60D05-LexA), and a GAL4 driver representing the R3d&p neurons (VT42759-GAL4), we pre-determined the direction of synaptic connectivity to test whether the R3 neurons were presynaptic partners of the E-PG neurons. Sure enough, there was a faint GRASP signal observed in the region of the EB, validating our hypothesis that the E-PG neurons do receive synaptic input from the R3 neurons (Figure 40A). Reversal of this experiment

where the R3 neurons (R54B05-LexA) were pre-determined to be the postsynaptic partners of the E-PG neurons (R19G02-GAL4), led to a surprising finding. The GRASP signal obtained in this case was much stronger than the one found in Figure 40A, by multifolds (Figure 41A). Additionally, we also observed DenMark in the R3 region of the EB (Figure 34A'), indicating that these neurons have the potential to receive synaptic input. We thus came to the conclusion that the strength of synaptic transmission from the E-PG neurons to the R3d & R3p neurons, was much more pronounced than in the opposing direction i.e., from the R3 neurons to the E-PG neurons. Thus, R3d&p neurons are definitely important for visual working memory, where this memory is presumably formed with the help of the excitatory input received from the E-PG neurons.

Moving on to the remaining two ring neuron subclasses that affected visual working memory, the fairly recently classified R5 neurons (R58H05-GAL4; (Omoto et al., 2017)), when hyperactivated with UAS-*TrpA1*, showed a complete loss of visual working memory (Figure 30E), which was very interesting to us. We were puzzled as to how these neurons, which have been associated with sleep (Raccuglia et al., 2019), also seem to have an effect on visual working memory. A hypothesis would be that the maintenance of activity of these neurons to mediate optimal sleep levels, is necessary in the long run for maintenance of the functioning of this memory, even though sleep may not have a direct role in the four-second visual working memory. Recently, Liang and colleagues have found that the R5 neurons also have a significant role in locomotor activity, which is dependent on the circadian system (Liang et al., 2019). The authors of this study show that the R5 neurons display bimodal neural activity spikes during dawn and dusk, which correlates with the locomotor activity pattern in flies. They show that the neural activity of R5 neurons relies more on the independent input from the circadian pacemaker cells, the morning (M) and evening (E) cells, but not from visual input. Since the inactivation of these neurons with *shibire*^{ts1} led to a complete loss of visual working memory (Figure 32E), we conclude that these neurons are genuinely necessary for the functioning of this memory. Although, further probing is required to reveal their postsynaptic partners.

The most recently discovered R6 neurons (VT011965-GAL4), have also proven to be vital for the functioning of detour memory. This subtype of neurons severely affected visual working memory when hyperactivated by TrpA1 (Figure 30F)

and when inactivated using *shibire*^{ts1} (Figure 32F), strongly suggesting that it is an important participant in the functioning of detour memory, even though these neurons have no known functions in *Drosophila*, as of yet. Once again, their postsynaptic partners need to be elucidated in order to get a clearer view on how they are connected to the rest of the rings of the EB and the substructures within the CC.

4.2 (b) Role of non-canonical ring neurons in *detour* memory

The non-canonical ring neurons, identified by Franconville and colleagues, are a few of the extrinsic ring neurons which innervate the LAL, and the gall, but not the bulb regions (Franconville et al., 2018). The reason we included the non-canonical ring neurons in the screen, was to observe how these neurons, which innervate the EB, but are not intrinsic to it, influence visual working memory. These neurons were identified to have inputs into the CC, which were inhibitory and picrotoxin-sensitive, indicating that they might be either GABA-ergic ($GABA_A$) or glutamatergic.

Starting with the L-Ei ($LAL\text{-}EB_{inner}$) neurons (R75H04-GAL4), the overactivation of these neurons with UAS-*TrpA1*, seemed to negatively influence the visual working memory, which was significantly reduced compared to the control groups (Figure 42A). This prompted us to consider the possibility that the region of the ring neurons addressed by this driver, is necessary for the functioning of this memory. trans-Tango studies revealed that the expression pattern of these neurons, included the bulb regions (superior and inferior), the LAL, along with multiple rings of the EB, instead of just the innermost ring (Figure 44A). This immunohistochemistry analysis also revealed strong postsynaptic partners of L-Ei in the region of R3(d/m/p) ring neurons of the EB (Figure 44B). The innervations in the inferior regions of the bulb suggest that the postsynaptic partners might be any of these neurons according to the immunohistochemistry results of Omoto and colleagues (Omoto et al., 2018). Thus, it was no surprise that when we inactivated these neurons with UAS-*shibire*^{ts1} (Figure 43A), we once again observed a deficit in detour memory, suggesting that the input from the L-Ei neurons to the EB, might be important for visual working memory.

As for the L-Em neurons (R32A11-GAL4), immunohistochemistry results revealed that these neurons observably innervated the LAL, and middle regions of the EB, along with some arborizations in the inner regions as well (Figure 45A). Upon a closer look at the projection of these neurons, we could identify that they innervated around the same regions as the axons of the R1 and the R3a in the EB. The

complete loss of detour memory when UAS-*TrpA1* (Figure 42B) activated these neurons was therefore explicable, since the middle region of the EB is where the R3 neurons reside, and we suspected whether there were any synaptic connections between these L-Em neurons and the canonical R3 neurons, that could be important for detour memory functioning. However, these neurons (L-Em) did not display any conspicuous postsynaptic partners in the region of the CC. However, upon careful obervation, we could notice a faint shadow of mCherry, presumably in the region of the R3m neurons, extending into a single microglomeruli in the region of the inferior bulb (BUi), which was connected to an exclusively postsynaptic cell body (Figure 45B). The silencing of these L-Em neurons with *shibire*^{ts1} led to a complete loss of visual working memory (Figure 43B). Nevertheless, it is important to perform a DenMark-Synaptotagmin staining of these neurons to identify the pattern of their axonal and dendritic arborizations.

The final subset of non-canonical neurons that we addressed, were the GB-Eo (Gall-EB$_{outer}$), neurons, which, according to literature, have inhibitory inputs into the E-PG neurons (Franconville et al., 2018). We were unsure as to which outer rings might be innervated by these neurons. The outer rings of the EB include the R2, R4(EBoc) and the R6(EBop) neurons (Omoto et al., 2018). The expression pattern of these neurons, elucidated by the trans-Tango technique, revealed innervations in the gall, the LAL and limited expression in the outer regions of the EB (Figure 46A). Surprisingly, the GB-Eo neurons did not appear to possess any distinct postsynaptic partners in the substructures belonging to the CC (Figure 46B). This might suggest that the synaptic interaction between GB-Eo and the E-PG neurons is not direct and might occur through interneurons that are yet to be identified. Another possibility is that the trans-Tango technique is not an efficient method to target this particular synaptic connection. Gauging by our experience with using trans-Tango as a method to identify postsynaptic partners of neurons innervating the EB, it could be concluded that this technique has considerable drawbacks when it comes to establishing the synaptic partners of both canonical and non-canonical ring neurons. On the behavioural front, the activation of these neurons using UAS-*TrpA1*, did not negatively impact detour memory (Figure 42C), which was even more puzzling. If these neurons do have direct inhibitory input into the E-PG neurons, then the hyperactivation of these neruons should have resulted in increased inhibition of the E-PG neurons, which have been shown to be required for visual working memory

(Figure 31A, Figure 33A). However, these neurons did not have any effect on visual working memory when inactivated with UAS-*shibire*^{ts1} either (Figure 43C). This result leans in the direction that these GB-Eo neurons could possibly lack direct synaptic interactions with the EB ring neurons, as well as other components of the CC that might be critical for visual working memory functioning (Figure 46B).

4.2 (c) Role of P-EN neurons in *detour* memory

The “shift” neurons, also known as the P-EN neurons, have been predicted to perform the function of moving the dendritic E-PG bump across the wedges of the EB based on the movement of the fly (Turner-Evans et al., 2017). Within the EB, the P-EN and E-PG neurons have shifted processes, whereas in the bridge, they arborize in the same glomerulus. Although only a single bump is localised in a single wedge of the EB, this bump would represent two individual bumps on the PB, on either side (left and right). When a fly decides to turn its head in either direction, the activity bump in the bridge can potentially be captured by the P-EN dendrites, which in turn would directionally activate an axonal wedge of the EB, different from the wedge containing the dendritic activity bump of the E-PG neurons.

Assuming that the P-EN neurons make excitatory connections with the E-PG neurons (Franconville et al., 2018), the activation of a particular wedge in the EB by the P-EN axons, would shift the dendritic activity bump of the E-PG neurons to that particular wedge of the EB, in a clockwise or anticlockwise direction (depending on the direction of the fly’s turning). We were persistent to study the importance of this mechanism in visual working memory, since the behaviour in the detour paradigm presumably involves the shifting of the dendritic E-PG bump within the wedges of the EB to efficiently represent the landmarks and the distractor. Overactivation of the P-EN (R12D09-GAL4; (Wolff et al., 2015)) neurons, led to complete loss of memory (Figure 31B). One would expect that excessive Ca^{2+} influx in these neurons might potentially lead to the activation of multiple glomeruli in the bridge, in addition to the two originally existing bumps representing the E-PG bump in a single wedge of the EB. This in turn can result in the activation of multiple axonal wedges of the EB, leading to erratic and unregulated movement of the dendritic E-PG bump across different wedges of the EB, and consequently a complete loss of visual working memory in these flies upon the neuronal activation by *TrpA1* (Figure 31B). Inactivation/silencing of the P-EN neurons with *shibire*^{ts1} led to a complete loss of

visual working memory once again (Figure 33B). The inactivation of these neurons, in this case, would not permit the efficient movement of dendritic activity bump across the glomeruli in the bridge. Thus, a failure in the shifting of the E-PG bump across the wedges of the EB might potentially occur, limiting the activity bump in the EB to remain stationary in one wedge. Further experiments focussing on the synaptic partners of the P-EN neurons to identify whether they interact with the E-PG neurons or any of the ring neurons of the EB, would be useful in understanding their role in visual working memory, in terms of connectomics.

4.2 (d) Predicted model for connectivity of neurons needed for *detour* memory

The EB, houses six different subfamilies of ring neurons of which four (R2,R3,R5 and R6), have been shown to play a vital role in visual working memory. Even though we are familiar with the functional aspects of R5 and R6 neurons, these neurons have been less explored in terms of their connectomics within the CC for us to deduce the reason for their involvement in this visual working memory. When it comes to recognizing visual objects, the R2/R4m neurons have been known to play a critical role (Pan et al., 2009). Since the R4 neurons did not seem to play a role in visual working memory in our temperature-shift experiments (Figure 30D, Figure 32D), we could deduce that the recognition of the landmarks and the distractor bar within the realm of the detour paradigm is performed solely by the R2 neurons.

According to recently published literature, R2 neurons are presynaptic partners of the R3d neurons (Omoto et al., 2018). However, the nature of neurotransmission between the ring neurons have been found to be predominantly GABA-ergic (Hanesch et al., 1989). This would mean that R3d recieves an inhibitory input from the R2 neurons when the landmarks are still present. According to the trans-Tango experiments conducted by Omoto and colleagues, the R3d neurons are presynaptic partners of R3p neurons (Omoto et al., 2018). The same paper also declares that the 189Y-GAL4 driver addresses both R3d and R3p neuronal subclasses. Temperature-shift experiments using this driver also negatively impacted detour memory (Figure 30C, Figure 32C), indicating that either R3d/R3p, or both of these neuronal subtypes, are crucial for visual working memory functioning. In terms of the connectivity between R2 and E-PG neurons, GRASP and trans-Tango experiments from literature have shown that R2 neurons are presynaptic, as well as postsynaptic partners to the E-PG neurons (Omoto et al., 2018; Kottler et al., 2019).

The nature of this synaptic input from R2-E-PG has been explored by Fisher and colleagues and revealed to be predominantly inhibitory (Fisher et al., 2019). Thus, it can be deduced that the E-PG neurons are silenced by an R2 neuron when the landmarks are still present. On the flip side, the nature of the synaptic input from the E-PG neurons to the R2 neurons has not yet been identified, and has the potential to be excitatory since physiological studies reveal the E-PG neurons to be predominantly excitatory (Franconville et al., 2018). This leads to the idea that the R2 neurons might receive an activational input from the E-PG neurons regarding the orientation of the fly towards the landmarks and the distractor (Figure 55).

When it comes to the interaction between the R3 and E-PG neurons, our GRASP experiments have shown that there exists a synaptic connectivity between the two, where they are each other's pre- and postsynaptic partners. However, it should be kept in mind that the neuroanatomical signal from the R3d & R3p neurons to the E-PG neurons, was significantly weaker than the signal received by the R3d & R3p neurons, from the E-PG neurons, indicating that the R3d & R3p neurons are presumably continuously activated by the E-PG neurons, even after the visual cues disappear. These R3 neurons communicate with each other, according to the trans-Tango results by Omoto and colleagues. However, it should be kept in mind that all of the inputs between the different R3 neuronal subclasses are presumably GABAergic, i.e., inhibitory (Figure 55). Having stated that, it is unlikely that most of the R3 subtypes remain completely inhibited for this working memory to function.

Therefore, we can make a deduction that the potential difference in the "weight" of inhibition amongst these neuronal subtypes, decides which R3 neurons remain active during this memory functioning. This would mean that there exists a degree of differential inhibition within these R3 subtypes. Our behavioural results indicate that R3p and R3d are potentially important candidates (189Y-GAL4 / VT42759-GAL4). Additionally, the R3m neurons (R28D01-GAL4; (Omoto et al., 2018)), were also tested in TrpA1 temperature-shift experiments and were proven to play a role in detour memory mechanism (see Appendix, Figure 57B). Thus, based on the behavioural results we have collected so far, we can declare that the R3/d/p/m are the regions where visual working memory is formed in *Drosophila*. The next step was to decipher how this memory is communicated to the PB. Shifting our focus now to the postsynaptic partners of R3 neurons, our GRASP experiments have depicted

that R3d & R3p neurons are presynaptic partners of E-PG neurons (Figure 55). However, looking at the trans-Tango data produced by Omoto and colleagues (Omoto et al., 2018), only R3a, R3m, and R3p subtypes of the R3 ring neurons have the E-PG neurons as their postsynaptic partner (Figure 55).

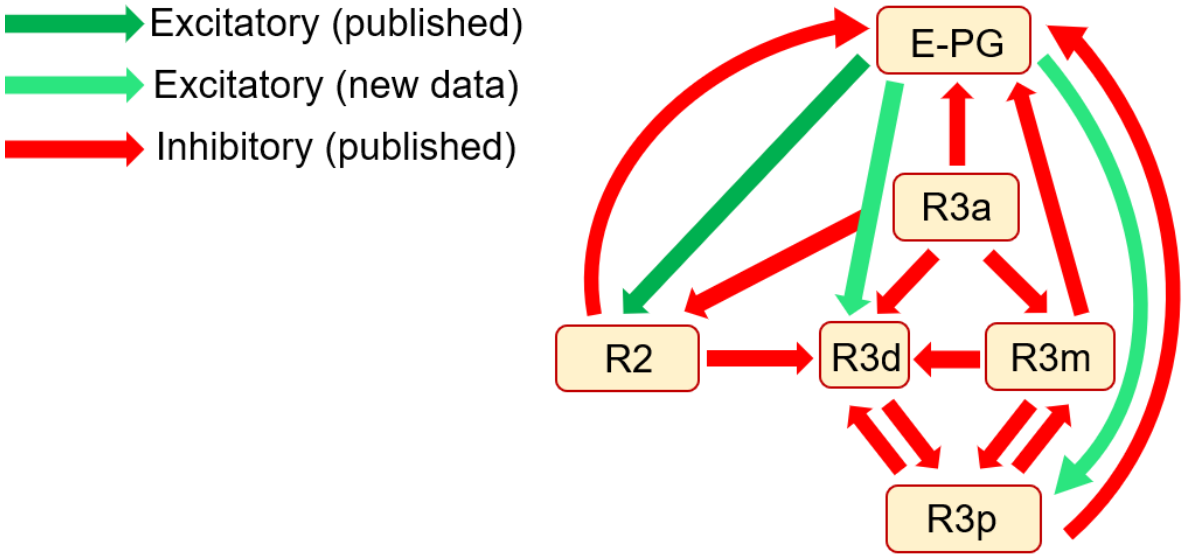

Figure 55: Connectivity between the EB ring neurons and the E-PG neurons

Block diagram of the neuronal network between the ring neurons and the E-PG neurons. The R3d & R3p neurons receive excitatory input from the E-PG neurons. The R3a neurons have inhibitory input into the R3d/m neurons which both have inhibitory input into the R3p neurons. The R3p neurons have inhibitory input into the E-PG neurons. The R2 neurons transmits an inhibitory input to the R3d as well as the E-PG neurons while receiving presynaptic input from the R3a neurons (inhibitory) and the E-PG neurons (excitatory).

The nature of the input from the R3 neurons to the E-PG neurons appears to be inhibitory in nature, according to the data published by Fisher and colleagues (Fisher et al., 2019). They used the R20A02-GAL4 driver to address the entire EB ring neurons which predominantly addressed the R3d/m/p neurons. Upon the silencing of these neurons (R3d/m/p) using UAS-*Kir2.1*, the hyperpolarization of the E-PG neurons was attenuated (Fisher et al., 2019), leading us to believe that the inputs from the R3p to the E-PG neurons are mostly inhibitory (Figure 55). Thus, with the information that is available to us from literature, and data from our own behaviour and network analysis, we attempted to predict a model for the connectome that allows for the functioning of visual working memory in *Drosophila*.

Firstly, the R2/R4m neurons of the EB obtain the visual information of the landmarks/distractor from the AOTU, which is processed through the superior regions of the bulb (BUs) (Omoto et al., 2017), and is received by individual R2 neurons, in addition to the excitatory input regarding the orientation of the landmarks/distractor

from the E-PG neurons. When the visual cues are still available, the R3 neurons (R3d), receives presynaptic input from a given R2 neuron, which is presumably GABAergic (inhibitory) (Figure 56B). This R2 neuron also transmits inhibitory input to the E-PG neurons (Figure 56B). On the other hand, some of the E-PG neurons which were not/less inactivated by the R2 neuron, presumably send excitatory input into the R3 (d&p) neurons regarding the orientation of the landmarks, which aids in the memory formation in the R3d/m/p neurons (Figure 56B), which presumably inhibit each other with differential strength (Figure 55). The idiothetic memory is built in the R3 neurons (R3d/m/p), based on the visual information received from the R2 neurons, and the orientation input from the E-PG neurons (Figure 56C). Once all visual cues disappear, the inhibitory signal recieved from the R2 neurons to R3 is attenuated, and the memory which was formed in the R3 neurons in the presence of visual cues is now used to help the fly decide the direction of turning. This “choice” is the read-out of the visual working memory.

In addition, the excitatory input from the E-PG neurons to the R3 neurons potentially continues for at least 30 seconds after the disappearance of the visual cue, according to the report by Seelig and Jayaraman (Seelig and Jayaraman, 2015). However, this memory cannot be communicated to the bridge via the E-PG neurons for two reasons: 1) this signal is GABAergic (inhibitory), and 2) according to our GRASP results, the strength of this transmission is fairly weak (Figure 40A), and would be an unlikely mechanism for the execution of this visual working memory. We therefore hypothesized that there might be other “executing neurons” within, and outside of the EB (Figure 56C) that receive the memory information from the R3 neurons, and form a network with the other regions of the CC. This network might potentially include the Δ7 and the P-EN neurons in a loop, since Franconville and colleagues suggest that E-PG neurons have excitatory input into the Δ7 neurons, which in turn have an excitatory input into the P-EN1 neurons, which transmit back into the E-PG neurons, once again through an excitatory input (Franconville et al., 2018). GRASP experiments within individual EB ring neuronal subtypes, as well as with other substructures of the CC alongside calcium imaging of R3 and other neurons during detour memory functioning, might be the way forward to solve the mystery of this connectome. Thus, we conclude that the R3 neurons (R3d,p&m) are the location for visual working memory. However, as for their synaptic partners which help execute detour memory, we are as of now, lost within the rings of the EB.

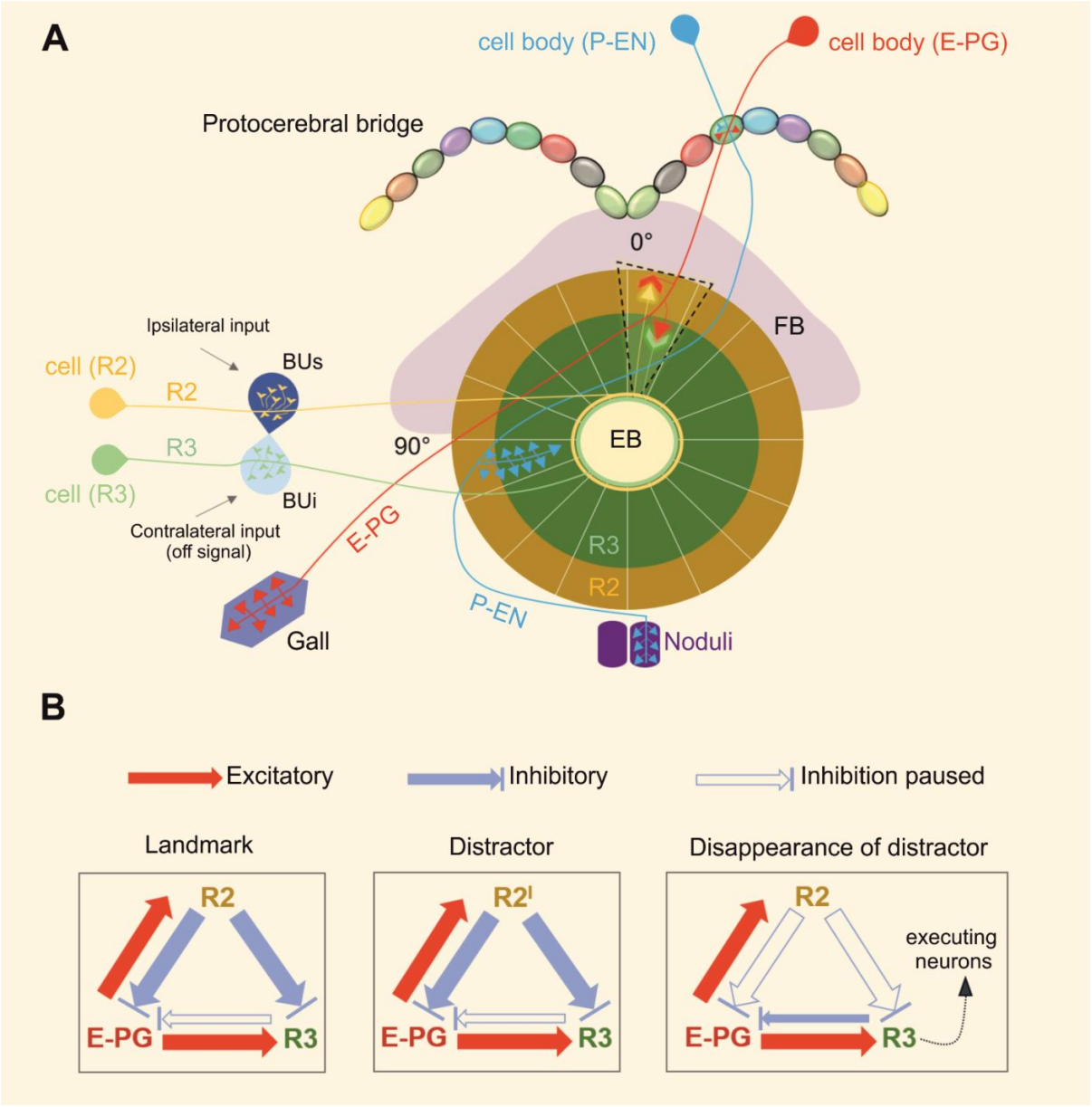

Figure 56: Predicted model for visual working memory in *Drosophila*

(A) Connectome between the EB ring neurons and E-PG/P-EN neurons during detour behaviour. The highlighted wedge represents the landmark (at 0°). The R2 neurons (yellow) recieve ipsilateral input from superior bulb (BUs) region. Contrastingly, the R3 neurons (green) are activated by contralateral input (off signal) from the inferior bulb (BUi) region. The E-PG neurons (red) send excitatory input into R3 and are inhibited by R2 when the landmark is present. The P-EN neurons (blue) aid in the shifting of the dendritic E-PG bump from the wedge representing the landmark (at 0°) to that of the distractor (at 90°) when the landmark is turned off and the distractor bar comes on.
(B) Predicted model for visual working memory. When the landmarks are present, the R2 neurons receive excitatory input from the visual cue as well as from the E-PG neurons. The R2 neurons in turn, send inhibitory inputs to R3 as well as the E-PG neurons, while the landmarks are present. The same trend continues when the landmark disappears and the distractor bar appears, however, this time the inhibitory function is carried out by a different R2 neuron ($R2^{I}$) that has been activated by the distractor bar as the visual cue. In parallel, the R3 neurons are activated by the E-PG neurons that have not been inactivated by R2. Using the visual input received from R2 and orientation input received from the E-PG neurons, the idiothetic memory is formed in the R3 neurons, when the landmarks are still present. Once all visual cues disappear, the inhibition of R3 neurons by R2 is attenuated while the activation of R3 neurons by E-PG neurons continues for at least 30 seconds. Simultaneously, the E-PG neurons receive weak inhibitory input from the R3 neurons. The idiothetic memory which was already formed in the R3 neurons, is then communicated to the “executing neurons” which might be a part of the EB as well as other regions of the CC, and execute the turning behavior, which is seen as a read-out for the visual working memory.

4.3 Effect of Tau on visual working memory in *Drosophila*

4.3 (a) Visual working memory in *Tau* knock-out flies

Functions of dTau

The existence of the *Drosophila* Tau protein was first predicted when it was recognized after the human Tau antibody cross-reacted with the microtubule-rich tissues in *Drosophila* (Wandosell and Avila, 1987). The first study focussing on the characterization of *Drosophila* Tau, stated that the localisation of the Tau protein is in the same compartments as that of the microtubules. This was seen to occur during development, as well as in adulthood, suggesting that this protein may perform critical cellular functions in post-mitotic cells, in addition to regulating the shape, and structural changes that a cell is bound to undergo (Heidary and Fortini, 2001). The paper also acknowledged the importance of Tau for the general functioning of the fly, since it was also expressed in non-neuronal tissues. Through the interaction with cellular partners such as tubulin, and actin, Tau has been known to mediate the structural maintenance of a neuron, as well as the synaptic scaffold and signalling (Morris et al., 2011).

Hyperphosphorylation of Tau

The participation of the Tau protein in the pathology associated with AD has been well recorded in vertebrates throughout the years. One of the primary symptoms of the AD phenotype is the presence of paired helical filaments (PHF) in the brains of the patients, and these structures seemed to contain an abundance of the microtubule-associated Tau (Kosik, 1990). There was an indication that the difference between regular Tau and the Tau that is observed in these PHFs, was that they were “abnormally” phosphorylated in the latter case (Grundke-Iqbal et al., 1986). The transition between regular Tau and hyperphosphorylated Tau that is present in these NFTs, is due to the phosphorylation of serines at certain positions of the Tau protein, through the activity of kinases such as, mitogen activated protein kinase (MAPK) (Drewes et al., 1992), glycogen synthase kinase 3 (GSK-3) (Mandelkow et al., 1992), and cyclin-dependent kinases (Baumann et al., 1993). This hyperphosphorylated state of Tau, disallows it from binding to microtubules, which can result in the breakdown of axonal transport, and other pathological effects (Jameson et al., 1980). In addition to causing NFT and neurodegeneration in

photoreceptors, hyperphosphorylation of Tau has also been proven to cause defects related to learning and memory (Beharry et al., 2013). However, one of the learnings that came out through Tau research in memory was that, the sequence in which the serines are phosphorylated on the Tau protein, is more important than the process of hyperphosphorylation itself (Papanikolopoulou and Skoulakis, 2015).

One of the earlier studies by Mershin and colleagues reported that the accumulation of wild-type Tau in the *Drosophila* MB neurons, led to olfactory learning and memory deficits, despite not causing neurodegeneration or decline in sensory perception (Mershin et al., 2004). A study from 2010 supported this finding, and identified ser^{238} and thr^{245} to be two the novel phosphorylation sites on the Tau protein, which caused structural defects in the *Drosophila* MB. While simply blocking the phosphorylation of these sites rescued the morphological defects, the MB still remained highly dysfunctional with respect to associative learning, proving that the morphological development of the MBs, and its functional properties are differentially regulated by *Tau* expression (Kosmidis et al., 2010).

Comparison of Tau^{KO} phenotype between mice and *Drosophila*

In case of mice, *Tau* knock-out mutants have shown reduced synaptic plasticity (Ahmed et al., 2014). However, electrophysiological studies revealed that although the Tau^{KO} mice displayed a wild-type like long-term depression (LTD), they showed reduced long-term potentiation (LTP). In addition, the authors of this paper discuss that this particular form of LTP loss shown by the KO mice, was similar to that observed when the NMDA receptor (NMDAR) is blocked. The effect of blocking NMDAR has also been addressed in other learning mechanisms (Fedulov et al., 2007). The KO mice used in this particular study were also impaired in terms of fear responses, indicating a deficit in hippocampal processing. Thus, this article pointed out that the loss of LTP in mice might be a potential read-out for deficits in spatial learning, and that the loss of Tau protein could lead to complex outcomes related to cognition, once again proving that Tau plays a major physiological role in synaptic plasticity, and certain forms of learning (Ahmed et al., 2014).

A more recent study addressing the same topic as Ahmed and colleagues, demonstrated that the homozygous deletion of *Tau* (*Mapt* in mice), led to a slight impairment in short-term spatial recognition memory (Biundo et al., 2018). This phenotype worsened with age, indicating that loss of Tau has a negative impact on

short-term memory with ageing. However, these mutant mice interestingly showed an increased locomotor activity at both 7 and 11 months of age. Mice homozygous, as well as heterozygous for the deletion mutation showed a deficit in the preference for novel objects, indicating an impairment in visual recognition. 18-month-old mice homozygous for the *Tau* deletion mutation, showed impairments in context-dependent memory, as well as a complete loss of olfactory associative learning and memory, once again revealing a pattern of age-dependent memory deficits in *Tau* deletion mutants (Biundo et al., 2018). In the same study, it was also noted that the processes associated with long-term potentiation (LTP), were also compromised in homozygous *Tau* deletion mutants, which was consistent with the overall cognitive decline in these animals.

In terms of *Drosophila* research, there have been contradictory findings in terms of how important Tau is for the survival and functioning of fruit flies. In 2016, a study came out by Burnouf and colleagues, which categorically stated that the deletion of endogenous Tau is not detrimental to flies (Burnouf et al., 2016). The authors of this study, stained for dTau in wild-type flies, which seemed to be localised in the brain, the ventral nerve chord (VNC), and throughout the peripheral nervous system. A huge fraction of dTau proteins were also phosphorylated, meaning they have undergone significant post-translational modifications, which also led to differences in their molecular weight. In order to test for neuronal abnormalities, the authors did an electrophysiology experiment to quantitatively assess the status of the giant fibre pathway in Tau^{KO} flies in comparison to the wild-type flies. Surprisingly, they did not observe any deficit in response latency to an electrical impulse.

In fact, the same study (Burnouf et al., 2016) showed that flies lacking Tau, had a shorter response time in comparison to those with a fully functional Tau protein. This effect was confirmed to not be due to the compensatory effect of upregulation of other microtubule-associated proteins in *Drosophila* such as, Futsch (MAP1 homolog), and Encosin (MAP7 homolog), which were found to be at the same levels as in wild-type flies. Loss of dTau also showed no increase in Aß-induced toxicity, indicating that dTau does not regulate *Drosophila* survival through this pathway. On the behavioural front, climbing abilities/locomotion of these flies were also not significantly different from wild-type, even after the flies were aged upto 39 days.

On the other hand, literature has also shown that the regulation of photoreceptor cell polarity (Nam, 2016), and maintenance of retinal development (Bolkan and Kretzschmar, 2014), are a few of the important functions dependent on Tau in *Drosophila.* However, it has to be pointed out that certain phenotypes exhibited by the RNAi-mediated knockdown of *Tau* in the above mentioned articles, were not observed in the Tau^{KO} flies, even though they both have reduced expression of *Tau*. Thus, these phenotypes might simply be an off-target effect of the knock-down mechanism. Nonetheless, a very recent study by Talmat-Amar and colleagues, expanded on the effects of deleting, as well as overexpressing *Tau* in flies (Talmat-Amar et al., 2018). While the loss and overexpression of Tau led to a proportional decrease and increase in microtubule (MT) density respectively, these changes in MT density also seemingly impacted the axonal calibre. But more importantly, these *Tau* mutant flies showed an increase in the pausing time of vesicles, even though the number of putatively mobile vesicles remained unaffected. On the other hand, overexpression of *Tau* led to an increased pausing time, accompanied by lesser number of mobilized vesicles. This finding led the authors to believe that decrease in MT density, does negatively impact vesicular transport, meaning that an optimal level of Tau expression is necessary for vesicle mobilization.

As recent as in 2019, Papanikolopoulou and colleagues showed that loss of dTau (Tau^{KO}), results in the reduction of α and ß tubulin, but an elevation in the major microtubule-associated motor proteins (Papanikolopoulou et al., 2019). In addition, loss of dTau also resulted in the increase of α and ß catenin, which are both actin-binding proteins. The same study could also validate the specific interaction taking place between dTau and polymerized filamentous actin (F-actin), where the total actin levels remain unaltered while F-actin levels in dTau mutants, were significantly reduced. This suggests that the microtubule lattice is less rigid in flies lacking dTau, further underscoring the role of Tau in microtubule, and actin cytoskeleton dynamics, which is similar to its function in vertebrates. The authors of this study suggest that dTau functions in distinct pathways that govern conditional neurotransmitter traffic and release within the MB α/ß neurons by regulating the actin and microtubule motor proteins. They conclude that it is due to this reason, that loss of dTau in flies differentially affects footshock habituation, and protein synthesis-dependent long-term memory (PSD-LTM) (Papanikolopoulou et al., 2019).

Thus, in our study, we tested the functioning of two types of *Tau* knock-outs, one from the Burnouf study where the KO (Tau^{KO}) flies were generated via homologous recombination (Burnouf et al., 2016), and the other from the Kretzschmar group, where the flies with *Tau* deletion (Tau^{del}) were synthesized using the CRISPR/Cas9 method. Homozygous mutants from both these groups, at 3 days of age, had a significant loss of memory in the detour paradigm in comparison to the wild-type flies of the same age (Figure 47A). This was a very strong phenotype, indicating that Tau is required in flies even at a young age to perform visual working memory.

The previously mentioned study by Papanikolopoulou et al., showed that, the expression levels of *Pka-C1* and *Syn* were reduced in flies after pan-neuronally inducing the RNAi-mediated knock-down of *Tau* in the adult nervous system, but their levels were not reduced in the Tau^{KO} mutants (Papanikolopoulou et al., 2019). Although the reduced expression levels of these proteins could be an off-target effect of the RNAi, it does help explain the deficit in visual working memory in 3-day-old Tau^{KO} flies in our hands, since we have previously shown that both PKA-C1 and Synapsin are needed for this particular memory (see section 3.1). However, we were skeptical about this particular result (Figure 47A) since Burnouf and colleagues claimed that Tau^{KO} flies showed no phenotype in their study. Thus, we wondered whether the phenotype we were observing was simply a result of the poor health of the flies, and decided to test the Tau^{KO} as well as the Tau^{del} flies, after raising them on food laced with tetracycline.

One of the ways in which the overall health of the flies can be affected, is the potential presence of bacteria in the fly food which could lead to infections. In order to combat this possibility, we utilized tetracycline, a well-established antibiotic. A recent study showed that the loss of *Tau* in flies, led to the initiation of the stress-responsive C-Jun-N-Terminal Kinase (JNK) signalling pathway. This eventually prevented the formation of new synapses and the deprivation of the existing synapses, ultimately leading to their decay (Voelzmann et al., 2016). A very interesting study related to Parkinson's disease in *Drosophila*, could show that "minocycline", a derivative of tetracycline is capable of delaying the neuronal decay caused in dopaminergic (DA) neurons when the genes related to the JNK pathway are overexpressed (Inamdar et al., 2012). However, this drug could not prevent further neuronal loss from occuring

when these genes were overexpressed. This suggests that tetracycline has the potential to interact with, and influence the functioning of the JNK pathway, but not indefinitely.

When we fed the 3-day-old homozygous *Tau* knock-out mutants with food laced with a specific concentration of tetracycline, there was a tremendous rescue of the detour memory score, where the flies now behaved like wild-type flies (Figure 47B). Since these are young flies, it is possible that tetracycline has potentially interacted and suppressed the genes of the JNK pathway, which were presumably hyperactivated as a result of *Tau* deletion, thereby leading to a full rescue of visual working memory in our study (Figure 47B). By targeting the JNK signalling pathway, tetracycline might have, in a way, slowed down the process of synaptic decay, leading to a complete rescue of visual working memory in these young homozygous *Tau* mutant flies (Figure 47B). Similarly, 3-day-old heterozygous *Tau* knock-out flies seemed to have an intact memory when treated with tetracycline food (Figure 49B), while showing a complete loss of memory when raised on regular food (Figure 49A). After the interesting discovery that the food containing tetracycline had positive effects on Tau-related visual working memory, we continued to perform the rest of the experiments in regular, as well as tetracycline food to compare their behavioural phenotypes.

Another completely different context in which tetracycline could have affected the visual working memory in flies, is by potentially negatively regulating the translation of certain proteins, specifically in Tau^{KO} flies, in a way that it affects visual working memory. We base this assumption on a recent publication by Mortison and colleagues who took the approach of preoteomics to reveal that variants of tetracycline could recognize rRNA binding sites, and thereby subtly modify the ribosomal translation in humans (Mortison et al., 2018). This is a fairly new aspect of tetracycline function that is yet to be explored in *Drosophila* in order to identify how it might potentially affect the phenotypes exhibited by other mutants. A paper from 2015 by Moullan and colleagues also showed that tetracycline could induce mitochondrial proteotoxic stress, which in turn, could negatively regulate nuclear gene expression even when present at relatively lower concentrations (Moullan et al., 2015).

Age-related decline in memory and cognitive performance, is one of the debilitating symptoms of AD. Abnormal axonal transportation leading to the accumulation of axonal cargo, is one of the major symptoms of AD. The axonal transport of amyloid precursor protein (APP) by means of Kinesin, a microtubule (MT) motor protein, is negatively regulated by GSK-3 (Weaver et al., 2013). Thus GSK-3 has been deemed responsible for serving as a contributing factor in AD pathology, by slowing down the bidirectional axonal transport of APP through the specific genetic interaction of GSK-3 with Kinesin 1 (Weaver et al., 2013). The key observation from this study was that the run length of APP transport was increased in both the anterograde, and retrograde directions while the frequency of pauses were reduced when dGSK-3 levels were reduced. The study brought to light the importance of axonal transport of APP, which is Kinesin-dependent.

Interestingly, Rieche and colleagues have reported that full-length *Drosophila* APPL (Amyloid Precursor Protein Like) is required in the R3 neurons for the functioning of visual working memory (Rieche et al., 2018). With the help of a double-tagged version of APPL (dtAPPL) driven in the R3 neurons, this study could visually prove that there was a reduction in the levels of dtAPPL in the axons of R3 neurons in aged flies (6 weeks old), which showed a deficit in visual working memory in comparison to 3-day-old flies, which had a significantly higher level of dtAPPL in the R3 neuronal axons, and a fully-functioning visual working memory. If we looked at this data in line with the recent reports stating that loss of Tau in *Drosophila* leads to reduced microtubule density and decreased axonal vesicular transport (Talmat-Amar et al., 2018), it appears that the loss of Tau would lead to a reduction in the level of MT protein Kinesin, which in turn leads to reduced levels of APPL. This phenomenon would result in an accelerated reduction in visual working memory, especially in ageing flies, which already experience a reduction of dtAPPL in their R3 axons. This was observed in visual working memory, where the 2-week-old *Tau* knock-out mutants had a complete loss of memory, despite being raised in tetracycline-containing food, in comparison to the 2-week-old wild-type flies, which perfomed with a high detour memory score (Figure 48). This indicates that loss of Tau affects visual working memory, which gets worse with ageing, specifically in homozygous deletion mutants completely lacking the Tau protein. In the ageing heterozygous mutants, however, an interesting phenomenon is observed.

Unlike in the case of 2-week-old homozygous mutants, the heterozygous *Tau* knock-outs did not experience a complete loss of memory, but an intermediate loss instead (Figure 50A). As time progressed, ageing was accelerated in the 3-week-old flies, leading to a complete loss of working memory in the heterozygous mutant flies in comparison to the 3-week-old WT-CS flies and $hTau^{WT}$/III flies, which performed with a fully-functioning visual working memory (Figure 50B). A reason for this, might be that the presence of 50% of endogenous dTau activity, can still facilitate the axonal transport of APPL, leading to a better memory than in the homozygous mutants. A way to test this hypothesis would be, to attempt to rescue the phenotype of these heterozygous mutants, by overexpressing full-length APPL (flAPPL) in aged flies. If the transport of flAPPL is vital for visual working memory, then increasing the cargo may potentially compensate for the partially-compromised Kinesin activity.

4.3 (b) Role of human *Tau* variants in visual working memory

Fronto-temporal dementia with parkinsonism linked to chromosome 17 (FTDP-17), encompasses a collection of neurodegenerative pathologies that are seemingly diverse, yet have several overlapping features. Since human *Tau* is also located on chromosome 17, it was considered for a genetic linkage analysis, which revealed that the *Tau* gene was indeed associated with these hereditary neurodegenerative diseases (Clark et al., 1998). A common mechanism that occurs in these pathologies, is the presence of hyperphosphorylated Tau aggregates (Hong et al., 1998). The earliest indication of the involvement of Tau in FTDP-17, was when Poorkaj and colleagues, reported a co-segregation of a missense mutation in the longest isoform of Tau (*hTauV337M*) with FTD (Poorkaj et al., 1998).

A study from 2004 showed that the missense mutations in *Tau*, have gain of toxic functions, where these mutations lead to higher susceptibility for Tau hyperphosphorylation. (Alonso et al., 2004). This study by Alonso and colleagues, recognized several mutations of *Tau* that causes this hyperphosphorylation effect, viz., *hTauV337M* ($hTau^{V/M}$) and *hTauP301L* ($hTau^{P/L}$). As mentioned earlier in this section, the hyperphosphorylation of Tau precedes neurofibrillary tangle formation in AD (Bancher et al., 1989), and is also associated with the depolymerization of microtubules *in vitro* (Alonso et al., 1996). Additionally, $hTau^{P/L}$ and $hTau^{V/M}$ are also associated with heightened aggregate formation, which accelerated paired helical filament (PHF) formation (Barghorn et al., 2000; Hutton, 2000), suggesting that this

point mutation plays a dual role in aggravating the pathology related to AD, and other neurodegenerative diseases.

When we tested the flies expressing the homozygous forms of these missense mutations (*hTau*$^{V/M}$ and *hTau*$^{P/L}$), their visual working memory was significantly reduced compared to the memory of the wild-type homozygous *hTau*^{WT} as well as the wild-type control flies (Figure 51A). This signifies that both human Tau, as well as endogenous *Drosophila* Tau, could aid in the functioning of visual working memory. An additional missense mutation that we tested in visual working memory, was the *hTauK369I* (*hTau*$^{K/I}$), which was first reported in the neuropathology associated with Pick's disease, and was also related to reduced capacity for microtubule assembly (Neumann et al., 2001). Flies homozygous for this mutation (*hTau*$^{K/I}$), completely lost their visual working memory even at 3 days (Figure 51A), indicating that this mutation affects visual working memory slightly differently than the other two mutations, which also target microtubule-assembly.

As we had previously discussed regarding the *Tau* knock-out and deletion mutants, we pondered whether treating the three-day old homozygous mutant flies with food containing tetracycline, could potentially rescue their visual working memory. When we applied the same methodology to the *Tau* variants at 3 days of age, their memory could not be rescued, and the flies containing the missense mutations for *hTau*, continued to have a significantly lower memory score compared to the *hTau*^{WT} and the WT-CS flies (Figure 51B). This can be due to many reasons such as, the inherent genetic difference between mutations and the deletion of the entire coding region of the gene and the functional defects elicited in both these cases.

Since the Tau variants are autosomal dominant (Gistelinck et al., 2012), we decided to test the heterozygous mutants to observe how they impact visual working memory. Testing of young (3-day old), heretozygous mutants for the human *Tau* variants, however, showed a wild-type like visual working memory in two out of the three variants. The heterozygous mutants for *hTau*$^{K/I}$ and *hTau*$^{P/L}$ behaved like wild-type flies. This could signify that the availability of 50% intact *dTau*, can potentially compensate for the other copy of the gene coding for the Tau protein with defective microtubule binding. Heterozygous *hTau*$^{V/M}$, on the other hand, had a significantly reduced memory score compared to the *hTau*^{WT}/III, and the WT-CS flies (Figure 52).

The *hTau*$^{V/M}$ mutation, is associated with a type of dementia identified in an American family with Czech descent (Seattle family A), and one of the neuropathological symptoms of this disease is memory loss (Sumi et al., 1992). In mice, it has been shown that this mutation has a very specific effect on impulsive behaviour and the executive functions, which are governed by the frontal cortex (Lambourne et al., 2007; Reichelt et al., 2013). Thus, its differential impact on visual working memory compared to the other *Tau* mutants, could be due to its effect on the executive functions related to memory and instantaneous decision making. The study also showed an age-related exacerbation in impulse response behaviour in mice, showing that this mutation has the potential to express incremental defects with ageing.

In the detour paradigm, heterozygous *hTau*$^{V/M}$, along with the *hTau*$^{K/I}$ mutants, experienced a loss of visual working memory after two weeks of ageing, when compared to the heterozygous *hTau*^{WT} group, and the WT-CS group (Figure 53A). The group which seemed to be most affected by ageing, was the *hTau*$^{P/L}$ group, which exhibited a complete loss of memory. An explanation for this, could be that this mutation leads to multiple negative effects, which can get exponentially worse with ageing. Some of the effects elicited by the *hTau*$^{P/L}$ mutation in vertebrates are, 1) accelerated aggregation (Barghorn et al., 2000), 2) beta sheet formation (von Bergen et al., 2001) *in vitro*, 3) increasing the propensity for hyperphosphorylation of Tau (Alonso et al., 2004) and 4) increased neurodegeneration caused by the upregulation of *vapb* (coding for a vesicle trafficking protein) in the brainstem, which was thought to be a potential enhancer or mediator of the *hTau*$^{P/L}$-induced neurodegeneration (Karsten et al., 2006). After three weeks of ageing, it appeared as though all the heterozygous *Tau* missense mutations caused enough neurodegeneration through individual mechanisms related to microtubule disassembly, finally resulting in a complete loss of visual working memory in *Drosophila* (Figure 53B).

With these findings, we can confirm that the human *Tau* variants do show deficits related to visual working memory, which became progressively worse with ageing and was completely lost after 3 weeks of ageing. This shows us that *Drosophila* has the potential to be an efficient model to study the behavioural phenotypes accompanying FTDP-17, and other forms of Tauopathies in terms of short-term visual orientation memory.

5. Summary

In our present study, we could prove that the cyclic AMP-dependent Protein Kinase A (PKA), plays a critical role in the functioning of visual working memory in *Drosophila melanogaster*. The detour paradigm (Neuser et al., 2008), was used to assess the visual working memory in flies, where a fly is allowed to walk back and forth towards two opposing vertical stripes, until stopped by a water moat. Once these landmarks disappear, a new distractor bar appears at right angles to the original landmarks. This distractor bar is also removed one second after the fly turns towards it, and the fly is now left without visual cues, and is reliant on its idiothetic memory to remember the direction of the original landmark it was walking towards. This memory is built in the R3 neurons of the ellipsoid body (Kuntz et al., 2012). In my dissertation, we show that PKA activity is required specifically in the presynaptic region of the R3 ring neurons of the ellipsoid body for this memory to function. The availability of PKA at the presynaptic sites of the R3 neurons, is regulated by an AKAP, Rugose. This Golgi-associated protein, potentially attaches itself to the PKA complex, and sequesters it to the Golgi network, thereby preventing its phosphorylating activity at the presynapse of the R3 neurons. Reducing the levels of Rugose by means of a hypomorphic allele or an RNAi-mediated knock-down, specifically in the R3 neurons, helped increase the levels of PKA-C1 available at the presynapse to phosphorylate Synapsin at PKA phosphorylation site-1. Synapsin performs the function of binding to, and tethering neurotransmitter-filled synaptic vesicles to the cytoskeleton. Phosphorylation of Synapsin by PKA, would facilitate in the deployment of these vesicles from the reserve pool to the readily releasable pool, thereby creating a shift between the reserve and the recyclable pool, which ultimately leads to the functioning of visual working memory. The PKA recognition site-1 on the A domain of the Synapsin protein, is edited by ADAR (Diegelmann et al., 2006), leading to a consenus sequence change from RRFS to RGFS, and consequently to an equal proportion of edited, and non-edited Synapsin protein. However, the cyclic guanosine monophosphate (cGMP), induced by nitric oxide synthase (NOS), potentially allows for the influx of Ca^{2+} ions through the cGMP-gated channels, by interacting with cyclic nucleotide-gated (CNG) channel subunits at the presynapse. This calcium influx can now activate CaMKII at the presynapse, thereby allowing the phosphorylation of Synapsin at this site by CaMKII, and enabling the functioning of this working memory when PKA is unable to.

Secondly, this work has also revealed that although the visual working memory is formed in the R3 ring neurons, additional ring-neuron types such as, the R2, R5, and R6 ring, along with the non-canonical ring neuron subfamilies, i.e. L-Ei and L-Em neurons, are also involved in the functioning of this memory. Additionally, we uncovered the importance of the neurons that govern heading representation in *Drosophila,* i.e. the compass and shift neurons, for the functioning of visual working memory. Subsequently, we attempted to understand the neuroanatomics between the compass neurons, and the R3 neurons in the context of visual working memory. We could prove that the R3 neurons and E-PG neurons are synaptic partners of each other in a bidirectional manner, and that the nature of this synaptic interaction is stronger in one direction (E-PG→R3). When the visual cues are still present, the idiothetic memory is formed, and constantly updated in the R3 (d,m&p) neurons with the aid of the orientation information provided by the E-PG neurons, and the visual input from the R2 neurons. We therefore predict that once all landmarks disappear in the detour arena, this information regarding the idiothetic memory is presumably communicated to the “executing neurons”, which facilitate its execution either independently, or via excitatory synaptic connections with other areas of the CC.

Finally, we proved that the microtubule-associated protein (MAP) Tau, is important for visual working memory in *Drosophila*. Young, homozygous *Tau* deletion mutants had a complete loss of visual working memory, while heterozygous *Tau* deletion mutants showcased a wild-type like detour memory. These heterozygous *Tau* deletion mutants also rapidly lost their visual working memory after 3 weeks in comparison to age-matched wild-type flies. This was potentially because of the slowing down of Kinesin-mediated axonal transport of APPL in the *Tau* deletion mutants since APPL is required in the R3 axons for visual working memory in *Drosophila* (Rieche et al., 2018). Additionally, when we replaced the *Drosophila Tau* (*dTau*) with human *Tau* (*hTau*) containing point mutations associated with fronto-temporal dementia (FTD) in humans, a complete lack of memory was seen, even in young homozygous mutants. The heterozygous mutant flies, behaved wild-type like at 3 days but completely lost their visual memory after 3 weeks in comaparison to age-matched wild-type flies. Thus, it can be concluded that the absence of Tau activity, tremendously accelerates the deficits in visual working memory in an age-dependent manner in *Drosophila*.

6. References

Ahmed, T., Van der Jeugd, A., Blum, D., Galas, M. C., D'Hooge, R., Buee, L. and Balschun, D. (2014) 'Cognition and hippocampal synaptic plasticity in mice with a homozygous Tau deletion', *Neurobiol Aging* 35(11): 2474-2478.

Alonso, A. C., Grundke-Iqbal, I. and Iqbal, K. (1996) 'Alzheimer's disease hyperphosphorylated tau sequesters normal tau into tangles of filaments and disassembles microtubules', *Nat Med* 2(7): 783-7.

Alonso, A. D., Mederlyova, A., Novak, M., Grundke-Iqbal, I. and Iqbal, K. (2004) 'Promotion of hyperphosphorylation by frontotemporal dementia Tau mutations', *Journal of Biological Chemistry* 279(33): 34873-34881.

Angelo, R. and Rubin, C. S. (1998) 'Molecular characterization of an anchor protein (AKAPCE) that binds the RI subunit (RCE) of type I Protein Kinase A from *Caenorhabditis elegans*', *J Biol Chem* 273(23): 14633-43.

Armstrong, J. D., Kaiser, K., Muller, A., Fischbach, K. F., Merchant, N. and Strausfeld, N. J. (1995) 'Flybrain, an on-line atlas and database of the *Drosophila* nervous system', *Neuron* 15(1): 17-20.

Ashley, J., Packard, M., Ataman, B. and Budnik, V. (2005) 'Fasciclin II signals new synapse formation through amyloid precursor protein and the scaffolding protein dX11/Mint', *J Neurosci* 25(25): 5943-55.

Atwood, H. L., Govind, C. K. and Wu, C. F. (1993) 'Differential ultrastructure of synaptic terminals on ventral longitudinal abdominal muscles in *Drosophila* larvae', *J Neurobiol* 24(8): 1008-24.

Bahler, M., Benfenati, F., Valtorta, F. and Greengard, P. (1990) 'The Synapsins and the Regulation of Synaptic Function', *Bioessays* 12(6): 259-263.

Bahler, M. and Greengard, P. (1987) 'Synapsin I bundles F-actin in a phosphorylation-dependent manner', *Nature* 326(6114): 704-7.

Baker, B. S., Taylor, B. J. and Hall, J. C. (2001) 'Are complex behaviors specified by dedicated regulatory genes? Reasoning from *Drosophila*', *Cell* 105(1): 13-24.

Bancher, C., Brunner, C., Lassmann, H., Budka, H., Jellinger, K., Wiche, G., Seitelberger, F., Grundke-Iqbal, I., Iqbal, K. and Wisniewski, H. M. (1989)

'Accumulation of abnormally phosphorylated Tau precedes the formation of neurofibrillary tangles in Alzheimer's disease', *Brain Res* 477(1-2): 90-9.

Barghorn, S., Zheng-Fischhofer, Q., Ackmann, M., Biernat, J., von Bergen, M., Mandelkow, E. M. and Mandelkow, E. (2000) 'Structure, microtubule interactions, and paired helical filament aggregation by Tau mutants of frontotemporal dementias', *Biochemistry* 39(38): 11714-11721.

Bass, B. L. (2002) 'RNA editing by adenosine deaminases that act on RNA', *Annual Review of Biochemistry* 71: 817-846.

Bass, B. L., Nishikura, K., Keller, W., Seeburg, P. H., Emeson, R. B., OConnell, M. A., Samuel, C. E. and Herbert, A. (1997) 'A standardized nomenclature for adenosine deaminases that act on RNA', *RNA* 3(9): 947-949.

Baumann, K., Mandelkow, E. M., Biernat, J., Piwnica-Worms, H. and Mandelkow, E. (1993) 'Abnormal Alzheimer-like phosphorylation of Tau-protein by cyclin-dependent kinases cdk2 and cdk5', *FEBS Lett* 336(3): 417-24.

Bausenwein, B., Muller, N. R. and Heisenberg, M. (1994) 'Behavior-dependent activity labeling in the central complex of *Drosophila* during controlled visual stimulation', *J Comp Neurol* 340(2): 255-68.

Beharry, C., Alaniz, M. E. and Alonso Adel, C. (2013) 'Expression of Alzheimer-like pathological human Tau induces a behavioral motor and olfactory learning deficit in *Drosophila melanogaster*', *J Alzheimers Dis* 37(3): 539-50.

Belay, A. T., Scheiner, R., So, A. K., Douglas, S. J., Chakaborty-Chatterjee, M., Levine, J. D. and Sokolowski, M. B. (2007) 'The foraging gene of *Drosophila melanogaster*: spatial-expression analysis and sucrose responsiveness', *J Comp Neurol* 504(5): 570-82.

Benfenati, F., Valtorta, F. and Greengard, P. (1991) 'Computer Modeling of Synapsin-I Binding to Synaptic Vesicles and F-Actin - Implications for Regulation of Neurotransmitter Release', *Proc Natl Acad Sci U S A* 88(2): 575-579.

Benfenati, F., Valtorta, F., Rossi, M. C., Onofri, F., Sihra, T. and Greengard, P. (1993) 'Interactions of Synapsin I with phospholipids: possible role in synaptic vesicle clustering and in the maintenance of bilayer structures', *J Cell Biol* 123(6 Pt 2): 1845-55.

Benzer, S. (1967) 'Behavioral mutants of *Drosophila* isolated by countercurrent distribution', *Proc Natl Acad Sci U S A* 58(3): 1112-9.

Benzer, S. (1973) 'Genetic dissection of behavior', *Sci Am* 229(6): 24-37.

Betz, W. J. and Bewick, G. S. (1992) 'Optical analysis of synaptic vesicle recycling at the frog neuromuscular junction', *Science* 255(5041): 200-3.

Biernat, J., Gustke, N., Drewes, G., Mandelkow, E. M. and Mandelkow, E. (1993) 'Phosphorylation of Ser^{262} strongly reduces binding of Tau to microtubules: distinction between PHF-like immunoreactivity and microtubule binding', *Neuron* 11(1): 153-63.

Biundo, F., Del Prete, D., Zhang, H., Arancio, O. and D'Adamio, L. (2018) 'A role for tau in learning, memory and synaptic plasticity', *Sci Rep* 8(1): 3184.

Blanco-Redondo, B., Nuwal, N., Kneitz, S., Nuwal, T., Halder, P., Liu, Y., Ehmann, N., Scholz, N., Mayer, A., Kleber, J. et al. (2019) 'Implications of the Sap47 null mutation for Synapsin phosphorylation, longevity, climbing proficiency and behavioural plasticity in adult *Drosophila*', *J Exp Biol* 222(Pt 19).

Bolkan, B. J. and Kretzschmar, D. (2014) 'Loss of Tau results in defects in photoreceptor development and progressive neuronal degeneration in *Drosophila*', *Dev Neurobiol* 74(12): 1210-25.

Booker, R. and Quinn, W. G. (1981) 'Conditioning of leg position in normal and mutant *Drosophila*', *Proc Natl Acad Sci U S A* 78(6): 3940-4.

Borrell, V. (2019) 'Recent advances in understanding neocortical development', *F1000Res* 8.

Brand, A. H. and Perrimon, N. (1993) 'Targeted gene expression as a means of altering cell fates and generating dominant phenotypes', *Development* 118(2): 401-15.

Burnouf, S., Gronke, S., Augustin, H., Dols, J., Gorsky, M. K., Werner, J., Kerr, F., Alic, N., Martinez, P. and Partridge, L. (2016) 'Deletion of endogenous Tau proteins is not detrimental in *Drosophila*', *Sci Rep* 6: 23102.

Byers, D., Davis, R. L. and Kiger, J. A., Jr. (1981) 'Defect in cyclic AMP phosphodiesterase due to the dunce mutation of learning in *Drosophila melanogaster*', *Nature* 289(5793): 79-81.

Cervantes-Sandoval, I., Martin-Pena, A., Berry, J. A. and Davis, R. L. (2013) 'System-like consolidation of olfactory memories in *Drosophila*', *J Neurosci* 33(23): 9846-54.

Cesca, F., Baldelli, P., Valtorta, F. and Benfenati, F. (2010) 'The synapsins: key actors of synapse function and plasticity', *Prog Neurobiol* 91(4): 313-48.

Chen, S., Lee, A. Y., Bowens, N. M., Huber, R. and Kravitz, E. A. (2002) 'Fighting fruit flies: a model system for the study of aggression', *Proc Natl Acad Sci U S A* 99(8): 5664-8.

Chen, Y., Akin, O., Nern, A., Tsui, C. Y., Pecot, M. Y. and Zipursky, S. L. (2014) 'Cell-type-specific labeling of synapses in vivo through synaptic tagging with recombination', *Neuron* 81(2): 280-93.

Cho, R. W., Buhl, L. K., Volfson, D., Tran, A., Li, F., Akbergenova, Y. and Littleton, J. T. (2015) 'Phosphorylation of Complexin by PKA Regulates Activity-Dependent Spontaneous Neurotransmitter Release and Structural Synaptic Plasticity', *Neuron* 88(4): 749-61.

Chopra, I. and Roberts, M. (2001) 'Tetracycline antibiotics: mode of action, applications, molecular biology, and epidemiology of bacterial resistance', *Microbiol Mol Biol Rev* 65(2): 232-60 ; second page, table of contents.

Clapham, D. E. (2015) 'Structural biology: Pain-sensing TRPA1 channel resolved', *Nature* 520(7548): 439-41.

Clark, L. N., Poorkaj, P., Wszolek, Z., Geschwind, D. H., Nasreddine, Z. S., Miller, B., Li, D., Payami, H., Awert, F., Markopoulou, K. et al. (1998) 'Pathogenic implications of mutations in the Tau gene in pallido-ponto-nigral degeneration and related neurodegenerative disorders linked to chromosome 17', *Proc Natl Acad Sci U S A* 95(22): 13103-7.

Coffino, P., Bourne, H. R., Friedrich, U., Hochman, J., Insel, P. A., Lemaire, I., Melmon, K. L. and Tomkins, G. M. (1976) 'Molecular mechanisms of cyclic AMP action: a genetic approach', *Recent Prog Horm Res* 32: 669-84.

Collett, M. (2009) 'Spatial memories in insects', *Curr Biol* 19(24): R1103-8.

Collett, M., Chittka, L. and Collett, T. S. (2013) 'Spatial memory in insect navigation', *Curr Biol* 23(17): R789-800.

Cooley, L., Kelley, R. and Spradling, A. (1988) 'Insertional mutagenesis of the *Drosophila* genome with single P elements', *Science* 239(4844): 1121-8.

Cruse, H. and Wehner, R. (2011) 'No need for a cognitive map: decentralized memory for insect navigation', *PLoS Comput Biol* 7(3): e1002009.

Davis, G. W., DiAntonio, A., Petersen, S. A. and Goodman, C. S. (1998) 'Postsynaptic PKA controls quantal size and reveals a retrograde signal that regulates presynaptic transmitter release in *Drosophila*', *Neuron* 20(2): 305-15.

Davis, R. L. (1993) 'Mushroom bodies and *Drosophila* learning', *Neuron* 11(1): 1-14.

Davis, R. L., Cherry, J., Dauwalder, B., Han, P. L. and Skoulakis, E. (1995) 'The cyclic AMP system and *Drosophila* learning', *Mol Cell Biochem* 149-150: 271-8.

de Belle, J. S. and Heisenberg, M. (1994) 'Associative odor learning in *Drosophila* abolished by chemical ablation of mushroom bodies', *Science* 263(5147): 692-5.

Delgado, R., Hidalgo, P., Diaz, F., Latorre, R. and Labarca, P. (1991) 'A Cyclic AMP-Activated K^+ Channel in *Drosophila* Larval Muscle Is Persistently Activated in Dunce', *Proc Natl Acad Sci U S A* 88(2): 557-560.

Dell'Acqua, M. L., Smith, K. E., Gorski, J. A., Horne, E. A., Gibson, E. S. and Gomez, L. L. (2006) 'Regulation of neuronal PKA signaling through AKAP targeting dynamics', *Eur J Cell Biol* 85(7): 627-33.

Dhallan, R. S., Yau, K. W., Schrader, K. A. and Reed, R. R. (1990) 'Primary Structure and Functional Expression of a Cyclic Nucleotide-Activated Channel from Olfactory Neurons', *Nature* 347(6289): 184-187.

Diegelmann, S., Klagges, B., Michels, B., Schleyer, M. and Gerber, B. (2013) 'Maggot learning and Synapsin function', *J Exp Biol* 216(Pt 6): 939-51.

Diegelmann, S., Nieratschker, V., Werner, U., Hoppe, J., Zars, T. and Buchner, E. (2006) 'The conserved Protein Kinase-A target motif in Synapsin of *Drosophila* is effectively modified by pre-mRNA editing', *BMC Neurosci* 7: 76.

Dietzl, G., Chen, D., Schnorrer, F., Su, K. C., Barinova, Y., Fellner, M., Gasser, B., Kinsey, K., Oppel, S., Scheiblauer, S. et al. (2007) 'A genome-wide transgenic RNAi library for conditional gene inactivation in *Drosophila*', *Nature* 448(7150): 151-6.

Dill, M., Wolf, R. and Heisenberg, M. (1993) 'Visual pattern recognition in *Drosophila* involves retinotopic matching', *Nature* 365(6448): 751-3.

Dill, M., Wolf, R. and Heisenberg, M. (1995) 'Behavioral analysis of *Drosophila* landmark learning in the flight simulator', *Learn Mem* 2(3-4): 152-60.

Dissel, S., Angadi, V., Kirszenblat, L., Suzuki, Y., Donlea, J., Klose, M., Koch, Z., English, D., Winsky-Sommerer, R., van Swinderen, B. et al. (2015) 'Sleep restores behavioral plasticity to *Drosophila* mutants', *Curr Biol* 25(10): 1270-81.

Drain, P., Folkers, E. and Quinn, W. G. (1991) 'cAMP-dependent protein kinase and the disruption of learning in transgenic flies', *Neuron* 6(1): 71-82.

Drewes, G., Lichtenberg-Kraag, B., Doring, F., Mandelkow, E. M., Biernat, J., Goris, J., Doree, M. and Mandelkow, E. (1992) 'Mitogen activated protein (MAP) kinase transforms Tau protein into an Alzheimer-like state', *EMBO J* 11(6): 2131-8.

Dubruille, R., Laurencon, A., Vandaele, C., Shishido, E., Coulon-Bublex, M., Swoboda, P., Couble, P., Kernan, M. and Durand, B. (2002) '*Drosophila* regulatory factor X is necessary for ciliated sensory neuron differentiation', *Development* 129(23): 5487-98.

Dudai, Y. (1988) 'Neurogenetic dissection of learning and short-term memory in *Drosophila*', *Annu Rev Neurosci* 11: 537-63.

Dudai, Y., Buxbaum, J., Corfas, G., Orgad, S., Segal, D., Sher, B., Uzzan, A. and Zvi, S. (1986) 'Defective cAMP metabolism and defective memory in *Drosophila*', *Acta Biochim Biophys Hung* 21(3): 177-92.

Fedulov, V., Rex, C. S., Simmons, D. A., Palmer, L., Gall, C. M. and Lynch, G. (2007) 'Evidence that long-term potentiation occurs within individual hippocampal synapses during learning', *Journal of Neuroscience* 27(30): 8031-8039.

Feinberg, E. H., Vanhoven, M. K., Bendesky, A., Wang, G., Fetter, R. D., Shen, K. and Bargmann, C. I. (2008) 'GFP Reconstitution Across Synaptic Partners (GRASP) defines cell contacts and synapses in living nervous systems', *Neuron* 57(3): 353-63.

Ferreira, A., Kosik, K. S., Greengard, P. and Han, H. Q. (1994) 'Aberrant Neurites and Synaptic Vesicle Protein-Deficiency in Synapsin II-Depleted Neurons', *Science* 264(5161): 977-979.

Ferreira, A. and Rapoport, M. (2002) 'The Synapsins: beyond the regulation of neurotransmitter release', *Cellular and Molecular Life Sciences* 59(4): 589-595.

Fire, A., Xu, S., Montgomery, M. K., Kostas, S. A., Driver, S. E. and Mello, C. C. (1998) 'Potent and specific genetic interference by double-stranded RNA in *Caenorhabditis elegans*', *Nature* 391(6669): 806-11.

Fisher, Y. E., Lu, J., D'Alessandro, I. and Wilson, R. I. (2019) 'Sensorimotor experience remaps visual input to a heading-direction network', *Nature*. 2019 Dec;576(7785):121-125. 10.1038/s41586-019-1772-4.

Fiumara, F., Giovedi, S., Menegon, A., Milanese, C., Merlo, D., Montarolo, P. G., Valtorta, F., Benfenati, F. and Ghirardi, M. (2004) 'Phosphorylation by cAMP-dependent protein kinase is essential for Synapsin-induced enhancement of neurotransmitter release in invertebrate neurons', *J Cell Sci* 117(Pt 21): 5145-54.

Franconville, R., Beron, C. and Jayaraman, V. (2018) 'Building a functional connectome of the *Drosophila* central complex', *Elife* 7. 10.7554/eLife.37017

Friedrich, P., Solti, M. and Gyurkovics, H. (1984) 'Microcompartmentation of cAMP in wild-type and memory-mutant dunce strains of *Drosophila melanogaster*', *J Cell Biochem* 26(3): 197-203.

Gervasi, N., Tchenio, P. and Preat, T. (2010) 'PKA dynamics in a *Drosophila* learning center: coincidence detection by rutabaga adenylyl cyclase and spatial regulation by dunce phosphodiesterase', *Neuron* 65(4): 516-29.

Gillespie, J. M. and Hodge, J. J. (2013) 'CASK regulates CaMKII autophosphorylation in neuronal growth, calcium signaling, and learning', *Front Mol Neurosci* 6: 27.

Giraldo, Y. M., Leitch, K. J., Ros, I. G., Warren, T. L., Weir, P. T. and Dickinson, M. H. (2018) 'Sun Navigation Requires Compass Neurons in *Drosophila*', *Curr Biol* 28(17): 2845-2852 e4.

Gistelinck, M., Lambert, J. C., Callaerts, P., Dermaut, B. and Dourlen, P. (2012) '*Drosophila* models of tauopathies: what have we learned?', *Int J Alzheimers Dis* 2012: 970980.

Godenschwege, T. A., Reisch, D., Diegelmann, S., Eberle, K., Funk, N., Heisenberg, M., Hoppe, V., Hoppe, J., Klagges, B. R., Martin, J. R. et al. (2004) 'Flies lacking all Synapsins are unexpectedly healthy but are impaired in complex behaviour', *Eur J Neurosci* 20(3): 611-22.

Goedert, M., Spillantini, M. G., Jakes, R., Rutherford, D. and Crowther, R. A. (1989) 'Multiple Isoforms of Human Microtubule-Associated Protein-Tau - Sequences and Localization in Neurofibrillary Tangles of Alzheimers-Disease', *Neuron* 3(4): 519-526.

Green, J., Adachi, A., Shah, K. K., Hirokawa, J. D., Magani, P. S. and Maimon, G. (2017) 'A neural circuit architecture for angular integration in *Drosophila*', *Nature* 546(7656): 101-106.

Greengard, P., Valtorta, F., Czernik, A. J. and Benfenati, F. (1993) 'Synaptic vesicle phosphoproteins and regulation of synaptic function', *Science* 259(5096): 780-5.

Greenspan, R. J. (1995) 'Flies, genes, learning, and memory', *Neuron* 15(4): 747-50.

Griffith, L. C., Verselis, L. M., Aitken, K. M., Kyriacou, C. P., Danho, W. and Greenspan, R. J. (1993) 'Inhibition of calcium/calmodulin-dependent protein kinase in *Drosophila* disrupts behavioral plasticity', *Neuron* 10(3): 501-9.

Groth, A. C., Fish, M., Nusse, R. and Calos, M. P. (2004) 'Construction of transgenic *Drosophila* by using the site-specific integrase from phage phiC31', *Genetics* 166(4): 1775-82.

Grundke-Iqbal, I., Iqbal, K., Tung, Y. C., Quinlan, M., Wisniewski, H. M. and Binder, L. I. (1986) 'Abnormal phosphorylation of the microtubule-associated protein Tau (Tau) in Alzheimer cytoskeletal pathology', *Proc Natl Acad Sci U S A* 83(13): 4913-7.

Guo, C., Du, Y., Yuan, D., Li, M., Gong, H., Gong, Z. and Liu, L. (2014) 'A conditioned visual orientation requires the ellipsoid body in *Drosophila*', *Learn Mem* 22(1): 56-63.

Guo, C., Pan, Y. and Gong, Z. (2019) 'Recent Advances in the Genetic Dissection of Neural Circuits in *Drosophila*', *Neurosci Bull*.

Guven-Ozkan, T. and Davis, R. L. (2014) 'Functional neuroanatomy of *Drosophila* olfactory memory formation', *Learn Mem* 21(10): 519-26.

Hamada, F. N., Rosenzweig, M., Kang, K., Pulver, S. R., Ghezzi, A., Jegla, T. J. and Garrity, P. A. (2008) 'An internal thermal sensor controlling temperature preference in *Drosophila*', *Nature* 454(7201): 217-20.

Han, P. L., Levin, L. R., Reed, R. R. and Davis, R. L. (1992) 'Preferential expression of the *Drosophila* rutabaga gene in mushroom bodies, neural centers for learning in insects', *Neuron* 9(4): 619-27.

Hanesch, U., Fischbach, K. F. and Heisenberg, M. (1989) 'Neuronal Architecture of the Central Complex in *Drosophila melanogaster*', *Cell Tissue Res* 257(2): 343-366.

Heidary, G. and Fortini, M. E. (2001) 'Identification and characterization of the *Drosophila* Tau homolog', *Mech Dev* 108(1-2): 171-8.

Heisenberg, M. (2003) 'Mushroom body memoir: from maps to models', *Nat Rev Neurosci* 4(4): 266-75.

Heisenberg, M., Borst, A., Wagner, S. and Byers, D. (1985) '*Drosophila* mushroom body mutants are deficient in olfactory learning', *J Neurogenet* 2(1): 1-30.

Herberg, F. W., Maleszka, A., Eide, T., Vossebein, L. and Tasken, K. (2000) 'Analysis of A-kinase anchoring protein (AKAP) interaction with protein kinase A (PKA) regulatory subunits: PKA isoform specificity in AKAP binding', *J Mol Biol* 298(2): 329-39.

Higham, J. P., Malik, B. R., Buhl, E., Dawson, J. M., Ogier, A. S., Lunnon, K. and Hodge, J. J. L. (2019) 'Alzheimer's Disease Associated Genes Ankyrin and Tau Cause Shortened Lifespan and Memory Loss in *Drosophila*', *Front Cell Neurosci* 13: 260.

Higuchi, M., Single, F. N., Kohler, M., Sommer, B., Sprengel, R. and Seeburg, P. H. (1993) 'RNA editing of AMPA receptor subunit GluR-B: a base-paired intron-exon structure determines position and efficiency', *Cell* 75(7): 1361-70.

Hilfiker, S., Pieribone, V. A., Czernik, A. J., Kao, H. T., Augustine, G. J. and Greengard, P. (1999) 'Synapsins as regulators of neurotransmitter release', *Philos Trans R Soc Lond B Biol Sci* 354(1381): 269-79.

Hong, M., Zhukareva, V., Vogelsberg-Ragaglia, V., Wszolek, Z., Reed, L., Miller, B. I., Geschwind, D. H., Bird, T. D., McKeel, D., Goate, A. et al. (1998) 'Mutation-specific functional impairments in distinct tau isoforms of hereditary FTDP-17', *Science* 282(5395): 1914-7.

Hoopengardner, B., Bhalla, T., Staber, C. and Reenan, R. (2003) 'Nervous system targets of RNA editing identified by comparative genomics', *Science* 301(5634): 832-6.

Hopp, T. P., Prickett, K. S., Price, V. L., Libby, R. T., March, C. J., Cerretti, D. P., Urdal, D. L. and Conlon, P. J. (1988) 'A Short Polypeptide Marker Sequence Useful for Recombinant Protein Identification and Purification', *Bio-Technology* 6(10): 1204-1210.

Hosaka, M., Hammer, R. E. and Sudhof, T. C. (1999) 'A phospho-switch controls the dynamic association of synapsins with synaptic vesicles', *Neuron* 24(2): 377-87.

Huang, L. J., Durick, K., Weiner, J. A., Chun, J. and Taylor, S. S. (1997a) 'D-AKAP2, a novel protein kinase A anchoring protein with a putative RGS domain', *Proc Natl Acad Sci U S A* 94(21): 11184-9.

Huang, L. J., Durick, K., Weiner, J. A., Chun, J. and Taylor, S. S. (1997b) 'Identification of a novel protein kinase A anchoring protein that binds both type I and type II regulatory subunits', *J Biol Chem* 272(12): 8057-64.

Huttner, W. B., DeGennaro, L. J. and Greengard, P. (1981) 'Differential phosphorylation of multiple sites in purified protein I by cyclic AMP-dependent and calcium-dependent protein kinases', *J Biol Chem* 256(3): 1482-8.

Hutton, M. (2000) 'Molecular genetics of chromosome 17 tauopathies', *Ann N Y Acad Sci* 920: 63-73.

Iijima, K., Gatt, A. and Iijima-Ando, K. (2010) 'Tau Ser^{262} phosphorylation is critical for Aβ42-induced Tau toxicity in a transgenic *Drosophila* model of Alzheimer's disease', *Hum Mol Genet* 19(15): 2947-57.

Ilius, M., Wolf, R. and Heisenberg, M. (1994) 'The central complex of *Drosophila melanogaster* is involved in flight control: studies on mutants and mosaics of the gene ellipsoid body open', *J Neurogenet* 9(3): 189-206.

Inamdar, A. A., Chaudhuri, A. and O'Donnell, J. (2012) 'The Protective Effect of Minocycline in a Paraquat-Induced Parkinson's Disease Model in *Drosophila* is Modified in Altered Genetic Backgrounds', *Parkinsons Disease*.

Jameson, L., Frey, T., Zeeberg, B., Dalldorf, F. and Caplow, M. (1980) 'Inhibition of microtubule assembly by phosphorylation of microtubule-associated proteins', *Biochemistry* 19(11): 2472-9.

Jenett, A., Rubin, G. M., Ngo, T. T., Shepherd, D., Murphy, C., Dionne, H., Pfeiffer, B. D., Cavallaro, A., Hall, D., Jeter, J. et al. (2012) 'A GAL4-driver line resource for *Drosophila* neurobiology', *Cell Rep* 2(4): 991-1001.

Jin, P., Griffith, L. C. and Murphey, R. K. (1998) 'Presynaptic calcium/calmodulin-dependent protein kinase II regulates habituation of a simple reflex in adult *Drosophila*', *J Neurosci* 18(21): 8955-64.

Jinek, M., Chylinski, K., Fonfara, I., Hauer, M., Doudna, J. A. and Charpentier, E. (2012) 'A Programmable Dual-RNA-Guided DNA Endonuclease in Adaptive Bacterial Immunity', *Science* 337(6096): 816-821.

Jing, M., Zhang, P., Wang, G., Feng, J., Mesik, L., Zeng, J., Jiang, H., Wang, S., Looby, J. C., Guagliardo, N. A. et al. (2018) 'A genetically encoded fluorescent acetylcholine indicator for in vitro and in vivo studies', *Nat Biotechnol* 36(8): 726-737.

Kahsai, L., Carlsson, M. A., Winther, A. M. and Nassel, D. R. (2012) 'Distribution of metabotropic receptors of serotonin, dopamine, GABA, glutamate, and short neuropeptide F in the central complex of *Drosophila*', *Neuroscience* 208: 11-26.

Kahsai, L., Martin, J. R. and Winther, A. M. (2010) 'Neuropeptides in the *Drosophila* central complex in modulation of locomotor behavior', *J Exp Biol* 213(Pt 13): 2256-65.

Kalderon, D. and Rubin, G. M. (1988) 'Isolation and characterization of *Drosophila* cAMP-dependent protein kinase genes', *Genes Dev* 2(12A): 1539-56.

Kalderon, D. and Rubin, G. M. (1989) 'cGMP-dependent protein kinase genes in *Drosophila*', *J Biol Chem* 264(18): 10738-48.

Kandel, E. R. (2001) 'The molecular biology of memory storage: a dialogue between genes and synapses', *Science* 294(5544): 1030-8.

Kao, H. T., Porton, B., Hilfiker, S., Stefani, G., Pieribone, V. A., DeSalle, R. and Greengard, P. (1999) 'Molecular evolution of the Synapsin gene family', *J Exp Zool* 285(4): 360-77.

Karsten, S. L., Sang, T. K., Gehman, L. T., Chatterjee, S., Liu, J. K., Lawless, G. M., Sengupta, S., Berry, R. W., Pomakian, J., Oh, H. S. et al. (2006) 'A genomic screen for modifiers of tauopathy identifies puromycin-sensitive aminopeptidase as an inhibitor of Tau-induced neurodegeneration', *Neuron* 51(5): 549-560.

Kasuya, J., Ishimoto, H. and Kitamoto, T. (2009) 'Neuronal mechanisms of learning and memory revealed by spatial and temporal suppression of neurotransmission using shibire, a temperature-sensitive dynamin mutant gene in *Drosophila melanogaster*', *Front Mol Neurosci* 2: 11.

Kazama, H. (2015) 'Systems neuroscience in *Drosophila*: Conceptual and technical advantages', *Neuroscience* 296: 3-14.

Kennedy, M. B. and Greengard, P. (1981) 'Two calcium/calmodulin-dependent protein kinases, which are highly concentrated in brain, phosphorylate protein I at distinct sites', *Proc Natl Acad Sci U S A* 78(2): 1293-7.

Kennedy, M. B., McGuinness, T. and Greengard, P. (1983) 'A calcium/calmodulin-dependent protein kinase from mammalian brain that phosphorylates Synapsin I: partial purification and characterization', *J Neurosci* 3(4): 818-31.

Khan, A., Paro, S., McGurk, L., Sambrani, N., Hogg, M. C., Brindle, J., Pennetta, G., Keegan, L. P. and O'Connell, M. A. (2020) 'Membrane and synaptic defects leading to neurodegeneration in Adar mutant *Drosophila* are rescued by increased autophagy', *BMC Biol* 18(1): 15.

Kiger, J. A., Jr., Eklund, J. L., Younger, S. H. and O'Kane, C. J. (1999) 'Transgenic inhibitors identify two roles for protein kinase A in *Drosophila* development', *Genetics* 152(1): 281-90.

Kim, S. S., Hermundstad, A. M., Romani, S., Abbott, L. F. and Jayaraman, V. (2019) 'Generation of stable heading representations in diverse visual scenes', *Nature*.

Kim, S. S., Rouault, H., Druckmann, S. and Jayaraman, V. (2017) 'Ring attractor dynamics in the *Drosophila* central brain', *Science* 356(6340): 849-853.

Kim, Y. T. and Wu, C. F. (1996) 'Reduced growth cone motility in cultured neurons from *Drosophila* memory mutants with a defective cAMP cascade', *J Neurosci* 16(18): 5593-602.

Kitamoto, T. (2001) 'Conditional modification of behavior in *Drosophila* by targeted expression of a temperature-sensitive shibire allele in defined neurons', *J Neurobiol* 47(2): 81-92.

Kitamoto, T. (2002) 'Targeted expression of temperature-sensitive dynamin to study neural mechanisms of complex behavior in *Drosophila*', *J Neurogenet* 16(4): 205-28.

Klagges, B. R., Heimbeck, G., Godenschwege, T. A., Hofbauer, A., Pflugfelder, G. O., Reifegerste, R., Reisch, D., Schaupp, M., Buchner, S. and Buchner, E. (1996) 'Invertebrate Synapsins: a single gene codes for several isoforms in *Drosophila*', *J Neurosci* 16(10): 3154-65.

Klapoetke, N. C., Murata, Y., Kim, S. S., Pulver, S. R., Birdsey-Benson, A., Cho, Y. K., Morimoto, T. K., Chuong, A. S., Carpenter, E. J., Tian, Z. et al. (2014) 'Addendum: independent optical excitation of distinct neural populations', *Nat Methods* 11(9): 972.

Konopka, R. J. and Benzer, S. (1971) 'Clock mutants of *Drosophila melanogaster*', *Proc Natl Acad Sci U S A* 68(9): 2112-6.

Kosaka, T. and Ikeda, K. (1983) 'Possible temperature-dependent blockage of synaptic vesicle recycling induced by a single gene mutation in *Drosophila*', *J Neurobiol* 14(3): 207-25.

Kosik, K. S. (1990) 'Tau protein and Alzheimer's disease', *Curr Opin Cell Biol* 2(1): 101-4.

Kosmidis, S., Grammenoudi, S., Papanikolopoulou, K. and Skoulakis, E. M. (2010) 'Differential effects of Tau on the integrity and function of neurons essential for learning in *Drosophila*', *J Neurosci* 30(2): 464-77.

Kottler, B., Faville, R., Bridi, J. C. and Hirth, F. (2019) 'Inverse Control of Turning Behavior by Dopamine D1 Receptor Signaling in Columnar and Ring Neurons of the Central Complex in *Drosophila*', *Curr Biol* 29(4): 567-577 e6.

Krause, T., Spindler, L., Poeck, B. and Strauss, R. (2019) '*Drosophila* Acquires a Long-Lasting Body-Size Memory from Visual Feedback', *Curr Biol* 29(11): 1833-1841 e3.

Kuntz, S., Poeck, B., Sokolowski, M. B. and Strauss, R. (2012) 'The visual orientation memory of *Drosophila* requires Foraging (PKG) upstream of Ignorant (RSK2) in ring neurons of the central complex', *Learn Mem* 19(8): 337-40.

Kuntz, S., Poeck, B. and Strauss, R. (2017) 'Visual Working Memory Requires Permissive and Instructive NO/cGMP Signaling at Presynapses in the *Drosophila* Central Brain', *Curr Biol* 27(5): 613-623.

Kuntz, Sara (2015) 'Analyse biochemischer Signalwege eines visuellen Orientierungsgedächtnisses von *Drosophila*': 231.

Kuromi, H. and Kidokoro, Y. (1998) 'Two distinct pools of synaptic vesicles in single presynaptic boutons in a temperature-sensitive *Drosophila* mutant, shibire', *Neuron* 20(5): 917-25.

Kuromi, H. and Kidokoro, Y. (2000) 'Tetanic stimulation recruits vesicles from reserve pool via a cAMP-mediated process in *Drosophila* synapses', *Neuron* 27(1): 133-43.

Kvon, E. Z., Kazmar, T., Stampfel, G., Yanez-Cuna, J. O., Pagani, M., Schernhuber, K., Dickson, B. J. and Stark, A. (2014) 'Genome-scale functional characterization of *Drosophila* developmental enhancers in vivo', *Nature* 512(7512): 91-5.

Lai, S. L. and Lee, T. (2006) 'Genetic mosaic with dual binary transcriptional systems in *Drosophila*', *Nat Neurosci* 9(5): 703-9.

Lalotra, Dennis (2014) 'Genetische Analyse des PKA Signalweges für ein Arbeitsgedächtnis von *Drosophila* mittels Enhancer/Suppressor Durchmusterung': 96.

Lambourne, S. L., Humby, T., Isles, A. R., Emson, P. C., Spillantini, M. G. and Wilkinson, L. S. (2007) 'Impairments in impulse control in mice transgenic for the human FTDP-17 Tau^{V337M} mutation are exacerbated by age', *Hum Mol Genet* 16(14): 1708-19.

Lane, M. E. and Kalderon, D. (1993) 'Genetic investigation of cAMP-dependent protein kinase function in *Drosophila* development', *Genes Dev* 7(7A): 1229-43.

Lee, G., Cowan, N. and Kirschner, M. (1988) 'The primary structure and heterogeneity of Tau protein from mouse brain', *Science* 239(4837): 285-8.

Lee, G., Neve, R. L. and Kosik, K. S. (1989) 'The microtubule binding domain of Tau protein', *Neuron* 2(6): 1615-24.

Lee, T. (2017) 'Wiring the *Drosophila* Brain with Individually Tailored Neural Lineages', *Curr Biol* 27(2): R77-R82.

Lee, T. and Luo, L. (1999) 'Mosaic analysis with a repressible cell marker for studies of gene function in neuronal morphogenesis', *Neuron* 22(3): 451-61.

Lee, Y. (2013) 'Contribution of *Drosophila* TRPA1-expressing neurons to circadian locomotor activity patterns', *PLoS One* 8(12): e85189.

Lee, Y. S., Nakahara, K., Pham, J. W., Kim, K., He, Z., Sontheimer, E. J. and Carthew, R. W. (2004) 'Distinct roles for *Drosophila* Dicer-1 and Dicer-2 in the siRNA/miRNA silencing pathways', *Cell* 117(1): 69-81.

Levin, R. M. and Weiss, B. (1976) 'Mechanism by which psychotropic drugs inhibit adenosine cyclic 3',5'-monophosphate phosphodiesterase of brain', *Mol Pharmacol* 12(4): 581-9.

Li, W., Ohlmeyer, J. T., Lane, M. E. and Kalderon, D. (1995) 'Function of protein kinase A in hedgehog signal transduction and *Drosophila* imaginal disc development', *Cell* 80(4): 553-62.

Li, W., Tully, T. and Kalderon, D. (1996) 'Effects of a conditional *Drosophila* PKA mutant on olfactory learning and memory', *Learn Mem* 2(6): 320-33.

Li, X., Yu, F. and Guo, A. (2009) 'Sleep deprivation specifically impairs short-term olfactory memory in *Drosophila*', *Sleep* 32(11): 1417-24.

Liang, X., Ho, M. C. W., Zhang, Y., Li, Y., Wu, M. N., Holy, T. E. and Taghert, P. H. (2019) 'Morning and Evening Circadian Pacemakers Independently Drive Premotor Centers via a Specific Dopamine Relay', *Neuron* 102(4): 843-857 e4.

Lin, C. Y., Chuang, C. C., Hua, T. E., Chen, C. C., Dickson, B. J., Greenspan, R. J. and Chiang, A. S. (2013) 'A comprehensive wiring diagram of the protocerebral bridge for visual information processing in the *Drosophila* brain', *Cell Rep* 3(5): 1739-53.

Lin, H. H., Lai, J. S., Chin, A. L., Chen, Y. C. and Chiang, A. S. (2007) 'A map of olfactory representation in the *Drosophila* mushroom body', *Cell* 128(6): 1205-17.

Lin, S., Ewen-Campen, B., Ni, X., Housden, B. E. and Perrimon, N. (2015) 'In Vivo Transcriptional Activation Using CRISPR/Cas9 in *Drosophila*', *Genetics* 201(2): 433-42.

Liu, G., Seiler, H., Wen, A., Zars, T., Ito, K., Wolf, R., Heisenberg, M. and Liu, L. (2006) 'Distinct memory traces for two visual features in the *Drosophila* brain', *Nature* 439(7076): 551-6.

Livingstone, M. S., Sziber, P. P. and Quinn, W. G. (1984) 'Loss of calcium/calmodulin responsiveness in adenylate cyclase of rutabaga, a *Drosophila* learning mutant', *Cell* 37(1): 205-15.

Livingstone, M. S. and Tempel, B. L. (1983) 'Genetic dissection of monoamine neurotransmitter synthesis in *Drosophila*', *Nature* 303(5912): 67-70.

Lohr, R., Godenschwege, T., Buchner, E. and Prokop, A. (2002) 'Compartmentalization of central neurons in *Drosophila*: a new strategy of mosaic analysis reveals localization of presynaptic sites to specific segments of neurites', *J Neurosci* 22(23): 10357-67.

Lovick, J. K., Omoto, J. J., Ngo, K. T. and Hartenstein, V. (2017) 'Development of the anterior visual input pathway to the *Drosophila* central complex', *J Comp Neurol* 525(16): 3458-3475.

Luan, H., Peabody, N. C., Vinson, C. R. and White, B. H. (2006) 'Refined spatial manipulation of neuronal function by combinatorial restriction of transgene expression', *Neuron* 52(3): 425-36.

Lyons, L. C. and Roman, G. (2009) 'Circadian modulation of short-term memory in *Drosophila*', *Learn Mem* 16(1): 19-27.

Macpherson, L. J., Zaharieva, E. E., Kearney, P. J., Alpert, M. H., Lin, T. Y., Turan, Z., Lee, C. H. and Gallio, M. (2015) 'Dynamic labelling of neural connections in multiple colours by trans-synaptic fluorescence complementation', *Nat Commun* 6: 10024.

Maimon, G., Straw, A. D. and Dickinson, M. H. (2008) 'A simple vision-based algorithm for decision making in flying *Drosophila*', *Curr Biol* 18(6): 464-70.

Maistrenko, O. M., Serga, S. V., Vaiserman, A. M. and Kozeretska, I. A. (2015) 'Effect of Wolbachia Infection on Aging and Longevity-Associated Genes in *Drosophila*', *Life Extension: Lessons from Drosophila* 3: 83-104.

Mandelkow, E. M., Drewes, G., Biernat, J., Gustke, N., Van Lint, J., Vandenheede, J. R. and Mandelkow, E. (1992) 'Glycogen synthase kinase-3 and the Alzheimer-like state of microtubule-associated protein Tau', *FEBS Lett* 314(3): 315-21.

Marlène Cassar, Alexander D. Law, Eileen S. Chow, Jadwiga M. Giebultowicz, Doris Kretzschmar (2020) 'Disease-Associated Mutant Tau Prevents Circadian Changes in the Cytoskeleton of Central Pacemaker Neurons', *Front Neurosci* Volume 14(Article 232): 9.

Martin, J. R., Raabe, T. and Heisenberg, M. (1999) 'Central complex substructures are required for the maintenance of locomotor activity in *Drosophila melanogaster*', *J Comp Physiol A* 185(3): 277-88.

McBride, S. M., Giuliani, G., Choi, C., Krause, P., Correale, D., Watson, K., Baker, G. and Siwicki, K. K. (1999) 'Mushroom body ablation impairs short-term memory and long-term memory of courtship conditioning in *Drosophila melanogaster*', *Neuron* 24(4): 967-77.

McGuire, S. E., Mao, Z. and Davis, R. L. (2004) 'Spatiotemporal gene expression targeting with the TARGET and gene-switch systems in *Drosophila*', *Sci STKE* 2004(220): pl6.

McKnight, G. S., Cadd, G. G., Clegg, C. H., Otten, A. D. and Correll, L. A. (1988) 'Expression of wild-type and mutant subunits of the cAMP-dependent protein kinase', *Cold Spring Harb Symp Quant Biol* 53 Pt 1: 111-9.

Menne, D. and Spatz, H. C. (1977) 'Color-Vision in *Drosophila melanogaster*', *Journal of Comparative Physiology* 114(3): 301-312.

Mershin, A., Pavlopoulos, E., Fitch, O., Braden, B. C., Nanopoulos, D. V. and Skoulakis, E. M. (2004) 'Learning and memory deficits upon TAU accumulation in *Drosophila* mushroom body neurons', *Learn Mem* 11(3): 277-87.

Mery, F. (2007) 'Aging and its differential effects on consolidated memory forms in *Drosophila*', *Exp Gerontol* 42(1-2): 99-101.

Michels, B., Chen, Y. C., Saumweber, T., Mishra, D., Tanimoto, H., Schmid, B., Engmann, O. and Gerber, B. (2011) 'Cellular site and molecular mode of Synapsin action in associative learning', *Learn Mem* 18(5): 332-44.

Michels, B., Diegelmann, S., Tanimoto, H., Schwenkert, I., Buchner, E. and Gerber, B. (2005) 'A role for Synapsin in associative learning: the *Drosophila* larva as a study case', *Learn Mem* 12(3): 224-31.

Miller, S. G. and Kennedy, M. B. (1986) 'Regulation of brain type II Ca^{2+}/calmodulin-dependent protein kinase by autophosphorylation: a Ca^{2+}-triggered molecular switch', *Cell* 44(6): 861-70.

Mitschulat, H. (1989) 'Dynamic properties of the Ca^{2+}/calmodulin-dependent protein kinase in Drosophila: identification of a synapsin I-like protein', *Proc Natl Acad Sci U S A* 86(15): 5988-92.

Morris, M., Maeda, S., Vossel, K. and Mucke, L. (2011) 'The many faces of Tau', *Neuron* 70(3): 410-26.

Mortison, J. D., Schenone, M., Myers, J. A., Zhang, Z. Y., Chen, L. F., Ciarlo, C., Comer, E., Natchiar, S. K., Carr, S. A., Klaholz, B. P. et al. (2018) 'Tetracyclines Modify Translation by Targeting Key Human rRNA Substructures', *Cell Chemical Biology* 25(12): 1506-1518e13. 10.1016/j.chembiol.2018.09.010

Moser, E. I., Roudi, Y., Witter, M. P., Kentros, C., Bonhoeffer, T. and Moser, M. B. (2014) 'Grid cells and cortical representation', *Nat Rev Neurosci* 15(7): 466-81.

Moullan, N., Mouchiroud, L., Wang, X., Ryu, D., Williams, E. G., Mottis, A., Jovaisaite, V., Frochaux, M. V., Quiros, P. M., Deplancke, B. et al. (2015) 'Tetracyclines Disturb Mitochondrial Function across Eukaryotic Models: A Call for Caution in Biomedical Research', *Cell Rep* 10(10): 1681-1691.

Nam, S. C. (2016) 'Role of Tau, a microtubule associated protein, in *Drosophila* photoreceptor morphogenesis', *Genesis* 54(11): 553-561.

Neumann, M., Schulz-Schaeffer, W., Crowther, R. A., Smith, M. J., Spillantini, M. G., Goedert, M. and Kretzschmar, H. A. (2001) 'Pick's disease associated with the novel Tau gene mutation K369I', *Ann Neurol* 50(4): 503-13.

Neuser, K., Triphan, T., Mronz, M., Poeck, B. and Strauss, R. (2008) 'Analysis of a spatial orientation memory in *Drosophila*', *Nature* 453(7199): 1244-7.

Ni, J. Q., Markstein, M., Binari, R., Pfeiffer, B., Liu, L. P., Villalta, C., Booker, M., Perkins, L. and Perrimon, N. (2008) 'Vector and parameters for targeted transgenic RNA interference in *Drosophila melanogaster*', *Nat Methods* 5(1): 49-51.

Nicolai, L. J., Ramaekers, A., Raemaekers, T., Drozdzecki, A., Mauss, A. S., Yan, J., Landgraf, M., Annaert, W. and Hassan, B. A. (2010) 'Genetically encoded dendritic marker sheds light on neuronal connectivity in *Drosophila*', *Proc Natl Acad Sci U S A* 107(47): 20553-8.

Niewalda, T., Michels, B., Jungnickel, R., Diegelmann, S., Kleber, J., Kahne, T. and Gerber, B. (2015) 'Synapsin determines memory strength after punishment- and relief-learning', *J Neurosci* 35(19): 7487-502.

Nighorn, A., Healy, M. J. and Davis, R. L. (1991) 'The cyclic AMP phosphodiesterase encoded by the *Drosophila* dunce gene is concentrated in the mushroom body neuropil', *Neuron* 6(3): 455-67.

Nitabach, M. N., Wu, Y., Sheeba, V., Lemon, W. C., Strumbos, J., Zelensky, P. K., White, B. H. and Holmes, T. C. (2006) 'Electrical hyperexcitation of lateral ventral pacemaker neurons desynchronizes downstream circadian oscillators in the fly circadian circuit and induces multiple behavioral periods', *J Neurosci* 26(2): 479-89.

O'Kane, C. J. and Gehring, W. J. (1987) 'Detection in situ of genomic regulatory elements in *Drosophila*', *Proc Natl Acad Sci U S A* 84(24): 9123-7.

Ofstad, T. A., Zuker, C. S. and Reiser, M. B. (2011) 'Visual place learning in *Drosophila melanogaster*', *Nature* 474(7350): 204-7.

Olsen, S. R. and Wilson, R. I. (2008) 'Cracking neural circuits in a tiny brain: new approaches for understanding the neural circuitry of *Drosophila*', *Trends Neurosci* 31(10): 512-20.

Omoto, J. J., Keles, M. F., Nguyen, B. M., Bolanos, C., Lovick, J. K., Frye, M. A. and Hartenstein, V. (2017) 'Visual Input to the *Drosophila* Central Complex by Developmentally and Functionally Distinct Neuronal Populations', *Curr Biol* 27(8): 1098-1110.

Omoto, J. J., Nguyen, B. M., Kandimalla, P., Lovick, J. K., Donlea, J. M. and Hartenstein, V. (2018) 'Neuronal Constituents and Putative Interactions Within the *Drosophila* Ellipsoid Body Neuropil', *Front Neural Circuits* 12: 103.

Otsuna, H. and Ito, K. (2006) 'Systematic analysis of the visual projection neurons of *Drosophila melanogaster*. I. Lobula-specific pathways', *J Comp Neurol* 497(6): 928-58.

Palladino, M. J., Keegan, L. P., O'Connell, M. A. and Reenan, R. A. (2000) 'dADAR, a *Drosophila* double-stranded RNA-specific adenosine deaminase is highly developmentally regulated and is itself a target for RNA editing', *RNA* 6(7): 1004-1018.

Pan, Y., Zhou, Y., Guo, C., Gong, H., Gong, Z. and Liu, L. (2009) 'Differential roles of the fan-shaped body and the ellipsoid body in *Drosophila* visual pattern memory', *Learn Mem* 16(5): 289-95.

Papanikolopoulou, K., Roussou, I. G., Gouzi, J. Y., Samiotaki, M., Panayotou, G., Turin, L. and Skoulakis, E. M. C. (2019) '*Drosophila* Tau Negatively Regulates Translation and Olfactory Long-Term Memory, But Facilitates Footshock Habituation and Cytoskeletal Homeostasis', *J Neurosci* 39(42): 8315-8329.

Papanikolopoulou, K. and Skoulakis, E. M. (2015) 'Temporally distinct phosphorylations differentiate Tau-dependent learning deficits and premature mortality in *Drosophila*', *Hum Mol Genet* 24(7): 2065-77.

Paradis, S., Sweeney, S. T. and Davis, G. W. (2001) 'Homeostatic control of presynaptic release is triggered by postsynaptic membrane depolarization', *Neuron* 30(3): 737-49.

Park, D., Coleman, M. J., Hodge, J. J., Budnik, V. and Griffith, L. C. (2002) 'Regulation of neuronal excitability in *Drosophila* by constitutively active CaMKII', *J Neurobiol* 52(1): 24-42.

Pascual, A. and Preat, T. (2001) 'Localization of long-term memory within the *Drosophila* mushroom body', *Science* 294(5544): 1115-7.

Pech, U., Dipt, S., Barth, J., Singh, P., Jauch, M., Thum, A. S., Fiala, A. and Riemensperger, T. (2013) 'Mushroom body miscellanea: transgenic *Drosophila* strains expressing anatomical and physiological sensor proteins in Kenyon cells', *Front Neural Circuits* 7: 147.

Pereanu, W., Younossi-Hartenstein, A., Lovick, J., Spindler, S. and Hartenstein, V. (2011) 'Lineage-based analysis of the development of the central complex of the *Drosophila* brain', *J Comp Neurol* 519(4): 661-89.

Perkins, L. A., Holderbaum, L., Tao, R., Hu, Y., Sopko, R., McCall, K., Yang-Zhou, D., Flockhart, I., Binari, R., Shim, H. S. et al. (2015) 'The Transgenic RNAi Project at Harvard Medical School: Resources and Validation', *Genetics* 201(3): 843-52.

Pfeiffer, B. D., Jenett, A., Hammonds, A. S., Ngo, T. T., Misra, S., Murphy, C., Scully, A., Carlson, J. W., Wan, K. H., Laverty, T. R. et al. (2008) 'Tools for neuroanatomy and neurogenetics in *Drosophila*', *Proc Natl Acad Sci U S A* 105(28): 9715-20.

Pfeiffer, B. D., Ngo, T. T., Hibbard, K. L., Murphy, C., Jenett, A., Truman, J. W. and Rubin, G. M. (2010) 'Refinement of tools for targeted gene expression in *Drosophila*', *Genetics* 186(2): 735-55.

Poeck, B., Triphan, T., Neuser, K. and Strauss, R. (2008) 'Locomotor control by the central complex in *Drosophila*-An analysis of the tay bridge mutant', *Dev Neurobiol* 68(8): 1046-58.

Poorkaj, P., Bird, T. D., Wijsman, E., Nemens, E., Garruto, R. M., Anderson, L., Andreadis, A., Wiederholt, W. C., Raskind, M. and Schellenberg, G. D. (1998) 'Tau is a candidate gene for chromosome 17 frontotemporal dementia', *Ann Neurol* 43(6): 815-25.

Postle, B. R. (2006) 'Working memory as an emergent property of the mind and brain', *Neuroscience* 139(1): 23-38.

Potter, C. J., Tasic, B., Russler, E. V., Liang, L. and Luo, L. (2010) 'The Q system: a repressible binary system for transgene expression, lineage tracing, and mosaic analysis', *Cell* 141(3): 536-48.

Putz, G., Bertolucci, F., Raabe, T., Zars, T. and Heisenberg, M. (2004) 'The S6KII (rsk) gene of *Drosophila melanogaster* differentially affects an operant and a classical learning task', *J Neurosci* 24(44): 9745-51.

Quinn, W. G. and Dudai, Y. (1976) 'Memory phases in *Drosophila*', *Nature* 262(5569): 576-7.

Quinn, W. G., Harris, W. A. and Benzer, S. (1974) 'Conditioned behavior in *Drosophila melanogaster*', *Proc Natl Acad Sci U S A* 71(3): 708-12.

Raccuglia, D., Huang, S., Ender, A., Heim, M. M., Laber, D., Suarez-Grimalt, R., Liotta, A., Sigrist, S. J., Geiger, J. R. P. and Owald, D. (2019) 'Network-Specific Synchronization of Electrical Slow-Wave Oscillations Regulates Sleep Drive in *Drosophila*', *Curr Biol* 29(21): 3611-3621 e3.

Reichelt, A. C., Killcross, S., Wilkinson, L. S., Humby, T. and Good, M. A. (2013) 'Transgenic expression of the FTDP-17 Tau^{V337M} mutation in brain dissociates components of executive function in mice', *Neurobiol Learn Mem* 104: 73-81.

Ren, D., Navarro, B., Xu, H., Yue, L., Shi, Q. and Clapham, D. E. (2001) 'A prokaryotic voltage-gated Sodium channel', *Science* 294(5550): 2372-5.

Ren, X., Yang, Z., Xu, J., Sun, J., Mao, D., Hu, Y., Yang, S. J., Qiao, H. H., Wang, X., Hu, Q. et al. (2014) 'Enhanced specificity and efficiency of the CRISPR/Cas9 system with optimized sgRNA parameters in *Drosophila*', *Cell Rep* 9(3): 1151-62.

Renn, S. C., Armstrong, J. D., Yang, M., Wang, Z., An, X., Kaiser, K. and Taghert, P. H. (1999) 'Genetic analysis of the *Drosophila* ellipsoid body neuropil: organization and development of the central complex', *J Neurobiol* 41(2): 189-207.

Riabinina, O., Luginbuhl, D., Marr, E., Liu, S., Wu, M. N., Luo, L. and Potter, C. J. (2015) 'Improved and expanded Q-system reagents for genetic manipulations', *Nat Methods* 12(3): 219-22, 5 p following 222.

Rieche, F., Carmine-Simmen, K., Poeck, B., Kretzschmar, D. and Strauss, R. (2018) '*Drosophila* Full-Length Amyloid Precursor Protein Is Required for Visual Working Memory and Prevents Age-Related Memory Impairment', *Curr Biol* 28(5): 817-823 e3.

Ries, A. S., Hermanns, T., Poeck, B. and Strauss, R. (2017) 'Serotonin modulates a depression-like state in *Drosophila* responsive to lithium treatment', *Nat Commun* 8: 15738.

Rorth, P., Szabo, K., Bailey, A., Laverty, T., Rehm, J., Rubin, G. M., Weigmann, K., Milan, M., Benes, V., Ansorge, W. et al. (1998) 'Systematic gain-of-function genetics in *Drosophila*', *Development* 125(6): 1049-57.

Rosahl, T. W., Spillane, D., Missler, M., Herz, J., Selig, D. K., Wolff, J. R., Hammer, R. E., Malenka, R. C. and Sudhof, T. C. (1995) 'Essential Functions of Synapsin-I and Synapsin-II in Synaptic Vesicle Regulation', *Nature* 375(6531): 488-493.

Rosenzweig, M., Brennan, K. M., Tayler, T. D., Phelps, P. O., Patapoutian, A. and Garrity, P. A. (2005) 'The *Drosophila* ortholog of vertebrate TRPA1 regulates thermotaxis', *Genes Dev* 19(4): 419-24.

Rosenzweig, M., Kang, K. J. and Garrity, P. A. (2008) 'Distinct TRP channels are required for warm and cool avoidance in *Drosophila melanogaster*', *Proc Natl Acad Sci U S A* 105(38): 14668-14673.

Rubin, C. S. (1994) 'A kinase anchor proteins and the intracellular targeting of signals carried by cyclic AMP', *Biochim Biophys Acta* 1224(3): 467-79.

Rubin, G. M. and Spradling, A. C. (1982) 'Genetic transformation of *Drosophila* with transposable element vectors', *Science* 218(4570): 348-53.

Sadanandappa, M. K., Blanco Redondo, B., Michels, B., Rodrigues, V., Gerber, B., VijayRaghavan, K., Buchner, E. and Ramaswami, M. (2013) 'Synapsin function in GABA-ergic interneurons is required for short-term olfactory habituation', *J Neurosci* 33(42): 16576-85.

Schindelin, J., Arganda-Carreras, I., Frise, E., Kaynig, V., Longair, M., Pietzsch, T., Preibisch, S., Rueden, C., Saalfeld, S., Schmid, B. et al. (2012) 'Fiji: an open-source platform for biological-image analysis', *Nat Methods* 9(7): 676-82.

Schwaerzel, M., Jaeckel, A. and Mueller, U. (2007) 'Signaling at A-kinase anchoring proteins organizes anesthesia-sensitive memory in *Drosophila*', *J Neurosci* 27(5): 1229-33.

Sears, J. C., Choi, W. J. and Broadie, K. (2019) 'Fragile X Mental Retardation Protein positively regulates PKA anchor Rugose and PKA activity to control actin assembly in learning/memory circuitry', *Neurobiol Dis* 127: 53-64.

Seelig, J. D. and Jayaraman, V. (2013) 'Feature detection and orientation tuning in the *Drosophila* central complex', *Nature* 503(7475): 262-6.

Seelig, J. D. and Jayaraman, V. (2015) 'Neural dynamics for landmark orientation and angular path integration', *Nature* 521(7551): 186-91.

Seugnet, L., Galvin, J. E., Suzuki, Y., Gottschalk, L. and Shaw, P. J. (2009a) 'Persistent short-term memory defects following sleep deprivation in a *Drosophila* model of Parkinson disease', *Sleep* 32(8): 984-92.

Seugnet, L., Suzuki, Y., Stidd, R. and Shaw, P. J. (2009b) 'Aversive phototaxic suppression: evaluation of a short-term memory assay in *Drosophila melanogaster*', *Genes Brain Behav* 8(4): 377-89.

Shamloula, H. K., Mbogho, M. P., Pimentel, A. C., Chrzanowska-Lightowlers, Z. M., Hyatt, V., Okano, H. and Venkatesh, T. R. (2002) 'rugose (rg), a *Drosophila* A kinase anchor protein, is required for retinal pattern formation and interacts genetically with multiple signaling pathways', *Genetics* 161(2): 693-710.

Shearin, H. K., Macdonald, I. S., Spector, L. P. and Stowers, R. S. (2014) 'Hexameric GFP and mCherry reporters for the *Drosophila* GAL4, Q, and LexA transcription systems', *Genetics* 196(4): 951-60.

Siegel, R. W. and Hall, J. C. (1979) 'Conditioned responses in courtship behavior of normal and mutant *Drosophila*', *Proc Natl Acad Sci U S A* 76(7): 3430-4.

Silva, A. J., Paylor, R., Wehner, J. M. and Tonegawa, S. (1992) 'Impaired spatial learning in alpha-calcium-calmodulin kinase II mutant mice', *Science* 257(5067): 206-11.

Sitaraman, D., LaFerriere, H., Birman, S. and Zars, T. (2012) 'Serotonin is critical for rewarded olfactory short-term memory in *Drosophila*', *J Neurogenet* 26(2): 238-44.

Skoulakis, E. M., Kalderon, D. and Davis, R. L. (1993) 'Preferential expression in mushroom bodies of the catalytic subunit of protein kinase A and its role in learning and memory', *Neuron* 11(2): 197-208.

Spindler, S. R. and Hartenstein, V. (2010) 'The *Drosophila* neural lineages: a model system to study brain development and circuitry', *Dev Genes Evol* 220(1-2): 1-10.

Srinivasan, M., Zhang, S., Lehrer, M. and Collett, T. (1996) 'Honeybee navigation en route to the goal: visual flight control and odometry', *J Exp Biol* 199(Pt 1): 237-44.

Strauss, R. and Heisenberg, M. (1993) 'A higher control center of locomotor behavior in the *Drosophila* brain', *J Neurosci* 13(5): 1852-61.

Strauss, R. and Pichler, J. (1998) 'Persistence of orientation toward a temporarily invisible landmark in *Drosophila melanogaster*', *J Comp Physiol A* 182(4): 411-23.

Strauss, R., Schuster, S. and Gotz, K. G. (1997) 'Processing of artificial visual feedback in the walking fruit fly *Drosophila melanogaster*', *J Exp Biol* 200(Pt 9): 1281-96.

Sudhof, T. C. (1990) 'The Structure of the Human Synapsin-I Gene and Protein', *Journal of Biological Chemistry* 265(14): 7849-7852.

Sudhof, T. C., Czernik, A. J., Kao, H. T., Takei, K., Johnston, P. A., Horiuchi, A., Kanazir, S. D., Wagner, M. A., Perin, M. S., De Camilli, P. et al. (1989) 'Synapsins: mosaics of shared and individual domains in a family of synaptic vesicle phosphoproteins', *Science* 245(4925): 1474-80.

Sumi, S. M., Bird, T. D., Nochlin, D. and Raskind, M. A. (1992) 'Familial presenile dementia with psychosis associated with cortical neurofibrillary tangles and degeneration of the amygdala', *Neurology* 42(1): 120-7.

Sweeney, L. B., Couto, A., Chou, Y. H., Berdnik, D., Dickson, B. J., Luo, L. and Komiyama, T. (2007) 'Temporal target restriction of olfactory receptor neurons by Semaphorin-1a/PlexinA-mediated axon-axon interactions', *Neuron* 53(2): 185-200.

Sweeney, S. T., Broadie, K., Keane, J., Niemann, H. and O'Kane, C. J. (1995) 'Targeted expression of tetanus toxin light chain in *Drosophila* specifically eliminates synaptic transmission and causes behavioral defects', *Neuron* 14(2): 341-51.

Talay, M., Richman, E. B., Snell, N. J., Hartmann, G. G., Fisher, J. D., Sorkac, A., Santoyo, J. F., Chou-Freed, C., Nair, N., Johnson, M. et al. (2017) 'Transsynaptic Mapping of Second-Order Taste Neurons in Flies by trans-Tango', *Neuron* 96(4): 783-795 e4.

Talmat-Amar, Y., Arribat, Y. and Parmentier, M. L. (2018) 'Vesicular Axonal Transport is Modified In Vivo by Tau Deletion or Overexpression in *Drosophila*', *Int J Mol Sci* 19(3).

Tanaka, Y., Takase, M. and Gamo, S. (2007) 'Relationship between general anesthesia and memory in *Drosophila* involving the cAMP/PKA pathways and adhesion-related molecules', *Curr Med Chem* 14(13): 1479-88.

Thran, J., Poeck, B. and Strauss, R. (2013) 'Serum response factor-mediated gene regulation in a *Drosophila* visual working memory', *Curr Biol* 23(18): 1756-63.

Tian, L., Hires, S. A., Mao, T., Huber, D., Chiappe, M. E., Chalasani, S. H., Petreanu, L., Akerboom, J., McKinney, S. A., Schreiter, E. R. et al. (2009) 'Imaging neural activity in worms, flies and mice with improved GCaMP calcium indicators', *Nat Methods* 6(12): 875-81.

Tower, J., Karpen, G. H., Craig, N. and Spradling, A. C. (1993) 'Preferential transposition of *Drosophila* P elements to nearby chromosomal sites', *Genetics* 133(2): 347-59.

Tully, T. (1984) '*Drosophila* learning: behavior and biochemistry', *Behav Genet* 14(5): 527-57.

Tully, T. and Quinn, W. G. (1985) 'Classical conditioning and retention in normal and mutant *Drosophila melanogaster*', *J Comp Physiol A* 157(2): 263-77.

Turner-Evans, D., Wegener, S., Rouault, H., Franconville, R., Wolff, T., Seelig, J. D., Druckmann, S. and Jayaraman, V. (2017) 'Angular velocity integration in a fly heading circuit', *Elife* 6. 10.7554/eLife.23496

Ueda, T., Maeno, H. and Greengard, P. (1973) 'Regulation of endogenous phosphorylation of specific proteins in synaptic membrane fractions from rat brain by adenosine 3':5'-monophosphate', *J Biol Chem* 248(23): 8295-305.

Ushkaryov, Y. A., Hata, Y., Ichtchenko, K., Moomaw, C., Afendis, S., Slaughter, C. A. and Sudhof, T. C. (1994) 'Conserved domain structure of beta-neurexins. Unusual cleaved signal sequences in receptor-like neuronal cell-surface proteins', *J Biol Chem* 269(16): 11987-92.

van Swinderen, B. (2007) 'Attention-like processes in *Drosophila* require short-term memory genes', *Science* 315(5818): 1590-3.

van Swinderen, B. and Greenspan, R. J. (2003) 'Salience modulates 20-30 Hz brain activity in *Drosophila*', *Nat Neurosci* 6(6): 579-86.

Voelzmann, A., Okenve-Ramos, P., Qu, Y., Chojnowska-Monga, M., del Cano-Espinel, M., Prokop, A. and Sanchez-Soriano, N. (2016) 'Tau and spectraplakins promote synapse formation and maintenance through Jun kinase and neuronal trafficking', *Elife* 5. 10.7554/eLife.14694

Volders, K., Scholz, S., Slabbaert, J. R., Nagel, A. C., Verstreken, P., Creemers, J. W., Callaerts, P. and Schwarzel, M. (2012) '*Drosophila* rugose is a functional homolog of mammalian Neurobeachin and affects synaptic architecture, brain morphology, and associative learning', *J Neurosci* 32(43): 15193-204.

von Bergen, M., Barghorn, S., Li, L., Marx, A., Biernat, J., Mandelkow, E. M. and Mandelkow, E. (2001) 'Mutations of Tau protein in frontotemporal dementia promote aggregation of paired helical filaments by enhancing local beta-structure', *J Biol Chem* 276(51): 48165-74.

Waddell, S., Armstrong, J. D., Kitamoto, T., Kaiser, K. and Quinn, W. G. (2000) 'The amnesiac gene product is expressed in two neurons in the *Drosophila* brain that are critical for memory', *Cell* 103(5): 805-13.

Walsh, D. A., Ashby, C. D., Gonzalez, C., Calkins, D. and Fischer, E. H. (1971) 'Krebs EG: Purification and characterization of a protein inhibitor of adenosine 3',5'-monophosphate-dependent protein kinases', *J Biol Chem* 246(7): 1977-85.

Wandosell, F. and Avila, J. (1987) 'Microtubule-associated proteins present in different developmental stages of *Drosophila melanogaster*', *J Cell Biochem* 35(2): 83-92.

Wang, H., Feng, R., Phillip Wang, L., Li, F., Cao, X. and Tsien, J. Z. (2008a) 'CaMKII activation state underlies synaptic labile phase of LTP and short-term memory formation', *Curr Biol* 18(20): 1546-54.

Wang, X., Liu, L., Xia, S., Feng, C. and Guo, A. (1998) 'Relationship between visual learning/memory ability and brain cAMP level in *Drosophila*', *Sci China C Life Sci* 41(5): 503-11.

Wang, Z., Pan, Y., Li, W., Jiang, H., Chatzimanolis, L., Chang, J., Gong, Z. and Liu, L. (2008b) 'Visual pattern memory requires foraging function in the central complex of *Drosophila*', *Learn Mem* 15(3): 133-42.

Weaver, C., Leidel, C., Szpankowski, L., Farley, N. M., Shubeita, G. T. and Goldstein, L. S. (2013) 'Endogenous GSK-3/shaggy regulates bidirectional axonal transport of the amyloid precursor protein', *Traffic* 14(3): 295-308.

Wehner, R. and Muller, M. (2006) 'The significance of direct sunlight and polarized skylight in the ant's celestial system of navigation', *Proc Natl Acad Sci U S A* 103(33): 12575-9.

Weingarten, M. D., Lockwood, A. H., Hwo, S. Y. and Kirschner, M. W. (1975) 'A protein factor essential for microtubule assembly', *Proc Natl Acad Sci U S A* 72(5): 1858-62.

Weir, P. T., Schnell, B. and Dickinson, M. H. (2014) 'Central complex neurons exhibit behaviorally gated responses to visual motion in *Drosophila*', *J Neurophysiol* 111(1): 62-71.

Wiedenheft, B., Sternberg, S. H. and Doudna, J. A. (2012) 'RNA-guided genetic silencing systems in bacteria and archaea', *Nature* 482(7385): 331-8.

Wilson, R. I. and Laurent, G. (2005) 'Role of GABAergic inhibition in shaping odor-evoked spatiotemporal patterns in the *Drosophila* antennal lobe', *J Neurosci* 25(40): 9069-79.

Winer, J. A. (1977) 'Atlas of an Insect Brain - Strausfeld,Nj', *Journal of Biological Psychology* 19(1): 52-54.

Wittlinger, M., Wehner, R. and Wolf, H. (2006) 'The ant odometer: stepping on stilts and stumps', *Science* 312(5782): 1965-7.

Wolf, R. and Heisenberg, M. (1991) 'Basic organization of operant behavior as revealed in *Drosophila* flight orientation', *J Comp Physiol A* 169(6): 699-705.

Wolff, T., Iyer, N. A. and Rubin, G. M. (2015) 'Neuroarchitecture and neuroanatomy of the *Drosophila* central complex: A GAL4-based dissection of protocerebral bridge neurons and circuits', *J Comp Neurol* 523(7): 997-1037.

Wolff, T. and Rubin, G. M. (2018) 'Neuroarchitecture of the *Drosophila* central complex: A catalog of nodulus and asymmetrical body neurons and a revision of the protocerebral bridge catalog', *J Comp Neurol* 526(16): 2585-2611.

Wustmann, G. and Heisenberg, M. (1997) 'Behavioral manipulation of retrieval in a spatial memory task for *Drosophila melanogaster*', *Learn Mem* 4(4): 328-336.

Xi, W., Peng, Y., Guo, J., Ye, Y., Zhang, K., Yu, F. and Guo, A. (2008) 'Mushroom bodies modulate salience-based selective fixation behavior in *Drosophila*', *Eur J Neurosci* 27(6): 1441-51.

Xia, S., Liu, L., Feng, C. and Guo, A. (1997a) 'Drug disruption of short-term memory in *Drosophila melanogaster*', *Pharmacol Biochem Behav* 58(3): 727-35.

Xia, S., Liu, L., Feng, C. and Guo, A. (1997b) 'Memory consolidation in *Drosophila* operant visual learning', *Learn Mem* 4(2): 205-18.

Xie, X., Tabuchi, M., Brown, M. P., Mitchell, S. P., Wu, M. N. and Kolodkin, A. L. (2017) 'The laminar organization of the *Drosophila* ellipsoid body is semaphorin-dependent and prevents the formation of ectopic synaptic connections', *Elife* 6.

Xu, J., Ren, X., Sun, J., Wang, X., Qiao, H. H., Xu, B. W., Liu, L. P. and Ni, J. Q. (2015) 'A Toolkit of CRISPR-Based Genome Editing Systems in *Drosophila*', *J Genet Genomics* 42(4): 141-9.

Yamazaki, D., Horiuchi, J., Miyashita, T. and Saitoe, M. (2010) 'Acute inhibition of PKA activity at old ages ameliorates age-related memory impairment in *Drosophila*', *J Neurosci* 30(46): 15573-7.

Yamazaki, D., Horiuchi, J., Nakagami, Y., Nagano, S., Tamura, T. and Saitoe, M. (2007) 'The *Drosophila* DCO mutation suppresses age-related memory impairment without affecting lifespan', *Nat Neurosci* 10(4): 478-84.

Yang, J. S., Awasaki, T., Yu, H. H., He, Y., Ding, P., Kao, J. C. and Lee, T. (2013) 'Diverse neuronal lineages make stereotyped contributions to the *Drosophila* locomotor control center, the central complex', *J Comp Neurol* 521(12): 2645-Spc1.

Yin, J. C., Wallach, J. S., Del Vecchio, M., Wilder, E. L., Zhou, H., Quinn, W. G. and Tully, T. (1994) 'Induction of a dominant negative CREB transgene specifically blocks long-term memory in *Drosophila*', *Cell* 79(1): 49-58.

Young, J. M. and Armstrong, J. D. (2010a) 'Building the central complex in *Drosophila*: the generation and development of distinct neural subsets', *J Comp Neurol* 518(9): 1525-41.

Young, J. M. and Armstrong, J. D. (2010b) 'Structure of the adult central complex in *Drosophila*: organization of distinct neuronal subsets', *J Comp Neurol* 518(9): 1500-24.

Yu, H. H., Araj, H. H., Ralls, S. A. and Kolodkin, A. L. (1998) 'The transmembrane Semaphorin Sema I is required in *Drosophila* for embryonic motor and CNS axon guidance', *Neuron* 20(2): 207-20.

Zars, T. (2010) 'Short-term memories in *Drosophila* are governed by general and specific genetic systems', *Learn Mem* 17(5): 246-51.

Zars, T., Fischer, M., Schulz, R. and Heisenberg, M. (2000) 'Localization of a short-term memory in *Drosophila*', *Science* 288(5466): 672-5.

Zhang, X., Zheng, Y., Ren, Q. and Zhou, H. (2017) 'The involvement of potassium channel ORK1 in short-term memory and sleep in *Drosophila*', *Medicine (Baltimore)* 96(27): e7299.

Zhang, Y. Q., Rodesch, C. K. and Broadie, K. (2002) 'Living synaptic vesicle marker: synaptotagmin-GFP', *Genesis* 34(1-2): 142-5.

Zhao, J., Lu, Y., Zhao, X., Yao, X., Shuai, Y., Huang, C., Wang, L., Jeong, S. H. and Zhong, Y. (2013) 'Dissociation of rugose-dependent short-term memory component from memory consolidation in *Drosophila*', *Genes Brain Behav* 12(6): 626-32.

Zhong, Y., Budnik, V. and Wu, C. F. (1992) 'Synaptic plasticity in *Drosophila* memory and hyperexcitable mutants: role of cAMP cascade', *J Neurosci* 12(2): 644-51.

Zhong, Y. and Wu, C. F. (1991) 'Altered synaptic plasticity in *Drosophila* memory mutants with a defective cyclic AMP cascade', *Science* 251(4990): 198-201.

7. Directories

7.1 List of figures

7.2 List of tables

7.3 Abbreviations

Aβ	Amyloid Beta
AC	Anterior Cell
AD	Alzheimer's Disease
ADAR	Adenosine Deaminase Acting on RNA
AKAP	A Kinase Anchoring Protein
AKAR	A Kinase Reporter
AMI	Age-related Memory Impairment
AOTU	Anterior Optic Tubercle
APS	Aversive Phototaxic Stimulus
APPL	Amyloid Precursor Protein Like
ARM	Anesthesia-Resistant Memory
ASD	Autism Spectrum Disorder
ASM	Anesthesia-Sensitive Memory

BU	Bulb
BUa	Bulb Anterior
BUi	Bulb Inferior
BUs	Bulb Superior
Ca^{2+}	Calcium
cAMP	Cyclic Adenosine Monophosphate
CaMKII	Calmodulin Kinase II
CASK	CaM Associated Serine Kinase
CBS	Cystathionine-β-synthase
CC	Central Complex
CD4	Cluster of Differentiation 4
Cdk	Cyclin dependent kinase
cGMP	Cyclic Guanosine Monophosphate
CNG	Cyclic Nucleotide-Gated
CNS	Central Nervous System
CR	Conditioned Response
CREB	cAMP Response Element Binding Protein
CRISPR	Clustered Regularly Interspaced Short Palindromic Sequence
CS	Conditioned Stimulus
dTRPA1	*Drosophila* Transient Receptor Potential Ankyrin 1
DAN	Dopaminergic Neuron
DenSyt	DenMark Synaptotagmin
DGluRII	*Drosophila* Glutamate ReceptorII
DLS	Depression-Like State
DNA	Deoxyribonucleic Acid
dnc	*dunce*
DPSS Laser	Diode Pump Solid State Laser
DTK	*Drosophila* tachykinin
dtAPPL	Double-Tagged APPL
E cells	Evening cells
EB	Ellipsoid Body
EBa	Ellipsoid Body anterior

EBic	Ellipsoid Body inner central
EBoc	Ellipsoid Body outer central
EBip	Ellipsoid Body inner posterior
EBop	Ellipsoid Body outer posterior
eCORP2	Endogenous Competitor of PKA-R2
ECS	Editing site Complementary Sequence
EGFR	Epidermal Growth Factor Receptor
EJC	Excitatory Junctional Currents
F-Actin	Filamentous Actin
FASII	Fasciclin II
FB	Fan-shaped Body
FLAG	Fluorescent Tag
flAPPL	Full-Length APPL
FMRP	Fragile X Mental Retardation Potein
for	*foraging*
FRET	Forster Resonance Energy Transfer
FTD17 with chromosome 17	Fronto-Temporal Dementia with Parkinsonism associated
GAD1	Glutamate Decarboxylase 1
GFP	Green Fluorescent Protein
GPCR	G Protein-Coupled Receptor
GRASP	GFP Reconstitution Across Synaptic Partners
GSK	Glycogen Synthase Kinase
HD	Huntington's Disease
ign	*ignorant*
IR	Inverted Repeats
JNK	C-Jun-N-Terminal Kinase
KCl	Potassium Chloride
KO	Knock-out
LAL	Lateral Accessory Lobe
LC	Lateral Cell
LED	Light Emitting Diode
LTD	Long-Term Depression

LTM	Long-Term Memory
LTP	Long-Term Potentiation
LTR	Lateral Triangle
M cells	Morning cells
MAP	Microtubule Associated Protein
MAPK	Mitogen Activated Protein Kinase
MAPT	Microtubule Associated Protein Tau
MEC	Meso Entorhinal Cortex
MB	Mushroom Body
MT	Microtubule
MTM	Middle-Term Memory
NFT	Neurofibrillary Tangles
NMDA	N-Methyl D-Aspartate
NMDAR	N-Methyl D-Aspartate Receptor
NMJ	Neuromuscular Junction
NO	Noduli, Nitric Oxide
NOS	Nitric Oxide Synthase
OF	Object Fixation
ORF	Open Reading Frame
ORT	Optomotor Reversal Time
PB	Protocerebral Bridge
PBS	Phosphate Buffered Saline
PD	Parkinson’s Disease
PDE-2	Phosphodiesterase-II
PFA	Paraformaldehyde
PHF	Paired Helical Filaments
PKA	Protein Kinase A
PKA-C1	Protein Kinase A Catalytic subunit 1
PKA-R1	Protein Kinase A Regulatory subunit 1
PKG	Protein Kinase G
PKI [1-31]	Protein Kinase Inhibitor [1-31]
PSD-LTM	Protein Synthesis-Dependent Long-Term Memory

R3a	R3 anterior
R3d	R3 distal
R3m	R3 medial
R3p	R3 posterior
R3w	R3 wide
R4d	R4 distal
R4m	R4 medial
RFP	Red Fluorescent Protein
rg	*rugose*
RISC	RNA Induced Silencing Complex
RNA	Ribonucleic Acid
RNAi	RNA interference
ROI	Region of Interest
RSKII	Ribosomal Protein S6 Kinase II
rut	*rutabaga*
sdAPPL	Secretion-Defective APPL
shi	*shibire*
sNPF	short Neuropeptide F
STH	Short-Term Habituation
STM	Short-Term Memory
SV	Synaptic Vesicle
Syn	*Synapsin*
PSYN(S6)/SYN-P1	Phosphorylated Synapsin from site-1
TNT	Tetanus Toxin light chain
TRPA1	Transient Receptor Potential Ankyrin 1
UAS	Upstream Activation Sequence
US	Unconditioned Stimulus
VBO	Ventral Bodies
VC	Ventral Cell
VNC	Ventral Nerve Chord
WT-CS	Wild-Type Canton Special

8. Appendix

8.1 Roles of PKA and Syn in *Drosophila* visual working memory

Table 7: Statistical analysis for Figure 12

Table 7A Multiple comparison of genotypes using Kruskal-Wallis test (with in-built Bonferroni correction) where "N" is the total number of trials and "n" is the number of flies tested. All boxes contain p-values.

N/n	Genotype	WT-CS	*Pka-C1*^{H2}UAS-*Pka*/II	*Pka-C1*^{H2}UAS-*Pka*/189Y-GAL4	*Pka-C1*^{H2}UAS-*Pka*/II;EB1-GAL4/III
290/29	WT-CS		0.0000003	~1.000000	0.0000016
300/30	*Pka-C1*^{H2}UAS-*Pka*/II	0.0000003		0.0000011	~1.000000
300/30	*Pka-C1*^{H2}UAS-*Pka*/189Y-GAL4	~1.000000	0.0000011		0.0000054
300/30	*Pka-C1*^{H2}UAS-*Pka*/II;EB1-GAL4/III	0.0000016	~1.000000	0.0000054	

Table 7B Tests for normality (Shapiro-Wilk) and comparison against chance level (58%).

N/n	Genotype	Normality score	Statistical test	p-value
290/29	WT-CS	0.00076	Sign-Test	0.00000019
300/30	*Pka-C1*^{H2}UAS-*Pka*/II	0.01013	Sign-Test	0.0061699
300/30	*Pka-C1*^{H2}UAS-*Pka*/189Y-GAL4	0.00571	Sign-Test	0.00000011
300/30	*Pka-C1*^{H2}UAS-*Pka*/II;EB1-GAL4/III	0.01857	Sign-Test	0.0061699

Table 8: Statistical analysis for Figure 13

Table 8A Multiple comparison of genotypes using Kruskal-Wallis test (with in-built Bonferroni correction) where "N" is the total number of trials and "n" is the number of flies tested. All boxes contain p-values.

N/n	Genotype	WT-CS	*Pka-C1*^{H2} 189Y-GAL4/II	*Pka-C1*^{H2}189Y-GAL4/II; UAS-*Pka*-R1^{RNAi}/III
250/25	WT-CS		0.0000035	~1.000000
300/30	*Pka-C1*^{H2}189Y-GAL4/II	0.0000035		0.0000011
220/22	*Pka-C1*^{H2}189Y-GAL4/II;UAS-*Pka-R1*^{RNAi}/III	~1.00000	0.0000011	

Table 8B Tests for normality (Shapiro-Wilk) and comparison against chance level (58%).

N/n	Genotype	Normality score	Statistical test	p-value
250/25	WT-CS	0.00001	Sign-Test	0.0000015
300/30	*Pka-C1*^{H2}189Y-GAL4/II	0.02663	Sign-Test	0.0019107
220/22	*Pka-C1*^{H2}189Y-GAL4/II;UAS-*Pka-R1*^{RNAi}/III	0.00651	Sign-Test	0.0000075

Table 9: Statistical analysis for Figure 15

Table 9A Multiple comparison of genotypes using Kruskal-Wallis test (with in-built Bonferroni correction) where "N" is the total number of trials and "n" is the number of flies tested. All boxes contain p-values.

N/n	Genotype	WT-CS	189Y-GAL4/II;*Syn*^{97}	189Y-GAL4/UAS-*Syn*(cDNA8),*Syn*^{97}	189Y-GAL4/II;UAS-*Syn*(M1+M2),*Syn*^{97}/*Syn*^{97}	189Y-GAL4/II;UAS-*Syn*(M1+S2),*Syn*^{97}/*Syn*^{97}	189Y-GAL4/II;UAS-*Syn*(S1+M2),*Syn*^{97}/*Syn*^{97}
230/23	WT-CS		0.00000007	~1.0000000	0.0000580	0.0000045	~1.000000
200/20	189Y-GAL4/II; *Syn*^{97}	0.00000007		0.0000020	~1.000000	~1.0000000	0.0000114
250/25	189Y-GAL4/UAS-*Syn*(cDNA8); *Syn*^{97}	~1.0000000	0.0000020		0.0009684	0.0001001	~1.000000
250/25	189Y-GAL4/II;UAS-*Syn*(M1+M2),*Syn*^{97}/*Syn*^{97}	0.0000580	~1.000000	0.0009684		~1.000000	0.0039646
260/26	189Y-GAL4/II;UAS-*Syn*(M1+S2),*Syn*^{97}/*Syn*^{97}	0.0000045	~1.0000000	0.0001001	~1.000000		0.0004925
250/25	189Y-GAL4/II;UAS-*Syn*(S1+M2),*Syn*^{97}/*Syn*^{97}	~1.000000	0.0000114	~1.000000	0.0039646	0.0004925	

Table 9B Tests for normality (Shapiro-Wilk) and comparison against chance level (58%).

N/n	Genotype	Normality score	Statistical test	p-value
230/23	WT-CS	0.00137	Sign-Test	0.0000044
200/20	189Y-GAL4/II;*Syn*^{97}	0.38818	t-Test	0.5584694
250/25	189Y-GAL4/UAS-*Syn*(cDNA8); *Syn*^{97}	0.00747	Sign-Test	0.0000015
250/25	189Y-GAL4/II;UAS-*Syn*(M1+M2),*Syn*^{97}/*Syn*^{97}	0.02166	Sign-Test	0.0013742
260/26	189Y-GAL4/II;UAS-*Syn*(M1+S2),*Syn*^{97}/*Syn*^{97}	0.60437	t-Test	0.0661389
250/25	189Y-GAL4/II;UAS-*Syn*(S1+M2),*Syn*^{97}/*Syn*^{97}	0.01013	Sign-Test	0.0000015

Table 10: Statistical analysis for Figure 16

Table 10A Multiple comparison of genotypes using Kruskal-Wallis test (with in-built Bonferroni correction) where "N" is the total number of trials and "n" is the number of flies tested. All boxes contain p-values.

N/n	Genotype	WT-CS	*PkaC1^{H2}* 189Y-GAL4/II	*PkaC1^{H2}* 189Y-GAL4/II; *Syn^{97}*/III	*PkaC1^{H2}*189Y-GAL4/UAS-*Syn*(cDNA8); *Syn^{97}*/III	*PkaC1^{H2}*189Y-GAL4/II;UAS-*Syn*(M1+M2), *Syn^{97}*/III	*PkaC1^{H2}*189Y-GAL4/II;UAS-*Syn*(M1+S2), *Syn^{97}*/III	*PkaC1^{H2}*189Y-GAL4/II;UAS-*Syn*(S1+M2), *Syn^{97}*/III
300/30	WT-CS		0.0000037	0.0000090	~1.000000	$<10^{-7}$	0.0000007	~1.000000
300/30	*PkaC1^{H2}*189Y-GAL4/II	0.0000037		~1.000000	0.0000069	~1.0000000	~1.000000	0.0003213
230/23	*PkaC1^{H2}*189Y-GAL4/II;*Syn^{97}*/III	0.0000090	~1.000000		0.0000157	~1.0000000	~1.000000	0.0005038
290/29	*PkaC1^{H2}*189Y-GAL4/UAS-*Syn*(cDNA8); *Syn^{97}*/III	~1.000000	0.0000069	0.0000157		$<10^{-7}$	0.0000015	~1.000000
300/30	*PkaC1^{H2}*189Y-GAL4/II;UAS-*Syn*(M1+M2), *Syn^{97}*/III	$<10^{-7}$	~1.000000	~1.000000	$<10^{-7}$		~1.000000	0.00000004
270/27	*PkaC1^{H2}*189Y-GAL4/II;UAS-*Syn*(M1+S2), *Syn^{97}*/III	0.0000007	~1.000000	~1.000000	0.0000015	~1.0000000		0.0000796
280/28	*PkaC1^{H2}*189Y-GAL4/II;UAS-*Syn*(S1+M2), *Syn^{97}*/III	~1.000000	0.0003213	0.0005038	~1.000000	0.00000004	0.0000796	

Table 10B Tests for normality (Shapiro-Wilk) and comparison against chance level (58%).

N/n	Genotype	Normality score	Statistical test	p-value
300/30	WT-CS	0.00002	Sign-Test	0.0000001
300/30	*PkaC1*^{H2}189Y-GAL4/II	0.02663	Sign-Test	0.0019107
230/23	*PkaC1*^{H2}189Y-GAL4/II;*Syn*^{97}/III	0.02366	Sign-Test	0.0008492
290/29	*PkaC1*^{H2}189Y-GAL4/UAS-*Syn*(cDNA8);*Syn*^{97}/III	0.00020	Sign-Test	0.0000001
300/30	*PkaC1*^{H2}189Y-GAL4/II;UAS-*Syn*(M1+M2),*Syn*^{97}/III	0.01785	Sign-Test	0.3613104
270/27	*PkaC1*^{H2}189Y-GAL4/II;UAS-*Syn*(M1+S2),*Syn*^{97}/III	0.05405	t-Test	0.012825
280/28	*PkaC1*^{H2}189Y-GAL4/II;UAS-*Syn*(S1+M2),*Syn*^{97}/III	0.00982	Sign-Test	0.0000003

Table 11: Statistical analysis for Figure 17

Mann-Whitney-U test to compare two groups where N is the total number of samples.

Mann-Whitney U test: GFP (control group) (vs) GFP (experimental group)		
N	Genotype	p-value
7	UAS-mCD8::GFP/X;189Y-GAL4/II	0.1932332
10	UAS-mCD8::GFP/X;189Y-GAL4/II;UAS-*Pka*(mc*)/III	
Mann-Whitney U test: SYN-P1/GFP (control group) (vs) SYN-P1/GFP (experimental group)		
N	Genotype	p-value
7	UAS-mCD8::GFP/X;189Y-GAL4/II	0.0001028
10	UAS-mCD8::GFP/X;189Y-GAL4/II;UAS-*Pka*(mc*)/III	

Table 12: Statistical analysis for Figure 19A

Table 12A Multiple comparison of genotypes using Kruskal-Wallis test (with in-built Bonferroni correction) where “N” is the total number of trials and “n” is the number of flies tested. All boxes contain p-values.

N/n	Genotype	WT-CS	*Pka-C1*^{H2}189Y-GAL4/II	*Pka-C1*^{H2}189Y-GAL4/II;UAS-*Adar*^{RNAi}/III
170/17	WT-CS		0.0002467	~1.000000
300/30	*Pka-C1*^{H2}189Y-GAL4/II	0.0002467		0.0000016
240/24	*Pka*/189Y-GAL4/II; UAS-*Adar*^{RNAi}/III	~1.000000	0.0000016	

Table 12B Tests for normality (Shapiro-Wilk) and comparison against chance level (58%).

N/n	Genotype	Normality score	Statistical test	p-value
170/17	WT-CS	0.00046	Sign-Test	0.0001042
300/30	*Pka-C1*^{H2}189Y-GAL4/II	0.02663	Sign-Test	0.0019107
240/24	*Pka-C1*^{H2}189Y-GAL4/II;UAS-*Adar*^{RNAi}/III	0.00975	Sign-Test	0.0000026

Table 13: Statistical analysis for Figure 19B

Table 13A Multiple comparison of genotypes using Kruskal-Wallis test (with in-built Bonferroni correction) where “N” is the total number of trials and “n” is the number of flies tested. All boxes contain p-values.

N/n	Genotype	WT-CS	189Y-GAL4/II	UAS-*Adar*^{RNAi}/III	189Y-GAL4/II; UAS-*Adar*^{RNAi}/III
210/21	WT-CS		0.9797598	~1.000000	~1.000000
250/25	189Y-GAL4/II	0.9797598		~1.000000	~1.000000
250/25	UAS-*Adar*^{RNAi}/III	~1.000000	~1.000000		~1.000000
250/25	189Y-GAL4/II; UAS-*Adar*^{RNAi}/III	~1.000000	~1.000000	~1.000000	

Table 13B Tests for normality (Shapiro-Wilk) and comparison against chance level (58%)

N/n	Genotype	Normality score	Statistical test	p-value
210/21	WT-CS	0.00076	Sign-Test	0.0000127
250/25	189Y-GAL4/II	0.01013	Sign-Test	0.0000015
250/25	UAS-*Adar*^{RNAi}/III	0.00571	Sign-Test	0.00000011
250/25	189Y-GAL4/II;UAS-*Adar*^{RNAi}/III	0.01857	Sign-Test	0.0000015

Table 14: Statistical analysis for Figure 20

Mann-Whitney-U test to compare two groups where N is the total number of samples.

Mann-Whitney U test: GFP (control group) (vs) GFP (experimental group)

N	Genotype	p-value
12	UAS-mCD8::GFP/X;189Y-GAL4/II	0.1479399
9	UAS-mCD8::GFP/X;189Y-GAL4/II;UAS-*Adar*^{RNAi}/III	

Mann-Whitney U test: SYN-P1/GFP (control group) (vs) SYN-P1/GFP (experimental group)

N	Genotype	p-value
12	UAS-mCD8::GFP/X;189Y-GAL4/II	0.0000476
9	UAS-mCD8::GFP/X;189Y-GAL4/II;UAS-*Adar*^{RNAi}/III	

Table 15: Statistical analysis for Figure 21

Table 15A Multiple comparison of genotypes using Kruskal-Wallis test (with in-built Bonferroni correction) where “N” is the total number of trials and “n” is the number of flies tested. All boxes contain p-values.

N/n	Genotype	WT-CS	*Pka-C1*^{H2}189Y-GAL4/II;*Syn*^{97}/III	*Pka-C1*^{H2}189Y-GAL4/II; *Syn*^{97}/UAS-*Adar*^{RNAi}
250/25	WT-CS		0.0000007	~1.000000
250/25	*Pka-C1*^{H2}189Y-GAL4/II;*Syn*^{97}/III	0.0000007		0.0000698
250/25	*Pka-C1*^{H2}189Y-GAL4/II; UAS-*Adar*^{RNAi}/*Syn*^{97}	~1.000000	0.0000698	

Table 15B Tests for normality (Shapiro-Wilk) and comparison against chance level (58%).

N/n	Genotype	Normality score	Statistical test	p-value
250/25	WT-CS	0.00216	Sign-Test	0,0000015
250/25	*Pka-C1*^{H2}189Y-GAL4/II;*Syn*^{97}/III	0.00033	Sign-Test	0.0000633
250/25	*Pka-C1*^{H2}189Y-GAL4/II; UAS-*Adar*^{RNAi}/*Syn*^{97}	0.00659	Sign-Test	0.0000015

Table 16: Statistical analysis for Figure 22A

Table 16A Multiple comparison of genotypes using Kruskal-Wallis test (with in-built Bonferroni correction) where “N” is the total number of trials and “n” is the number of flies tested. All boxes contain p-values.

N/n	Genotype	WT-CS	189Y-GAL4/II	UAS-*CaMKII*^{RNAi}/III	189Y-GAL4; UAS-*CaMKII*^{RNAi}/III
250/25	WT-CS		~1.000000	~1.000000	0.0000109
250/25	189Y-GAL4/II	~1.00000		~1.000000	0.0000147
250/25	UAS-*CaMKII*^{RNAi} /III	~1.00000	~1.000000		0.0000226
250/25	189Y-GAL4/II;UAS-*CaMKII*^{RNAi}/III	0.0000109	0.0000147	0.0000226	

Table 16B Tests for normality (Shapiro-Wilk) and comparison against chance level (58%).

N/n	Genotype	Normality score	Statistical test	p-value
250/25	WT-CS	0.00216	Sign-Test	0.0000015
250/25	189Y-GAL4/II	0.00261	Sign-Test	0.0000015
250/25	UAS-*CaMKII*^{RNAi}/III	0.00085	Sign-Test	0.0000015
250/25	189Y-GAL4/II;UAS-*CaMKII*^{RNAi}/III	0.55382	t-Test	0.0431768

Table 17: Statistical analysis for Figure 22B

Table 17A Multiple comparison of genotypes using Kruskal-Wallis test (with in-built Bonferroni correction) where “N” is the total number of trials and “n” is the number of flies tested. All boxes contain p-values.

N/n	Genotype	WT-CS	189Y-GAL4/II	UAS-*CaMKII-I.Ala*/II	189Y-GAL4/ UAS-*CaMKII-I.Ala*
250/25	WT-CS		~1.000000	~1.0000000	0.0000413
250/25	189Y-GAL4/II	~1.00000		~1.0000000	0.0000615
250/25	UAS-*CaMKII-I.Ala*/II	~1.00000	~1.000000		0.0000061
250/25	189Y-GAL4/UAS-*CaMKII-I.Ala*	0.0000413	0.0000615	0.0000061	

Table 17B Tests for normality (Shapiro-Wilk) and comparison against chance level (58%).

N/n	Genotype	Normality score	Statistical test	p-value
250/25	WT-CS	0.00216	Sign-Test	0.0000015
250/25	189Y-GAL4/II	0.00261	Sign-Test	0.0000015
250/25	UAS-*CaMKII-I.Ala*/II	0.00049	Sign-Test	0.0000015
250/25	189Y-GAL4/UAS-*CaMKII-I.Ala*	0.03979	t-Test	0.0163950

Table 18: Statistical analysis for Figure 23

Table 18A Multiple comparison of genotypes using Kruskal-Wallis test (with in-built Bonferroni correction) where "N" is the total number of trials and "n" is the number of flies tested. All boxes contain p-values.

N/n	Genotype	WT-CS	*Pka-C1^{H2}*189Y-GAL4/II	*Pka-C1^{H2}*189Y-GAL4/II; UAS-*CaMK(II)*/III
250/25	WT-CS		0.0002888	~1.000000
250/25	*Pka-C1^{H2}*189Y-GAL4/II	0.0002888		0.0003868
250/25	*Pka-C1^{H2}*189Y-GAL4/II; UAS-*CaMKII*/III	~1.000000	0.0003868	

Table 18B Tests for normality (Shapiro-Wilk) and comparison against chance level (58%).

N/n	Genotype	Normality score	Statistical test	p-value
250/25	WT-CS	0.00296	Sign-Test	0.0000015
250/25	*Pka-C1^{H2}*189Y-GAL4/II	0.33223	t-Test	0.000695
250/25	*Pka-C1^{H2}*189Y-GAL4/II;UAS-*CaMKII*/III	0.00019	Sign-Test	0.0000108

Table 19: Statistical analysis for Figure 24

Mann-Whitney-U test to compare two groups where N is the total number of samples.

Mann-Whitney U test: GFP (control group) (vs) GFP (experimental group)

N	Genotype	p-value
9	UAS-mCD8::GFP/X;189Y-GAL4/II	0.1614973
9	UAS-mCD8::GFP/X;189Y-GAL4/II;UAS-*CaMKII*/III	

Mann-Whitney U test: SYN-P1/GFP (control group) (vs) SYN-P1/GFP (experimental group)

N	Genotype	p-value
9	UAS-mCD8::GFP/X;189Y-GAL4/II	0.0056355
9	UAS-mCD8::GFP/X;189Y-GAL4/II;UAS-*CaMKII*/III	

Table 20: Statistical analysis for Figure 25

Table 20A Multiple comparison of genotypes using Kruskal Wallis test (with in-built Bonferroni correction) where "N" is the total number of trials and "n" is the number of flies tested. All boxes contain p-values.

N/n	Genotype	WT-CS	*Pka-C1^{H2}*/II	*rg^{γ5}*/X	*rg^{γ5}*/X;*Pka-C1^{H2}*/II
300/30	WT-CS		0.0000804	~1.0000000	~1.0000000
300/30	*Pka-C1^{H2}*/II	0.0000804		0.0000003	0.0014629
300/30	*rg^{γ5}*/X	~1.00000	0.0000003		0.4712826
300/30	*rg^{γ5}*/X;*Pka-C1^{H2}*/II	~1.00000	0.0014629	0.4712826	

Table 20B Tests for normality (Shapiro-Wilk) and comparison against chance level (58%).

N/n	Genotype	Normality score	Statistical test	p-value
300/30	WT-CS	0.00001	Sign-Test	0.0000001
300/30	*Pka-C1^{H2}*/II	0.00009	Sign-Test	0.0000008
300/30	*rg$^{\gamma 5}$*/X	0.00010	Sign-Test	0.0000001
300/30	*rg$^{\gamma 5}$*/X;*Pka-C1^{H2}*/II	0.00214	Sign-Test	0.0000001

Table 21: Statistical analysis for Figure 26

Table 21A Multiple comparison of genotypes using Kruskal-Wallis test (with in-built Bonferroni correction) where "N" is the total number of trials and "n" is the number of flies tested. All boxes contain p-values.

N/n	Genotype	WT-CS	*Pka-C1^{H2}*189Y-GAL4/II	*Pka-C1^{H2}*189Y-GAL4/UAS-*rg^{RNAi}*	*Pka-C1^{H2}* 189Y-GAL4/ UAS-*rg*
250/25	WT-CS		0.0000419	~1.000000	0.0000610
300/30	*Pka-C1^{H2}*189Y-GAL4/II	0.0000419		$<10^{-7}$	~1.000000
300/30	*Pka-C1^{H2}*189Y-GAL4/UAS-*rg^{RNAi}*	~1.00000	$<10^{-7}$		$<10^{-7}$
240/24	*Pka-C1^{H2}*189Y-GAL4/UAS-*rg*	0.0000610	~1.000000	$<10^{-7}$	

Table 21B Tests for normality (Shapiro-Wilk) and comparison against chance level (58%).

N/n	Genotype	Normality score	Statistical test	p-value
250/25	WT-CS	0.00001	Sign-Test	0.0000015
300/30	*Pka-C1^{H2}*189Y-GAL4/II	0.02663	Sign-Test	0.0019107
300/30	*Pka-C1^{H2}*189Y-GAL4/UAS-*rg^{RNAi}*	0.00007	Sign-Test	0.0000001
240/24	*Pka-C1^{H2}*189Y-GAL4/UAS-*rg*	0.01163	Sign-Test	0.0005202

Table 22: Statistical analysis for Figure 27

Mann-Whitney-U test to compare two groups where N is the total number of samples.

Mann-Whitney U test: FAS-II (control group) (vs) FAS-II (experimental group)		
N	Genotype	p-value
8	VT42759-GAL4>UAS-Pka-C1[Fl5.9]/III	0.2369852
10	*rg$^{\gamma 5}$*/Y;VT42759-GAL4>UAS-Pka-C1[Fl5.9]/III	
Mann-Whitney U test: PKA-C1[Fl]/FAS-II (control group) (vs) PKA-C1[Fl]/FAS-II (experimental group)		
N	Genotype	p-value
8	VT42759-GAL4>UAS-Pka-C1[Fl5.9]/III	0.0342794
10	*rg$^{\gamma 5}$*/Y;VT42759-GAL4>UAS-Pka-C1[Fl5.9]/III	

Table 23: Statistical analysis for Figure 28

Table 23A Multiple comparison of genotypes using Kruskal-Wallis test (with in-built Bonferroni correction) where “N” is the total number of trials and “n” is the number of flies tested. All boxes contain p-values.

N/n	Genotype	WT-CS	189Y-GAL4/II	UAS-*rg*/II	189Y-GAL4/ UAS-*rg*
280/28	WT-CS		~1.000000	~1.000000	0.0000004
300/30	189Y-GAL4/II	~1.000000		~1.000000	0.0000001
300/30	UAS-*rg*/II	~1.000000	~1.000000		0.0000369
290/29	189Y-GAL4/UAS-*rg*	0.0000004	0.0000001	0.0000369	

Table 23B Tests for normality (Shapiro-Wilk) and comparison against chance level (58%).

N/n	Genotype	Normality score	Statistical test	p-value
280/28	WT-CS	0.00013	Sign-Test	0.0000003
300/30	189Y-GAL4/II	0.00015	Sign-Test	0.0000001
300/30	UAS-*rg*/II	0.00189	Sign-Test	0.0000001
290/29	189Y-GAL4/UAS-*rg*	0.00197	Sign-Test	0.0002040

Table 24: Statistical analysis for Figure 29

Mann-Whitney-U test to compare two groups where N is the total number of samples.

Mann Whitney.U test: FAS-II (control group) (vs) FAS-II (experimental group)		
N	Genotype	p-value
9	VT42759-GAL4>UAS-Pka-C1[Fl5.9]/III	0.3311621
11	UAS-*rg*/II;VT42759-GAL4>UAS-Pka-C1[Fl5.9]/III	
Mann-Whitney U test: PKA-C1[Fl]/FAS-II (control group) (vs) PKA-C1[Fl]/FAS-II (experimental group)		
N	Genotype	p-value
9	VT42759-GAL4>UAS-Pka-C1[Fl5.9]/III	0.0124672
11	UAS-*rg*/II;VT42759-GAL4>UAS-Pka-C1[Fl5.9]/III	

8.2 Temperature-mediated screening of neurons involved in visual working memory

Table 25: Statistical analysis for Figure 30A

Table 25A Pair-wise statistical analysis with Wilcoxon matched pair test where “N” is the total number of trials and “n” is the number of flies tested.

N/n	Genotype	Z value	p-value
240/24	R31A12-GAL4/III (at 21ºC)	1.3063122	0.1914473
	R31A12-GAL4/III (at 29ºC)		
240/24	UAS-*TrpA1*/II (at 21ºC)	0.4193139	0.6749869
	UAS-*TrpA1*/II (at 29ºC)		
240/24	UAS-*TrpA1*/II; R31A12-GAL4/III (at 21ºC)	0.0653255	0.9479148
	UAS-*TrpA1*/II; R31A12-GAL4/III (at 29ºC)		

Table 25B Tests for normality (Shapiro-Wilk) and comparison against chance level (58%)

N/n	Genotype	Normality score	Statistical test	p-value
240/24	R31A12-GAL4/III (at 21ºC)	0.00005	Sign-Test	0.0000026
240/24	R31A12-GAL4/III (at 29ºC)	0.00378	Sign-Test	0.0000026
240/24	UAS-*TrpA1*/II (at 21ºC)	0.04789	Sign-Test	0.0000026
240/24	UAS-*TrpA1*/II (at 29ºC)	0.00328	Sign-Test	0.0001051
240/24	UAS-*TrpA1*/II;R31A12-GAL4/III (at 21ºC)	0.00609	Sign-Test	0.0000026
240/24	UAS-*TrpA1*/II; R31A12-GAL4/III (at 29ºC)	0.00877	Sign-Test	0.0000026

Table 26: Statistical analysis for Figure 30B

Table 26A Pair-wise statistical analysis with Wilcoxon matched pair test where “N” is the total number of trials and “n” is the number of flies tested.

N/n	Genotype	Z value	p-value
190/19	R19C08-GAL4/III (at 21ºC)	1.2668648	0.2052045
	R19C08-GAL4/III (at 29ºC)		
240/24	UAS-*TrpA1*/II (at 21ºC)	0.4193139	0.6749869
	UAS-*TrpA1*/II (at 29ºC)		
250/25	UAS-*TrpA1*/II; R19C08-GAL4/III (at 21ºC)	4.0145085	0.0000595
	UAS-*TrpA1*/II; R19C08-GAL4/III (at 29ºC)		

Table 26B Tests for normality (Shapiro-Wilk) and comparison against chance level (58%)

N/n	Genotype	Normality score	Statistical test	p-value
190/19	R19C08-GAL4/III (at 21ºC)	0.00731	Sign-Test	0.0002419
190/19	R19C08-GAL4/III (at 29ºC)	0.00209	Sign-Test	0.0000363
240/24	UAS-*TrpA1*/II (at 21ºC)	0.04789	Sign-Test	0.0000026
240/24	UAS-*TrpA1*/II (at 29ºC)	0.00328	Sign-Test	0.0001051
250/25	UAS-*TrpA1*/II; R19C08-GAL4/III (at 21ºC)	0.00362	Sign-Test	0.0000015

250/25	UAS-*TrpA1*/II; R19C08-GAL4/III (at 29ºC)	0.02407	Sign-Test	0.6891565

Table 27: Statistical analysis for Figure 30C

Table 27A Pair-wise statistical analysis with Wilcoxon matched pair test where "N" is the total number of trials and "n" is the number of flies tested.

N/n	Genotype	Z value	p-value
220/22	189Y-GAL4/II (at 21ºC)	1.0358119	0.3002906
	189Y -GAL4/II (at 29ºC)		
240/24	UAS-*TrpA1*/II (at 21ºC)	0.4193139	0.6749869
	UAS-*TrpA1*/II (at 29ºC)		
210/21	189Y-GAL4/UAS-*TrpA1* (at 21ºC)	3.5929043	0.0003270
	189Y-GAL4/UAS-*TrpA1* (at 29ºC)		

Table 27B Tests for normality (Shapiro-Wilk) and comparison against chance level (58%)

N/n	Genotype	Normality score	Statistical test	p-value
220/22	189Y-GAL4/II (at 21ºC)	0.01903	Sign-Test	0.0000510
220/22	189Y-GAL4/II (at 29ºC)	0.01434	Sign-Test	0.0000510
240/24	UAS-*TrpA1*/II (at 21ºC)	0.04789	Sign-Test	0.0000026
240/24	UAS-*TrpA1*/II (at 29ºC)	0.00328	Sign-Test	0.0001051
210/21	189Y-GAL4/UAS-*TrpA1* (at 21ºC)	0.00202	Sign-Test	0.0000127
210/21	189Y-GAL4/UAS-*TrpA1* (at 29ºC)	0.00031	Sign-Test	0.0808556

Table 28: Statistical analysis for Figure 30D

Table 28A Pair-wise statistical analysis with Wilcoxon matched pair test where "N" is the total number of trials and "n" is the number of flies tested.

N/n	Genotype	Z value	p-value
290/29	*ftz-ng*-GAL4/III (at 21ºC)	0.7847225	0.4326168
	ftz-ng-GAL4/III (at 29ºC)		
250/25	UAS-*TrpA1*/II (at 21ºC)	1.0875992	0.2767728
	UAS-*TrpA1*/II (at 29ºC)		
300/30	UAS-*TrpA1*/II; *ftz-ng*-GAL4/III (at 21ºC)	1.1849962	0.2360198
	UAS-*TrpA1*/II; *ftz-ng*-GAL4/III (at 29ºC)		

Table 28B Tests for normality (Shapiro-Wilk) and comparison against chance level (58%)

N/n	Genotype	Normality score	Statistical test	p-value
290/29	*ftz-ng*-GAL4/III (at 21ºC)	0.00023	Sign-Test	0.0000013
290/29	*ftz-ng*-GAL4/III (at 29ºC)	0.00125	Sign-Test	0.0000013
250/25	UAS-*TrpA1*/II (at 21ºC)	0.00058	Sign-Test	0.0000015
250/25	UAS-*TrpA1*/II (at 29ºC)	0.00478	Sign-Test	0.0000108
300/30	UAS-*TrpA1*/II; *ftz-ng*-GAL4/III (at 21ºC)	0.00079	Sign-Test	0.0000050
300/30	UAS-*TrpA1*/II; *ftz-ng*-GAL4/III (at 29ºC)	0.00980	Sign-Test	0.0000267

Table 29: Statistical analysis for Figure 30E

Table 29A Pair-wise statistical analysis with Wilcoxon matched pair test where “N” is the total number of trials and “n” is the number of flies tested.

N/n	Genotype	Z value	p-value
240/24	R58H05-GAL4/III (at 21ºC)	0.6722139	0.5014479
	R58H05-GAL4/III (at 29ºC)		
240/24	UAS-*TrpA1*/II (at 21ºC)	0.4193139	0.6749869
	UAS-*TrpA1*/II (at 29ºC)		
240/24	UAS-*TrpA1*/II; R58H05-GAL4/III (at 21ºC)	4.0744391	0.0000461
	UAS-*TrpA1*/II; R58H05-GAL4/III (at 29ºC)		

Table 29B Tests for normality (Shapiro-Wilk) and comparison against chance level (58%)

N/n	Genotype	Normality score	Statistical test	p-value
240/24	R58H05-GAL4/III (at 21ºC)	0.00031	Sign-Test	0.0000026
240/24	R58H05-GAL4/III (at 29ºC)	0.00242	Sign-Test	0.0000026
240/24	UAS-*TrpA1*/II (at 21ºC)	0.04789	Sign-Test	0.0000026
240/24	UAS-*TrpA1*/II (at 29ºC)	0.00328	Sign-Test	0.0001051
240/24	UAS-*TrpA1*/II; R58H05-GAL4/III (at 21ºC)	0.00019	Sign-Test	0.0000026
240/24	UAS-*TrpA1*/II; R58H05-GAL4/III (at 29ºC)	0.10240	t-Test	0.3183442

Table 30: Statistical analysis for Figure 30F

Table 30A Pair-wise statistical analysis with Wilcoxon matched pair test where “N” is the total number of trials and “n” is the number of flies tested.

N/n	Genotype	Z value	p-value
240/24	VT011965-GAL4/III (at 21ºC)	0.4023739	0.6874091
	VT011965-GAL4/III (at 29ºC)		
240/24	UAS-*TrpA1*/II (at 21ºC)	0.4193139	0.6749869
	UAS-*TrpA1*/II (at 29ºC)		
240/24	UAS-*TrpA1*/II; VT011965-GAL4/III (at 21ºC)	4.1972635	0.0000270
	UAS-*TrpA1*/II; VT011965-GAL4/III (at 29ºC)		

Table 30B Tests for normality (Shapiro-Wilk) and comparison against chance level (58%)

N/n	Genotype	Normality score	Statistical test	p-value
240/24	VT011965-GAL4/III (at 21ºC)	0.00183	Sign-Test	0.0000026
240/24	VT011965-GAL4/III (at 29ºC)	0.00041	Sign-Test	0.0000026
240/24	UAS-*TrpA1*/II (at 21ºC)	0.04789	Sign-Test	0.0000026
240/24	UAS-*TrpA1*/II (at 29ºC)	0.00328	Sign-Test	0.0001051
240/24	UAS-*TrpA1*/II; VT011965-GAL4/III (at 21ºC)	0.00043	Sign-Test	0.0000026
240/24	UAS-*TrpA1*/II; VT011965-GAL4/III (at 29ºC)	0.03255	Sign-Test	0.0079634

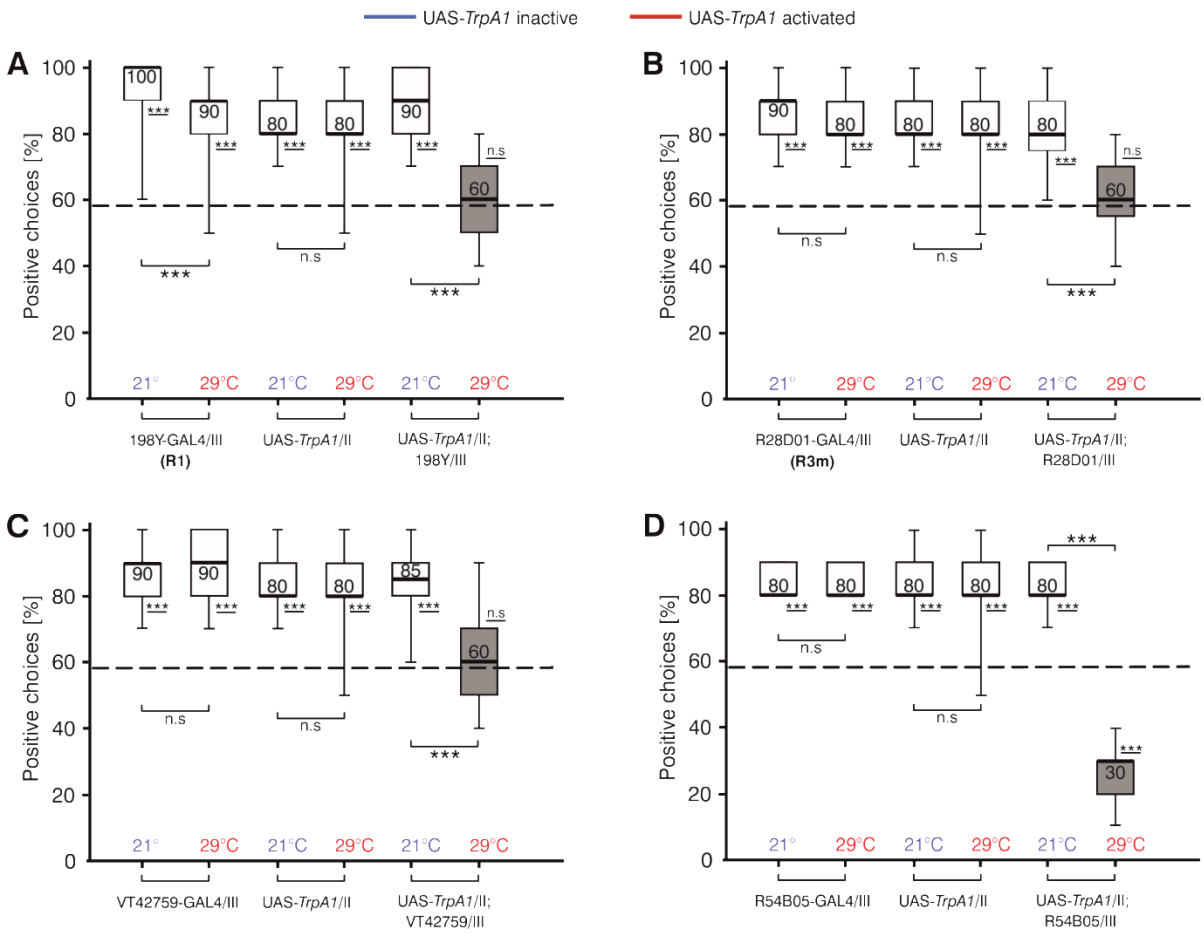

Figure 57: TrpA1 activation of R1 and R3 Ring neurons (additional drivers)

(A) Activation of R1 neurons (UAS-*TrpA1*/II;198-GAL4/III, n=30) elicited a defect in detour memory (median 60%) and was not significantly different from the chance level (58%). **(B&C)** Overactivation of R3m neurons (UAS-*TrpA1*/II;R28D01-GAL4/III, n=23) and R3d/p (UAS-*TrpA1*/II;VT42759-GAL4/III, n=24) neurons at 29°C led to a complete loss of memory (median=60%) which was not significantly different from the chance level. **(D)** R3 neurons (UAS-*TrpA1*/II;R54B05-GAL4/III, n=25) had a complete loss of memory in detour memory when activated at 29°C (median=30%) and was significantly lower than the chance level (58%).

Overactivation of the R1 neurons (198Y-GAL4; (Renn et al., 1999)) using UAS-*TrpA1* (29ºC) destroyed the detour memory in comparison to the inactivated state (21ºC) (Figure 57A). The GAL4 and UAS controls behaved like WT-CS flies at both temperatures, with a median of 90% and 80%, indicating that the control groups were reliable. UAS-*TrpA1* activation of different subtypes of the R3 neurons ie., R3m (R28D01-GAL4; (Omoto et al., 2018)) (Figure 57B), R3(d+p) (VT42759-GAL4; (Lin et al., 2013)) (Figure 57C), and R3 (R54B05-GAL4; (Ofstad et al., 2011)) (Figure 57D), also led to a complete loss of memory, which was not significantly different from the chance level. The GAL4 and UAS controls for all of the above mentioned neuronal subtypes behaved like wild-type flies, indicating that the reduction in detour memory is an effect of the neuronal activation at the restrictive temperature range (28-30ºC).

Table 31: Statistical analysis for Figure 57A

Table 31A Pair-wise statistical analysis with Wilcoxon matched pair test where “N” is the total number of trials and “n” is the number of flies tested.

N/n	Genotype	Z value	p-value
190/19	198Y-GAL4/III (at 21ºC)	2.5738357	0.0100582
	198Y -GAL4/III (at 29ºC)		
240/24	UAS-*TrpA1*/II (at 21ºC)	0.4193139	0.6749869
	UAS-*TrpA1*/II (at 29ºC)		
300/30	UAS-*TrpA1*/II; 198Y-GAL4/III (at 21ºC)	4.6175921	0.0000038
	UAS-*TrpA1*/II; 198Y-GAL4/III (at 29ºC)		

Table 31B Tests for normality (Shapiro-Wilk) and comparison against chance level (58%)

N/n	Genotype	Normality score	Statistical test	p-value
190/19	198Y-GAL4/III (at 21ºC)	0.00002	Sign-Test	0.0000363
190/19	198Y-GAL4/III (at 29ºC)	0.00010	Sign-Test	0.0002419
240/24	UAS-*TrpA1*/II (at 21ºC)	0.04789	Sign-Test	0.0000026
240/24	UAS-*TrpA1*/II (at 29ºC)	0.00328	Sign-Test	0.0001051
300/30	UAS-*TrpA1*/II; 198Y-GAL4/III (at 21ºC)	0.00004	Sign-Test	0.0000008
300/30	UAS-*TrpA1*/II; 198Y-GAL4/III (at 29ºC)	0.16451	t-Test	0.611523

Table 32: Statistical analysis for Figure 57B

Table 32A Pair-wise statistical analysis with Wilcoxon matched pair test where “N” is the total number of trials and “n” is the number of flies tested.

N/n	Genotype	Z value	p-value
230/23	R28D01-GAL4/III (at 21ºC)	0.8001976	0.4235969
	R28D01-GAL4/III (at 29ºC)		
240/24	UAS-*TrpA1*/II (at 21ºC)	0.4193139	0.6749869
	UAS-*TrpA1*/II (at 29ºC)		
230/23	UAS-*TrpA1*/II; R28D01-GAL4/III (at 21ºC)	3.8018691	0.0001436
	UAS-*TrpA1*/II; R28D01-GAL4/III (at 29ºC)		

Table 32B Tests for normality (Shapiro-Wilk) and comparison against chance level (58%)

N/n	Genotype	Normality score	Statistical test	p-value
230/23	R28D01-GAL4/III (at 21ºC)	0.03931	Sign-Test	0.0000044
230/23	R28D01-GAL4/III (at 29ºC)	0.02650	Sign-Test	0.0000304
240/24	UAS-*TrpA1*/II (at 21ºC)	0.04789	Sign-Test	0.0000026
240/24	UAS-*TrpA1*/II (at 29ºC)	0.00328	Sign-Test	0.0001051
230/23	UAS-*TrpA1*/II; R28D01-GAL4/III (at 21ºC)	0.06393	t-Test	0.0000000
230/23	UAS-*TrpA1*/II; R28D01-GAL4/III (at 29ºC)	0.09640	t-Test	0.3724289

Table 33: Statistical analysis for Figure 57C

Table 33A Pair-wise statistical analysis with Wilcoxon matched pair test where “N” is the total number of trials and “n” is the number of flies tested.

N/n	Genotype	Z value	p-value
240/24	VT42759-GAL4/III (at 21ºC)	1,5024872	0.1329723
	VT42759-GAL4/III (at 29ºC)		
240/24	UAS-*TrpA1*/II (at 21ºC)	0.4193139	0.6749869
	UAS-*TrpA1*/II (at 29ºC)		
240/24	UAS-*TrpA1*/II; VT42759-GAL4/III (at 21ºC)	3.7538261	0.0001741
	UAS-*TrpA1*/II; VT42759/III (at 29ºC)		

Table 33B Tests for normality (Shapiro-Wilk) and comparison against chance level (58%)

N/n	Genotype	Normality score	Statistical test	p-value
240/24	VT42759-GAL4/III (at 21ºC)	0.02058	Sign-Test	0.0000026
240/24	VT42759-GAL4/III (at 29ºC)	0.00354	Sign-Test	0.0000026
240/24	UAS-*TrpA1*/II (at 21ºC)	0.04789	Sign-Test	0.0000026
240/24	UAS-*TrpA1*/II (at 29ºC)	0.00328	Sign-Test	0.0001051
240/24	UAS-*TrpA1*/II; VT42759-GAL4/III (at 21ºC)	0.01249	Sign-Test	0.0000181
240/24	UAS-*TrpA1*/II; VT42759-GAL4/III (at 29ºC)	0.06698	t-Test	0.2943239

Table 34: Statistical analysis for Figure 57D

Table 34A Pair-wise statistical analysis with Wilcoxon matched pair test where “N” is the total number of trials and “n” is the number of flies tested.

N/n	Genotype	Z value	p-value
250/25	R54B05-GAL4/III (at 21ºC)	0.0000000	1.0000000
	R54B05-GAL4/III (at 29ºC)		
240/24	UAS-*TrpA1*/II (at 21ºC)	0.4193139	0.6749869
	UAS-*TrpA1*/II (at 29ºC)		
250/25	UAS-*TrpA1*/II; R54B05-GAL4/III (at 21ºC)	4.3723731	0.0000122
	UAS-*TrpA1*/II; R54B05-GAL4/III (at 29ºC)		

Table 34B Tests for normality (Shapiro-Wilk) and comparison against chance level (58%)

N/n	Genotype	Normality score	Statistical test	p-value
250/25	R54B05-GAL4/III (at 21ºC)	0.00000	Sign-Test	0.0000015
250/25	R54B05-GAL4/III (at 29ºC)	0.00000	Sign-Test	0.0000015
240/24	UAS-*TrpA1*/II (at 21ºC)	0.04789	Sign-Test	0.0000026
240/24	UAS-*TrpA1*/II (at 29ºC)	0.00328	Sign-Test	0.0001051
250/25	UAS-*TrpA1*/II; R54B05-GAL4/III (at 21ºC)	0.00247	Sign-Test	0.0000015
250/25	UAS-*TrpA1*/II; R54B05-GAL4/III (at 29ºC)	0.00953	Sign-Test	0.0000015

Table 35: Statistical analysis for Figure 31A

Table 35A Pair-wise statistical analysis with Wilcoxon matched pair test where “N” is the total number of trials and “n” is the number of flies tested.

N/n	Genotype	Z value	p-value
250/25	R19G02-GAL4/III (at 21ºC)	1.3382579	0.1808133
	R19G02-GAL4/III (at 29ºC)		
240/24	UAS-*TrpA1*/II (at 21ºC)	0.4193139	0.6749869
	UAS-*TrpA1*/II (at 29ºC)		
230/23	UAS-*TrpA1*/II; R19G02-GAL4/III (at 21ºC)	4.0145085	0.0000595
	UAS-*TrpA1*/II; R19G02-GAL4/III (at 29ºC)		

Table 35B Tests for normality (Shapiro-Wilk) and comparison against chance level (58%)

N/n	Genotype	Normality score	Statistical test	p-value
250/25	R19G02-GAL4/III (at 21ºC)	0.00145	Sign-Test	0.0000026
250/25	R19G02-GAL4/III (at 29ºC)	0.00960	Sign-Test	0.0000181
240/24	UAS-*TrpA1*/II (at 21ºC)	0.04789	Sign-Test	0.0000026
240/24	UAS-*TrpA1*/II (at 29ºC)	0.00328	Sign-Test	0.0001051
230/23	UAS-*TrpA1*/II; R19G02-GAL4/III (at 21ºC)	0.00292	Sign-Test	0.0000044
230/23	UAS-*TrpA1*/II; R19G02-GAL4/III (at 29ºC)	0.06795	t-Test	0.5575826

Table 36: Statistical analysis for Figure 31B

Table 36A Pair-wise statistical analysis with Wilcoxon matched pair test where “N” is the total number of trials and “n” is the number of flies tested.

N/n	Genotype	Z value	p-value
180/24	R12D09-GAL4/III (at 21ºC)	0,5963599	0,5509352
	R12D09-GAL4/III (at 29ºC)		
240/24	UAS-*TrpA1*/II (at 21ºC)	0.4193139	0.6749869
	UAS-*TrpA1*/II (at 29ºC)		
240/18	UAS-*TrpA1*/II; R12D09-GAL4/III (at 21ºC)	4.2857142	0.0000182
	UAS-*TrpA1*/II; R12D09-GAL4/III (at 29ºC)		

Table 36B Tests for normality (Shapiro-Wilk) and comparison against chance level (58%)

N/n	Genotype	Normality score	Statistical test	p-value
180/18	R12D09-GAL4/III (at 21ºC)	0.07689	t-Test	0.0000000
180/18	R12D09-GAL4/III (at 29ºC)	0.08488	t-Test	0.0000006
240/24	UAS-*TrpA1*/II (at 21ºC)	0.04789	Sign-Test	0.0000026
240/24	UAS-*TrpA1*/II (at 29ºC)	0.00328	Sign-Test	0.0001051
240/24	UAS-*TrpA1*/II; R12D09-GAL4/III (at 21ºC)	0.00179	Sign-Test	0.0000026
240/24	UAS-*TrpA1*/II; R12D09-GAL4/III (at 29ºC)	0.03646	Sign-Test	0.0661925

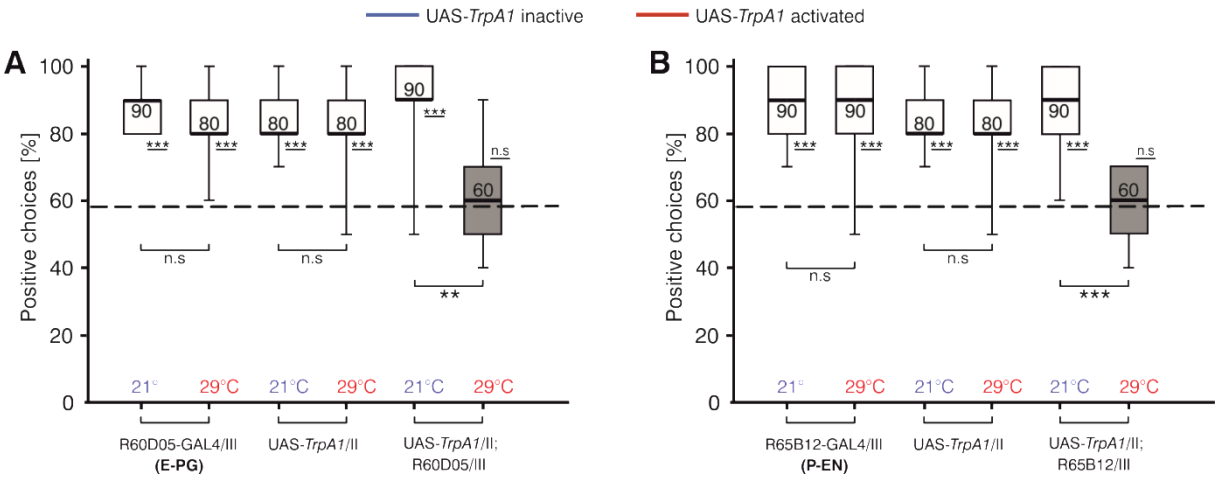

Figure 58: TrpA1 activation of compass and shift neurons (additional drivers)

(A) Overactivation of compass neurons (UAS-*TrpA1*/II; R60D05/III, n=19) led to a complete loss of memory at 29°C (median=60%) which was very highly significantly different from the median memory score of the same group at 21°C (median=90%). The GAL4 (R60D05-GAL4/III, n=23) and UAS (UAS-*TrpA1*/II, n=24) control groups exhibited memory scores of 90% and 80% respectively at both temperatures. **(B)** TrpA1 activation of the shift neurons (UAS-*TrpA1*/II; R65B12/III, n=23) led to a complete memory loss (median=60) which was very highly significantly different from the memory score of the same group (median=90, n=24) at 21°C. The GAL4 (R65B12-GAL4/III; n=24) and UAS (UAS-*TrpA1*/II, n=24) control groups behaved like wild-type flies with median memory scores ranging between 80-90% in both temperature conditions.

Activation of the E-PG neurons by driving UAS-*TrpA1* with the R60D05-GAL4 (Wolff et al., 2015) driver, led to a complete loss of visual working memory, where the median memory score of the activated group was highly significantly different from that of the same group in the inactivated scenario (Figure 58A). The GAL4 (R60D05-GAL4/III) and UAS controls (UAS-*TrpA1*/II) performed like WT-CS flies, with median memory scores ranging between 80% and 90%, which were very highly significantly different from the chance level (Figure 58A).

As for the P-EN neurons, the R65B12-GAL4 (Wolff et al., 2015) driver was used to drive UAS-*TrpA1* in these neurons where the visual short-term orientation memory was completely lost at 29ºC, while the same group of flies displayed wild-type like memory at 21ºC. The latter exhibited a memory score of 90% that was very highly significantly different from the chance level (Figure 58B). The GAL4 (R65B12-GAL4/III) and UAS control (UAS-*TrpA1*/II) groups behaved like wild-type flies with high memory median scores of 90% and 80% that were very highly significantly different from chance level (Figure 58B).

Table 37: Statistical analysis for Figure 58A

Table 37A Pair-wise statistical analysis with Wilcoxon matched pair test where “N” is the total number of trials and “n” is the number of flies tested.

N/n	Genotype	Z value	p-value
230/23	R60D05-GAL4/III (at 21ºC)	1.5467154	0.1219328
	R60D05-GAL4/III (at 29ºC)		
240/24	UAS-*TrpA1*/II (at 21ºC)	0.4193139	0.6749869
	UAS-*TrpA1*/II (at 29ºC)		
190/19	UAS-*TrpA1*/II; R60D05-GAL4/III (at 21ºC)	2.9614241	0.0030624
	UAS-*TrpA1*/II; R60D05-GAL4/III (at 29ºC)		

Table 37B Tests for normality (Shapiro-Wilk) and comparison against chance level (58%)

N/n	Genotype	Normality score	Statistical test	p-value
230/23	R60D05-GAL4/III (at 21ºC)	0.00323	Sign-Test	0.0000044
230/23	R60D05-GAL4/III (at 29ºC)	0.03950	Sign-Test	0.0000044
240/24	UAS-*TrpA1*/II (at 21ºC)	0.04789	Sign-Test	0.0000026
240/24	UAS-*TrpA1*/II (at 29ºC)	0.00328	Sign-Test	0.0001051
190/19	UAS-*TrpA1*/II; R60D05-GAL4/III (at 21ºC)	0.00015	Sign-Test	
190/19	UAS-*TrpA1*/II; R60D05-GAL4/III (at 29ºC)	0.14301	t-Test	0.09005

Table 38: Statistical analysis for Figure 58B

Table 38A Pair-wise statistical analysis with Wilcoxon matched pair test where “N” is the total number of trials and “n” is the number of flies tested.

N/n	Genotype	Z value	p-value
240/24	R65B12-GAL4/III (at 21ºC)	0.2068350	0.8361387
	R65B12-GAL4/III (at 29ºC)		
240/24	UAS-*TrpA1*/II (at 21ºC)	0.4193139	0.6749869
	UAS-*TrpA1*/II (at 29ºC)		
230/23	UAS-*TrpA1*/II; R65B12-GAL4/III (at 21ºC)	3.4977196	0.0004693
	UAS-*TrpA1*/II; R65B12-GAL4/III (at 29ºC)		

Table 38B Tests for normality (Shapiro-Wilk) and comparison against chance level (58%)

N/n	Genotype	Normality score	Statistical test	p-value
240/24	R65B12-GAL4/III (at 21ºC)	0.01134	Sign-Test	0.0000026
240/24	R65B12-GAL4/III (at 29ºC)	0.00046	Sign-Test	0.0001051
240/24	UAS-*TrpA1*/II (at 21ºC)	0.04789	Sign-Test	0.0000026
240/24	UAS-*TrpA1*/II (at 29ºC)	0.00328	Sign-Test	0.0001051
230/23	UAS-*TrpA1*/II; R65B12-GAL4/III (at 21ºC)	0.00001	Sign-Test	0.0000304
230/23	UAS-*TrpA1*/II; R65B12-GAL4/III (at 29ºC)	0.00569	Sign-Test	0.4042485

Table 39: Statistical analysis for Figure 42A

Table 39A Pair-wise statistical analysis with Wilcoxon matched pair test where “N” is the total number of trials and “n” is the number of flies tested.

N/n	Genotype	Z value	p-value
230/23	R75H04-GAL4/III (at 21ºC)	2.2646184	0.0235367
	R75H04-GAL4/III (at 29ºC)		
240/24	UAS-*TrpA1*/II (at 21ºC)	0.4193139	0.6749869
	UAS-*TrpA1*/II (at 29ºC)		
240/24	UAS-*TrpA1*/II; R75H04-GAL4/III (at 21ºC)	4.0145085	0.0000595
	UAS-*TrpA1*/II; R75H04-GAL4/III (at 29ºC)		

Table 39B Tests for normality (Shapiro-Wilk) and comparison against chance level (58%)

N/n	Genotype	Normality score	Statistical test	p-value
230/23	R75H04-GAL4/III (at 21ºC)	0.00002	Sign-Test	0.0000044
230/23	R75H04-GAL4/III (at 29ºC)	0.01137	Sign-Test	0.0000044
240/24	UAS-*TrpA1*/II (at 21ºC)	0.04789	Sign-Test	0.0000026
240/24	UAS-*TrpA1*/II (at 29ºC)	0.00328	Sign-Test	0.0001051
240/24	UAS-*TrpA1*/II; R75H04-GAL4/III (at 21ºC)	0.00135	Sign-Test	0.0000026
240/24	UAS-*TrpA1*/II; R75H04-GAL4/III (at 29ºC)	0.04798	Sign-Test	0.0021996

Table 40: Statistical analysis for Figure 42B

Table 40A Pair-wise statistical analysis with Wilcoxon matched pair test where “N” is the total number of trials and “n” is the number of flies tested.

N/n	Genotype	Z value	p-value
240/24	R32A11-GAL4/III (at 21ºC)	0.2800560	0.7794347
	R32A11-GAL4/III (at 29ºC)		
240/24	UAS-*TrpA1*/II (at 21ºC)	0.4193139	0.6749869
	UAS-*TrpA1*/II (at 29ºC)		
240/24	UAS-*TrpA1*/II; R32A11-GAL4/III (at 21ºC)	4.1972635	0.0000270
	UAS-*TrpA1*/II; R32A11-GAL4/III (at 29ºC)		

Table 40B Tests for normality (Shapiro-Wilk) and comparison against chance level (58%)

N/n	Genotype	Normality score	Statistical test	p-value
240/24	R32A11-GAL4/III (at 21ºC)	0.00028	Sign-Test	0.0000026
240/24	R32A11-GAL4/III (at 29ºC)	0.00358	Sign-Test	0.0000026
240/24	UAS-*TrpA1*/II (at 21ºC)	0.04789	Sign-Test	0.0000026
240/24	UAS-*TrpA1*/II (at 29ºC)	0.00328	Sign-Test	0.0001051
240/24	UAS-*TrpA1*/II; R32A11-GAL4/III (at 21ºC)	0.00320	Sign-Test	0.0000026
240/24	UAS-*TrpA1*/II; R32A11-GAL4/III (at 29ºC)	0.00788	Sign-Test	0.8382565

Table 41: Statistical analysis for Figure 42C

Table 41A Pair-wise statistical analysis with Wilcoxon matched pair test where “N” is the total number of trials and “n” is the number of flies tested.

N/n	Genotype	Z value	p-value
240/24	R18A05-GAL4/III (at 21ºC)	0.9307578	0.3519795
	R18A05-GAL4/III (at 29ºC)		
240/24	UAS-*TrpA1*/II (at 21ºC)	0.4193139	0.6749869
	UAS-*TrpA1*/II (at 29ºC)		
240/24	UAS-*TrpA1*/II; R18A05-GAL4/III (at 21ºC)	0.9824666	0.3258707
	UAS-*TrpA1*/II; R18A05-GAL4/III (at 29ºC)		

Table 41B Tests for normality (Shapiro-Wilk) and comparison against chance level (58%)

N/n	Genotype	Normality score	Statistical test	p-value
240/24	R18A05-GAL4/III (at 21ºC)	0.00004	Sign-Test	0.0000026
240/24	R18A05-GAL4/III (at 29ºC)	0.00019	Sign-Test	0.0000026
240/24	UAS-*TrpA1*/II (at 21ºC)	0.04789	Sign-Test	0.0000026
240/24	UAS-*TrpA1*/II (at 29ºC)	0.00328	Sign-Test	0.0001051
240/24	UAS-*TrpA1*/II; R18A05-GAL4/III (at 21ºC)	0.00188	Sign-Test	0.0000026
240/24	UAS-*TrpA1*/II; R18A05-GAL4/III (at 29ºC)	0.00112	Sign-Test	0.0000026

Table 42: Statistical analysis for Figure 32A

Table 42A Pair-wise statistical analysis with Wilcoxon matched pair test where “N” is the total number of trials and “n” is the number of flies tested.

N/n	Genotype	Z value	p-value
240/24	R31A12-GAL4/III (at 24ºC)	0.4136701	0.6791159
	R31A12-GAL4/III (at 32ºC)		
250/25	UAS-shi^{ts1}/III (at 24ºC)	0.0851942	0.9321069
	UAS-shi^{ts1}/III (at 32ºC)		
250/25	R31A12-GAL4/UAS-shi^{ts1} (at 24ºC)	0.7383503	0.4603021
	R31A12-GAL4/UAS-shi^{ts1} (at 32ºC)		

Table 42B Tests for normality (Shapiro-Wilk) and comparison against chance level (58%)

N/n	Genotype	Normality score	Statistical test	p-value
240/24	R31A12-GAL4/III (at 24ºC)	0.00308	Sign-Test	0.0000026
240/24	R31A12-GAL4/III (at 32ºC)	0.00000	Sign-Test	0.0000181
250/25	UAS-shi^{ts1}/III (at 24ºC)	0.00024	Sign-Test	0.0000108
250/25	UAS-shi^{ts1}/III (at 32ºC)	0.00604	Sign-Test	0.0000015
250/25	R31A12-GAL4/UAS-shi^{ts1} (at 24ºC)	0.00459	Sign-Test	0.0000015
250/25	R31A12-GAL4/UAS-shi^{ts1} (at 32ºC)	0.00389	Sign-Test	0.0000015

Table 43: Statistical analysis for Figure 32B

Table 43A Pair-wise statistical analysis with Wilcoxon matched pair test where “N” is the total number of trials and “n” is the number of flies tested.

N/n	Genotype	Z value	p-value
250/25	R19C08-GAL4/III (at 24ºC)	0.9704311	0.3318323
	R19C08-GAL4/III (at 32ºC)		
250/25	UAS-*shi*^{ts1}/III (at 24ºC)	0.0851942	0.9321069
	UAS-*shi*^{ts1}/III (at 32ºC)		
250/25	R19C08-GAL4/UAS-*shi*^{ts1} (at 24ºC)	4.1212261	0.0000376
	R19C08-GAL4/UAS-*shi*^{ts1} (at 32ºC)		

Table 43B Tests for normality (Shapiro-Wilk) and comparison against chance level (58%)

N/n	Genotype	Normality score	Statistical test	p-value
250/25	R19C08-GAL4/III (at 24ºC)	0.00007	Sign-Test	0.0000015
250/25	R19C08-GAL4/III (at 32ºC)	0.00124	Sign-Test	0,0000015
250/25	UAS-*shi*^{ts1}/III (at 24ºC)	0.00024	Sign-Test	0.0000108
250/25	UAS-*shi*^{ts1}/III (at 32ºC)	0.00604	Sign-Test	0.0000015
250/25	R19C08-GAL4/UAS-*shi*^{ts1} (at 24ºC)	0.00382	Sign-Test	0.0000015
250/25	R19C08-GAL4/UAS-*shi*^{ts1} (at 32ºC)	0.08973	t-Test	0.8739867

Table 44: Statistical analysis for Figure 32C

Table 44A Pair-wise statistical analysis with Wilcoxon matched pair test where “N” is the total number of trials and “n” is the number of flies tested.

N/n	Genotype	Z value	p-value
250/25	189Y-GAL4/II (at 24ºC)	1.0887764	0.2762532
	189Y-GAL4/II (at 32ºC)		
250/25	UAS-*shi*^{ts1}/III (at 24ºC)	0.0851942	0.9321069
	UAS-*shi*^{ts1}/III (at 32ºC)		
250/25	189Y-GAL4/II; UAS-*shi*^{ts1}/III (at 24ºC)	4.2000000	0.0000266
	189Y-GAL4/II; UAS-*shi*^{ts1}/III (at 32ºC)		

Table 44B Tests for normality (Shapiro-Wilk) and comparison against chance level (58%)

N/n	Genotype	Normality score	Statistical test	p-value
250/25	189Y-GAL4/II (at 24ºC)	0.00044	Sign-Test	0.0000015
250/25	189Y-GAL4/II (at 32ºC)	0.00017	Sign-Test	0.0000015
250/25	UAS-*shi*^{ts1}/III (at 24ºC)	0.00024	Sign-Test	0.0000108
250/25	UAS-*shi*^{ts1}/III (at 32ºC)	0.00604	Sign-Test	0.0000015
250/25	189Y-GAL4/II; UAS-*shi*^{ts1}/III (at 24ºC)	0.00030	Sign-Test	0.0000015
250/25	189Y-GAL4/II; UAS-*shi*^{ts1}/III (at 32ºC)	0.18404	t-Test	0.0364520

Table 45: Statistical analysis for Figure 32D

Table 45A Pair-wise statistical analysis with Wilcoxon matched pair test where “N” is the total number of trials and “n” is the number of flies tested.

N/n	Genotype	Z value	p-value
200/20	*ftz-ng*-GAL4/III (at 24ºC)	0.1568929	0.8753293
	ftz-ng-GAL4/III (at 32ºC)		
250/25	UAS-*shi*^{ts1}/III (at 24ºC)	0.0851942	0.9321069
	UAS-*shi*^{ts1}/III (at 32ºC)		
250/25	*ftz-ng*-GAL4/UAS-*shi*^{ts1} (at 24ºC)	0.6289709	0.5293685
	ftz-ng-GAL4/UAS-*shi*^{ts1} (at 32ºC)		

Table 45B Tests for normality (Shapiro-Wilk) and comparison against chance level (58%)

N/n	Genotype	Normality score	Statistical test	p-value
200/20	*ftz-ng*-GAL4/III (at 24ºC)	0.01343	Sign-Test	0.0000215
200/20	*ftz-ng*-GAL4/III (at 32ºC)	0.01929	Sign-Test	0.0000215
250/25	UAS-*shi*^{ts1}/III (at 24ºC)	0.00024	Sign-Test	0.0000108
250/25	UAS-*shi*^{ts1}/III (at 32ºC)	0.00604	Sign-Test	0.0000015
250/25	*ftz-ng*-GAL4/UAS-*shi*^{ts1} (at 24ºC)	0.00458	Sign-Test	0.0000015
250/25	*ftz-ng*-GAL4/UAS-*shi*^{ts1} (at 32ºC)	0.00131	Sign-Test	0.0000015

Table 46: Statistical analysis for Figure 32E

Table 46A Pair-wise statistical analysis with Wilcoxon matched pair test where “N” is the total number of trials and “n” is the number of flies tested.

N/n	Genotype	Z value	p-value
240/24	R58H05-GAL4/III (at 24ºC)	1.1927198	0.2329799
	R58H05-GAL4/III (at 32ºC)		
250/25	UAS-*shi*^{ts1}/III (at 24ºC)	0.0851942	0.9321069
	UAS-*shi*^{ts1}/III (at 32ºC)		
240/24	R58H05-GAL4/UAS-*shi*^{ts1} (at 24ºC)	4.1972635	0.0000270
	R58H05-GAL4/UAS-*shi*^{ts1} (at 32ºC)		

Table 46B Tests for normality (Shapiro-Wilk) and comparison against chance level (58%)

N/n	Genotype	Normality score	Statistical test	p-value
240/24	R58H05-GAL4/III (at 24ºC)	0.00118	Sign-Test	0.0000026
240/24	R58H05-GAL4/III (at 32ºC)	0.00667	Sign-Test	0.0000026
250/25	UAS-*shi*^{ts1}/III (at 24ºC)	0.00024	Sign-Test	0.0000108
250/25	UAS-*shi*^{ts1}/III (at 32ºC)	0.00604	Sign-Test	0.0000015
240/24	R58H05-GAL4/UAS-*shi*^{ts1} (at 24ºC)	0.00064	Sign-Test	0.0000026
240/24	R58H05-GAL4/UAS-*shi*^{ts1} (at 32ºC)	0.00909	Sign-Test	0.8382565

Table 47: Statistical analysis for Figure 32F

Table 47A Pair-wise statistical analysis with Wilcoxon matched pair test where “N” is the total number of trials and “n” is the number of flies tested.

N/n	Genotype	Z value	p-value
240/24	VT011965-GAL4/III (at 24ºC)	0.4023739	0.6874091
	VT011965-GAL4/III (at 32ºC)		
250/25	UAS-*shi*^{ts1}/III (at 24ºC)	0.0851942	0.9321069
	UAS-*shi*^{ts1}/III (at 32ºC)		
240/24	VT011965-GAL4/UAS-*shi*^{ts1} (at 24ºC)	3.9445765	0.0000799
	VT011965-GAL4/UAS-*shi*^{ts1} (at 32ºC)		

Table 47B Tests for normality (Shapiro-Wilk) and comparison against chance level (58%)

N/n	Genotype	Normality score	Statistical test	p-value
240/24	VT011965-GAL4/III (at 24ºC)	0.00183	Sign-Test	0.0000026
240/24	VT011965-GAL4/III (at 32ºC)	0.00041	Sign-Test	0.0000026
250/25	UAS-*shi*^{ts1}/III (at 24ºC)	0.00024	Sign-Test	0.0000108
250/25	UAS-*shi*^{ts1}/III (at 32ºC)	0.00604	Sign-Test	0.0000015
240/24	VT011965-GAL4/UAS-*shi*^{ts1} (at 24ºC)	0.00084	Sign-Test	0.0000026
240/24	VT011965-GAL4/UAS-*shi*^{ts1} (at 32ºC)	0.09159	t-Test	0.0044631

Table 48: Statistical analysis for Figure 33A

Table 48A Pair-wise statistical analysis with Wilcoxon matched pair test where “N” is the total number of trials and “n” is the number of flies tested.

N/n	Genotype	Z value	p-value
240/24	R19G02-GAL4/III (at 24ºC)	0.8586514	0.3905335
	R19G02-GAL4/III (at 32ºC)		
250/25	UAS-*shi*^{ts1}/III (at 24ºC)	0.0851942	0.9321069
	UAS-*shi*^{ts1}/III (at 32ºC)		
230/23	R19G02-GAL4/UAS-*shi*^{ts1} (at 24ºC)	4.1069047	0.0000401
	R19G02-GAL4/UAS-*shi*^{ts1} (at 32ºC)		

Table 48B Tests for normality (Shapiro-Wilk) and comparison against chance level (58%)

N/n	Genotype	Normality score	Statistical test	p-value
240/24	R19G02-GAL4/III (at 24ºC)	0.00746	Sign-Test	0.0000026
240/24	R19G02-GAL4/III (at 32ºC)	0.01043	Sign-Test	0.0000026
250/25	UAS-*shi*^{ts1}/III (at 24ºC)	0.00024	Sign-Test	0.0000108
250/25	UAS-*shi*^{ts1}/III (at 32ºC)	0.00604	Sign-Test	0.0000015
230/23	R19G02-GAL4/UAS-*shi*^{ts1} (at 24ºC)	0.00037	Sign-Test	0.0000044
230/23	R19G02-GAL4/UAS-*shi*^{ts1} (at 32ºC)	0.10436	t-Test	0.7027905

Table 49: Statistical analysis for Figure 33B

Table 49A Pair-wise statistical analysis with Wilcoxon matched pair test where “N” is the total number of trials and “n” is the number of flies tested.

N/n	Genotype	Z value	p-value
240/24	R12D09-GAL4/III (at 24ºC)	0.1703885	0.8647046
	R12D09-GAL4/III (at 32ºC)		
250/25	UAS-*shi*^{ts1}/III (at 24ºC)	0.0851942	0.9321069
	UAS-*shi*^{ts1}/III (at 32ºC)		
240/24	R12D09-GAL4/UAS-*shi*^{ts1} (at 24ºC)	4.1212261	0.0000376
	R12D09-GAL4/UAS-*shi*^{ts1} (at 32ºC)		

Table 49B Tests for normality (Shapiro-Wilk) and comparison against chance level (58%)

N/n	Genotype	Normality score	Statistical test	p-value
240/24	R12D09-GAL4/III (at 24ºC)	0.00803	Sign-Test	0.0000026
240/24	R12D09-GAL4/III (at 32ºC)	0.00217	Sign-Test	0.0000026
250/25	UAS-*shi*^{ts1}/III (at 24ºC)	0.00024	Sign-Test	0.0000108
250/25	UAS-*shi*^{ts1}/III (at 32ºC)	0.00604	Sign-Test	0.0000015
240/24	R12D09-GAL4/UAS-*shi*^{ts1} (at 24ºC)	0.00521	Sign-Test	0.0000026
240/24	R12D09-GAL4/UAS-*shi*^{ts1} (at 32ºC)	0.01003	Sign-Test	0.3074341

Table 50: Statistical analysis for Figure 43A

Table 50A Pair-wise statistical analysis with Wilcoxon matched pair test where “N” is the total number of trials and “n” is the number of flies tested.

N/n	Genotype	Z value	p-value
230/23	R75H04-GAL4/III (at 24ºC)	0.3919532	0.6950930
	R75H04-GAL4/III (at 32ºC)		
250/25	UAS-*shi*^{ts1}/III (at 24ºC)	0.0851942	0.9321069
	UAS-*shi*^{ts1}/III (at 32ºC)		
230/23	R75H04-GAL4/UAS-*shi*^{ts1} (at 24ºC)	4.1069047	0.0000401
	R75H04-GAL4/UAS-*shi*^{ts1} (at 32ºC)		

Table 50B Tests for normality (Shapiro-Wilk) and comparison against chance level (58%)

N/n	Genotype	Normality score	Statistical test	p-value
230/23	R75H04-GAL4/III (at 24ºC)	0.00305	Sign-Test	0.0000044
230/23	R75H04-GAL4/III (at 32ºC)	0.00426	Sign-Test	0.0000044
250/25	UAS-*shi*^{ts1}/III (at 24ºC)	0.00024	Sign-Test	0.0000108
250/25	UAS-*shi*^{ts1}/III (at 32ºC)	0.00604	Sign-Test	0.0000015
230/23	R75H04-GAL4/UAS-*shi*^{ts1} (at 24ºC)	0.00284	Sign-Test	0.0000044
230/23	R75H04-GAL4/UAS-*shi*^{ts1} (at 32ºC)	0.05063	t-Test	0.0179551

Table 51: Statistical analysis for Figure 43B

Table 51A Pair-wise statistical analysis with Wilcoxon matched pair test where “N” is the total number of trials and “n” is the number of flies tested.

N/n	Genotype	Z value	p-value
250/25	R32A11-GAL4/III (at 24ºC)	2.1065457	0.0351577
	R32A11-GAL4/III (at 32ºC)		
250/25	UAS-*shi*^{ts1}/III (at 24ºC)	0.0851942	0.9321069
	UAS-*shi*^{ts1}/III (at 32ºC)		
250/25	R32A11-GAL4/UAS-*shi*^{ts1} (at 24ºC)	4.2857142	0.0000182
	R32A11-GAL4/UAS-*shi*^{ts1} (at 32ºC)		

Table 51B Tests for normality (Shapiro-Wilk) and comparison against chance level (58%)

N/n	Genotype	Normality score	Statistical test	p-value
250/25	R32A11-GAL4/III (at 24ºC)	0.01293	Sign-Test	0.0000015
250/25	R32A11-GAL4/III (at 32ºC)	0.02949	Sign-Test	0.0000015
250/25	UAS-*shi*^{ts1}/III (at 24ºC)	0.00024	Sign-Test	0.0000108
250/25	UAS-*shi*^{ts1}/III (at 32ºC)	0.00604	Sign-Test	0.0000015
250/25	R32A11-GAL4/UAS-*shi*^{ts1} (at 24ºC)	0.00300	Sign-Test	0.0000015
250/25	R32A11-GAL4/UAS-*shi*^{ts1} (at 32ºC)	0.68450	t-Test	0.0641818

Table 52: Statistical analysis for Figure 43C

Table 52A Pair-wise statistical analysis with Wilcoxon matched pair test where “N” is the total number of trials and “n” is the number of flies tested.

N/n	Genotype	Z value	p-value
260/26	R18A05-GAL4/III (at 24ºC)	2.3113837	0.0208123
	R18A05-GAL4/III (at 32ºC)		
250/25	UAS-*shi*^{ts1}/III (at 24ºC)	0.0851942	0.9321069
	UAS-*shi*^{ts1}/III (at 32ºC)		
260/26	R18A05-GAL4/UAS-*shi*^{ts1} (at 24ºC)	0.9307578	0.3519795
	R18A05-GAL4/UAS-*shi*^{ts1} (at 32ºC)		

Table 52B Tests for normality (Shapiro-Wilk) and comparison against chance level (58%)

N/n	Genotype	Normality score	Statistical test	p-value
260/26	R18A05-GAL4/III (at 24ºC)	0.00133	Sign-Test	0.0000009
260/26	R18A05-GAL4/III (at 32ºC)	0.03012	Sign-Test	0.0000009
250/25	UAS-*shi*^{ts1}/III (at 24ºC)	0.00024	Sign-Test	0.0000108
250/25	UAS-*shi*^{ts1}/III (at 32ºC)	0.00604	Sign-Test	0.0000015
260/26	R18A05-GAL4/UAS-*shi*^{ts1} (at 24ºC)	0.00722	Sign-Test	0.0000009
260/26	R18A05-GAL4/UAS-*shi*^{ts1} (at 32ºC)	0.00224	Sign-Test	0.0000009

8.3 Role of Tau protein in visual working memory

Table 53: Statistical analysis for Figure 47A

Table 53A Multiple comparison of genotypes using Kruskal Wallis test (with in-built Bonferroni correction) where "N" is the total number of trials and "n" is the number of flies tested. All boxes contain p-values.

N/n	Genotype	WT-CS (3d)	*Tau*^{del} (3d)	*Tau*^{KO} (3d)
250/25	WT-CS (3d)		0.0000044	0.0000000
250/25	*Tau*^{del} (3d)	0.0000044		~1.000000
250/25	*Tau*^{KO} (3d)	0.0000000	~1.000000	

Table 53B Tests for normality (Shapiro-Wilk) and comparison against chance level (58%)

N/n	Genotype	Normality score	Statistical test	p-value
250/25	WT-CS (3d)	0.00466	Sign-Test	0.0000015
250/25	*Tau*^{del} (3d)	0.01401	Sign-Test	0.0013742
250/25	*Tau*^{KO} (3d)	0.04568	Sign-Test	0.0455002

Table 54: Statistical analysis for Figure 47B

Table 54A Multiple comparison of genotypes using Kruskal Wallis test (with in-built Bonferroni correction) where "N" is the total number of trials and "n" is the number of flies tested. All boxes contain p-values.

N/n	Genotype	WT-CS (3d)	*Tau*^{del} (3d, Tet. treated)	*Tau*^{KO} (3d, Tet. treated)
250/25	WT-CS (3d)		0,8269703	~1.000000
250/25	*Tau*^{del} (3d,Tet. treated)	0.8269703		0.6068636
250/25	*Tau*^{KO} (3d,Tet. treated)	~1.000000	0,6068636	

Table 54B Tests for normality (Shapiro-Wilk) and comparison against chance level (58%)

N/n	Genotype	Normality score	Statistical test	p-value
250/25	WT-CS (3d)	0.00850	Sign-Test	0.0000015
250/25	*Tau*^{del} (3d, Tet. treated)	0.01290	Sign-Test	0.0000633
250/25	*Tau*^{KO} (3d, Tet. treated)	0.00153	Sign-Test	0.0000015

Table 55: Statistical analysis for Figure 48

Table 55A Multiple comparison of genotypes using Kruskal Wallis test (with in-built Bonferroni correction) where "N" is the total number of trials and "n" is the number of flies tested. All boxes contain p-values.

N/n	Genotype	WT-CS (2w)	*Tau*^{del} (2w, Tet. treated)	*Tau*^{KO} (2w, Tet. treated)
250/25	WT-CS (2w)		0.0000008	0.0000000
250/25	*Tau*^{del} (2w, Tet. treated)	0.0000008		0.5698276
250/25	*Tau*^{KO} (2w, Tet. treated)	0.0000000	0.5698276	

Table 55B Tests for normality (Shapiro-Wilk) and comparison against chance level (58%)

N/n	Genotype	Normality score	Statistical test	p-value
250/25	WT-CS (2w)	0.00690	Sign-Test	0.0000015
250/25	*Tau*^{del} (2w, Tet. treated)	0.17405	t-Test	0.6796347
250/25	*Tau*^{KO} (2w, Tet. treated)	0.22764	t-Test	0.0039948

Table 56: Statistical analysis for Figure 49A

Table 56A Multiple comparison of genotypes using Kruskal Wallis test (with in-built Bonferroni correction) where "N" is the total number of trials and "n" is the number of flies tested. All boxes contain p-values.

N/n	Genotype	WT-CS (3d)	*Tau*^{del}/III (3d)	*Tau*^{KO}/III (3d)
250/25	WT-CS (3d)		0.0000335	0.0000451
250/25	*Tau*^{del}/III (3d)	0.0000335		~1.000000
250/25	*Tau*^{KO}/III (3d)	0.0000451	~1.000000	

Table 56B Tests for normality (Shapiro-Wilk) and comparison against chance level (58%)

N/n	Genotype	Normality score	Statistical test	p-value
250/25	WT-CS (3d)	0.00090	Sign-Test	0.0000015
250/25	*Tau*^{del}/III (3d)	0.01549	Sign-Test	0.0000633
250/25	*Tau*^{KO}/III (3d)	0.16570	t-Test	0.0000470

Table 57: Statistical analysis for Figure 49B

Table 57A Multiple comparison of genotypes using Kruskal Wallis test (with in-built Bonferroni correction) where "N" is the total number of trials and "n" is the number of flies tested. All boxes contain p-values.

N/n	Genotype	WT-CS (3d)	*Tau*^{del}/III (3d, Tet. treated)	*Tau*^{KO}/III (3d, Tet. treated)
250/25	WT-CS (3d)		~1.000000	~1.000000
250/25	*Tau*^{del}/III (3d,Tet. treated)	~1.000000		0.3892047
250/25	*Tau*^{KO}/III (3d,Tet. treated)	~1.000000	0.3892047	

Table 57B Tests for normality (Shapiro-Wilk) and comparison against chance level (58%)

N/n	Genotype	Normality score	Statistical test	p-value
250/25	WT-CS (3d)	0.00850	Sign-Test	0.0000015
250/25	*Tau*^{del}/III (3d, Tet. treated)	0.00466	Sign-Test	0.0000015
250/25	*Tau*^{KO}/III (3d, Tet. treated)	0.00281	Sign-Test	0.0000015

Table 58: Statistical analysis for Figure 50A

Table 58A Multiple comparison of genotypes using Kruskal Wallis test (with in-built Bonferroni correction) where “N” is the total number of trials and “n” is the number of flies tested. All boxes contain p-values.

N/n	Genotype	WT-CS (2w)	*Tau*^{del}/III (2w, Tet. treated)	*Tau*^{KO}/III (2w, Tet. treated)
250/25	WT-CS (2w)		0.0000063	0.0000001
250/25	*Tau*^{del}/III (2w, Tet. treated)	0.0000063		~1.000000
250/25	*Tau*^{KO}/III (2w, Tet. treated)	0.0000001	~1.000000	

Table 58B Tests for normality (Shapiro-Wilk) and comparison against chance level (58%)

N/n	Genotype	Normality score	Statistical test	p-value
250/25	WT-CS (2w)	0.00690	Sign-Test	0.0000015
250/25	*Tau*^{del}/III (2w, Tet. treated)	0.29898	t-Test	0.0120152
250/25	*Tau*^{KO}/III (2w, Tet. treated)	0.00445	Sign-Test	0.0013742

Table 59: Statistical analysis for Figure 50B

Table 59A Multiple comparison of genotypes using Kruskal Wallis test (with in-built Bonferroni correction) where “N” is the total number of trials and “n” is the number of flies tested. All values in the boxes are p-values

N/n	Genotype	WT-CS (3w)	*Tau*^{del}/III (3w, Tet. treated)	*Tau*^{KO}/III (3w, Tet. treated)
250/25	WT-CS (3w)		0.0000005	0.0000000
250/25	*Tau*^{del}/III (3w, Tet. treated)	0.0000005		~1.000000
250/25	*Tau*^{KO}/III (3w, Tet. treated)	0.0000000	~1.000000	

Table 59B Tests for normality (Shapiro-Wilk) and comparison against chance level (58%)

N/n	Genotype	Normality score	Statistical test	p-value
250/25	WT-CS (3w)	0.01380	Sign-Test	0.0000015
250/25	*Tau*^{del}/III (3w, Tet. treated)	0.01618	Sign-Test	0.6891565
250/25	*Tau*^{KO}/III (3w, Tet. treated)	0.00225	Sign-Test	0.2301393

Table 60: Statistical analysis for Figure 51A

Table 60A Multiple comparison of genotypes using Kruskal Wallis test (with in-built Bonferroni correction) where "N" is the total number of trials and "n" is the number of flies tested. All boxes contain p-values.

N/n	Genotype	WT-CS (3d)	*hTau*^{WT} (3d)	*hTau*$^{K/I}$ (3d)	*hTau*$^{P/L}$ (3d)	*hTau*$^{V/M}$(3d)
250/25	WT-CS (3d)		~1.000000	0.0000000	0.0001984	0.0004259
250/25	*hTau*^{WT} (3d)	~1.000000		0.0000000	0.0006097	0.0012541
250/25	*hTau*$^{K/I}$ (3d)	0.0000000	0.0000000		0.6684119	0.4480819
250/25	*hTau*$^{P/L}$ (3d)	0.0001984	0.0006097	0.6684119		~1.000000
250/25	*hTau*$^{V/M}$ (3d)	0.0004259	0.0012541	0.4480819	~1.000000	

Table 60B Tests for normality (Shapiro-Wilk) and comparison against chance level (58%)

N/n	Genotype	Normality score	Statistical test	p-value
250/25	WT-CS (3d)	0.00090	Sign-Test	0.0000015
250/25	*hTau*^{WT} (3d)	0.00065	Sign-Test	0.0000015
250/25	*hTau*$^{K/I}$ (3d)	0.18259	t-Test	~1.000000
250/25	*hTau*$^{P/L}$ (3d)	0.01480	Sign-Test	0.0003182
250/25	*hTau*$^{V/M}$ (3d)	0.01149	Sign-Test	0.0013742

Table 61: Statistical analysis for Figure 51B

Table 61A Multiple comparison of genotypes using Kruskal Wallis test (with in-built Bonferroni correction) where "N" is the total number of trials and "n" is the number of flies tested. All boxes contain p-values.

N/n	Genotype	WT-CS (3d)	*hTau*^{WT} (3d, Tet. treated)	*hTau*$^{K/I}$ (3d, Tet. treated)	*hTau*$^{P/L}$ (3d, Tet. treated)	*hTau*$^{V/M}$(3d, Tet. treated)
250/25	WT-CS (3d)		~1.000000	0,0000015	0,0001439	0,0000139
250/25	*hTau*^{WT} (3d, Tet. treated)	~1.000000		$<10^{-7}$	0.0000067	0.0000005
250/25	*hTau*$^{K/I}$ (3d, Tet. treated)	0.0000015	$<10^{-7}$		~1.000000	~1.000000
250/25	*hTau*$^{P/L}$ (3d, Tet. treated)	0.0001439	0.0000067	~1.000000		~1.000000
230/23	*hTau*$^{V/M}$ (3d, Tet. treated)	0.0000139	0.0000005	1.0000000	~1.000000	

Table 61B Tests for normality (Shapiro-Wilk) and comparison against chance level (58%)

N/n	Genotype	Normality score	Statistical test	p-value
250/25	WT-CS (3d)	0.00328	Sign-Test	0.0000015
250/25	*hTau*^{WT} (3d, Tet. treated)	0.00046	Sign-Test	0.0000015
250/25	*hTau*$^{K/I}$ (3d, Tet. treated)	0.03616	Sign-Test	0,0051102
250/25	*hTau*$^{P/L}$ (3d, Tet. treated)	0.05310	t-Test	0.0025100
230/23	*hTau*$^{V/M}$ (3d, Tet. treated)	0.03505	Sign-Test	0,0123433

Table 62: Statistical analysis for Figure 52

Table 62A Multiple comparison of genotypes using Kruskal Wallis test (with in-built Bonferroni correction) where “N” is the total number of trials and “n” is the number of flies tested. All boxes contain p-values.

N/n	Genotype	WT-CS (3d)	*hTau*^{WT}/III (3d)	*hTau*$^{K/I}$/III (3d)	*hTau*$^{P/L}$/III (3d)	*hTau*$^{V/M}$/III (3d)
250/23	WT-CS (3d)		0.0134216	~1.000000	~1.000000	0.0375044
250/20	*hTau*^{WT}/III (3d)	0.0134216		0.0101321	0.0049404	~1.000000
250/25	*hTau*$^{K/I}$/III (3d)	~1.000000	0.0101321		~1.000000	0.0289713
250/25	*hTau*$^{P/L}$/III (3d)	~1.000000	0.0049404	~1.000000		0.0149537
250/25	*hTau*$^{V/M}$/III (3d)	0.0375044	~1.000000	0.0289713	0.0149537	

Table 62B Tests for normality (Shapiro-Wilk) and comparison against chance level (58%)

N/n	Genotype	Normality score	Statistical test	p-value
250/25	WT-CS (3d)	0.00009	Sign-Test	0.0000015
250/25	*hTau*^{WT}/III (3d)	0.01964	Sign-Test	0.0000633
250/25	*hTau*$^{K/I}$/III (3d)	0.00014	Sign-Test	0.0000108
250/25	*hTau*$^{P/L}$/III (3d)	0.00017	Sign-Test	0.0000015
250/25	*hTau*$^{V/M}$/III (3d)	0.04878	Sign-Test	0.0000633

Table 63: Statistical analysis for Figure 53A

Table 63A Multiple comparison of genotypes using Kruskal Wallis test (with in-built Bonferroni correction) where “N” is the total number of trials and “n” is the number of flies tested. All boxes contain p-values.

N/n	Genotype	WT-CS (2w)	*hTau*^{WT}/III (2w)	*hTau*$^{K/I}$/III (2w)	*hTau*$^{P/L}$/III (2w)	*hTau*$^{V/M}$/III (2w)
250/25	WT-CS (2w)		~1.000000	0.0000890	$<10^{-7}$	0.0001578
250/25	*hTau*^{WT}/III (2w)	~1.000000		0.0022009	0.0000004	0.0035719
250/25	*hTau*$^{K/I}$/III (2w)	0.0000890	0.0022009		0.7475028	~1.000000
250/25	*hTau*$^{P/L}$/III (2w)	$<10^{-7}$	0.0000004	0.7475028		0.5653240
250/25	*hTau*$^{V/M}$/III (2w)	0.0001578	0.0035719	~1.000000	0.5653240	

Table 63B Tests for normality (Shapiro-Wilk) and comparison against chance level (58%)

N/n	Genotype	Normality score	Statistical test	p-value
250/25	WT-CS (2w)	0.00136	Sign-Test	0.0000015
250/25	*hTau*^{WT}/III (2w)	0.00511	Sign-Test	0.0000015
250/25	*hTau*$^{K/I}$/III (2w)	0.00726	Sign-Test	0.0013742
250/25	*hTau*$^{P/L}$/III (2w)	0.01049	Sign-Test	0.6891565
250/25	*hTau*$^{V/M}$/III (2w)	0.07652	t-Test	0.0007246

Table 64: Statistical analysis for Figure 53B

Table 64A Multiple comparison of genotypes using Kruskal Wallis test (with in-built Bonferroni correction) where “N” is the total number of trials and “n” is the number of flies tested. All boxes contain p-values.

N/n	Genotype	WT-CS (3w)	*hTau*^{WT}/III (3w)	*hTau*$^{K/I}$/III (3w)	*hTau*$^{P/L}$/III (3w)	*hTau*$^{V/M}$/III (3w)
250/25	WT-CS (3w)		~1.000000	0.0000003	0.0000004	$<10^{-7}$
220/22	*hTau*^{WT}/III (3w)	~1.000000		0.0002829	0.0006349	0.0000754
170/17	*hTau*$^{K/I}$/III (3w)	0.0000003	0.0002829		~1.000000	~1.000000
250/25	*hTau*$^{P/L}$/III (3w)	0.0000004	0.0006349	~1.000000		~1.000000
250/25	*hTau*$^{V/M}$/III (3w)	$<10^{-7}$	0.0000754	~1.000000	~1.000000	

Table 64B Tests for normality (Shapiro-Wilk) and comparison against chance level (58%)

N/n	Genotype	Normality score	Statistical test	p-value
250/25	WT-CS (3w)	0.00174	Sign-Test	0.0000015
220/22	*hTau*^{WT}/III (3w)	0.06855	t-Test	0.0000000
170/17	*hTau*$^{K/I}$/III (3w)	0.39421	t-Test	0.3378489
250/25	*hTau*$^{P/L}$/III (3w)	0.01332	Sign-Test	0.4237107
250/25	*hTau*$^{V/M}$/III (3w)	0.16975	t-Test	0.4091063

8.4 Licenses from publishing houses to reproduce figures

8.4.1 License from Elsevier to reproduce **Figure 4**

License Details

This Agreement between Johannes Gutenberg University Mainz -- Anjana Venkataramanan ("You") and Elsevier ("Elsevier") consists of your license details and the terms and conditions provided by Elsevier and Copyright Clearance Center.

Print Copy

License Number	4795450367837
License date	Mar 24, 2020
Licensed Content Publisher	Elsevier
Licensed Content Publication	Current Biology
Licensed Content Title	Visual Working Memory Requires Permissive and Instructive NO/cGMP Signaling at Presynapses in the Drosophila Central Brain
Licensed Content Author	Sara Kuntz,Burkhard Poeck,Roland Strauss
Licensed Content Date	Mar 6, 2017
Licensed Content Volume	27
Licensed Content Issue	5
Licensed Content Pages	11
Type of Use	reuse in a thesis/dissertation
Portion	figures/tables/illustrations
Number of figures/tables/illustrations	1
Format	both print and electronic
Are you the author of this Elsevier article?	No
Will you be translating?	No
Title	Behavioural and neuroanatomical analysis of a visual working memory in Drosophila melanogaster
Institution name	Johannes Gutenberg University
Expected presentation date	May 2020
Portions	Figure 7, Page 620
Requestor Location	Anjana Venkataramanan Johannes Gutenberg University Mainz iDN Hanns-Dieter-Hüsch-Weg 15 Mainz, Rhineland-Palatinate 55099 Germany Attn: Anjana Venkataramanan
Publisher Tax ID	GB 494 6272 12
Total	**0.00 EUR**

BACK

8.4.2 License from John Wiley and Sons to reproduce **Figure 6B**

License Details

This Agreement between Johannes Gutenberg University Mainz -- Anjana Venkataramanan ("You") and John Wiley and Sons ("John Wiley and Sons") consists of your license details and the terms and conditions provided by John Wiley and Sons and Copyright Clearance Center.

Print Copy

License Number	4795440027832
License date	Mar 24, 2020
Licensed Content Publisher	John Wiley and Sons
Licensed Content Publication	Annals of Neurology
Licensed Content Title	Pick's disease associated with the novel Tau gene mutation K369I
Licensed Content Author	Hans A. Kretzschmar, Michel Goedert, Maria Grazia Spillantini, et al
Licensed Content Date	Aug 27, 2001
Licensed Content Volume	50
Licensed Content Issue	4
Licensed Content Pages	11
Type of Use	Dissertation/Thesis
Requestor type	University/Academic
Format	Print and electronic
Portion	Figure/table
Number of figures/tables	1
Will you be translating?	No
Title of your thesis / dissertation	Behavioural and neuroanatomical analysis of a visual working memory in Drosophila melanogaster
Expected completion date	May 2020
Expected size (number of pages)	
Original Wiley figure/table number(s)	Figure 5
Requestor Location	Anjana Venkataramanan Johannes Gutenberg University Mainz iDN Hanns-Dieter-Hüsch-Weg 15 Mainz, Rhineland-Palatinate 55099 Germany Attn: Anjana Venkataramanan
Publisher Tax ID	EU826007151
Total	**0.00 EUR**

BACK

8.4.3 License from Springer Nature to reproduce **Figure 10**

License Details

This Agreement between Johannes Gutenberg University Mainz -- Anjana Venkataramanan ("You") and Springer Nature ("Springer Nature") consists of your license details and the terms and conditions provided by Springer Nature and Copyright Clearance Center.

Print Copy

License Number	4794430828830
License date	Mar 22, 2020
Licensed Content Publisher	Springer Nature
Licensed Content Publication	Nature
Licensed Content Title	Pain-sensing TRPA1 channel resolved
Licensed Content Author	David E. Clapham
Licensed Content Date	Apr 8, 2015
Type of Use	Thesis/Dissertation
Requestor type	academic/university or research institute
Format	print and electronic
Portion	figures/tables/illustrations
Number of figures/tables/illustrations	1
High-res required	no
Will you be translating?	no
Circulation/distribution	2000 - 4999
Author of this Springer Nature content	no
Title	Behavioural and neuroanatomical analysis of a visual working memory in Drosophila melanogaster
Institution name	Johannes Gutenberg University Mainz
Expected presentation date	May 2020
Portions	Figure 1, page 440
Requestor Location	Anjana Venkataramanan Johannes Gutenberg University Mainz iDN Hanns-Dieter-Hüsch-Weg 15 Mainz, Rhineland-Palatinate 55099 Germany Attn: Anjana Venkataramanan
Total	**0.00 EUR**

BACK

8.4.4 License from COMPANY OF BIOLOGISTS LTD. to reproduce **Figure 18**

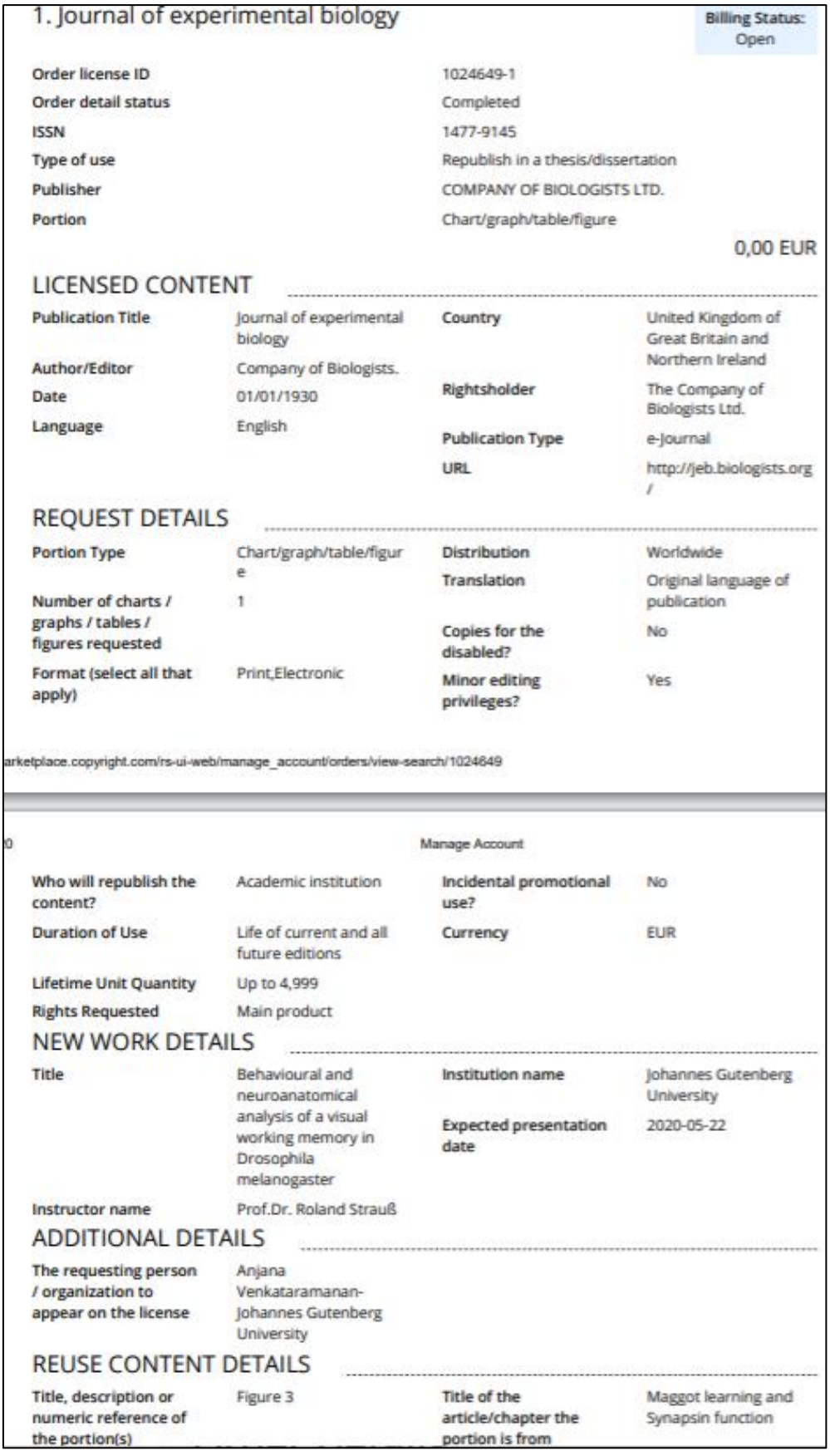

1. Journal of experimental biology

Billing Status: Open

Order license ID	1024649-1
Order detail status	Completed
ISSN	1477-9145
Type of use	Republish in a thesis/dissertation
Publisher	COMPANY OF BIOLOGISTS LTD.
Portion	Chart/graph/table/figure

0,00 EUR

LICENSED CONTENT

Publication Title	Journal of experimental biology	Country	United Kingdom of Great Britain and Northern Ireland
Author/Editor	Company of Biologists.	Rightsholder	The Company of Biologists Ltd.
Date	01/01/1930	Publication Type	e-Journal
Language	English	URL	http://jeb.biologists.org/

REQUEST DETAILS

Portion Type	Chart/graph/table/figure	Distribution	Worldwide
Number of charts / graphs / tables / figures requested	1	Translation	Original language of publication
Format (select all that apply)	Print,Electronic	Copies for the disabled?	No
		Minor editing privileges?	Yes

arketplace.copyright.com/rs-ui-web/manage_account/orders/view-search/1024649

0 Manage Account

Who will republish the content?	Academic institution	Incidental promotional use?	No
Duration of Use	Life of current and all future editions	Currency	EUR
Lifetime Unit Quantity	Up to 4,999		
Rights Requested	Main product		

NEW WORK DETAILS

Title	Behavioural and neuroanatomical analysis of a visual working memory in Drosophila melanogaster	Institution name	Johannes Gutenberg University
		Expected presentation date	2020-05-22
Instructor name	Prof.Dr. Roland Strauß		

ADDITIONAL DETAILS

The requesting person / organization to appear on the license	Anjana Venkataramanan-Johannes Gutenberg University

REUSE CONTENT DETAILS

Title, description or numeric reference of the portion(s)	Figure 3	Title of the article/chapter the portion is from	Maggot learning and Synapsin function

9. Acknowledgements

10. Curriculum Vitae